POLYCYCLIC AROMATIC HYDROCARBONS: EXPLORING NEW PROCESSES AND MATERIALS FOR ELECTRONICS

A Thesis
Presented to
The Academic Faculty

by

Jose Baltazar

In Partial Fulfillment
of the Requirements for the Degree
Doctor of Philosophy in the
School of Chemical and Biomolecular Engineering

Georgia Institute of Technology
May 2014

POLYCYCLIC AROMATIC HYDROCARBONS:

EXPLORING NEW PROCESSES AND MATERIALS FOR

ELECTRONICS

Approved by:

Dr. Clifford L. Henderson, Advisor
School of Chemical and Biomolecular
Engineering
Georgia Institute of Technology

Dr. Laren M. Tolbert
School of Chemistry and Biochemistry
Georgia Institute of Technology

Dr. Dennis W. Hess
School of Chemical and Biomolecular
Engineering
Georgia Institute of Technology

Dr. Elsa Reichmanis
School of Chemical and Biomolecular
Engineering
Georgia Institute of Technology

Dr. Samuel Graham
School of Mechanical Engineering
Georgia Institute of Technology

Date Approved:[December 13, 2013]

To all, whom I am lucky to have as "My Family".
Muito Obrigado!

ACKNOWLEDGEMENTS

TABLE OF CONTENTS

CHAPTER 3

CREATING GRAPHENE P-N JUNCTIONS USING SELF-ASSEMBLED

CHAPTER 4

PHOTOCHEMICAL DOPING AND TUNING OF THE WORK FUNCTION AND

DIRAC POINT IN GRAPHENE USING PHOTOACID AND PHOTOBASE

CHAPTER 5

CHAPTER 8

SYNTHESIS OF GRAPHITIC NANORIBBONS (GNRS) VIA ENCAPSULATION IN

CHAPTER 9

LIST OF TABLES

LIST OF FIGURES

LIST OF SYMBOLS

0-D	zero-dimensional
1-D	one-dimensional
3-D	three-dimensional
2D	2D or G' peak in Raman spectra of graphene
AFM	atomic force microscopy
Ar	argon
Au	gold
A_c	cross-sectional area of the thin film
APTES	3-Aminopropyltriethoxysilane
B.E	binding energy
BOE	Buffered oxide etch
BZ	Brillouin zone
C	carbon
C1s	core level carbon binding energy
C60	buckminsterfullerene (or buckyball) fullerene
C70	C70 fullerene
C=O	carbonyl group
C-OH	carboxyl group
CH_4	methane
C_g	gate capacitance
CMOS	complementary metal–oxide–semiconductor (CMOS)
Cu	copper
CVD	chemical vapor deposition
D-band	D peak in Raman spectra of graphene

DI water	deionized water
DR	double resonance Raman process
e	electron charge
E_{laser}	laser energy
E_{phonon}	phonon energy
EDX	energy-dispersive X-ray spectroscopy
F1s	core level fluorine binding energy
FET	field effect transistor
Fe 2p	iron core level binding energy
$FeCl_3$	iron chloride
FLG	few layer graphene
FoM	figure of merit
FWHM	Full width at half maximum
G	G peak in Raman spectra of graphene
GNRs	graphene nanoribbons/graphitic nanoribbons
GO	graphene oxide
G'	G' or 2D peak in Raman spectra of graphene
G^*	D+G peak in Raman spectra
H_2	hydrogen
hBN	hexagonal boron nitride
HCl	hydrochloric acid
HF	hydrofluoric acid
HNO_3	nitric acid
HOPG	highly oriented pyrolytic graphite
I_{C-}/I_{Cu-}	carbon to copper ion intensity ratio in SIMS measurements
I_{C-}/I_{Ni-}	carbon to nickel ion intensity ratio in SIMS measurements

ID	inner diameter
I_{2D}/I_G	2D over G peak intensity ratio
I_G/I_D	G over D peak intensity ratio
$I_{D/S}$	drain-to-source current
IPA	isopropanol
I-V	drain-to-source current vs. gate voltage
K, K'	Dirac cones in graphene Brillouin zone
L_{ch}	channel length
LEDs	light emitting devices
MEG	multi-layer epitaxial graphene
MLG	multi-layer graphene
$-NH_3^+$	protonated or hydrogen bonded amine
$-NH_2$	free amine
n, k	Optical constants of graphene
N 1s	core level nitrogen binding energy
N	negative
N_2	nitrogen
N1s	nitrogen binding energy
NH_3	amonia
NMP	N-methylpyrrolidone
Ni	nickel
NO_2	nitrogen dioxide
O	optical branches in phonon dispersion of graphene
O_2	oxygen
O 1s	core level oxygen binding energy
-OH	hydroxyl

OFETs	organic field effect transistors
OLEDs	organic light-emitting diodes
OPVs	organic photovoltaic cells
P	positive
PBG	photobase generator
PEIE	polyethylenimine ethoxylated
PAG	photoacid generator
PFES	1H,1H,2H,2H-Perfluorooctyltriethoxysilane
PMMA	Poly(methyl methacrylate)
R	bulk resistance
RGO	reduced graphene oxide
R_P , R_S	Fresnel reflection coefficients
R_{sh}	sheet resistance
Ru	rodinium
S_1, S_2, S_3	electrical probes
SAMs	self assembled monolayers
SEM	secondary electron spectroscopy
Si	silicon
SiC	silicon carbide
SiO_2	silicon dioxide
SKPM	scanning Kelvin probe microscope
sp^2	sp^2 orbital hybridization
t	thin film thickness
T	transmittance
T	transverse branches in phonon dispersion of graphene
TA	transverse acoustic branches in phonon dispersion of graphene

TEM	transmission electron microscopy
UPS	Ultraviolet photoelectron spectroscopy
UHV	ultra high vacuum
$V_{D/S}$	drain-to-source voltage
V_G	gate voltage
V_{NP}	voltage at neutrality point
W_{ch}	channel width
WF	work function
XPS	X-ray photoelectron spectroscopy
Z	out-of-plane branches in phonon dispersion of graphene
ZA	out-of-plane acoustic branches in phonon dispersion of graphene
ZO	out-of-plane optical branches in phonon dispersion of graphene
π	out-of-plane bond
v_F	Fermi velocity of the carriers in graphene
Γ	Brillouin zone center in graphene lattice
$\omega_{G'}$	the frequency in which G' or 2D peak occurs
ω_D	the frequency in which D peak occurs
μ_n	electron mobility
μ_p	hole mobility
μ_0	permeability of free space
$\in_0$	permittivity of free space

SUMMARY

Graphene is a two-dimensional sp^2 hybridized carbon lattice that is also the fundamental building block of graphite. Graphene has attracted significant interest recently due to its distinctive electrical, optical and mechanical properties. These properties have spurred research directed at modifying graphene for use in a variety of electronic, optoelectronic, and sensor technologies. However, before graphene can be used in products, it is necessary to find methods to tune, modify, grow and integrate graphene features while substantially boosting device performance and maintaining current processing compatibility and ease of integration with existing manufacturing infrastructure.

This dissertation focuses on developing techniques for controllably doping the graphene layer through scalable, industry friendly and simple chemical doping; using self-assembled monolayer compounds, photo-acid and photo-base generators, polymers and metal-organic species. We have, in fact, demonstrated simple p-n junctions fabricated in this manner. Characteristic I-V curves indicate the superposition of two separate Dirac points from the p and n regions, confirming an energy separation of neutrality points within the complementary regions; Raman studies of these methods have shown that these processes result in extremely low defect levels in the graphene. Our simple methods for producing patterned doping profiles in graphene films and devices open up a variety of new possibilities for forming complex doping profiles in a simple manner in graphene. This work can enable rapid testing, such as controlled work function tuning, complex doping profiles and simple post-fabrication tuning, of concepts for graphene that may be useful in both interconnect and transparent conductor applications.

In addition to graphene doping, we also investigated approaches to the synthesis of few-layer graphene flakes, since current techniques still produce inferior materials. Exfoliation of Graphene Sheets by an Electron Donor Surfactant was demonstrated to generate few-layers graphene flakes that rival the electrical quality of reduce graphene-oxide (rGO) flakes. Last but not least, Diels-Alder adducts on silica were explored as a controllable carbon precursor for pristine graphene; these allow for a rational direct-growth-of-graphene-on-surface reaction mediated by copper catalyst, without the use of flammable precursors, such as methane, that are used in current methods of chemical vapor deposition synthesis of graphene.

CHAPTER 1

INTRODUCTION AND BACKGROUND

1.1   Overview

Integrated circuit (IC) technology has undergone rapid and dramatic improvements over the past fifty years, which have led to the incredibly complex and powerful IC devices we enjoy today. Modern devices that are commercially available integrate more than a billion transistors in a single chip, a tremendous improvement over the single isolated transistor first developed in the early 1950s at Bell Labs(**Figure 1.1**).[1]

The transistor is the main building block for IC technology, and the principle of the field effect transistor was first proposed by Lilienfeld in 1930[2]. As illustrated in **Figure 1.1**, a transistor consists of a source and drain electrodes with a semi-conducting channel, which can be p or n doped (e.g. commonly through ion implantation[3] or thermal diffusion[4] in silicon electronics), between the two electrodes. The density of the charges carried in the channel is modulated by the voltage applied to the gate electrode.[5]
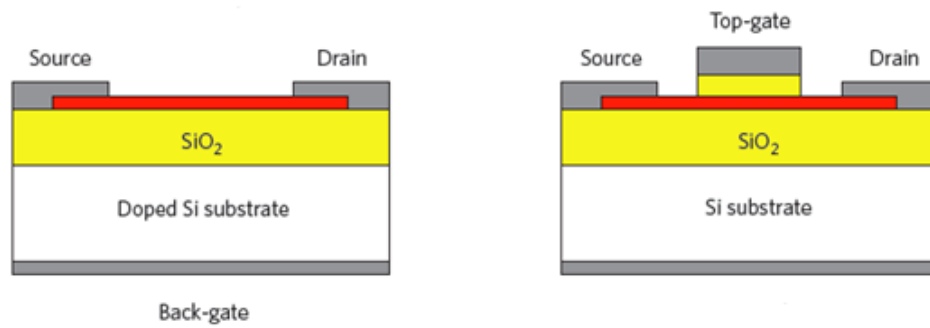
Figure 1.1: (Top) Replica of the first transistor. (Bottom) Schematic for a field effect transistor : Left-bottom-gated, top contact , Right-top gated, top contact (edited).[6]

Inorganic materials have been the dominant choice in building microelectronics technology since its inception in the mid 1900s. Silicon in particular has been by far the most common semiconductor material platform on which to build devices. The popularity of silicon is largely due to the relatively easy formation of a stable, high-quality dielectric on the material in the form of silicon oxide. But three forces are currently poised to drive a potential shift away from inorganic electronic (i.e., conductor and semiconductor) materials: (1) the continued scaling of device dimensions and transistor densities, (2) the interest in non-traditional device forms such as flexible electronics[7], and (3) the desire for very low cost, "printed", and large area electronics.

In the first case, Gordon Moore in 1965 predicted that, "the components of a chip will double every 18 months".[8] Amazingly, or perhaps as a result ultimately of the prediction, this trend has indeed continued from roughly the mid-1950s through today. **Figure 1.2** shows a plot of the number of transistors per single IC device/chip from roughly 1970 through today, consistent with this doubling of devices each 18 to 24 months. However, because this aggressive device scaling, silicon devices are reaching their physical limits in terms of channel mobility, operational frequency, thermal stability, heat dissipation, and many other factors.[8] There could be tremendous benefit to transitioning to semiconducting materials with higher mobilities. Unfortunately switching the IC infrastructure over to the next logical choice of relatively mature compound semiconductors (such as GaAs.) does not gain much in terms of mobility or device frequency at the cost of great expense to change the fabrication infrastructure. What would be desirable is a material that could provide a substantial boost in semiconductor mobility while maintaining compatibility with existing manufacturing infrastructure. Organic

materials in the form of complex nanostructures such as graphene may offer one potential solution to this need. The second force, that of building non-conventional form factor devices (e.g., flexible electronics) also could benefit from the use of organic electronic materials, which inherently may have better capacity to accommodate strain in such flexible applications.[9,10] Finally, the interest in printed, large-area, and low-cost electronics also could benefit from a move away from high-vacuum based processing to more solution-processed materials such as organic semiconductors. In particular, polyaromatic hydrocarbons, ranging from simple compounds such as pentacene to complex nanostructures such as graphene, offer the promise of an exciting array of physical, chemical, and electrical properties that may be useful as the basis for the next generation of electronic devices.
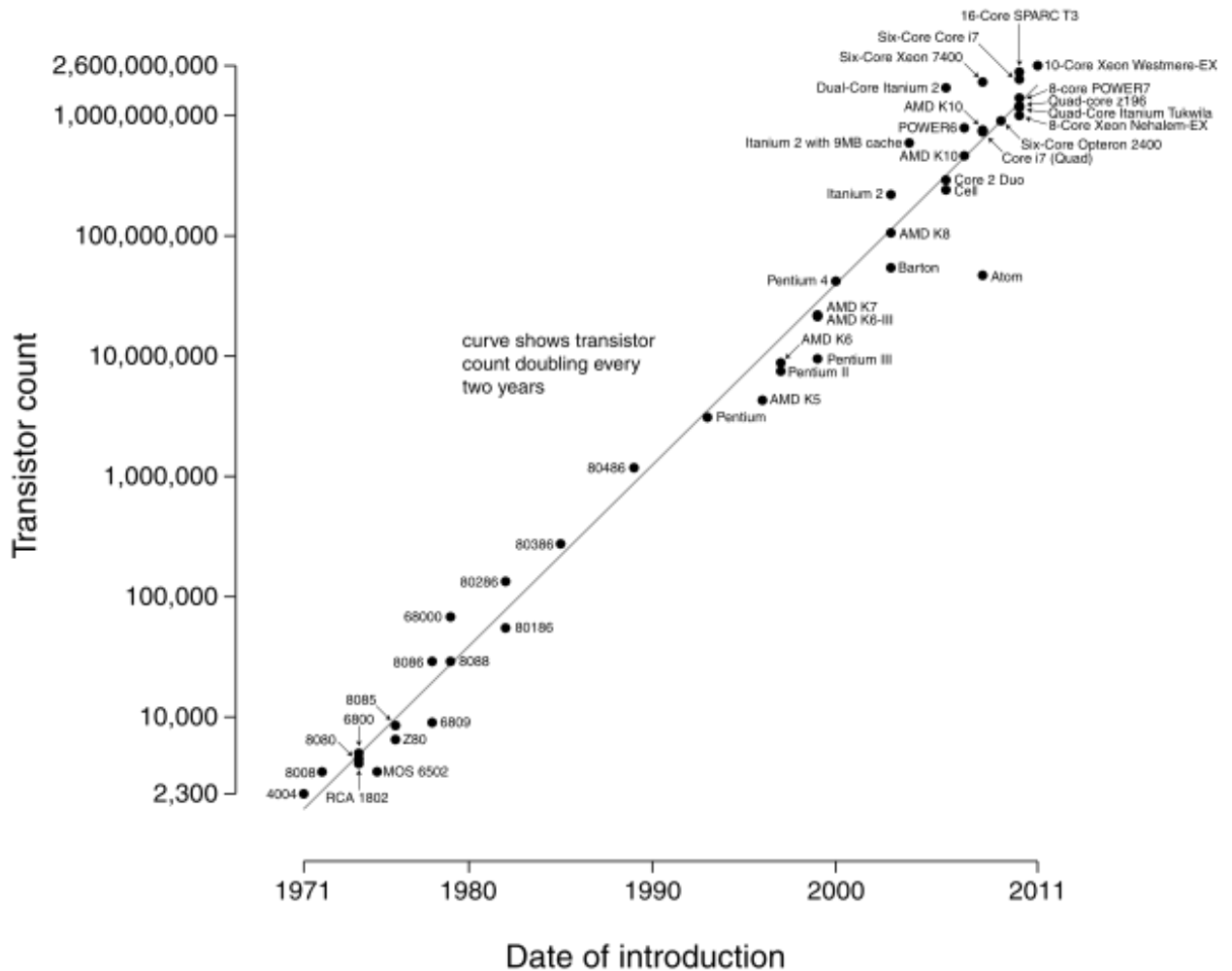
Figure 1.2: Illustration of Moore's law stating that the components of a chip will double every 18 months (Author: Wgsimon).[11]

Organic field-effect transistors (OFETs) based on solution-processable organic polymeric and small molecule organic semiconductors have obtained impressive improvements in their performance during recent years. These devices have been developed to realize low-cost, large-area electronic products and have obtained mobilities in excess of 5 cm^2/Vs.[12] Most of the high mobility organic semiconductor work has been

achieved in vapor deposited films[12,13] that require potentially high temperatures and vacuum. However, there is a real need and an opportunity for solution processable organic materials and low thermal budget processes, since they are compatible with low temperature processing, a fundamental requirement for much of the proposed flexible electronics devices.[7] Even though tremendous improvements have been achieved in organic electronic materials, the mobility values are still below that of silicon which is in the order of 1000 cm^2/Vs (doped silicon). Hence, other materials are being investigated for high performance/demand devices, as for example: graphene.[9,14,15]

1.2   Graphene and Its Properties

Graphene is a flat monolayer of carbon aromatic structures tightly packed into a two-dimensional honeycomb lattice, and it is a single sheet of building unit for all other dimensionalities of graphite structures.[16,17] It can be wrapped up into 0D fullerenes (C60, C70), rolled into 1D carbon nanotubes, or stacked into 3D graphite[15] (**Figure 1.3**). Graphene sheets are one-atom thick, have 2D layers of sp^2-bonded carbon, and are predicted to have unusual properties, including its nearly linear energy dispersion relation that results in electric field induced generation of electrons and holes which travel as massless Dirac fermions with high velocities (**Figure1.3**).[18-20] Carrier mobilities in pristine graphene have been estimated to be as large as 200,000 cm^2/Vs, and it has also demonstrated very high thermal conductivity.[15,17] Furthermore, graphene is one atom thick, making it a perfect substitute for silicon in small high performance devices(**Figure 1.3**).[6]

Graphene is also highly transparent (absorbs 2.3% of white light); it has been shown that reflectance from the monolayer is determined for the infra-red region by the intraband

Drude-Boltzmann conductivity and for higher frequencies by the interband absorption.[21] At low temperatures and high carrier densities, the reflectance from multilayers has a sharp downfall with a subsequent plateau which is caused by the excitations of weakly damped waves in conditions of direct interband electron transitions [22].
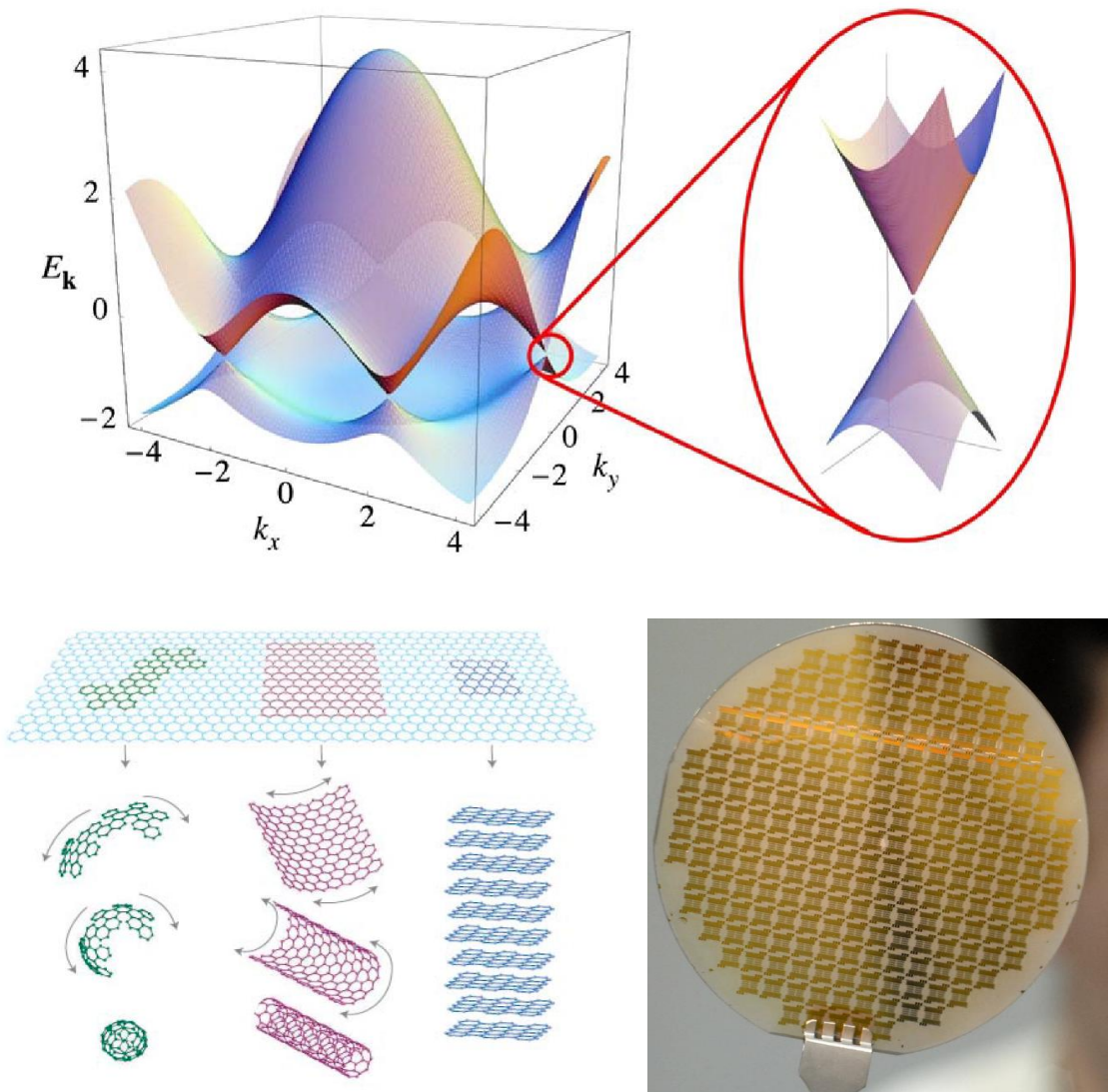
Figure 1.3 (Top-Left) Electronic dispersion in the graphene honeycomb lattice. Inset (Top-Right) Energy bands close to one of the Dirac points.[16] (Bottom-Left) Formation of 0D, 1D, and 3D carbon materials from graphene[15]. (Bottom-Right) Wafer contains more than 20,000 Graphene field effect transistor (G-FET) devices and test structures.[23]

1.3   Graphene Synthesis Methods

Several methods have emerged over the years for the synthesis of graphene. In 2004, Andre Geim and Kostya Novoselov's research group, at Manchester University, UK, used a technique called micromechanical cleavage to extract a single sheet (a monolayer of atoms) from three-dimensional graphite[24]. This exfoliated graphene proved to be an extremely important new 2-D electronic material, and as a result the two scientists were awarded the Nobel Prize in Physics in 2011.[9,15] Unfortunately, micromechanical cleavage cannot be scaled and used industrially.

Another method for graphene formation is epitaxial growth, which grows graphene from SiC substrates. The application of epitaxial graphene in electronic devices originated at Georgia Tech in 2004, created by a group led by Walter deHeer, but epitaxial graphene is expensive and it is not compatible with low temperature applications.[25] An additional method to make graphene is using chemical vapor deposition (CVD). Hydrocarbon gases, such as methane, are typically passed over the metal-catalyst surface under high temperature and low pressure causing the nucleation and growth of graphene. Solid precursors such as PMMA have also been used in CVD synthesis of graphene[26-28]. This technique offers the possibility for scalability, but it requires high temperature and uses hydrogen as the carrier gas. Additionally, the mobilities demonstrated to this point are about two orders of magnitude lower than those of mechanically exfoliated graphene flakes and the resulting films usually contain an uneven number of layers of graphene and spatially varying properties.[9,29 9,30] Last but not least, other methods for graphene formation are via reduction of graphene oxide (rGO)[31] and liquid exfoliation of graphite.[32,33] They both offer large volume processing but the low quality (of rGO) and limited size of the graphene flakes produced (liquid exfoliation) still remain issues that needs to be resolved.[34,35] **Table 1.1** provides a concisely summary of the advantages and disadvantages for each method to synthesize graphene

Table 1.1 Comparison of Common Graphene Production Methods

Synthesis Method	Advantages	Disadvantages
Micromechanical Exfoliation[20]	• High Quality (electrical properties)	• Low yield • Not scalable
Epitaxial SiC Growth[25,36,37]	• Large continuous film area • High quality	• Non- transferable • High temperature • Low vacuum
Reduction of GO[31,38-47]	• Solution processed • High yield • Low Temperature	• Poor electrical properties • Small area flakes
CVD[14,48-53]	• High "quality" • Large area • Transferable	• High temperature • Requires catalyst • Flammable Precursors
Solution Exfoliation[32-34,54]	• Fair Quality • Good Scalability • Low Temperature	• Small area flakes • Colloidal Stability

1.4   Graphene: Applications, Devices and Doping

The good transmittance coupled with high electrical conductivity and low sheet resistance make graphene a potential candidate for primary transparent conductive electrodes in applications such as touch screens, [55] liquid crystal displays, [56] organic photovoltaic cells (OPVs), [57,58] organic light-emitting diodes (OLEDs), [59] or as an interface modifier to improve charge injection or collection in devices. [60,61] Current prices of materials for such applications, such as indium tin oxide (ITO), continue to rise and these could be scarce by 2020.[62,63] This provides a clear window of opportunity for graphene (**Figure 1.4** shows a graphene-based touch-screen panel).
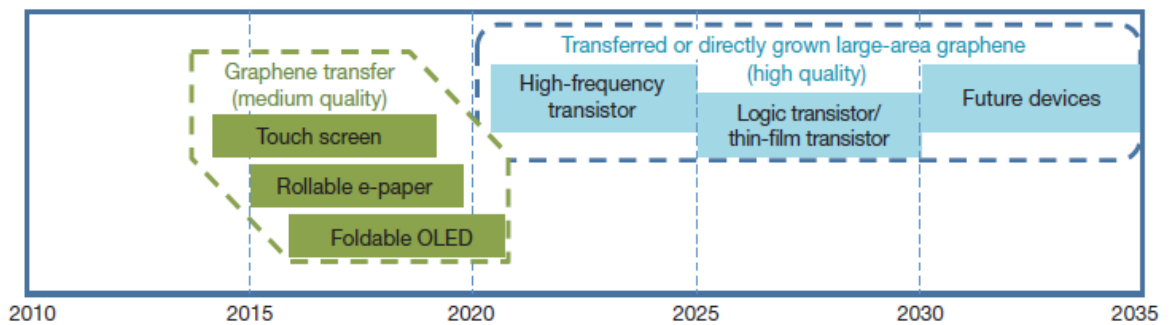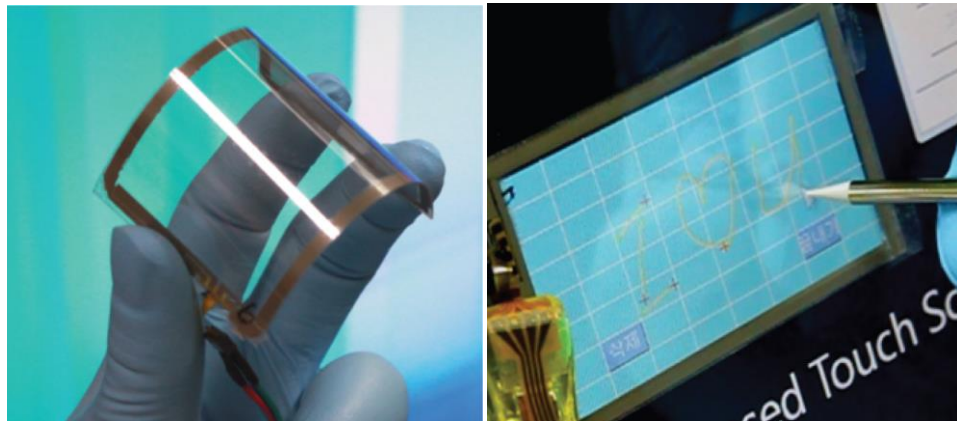
Figure 1.4 (Top-Left) assembled graphene/PET panel showing outstanding flexibility. (Top-Right) A graphene-based touch-screen panel connected to a computer(Picture taken from [55]). (Bottom) Expected Roadmap for graphene based devices.[9]

Other applications for graphene include utilization as detector materials for sensors, since its 2D configuration can also respond to a single gas molecule interaction[46,64,65]. Due to high conductivity in single layer graphene, any adsorption of gas molecules is detectable through measuring the change in resistance. Furthermore this change is detectable at room temperature and such devices have been reported in the literature.[66] As a result of such sensitivity, a variety of chemical species can become attached to the graphene during processing (as well as transfer), as graphene is typically exposed to both aqueous and atmospheric gas environments (adventitious dopants).[67-69] These groups have the ability to unintentionally dope the graphene and alter the electronic properties that are important for most sensor and transistor applications discussed above. The variation in mobility and charge carrier concentration depends on the donor or acceptor nature of the chemical groups.

Controlling the exposure of graphene to these groups provides the opportunity to further tailor its electronic structure by altering their concentration since, they give rise to p- and n-type materials that are important, for a variety of electronic applications (as discussed above). Therefore, understanding the mechanism by which graphene is doped and developing techniques for such doping are required in order to develop appropriate post-transfer treatments for adjusting the presence of these groups on the graphene surface and to obtain the desired electrical properties for the graphene film.
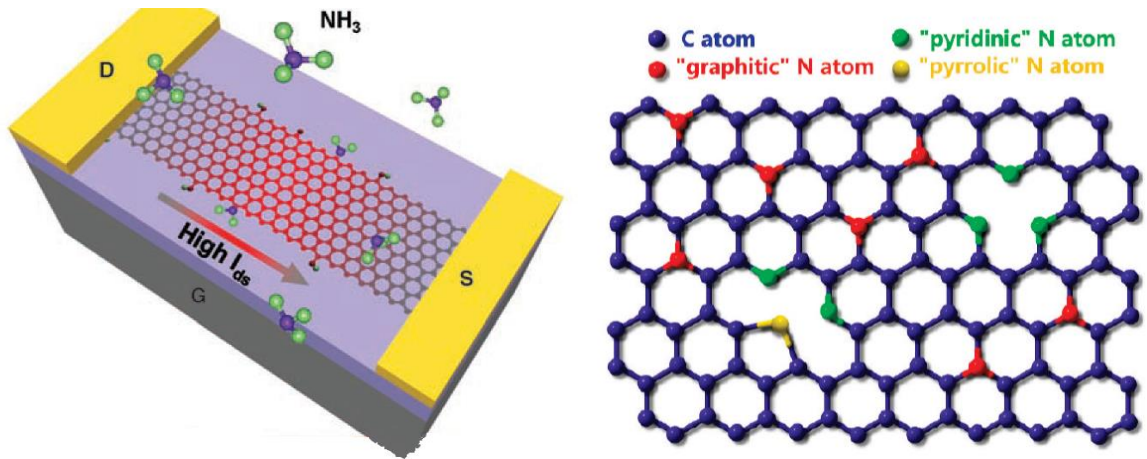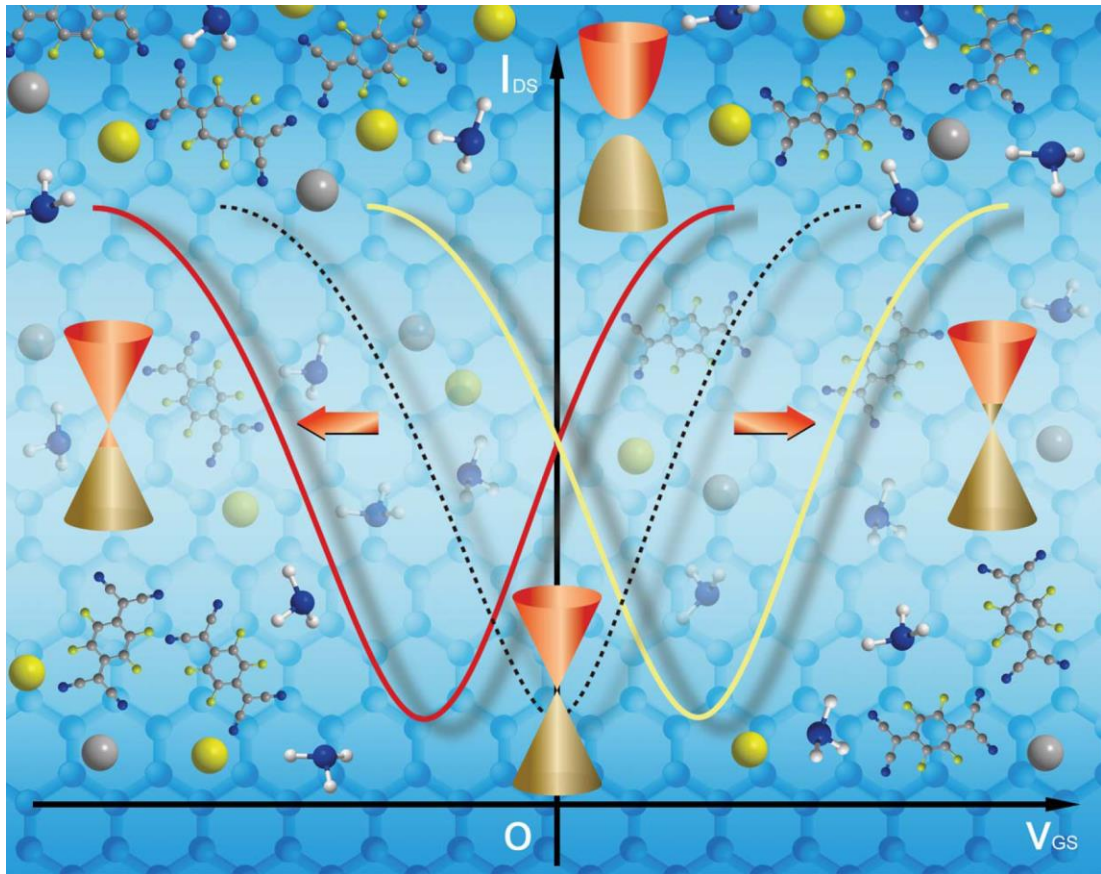
Figure 1.5 (Top) Overview of N and P-doping of graphene: Chemical doping of Graphene aimed at tuning the electronic properties (Band gap, Dirac point) for a variety of applications.[70] **(Bottom-Left)** N-doping of Graphene FET device by e-annealed under high current in NH3 atmosphere.[71] **(Bottom-Right)** Schematic representation of the N-doped graphene. The blue, red, green, and yellow spheres represent the C, "graphitic" N, "pyridinic" N, and "pyrrolic" N atoms in the N-doped graphene, respectively. Such atomic substitution leads to defects in the graphene structure [72]

Exploring such phenomena, Traversi et al developed the first integrated circuit (a complementary inverter) on graphene as shown in **Figure 1.6.**[73] On this study, the key to obtaining a functional integrated circuit was to change the type of one of the transistors from p to n by Joule heating. An ideal graphene FET is ambipolar, meaning electrons flow when a positive voltage is applied to the gate (n-type), but holes conduct the current when a negative voltage is applied (p-type) (**Figure 1.5 and 1.6**). As explained earlier, oxygen and moisture in the air adventitiously dope graphene, making p-type transistors. In this study, Joule heat treatment was utilized to remove these contaminants from one side and therefore restoring n-type behavior (excess electrons). In this way, two transistors of opposite type are integrated on the same graphene sheet. This pair of transistors forms a digital logic inverter, a basic building block of CMOS.

Other important elementary building blocks for most semiconductor devices (such as diodes, transistors, LED) are p-n junctions. Graphene p-n junctions have already displayed new and exciting phenomena such as Klein tunneling[74], where electrons traveling perpendicular to the junction experience zero resistance and fractional quantum Hall transport. [74,75] Such junctions are predicted to produce lensing effects for coherent electrons, so called Veselago lensing, where diverging electron waves are refocused by the junction.[76] Graphene junctions to date have been fabricated using multiple electrostatic gates,[77] electrical stress-induced doping,[78] UV light/laser irradiation,[79,80] and molecular modifications on top of the graphene.[81,82] **Figure 1.6** shows a typical conductance measurement as a function of gate voltage, indicating superposition of two separate Dirac points that confirm an energy separation of neutrality points within the complementary regions in the ambipolar graphene FET. [77]
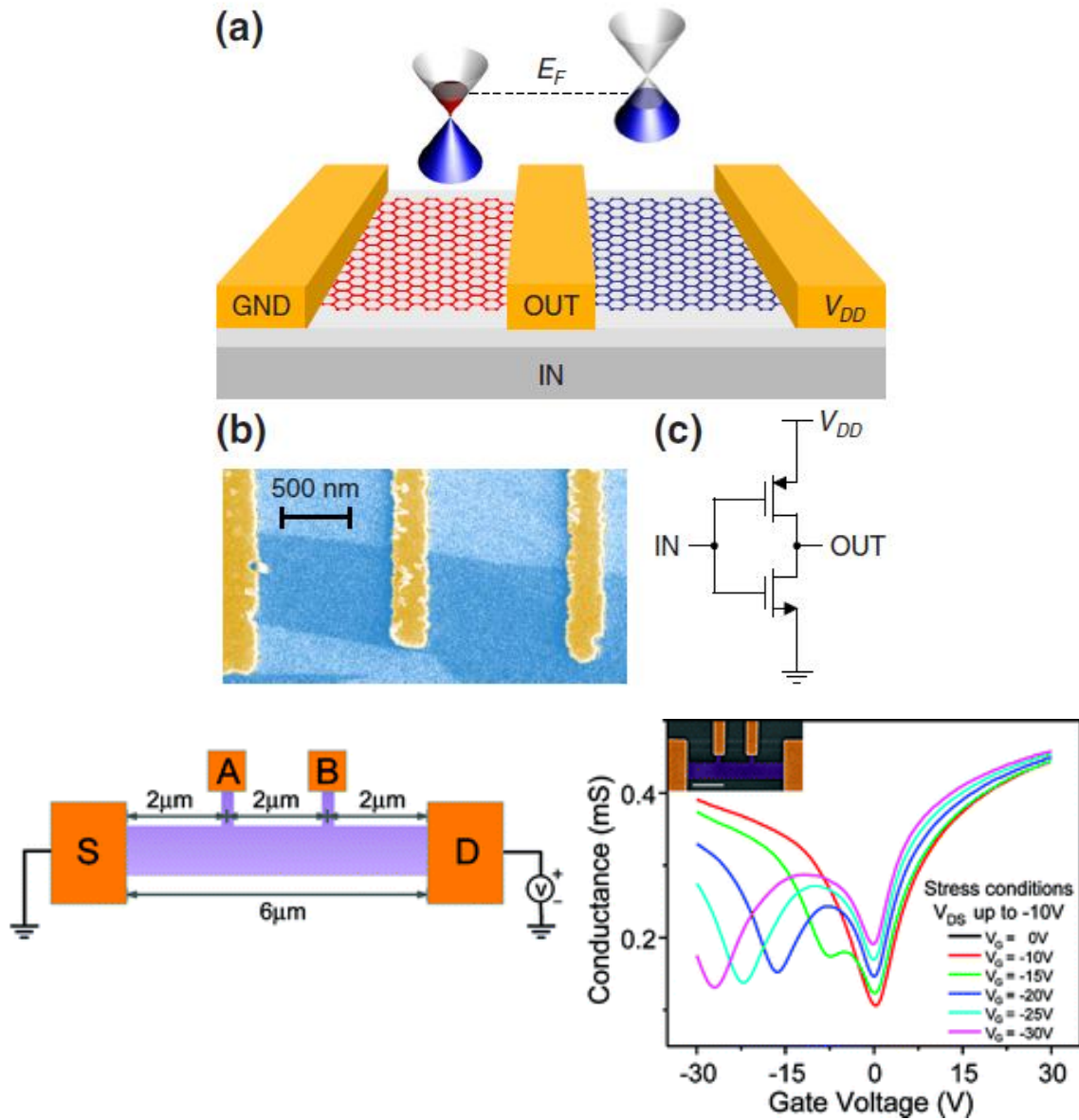
Figure 1.6 (Top- A,B and C): Schematic of graphene integrated circuit (complementary inverter). Picture taken from [73]. (Bottom): Right- Schematic of device configuration use to generated graphene p-n junction using electrostatic substrate engineering. Left- Output characteristic of a graphene p-n junction as a function of a gate voltage. Presence of two separate Dirac points confirms an energy separation of neutrality points within the complementary regions in the ambipolar graphene FET. [77]

1.5   Research Objective

Overall, as we approach the limits of Moore's law and faster, smaller electronics are demanded, it is critical to improve current techniques and explore the development of new techniques in order to fully produce interesting organic electronic material suitable for device fabrication. Having this in mind, we will focus on two specific aspects:

- First, how to modify the properties of these existing aromatic materials, in order to make them more compatible with current integrated circuits. In order to offer a true replacement for silicon or other semiconductor materials, we need to be able to controllably modify and characterize the doping profile of graphene. Such doping ability then allows one to fabricate useful electrical device constructs such as the P-N junctions which are the basis of almost any semiconductor electronic device.

- Second, how to fabricate lower temperature graphitic like materials with interesting electrical properties, and explore better methods for production of graphene from existing graphitic sources. In other words, the basic idea is to take intelligently designed precursors/molecules that can easily be converted thermally or chemically to form graphene or graphitic nanostructures.

1.6 Organization of Thesis

The work in this thesis can be primarily divided into two major categories, consisting of doping and synthesis of graphene, with the goal to improve current techniques and to explore the development of new techniques. Results from this work will enable researchers to apply the techniques and discoveries in broader fields, (either academic research or industry) and move closer towards producing useful electronic materials suitable for device fabrication.

To meet this objective, this study is organized as follows: graphene doping is discussed on chapters 2-4. We start by presenting the formation of graphene p-n junctions using 3-aminopropyltriethoxysilane (APTES) (chapter 2). We first explore transfer of CVD graphene onto monolithic and patterned APTES-layer-coated substrates in order to create n-doped graphene, graphene p-n junctions, and field effect transistor (FET) devices containing p-n junctions in the device channel. Next, we seek to control both the n and p-type doping characteristics of graphene; hence, in chapter 3, graphene p-n Junctions are created using a combination of two Self-Assembled Monolayers (SAM's). We use APTES and *1H,1H,2H,2H*-Perfluorooctyltriethoxysilane (PFES) to modify the interface between transferred CVD graphene films and its supporting dielectric, with the purpose of creating n-type and p-type graphene, respectively. A graphene p-n junction is obtained by patterning both modifiers on the same dielectric and is verified through the creation of an FET. In chapter 4, we further explore other doping techniques, borrowing lessons from traditional lithography and examining the use of photoacid generators (PAG) and photobase generators (PBG) as photochemical dopants for graphene. This work demonstrates that photochemical doping of CVD-grown graphene can be easily achieved using a PAG or

PBG such as triphenylsulfonium perfluoro-1-butanesufonate (TPS-Nf) and 2-nitrobenzyl N-cyclohexylcarbamate (NBC), respectively. Electrical measurements show that the doping concentrations can be modulated by controlling the deep ultraviolet (DUV) light exposure dose delivered to the sample. Furthermore, the photochemical doping process is able to tune the work function of the single layer of graphene samples used in this work from 3.4 eV to 5.3 eV and subsequently, a p-n junction is successfully fabricated and analyzed.

The second objective is to examine graphene synthesis and explore better methods for production of graphene. In chapter 5, we demonstrate exfoliation of graphene sheets by an electron donor surfactant. A novel macromolecular surfactant dicholesteryldithienothiophene (ChDTT) is synthesized and optimized for use in graphene exfoliation and dispersion. Using this surfactant, graphene flakes can be extracted directly from graphite or other graphitic sources without additional chemical treatment, producing larger flakes of higher quality compared to those obtained via reduced graphene-oxide (rGO). Next, we analyze the catalytic growth of graphene on copper (chapters 6-7) in order to test our hypothesis that intelligently designed precursors/molecules can easily be converted to form graphene. In chapter 6, we analyze surface Diels-Alder adducts on silica as a controllable carbon precursor for pristine graphene. A dienophile-modified SiO_2 surface serves as a platform for Diels-Alder mediated attachment of anthracene and 9, 9'-bianthryl. The resulting monolayers are investigated by x-ray photoelectron spectroscopy (XPS) and are directly used as precursors for graphene, as verified by Raman spectroscopy. The 9, 9'-bianthryl adduct yields the best quality graphene, which is attributed to the higher carbon precursor availability. As a result of this discovery, we seek to explore lower

temperature growth process using non-flammable precursors (chapter 7). We find that while our process was successful at 1000 ${}^\circ$C, we were unable to grow at lower temperatures. We establish that the factors responsible for such results can be related to vacuum and hydrogen conditions. Finally in chapter 8, we perform an exploratory study on the synthesis of graphitic nanoribbons (GNRs) via encapsulation in single-walled aluminosilicate nanotubes (AlSi-SWNT). The obtained results are promising and may allow for a rationale design of GNRs with varying size and width.

Last but not least, a conclusion and suggestion for future works are presented in chapter 9. Due to the specialty of each project, an introduction and background for each topic are provided separately in each chapter as applicable.

1.7　References

1　Arns, R. G. The other transistor: early history of the metal-oxide semiconductor field-effect transistor. *Engineering Science and Education Journal* **7**, 233-240 (1998).

2　Edgar, L. J. Method and apparatus for controlling electric currents. United States patent (1930).

3　Armini, A. J., Bunker, S. J. & Spitzer, M. B. *Non-mass-analyzed ion implantation equipment for high volume solar cell production*.　(1982).

4　Fuller, C. S. Diffusion of Donor and Acceptor Elements into Germanium. *Physical Review* **86**, 136 (1952).

5　Horowitz, G. Organic field-effect transistors. *Adv Mater* **10**, 365-377 (1998).

6　Schwierz, F. Graphene transistors. *Nat Nano* **5**, 487-496 (2010).

7　Nomura, K. *et al.* Room-temperature fabrication of transparent flexible thin-film transistors using amorphous oxide semiconductors. *Nature* **432**, 488-492 (2004).

8　Schaller, R. R. Moore's law: past, present and future. *Spectrum, IEEE* **34**, 52-59 (1997).

9　Novoselov, K. S. *et al.* A roadmap for graphene. *Nature* **490**, 192-200, doi:10.1038/nature11458 nature11458 [pii] (2012).

10　Bae, S. *et al.* Roll-to-roll production of 30-inch graphene films for transparent electrodes. *Nat Nanotechnol* **5**, 574-578, doi:Doi 10.1038/Nnano.2010.132 (2010).

11　Klopfer, B. *Powering Mobile Devices*, <http://large.stanford.edu/courses/2012/ph250/klopfer2/> (2012).

12　Podzorov, V., Sysoev, S. E., Loginova, E., Pudalov, V. M. & Gershenson, M. E. *Single-crystal organic field effect transistors with the hole mobility ? 8 cm2/V?s*. Vol. 83 (AIP, 2003).

13　Liu, S., Wang, W. M., Briseno, A. L., Mannsfeld, S. C. B. & Bao, Z. Controlled Deposition of Crystalline Organic Semiconductors for Field-Effect-Transistor Applications. *Adv Mater* **21**, 1217-1232, doi:10.1002/adma.200802202 (2009).

14　Ruoff, R. Calling all chemists. *Nat Nanotechnol* **3**, 10-11, doi:DOI 10.1038/nnano.2007.432 (2008).

15　Geim, A. K. & Novoselov, K. S. The rise of graphene. *Nat Mater* **6**, 183-191, doi:10.1038/nmat1849 (2007).

16   Neto, A. H. C. & Guinea, F. Electron-phonon coupling and Raman spectroscopy in graphene. *Phys Rev B* **75**, doi:Artn 045404 Doi 10.1103/Physrevb.75.045404 (2007).

17   Castro Neto, A. H., Guinea, F., Peres, N. M. R., Novoselov, K. S. & Geim, A. K. The electronic properties of graphene. *Rev Mod Phys* **81**, 109-162, doi:DOI 10.1103/RevModPhys.81.109 (2009).

18   Ohta, T., Bostwick, A., Seyller, T., Horn, K. & Rotenberg, E. Controlling the electronic structure of bilayer graphene. *Science* **313**, 951-954, doi:DOI 10.1126/science.1130681 (2006).

19   Du, X., Skachko, I., Barker, A. & Andrei, E. Y. Approaching ballistic transport in suspended graphene. *Nat Nanotechnol* **3**, 491-495, doi:10.1038/nnano.2008.199 (2008).

20   Novoselov, K. S. *et al.* Electric field effect in atomically thin carbon films. *Science* **306**, 666-669, doi:DOI 10.1126/science.1102896 (2004).

21   Falkovsky, L. A. in *International Conference on Theoretical Physics 'Dubna-Nano2008'* Vol. 129 *Journal of Physics Conference Series* (ed V. A. Nesterenko V. O. Shukrinov Y. M. Osipov) (2008).

22   Falkovsky, L. A. & Pershoguba, S. S. Optical far-infrared properties of a graphene monolayer and multilayer. *Physical Review B* **76**, doi:153410 10.1103/PhysRevB.76.153410 (2007).

23   Wu, Y. Q. *et al.* High-frequency, scaled graphene transistors on diamond-like carbon. *Nature* **472**, 74-78, doi:Doi 10.1038/Nature09979 (2011).

24   Novoselov, K. S. *et al.* fake. *Science* **306**, 666-669, doi:10.1126/science.1102896 (2004).

25   Berger, C. *et al.* Ultrathin Epitaxial Graphite:‚Äâ 2D Electron Gas Properties and a Route toward Graphene-based Nanoelectronics. *The Journal of Physical Chemistry B* **108**, 19912-19916, doi:10.1021/jp040650f (2004).

26   Reina, A. *et al.* Large area, few-layer graphene films on arbitrary substrates by chemical vapor deposition. *Nano Lett* **9**, 30-35, doi:10.1021/nl801827v (2009).

27   Somani, P. R., Somani, S. P. & Umeno, M. Planer nano-graphenes from camphor by CVD. *Chem Phys Lett* **430**, 56-59, doi:10.1016/j.cplett.2006.06.081 (2006).

28   Sun, Z. *et al.* Growth of graphene from solid carbon sources. *Nature* **468**, 549-552, doi:http://www.nature.com/nature/journal/v468/n7323/abs/nature09579.html#supplementary-information (2010).

29   Zhang, Y., Zhang, L. Y. & Zhou, C. W. Review of Chemical Vapor Deposition of Graphene and Related Applications. *Accounts Chem Res* **46**, 2329-2339, doi:Doi 10.1021/Ar300203n (2013).

30   Seyller, T. *et al.* Epitaxial graphene: a new material. *Phys Status Solidi B* **245**, 1436-1446, doi:DOI 10.1002/pssb.200844143 (2008).

31   Eda, G., Fanchini, G. & Chhowalla, M. Large-area ultrathin films of reduced graphene oxide as a transparent and flexible electronic material. *Nat Nano* **3**, 270-274, doi:http://www.nature.com/nnano/journal/v3/n5/suppinfo/nnano.2008.83_S1.html (2008).

32   Lotya, M. *et al.* Liquid Phase Production of Graphene by Exfoliation of Graphite in Surfactant/Water Solutions. *J Am Chem Soc* **131**, 3611-3620, doi:Doi 10.1021/Ja807449u (2009).

33   Hernandez, Y. *et al.* High-yield production of graphene by liquid-phase exfoliation of graphite. *Nat Nanotechnol* **3**, 563-568, doi:DOI 10.1038/nnano.2008.215 (2008).

34   Coleman, J. N. Liquid Exfoliation of Defect-Free Graphene. *Accounts Chem Res* **46**, 14-22, doi:Doi 10.1021/Ar300009f (2013).

35   Royall, S. Calling all chemists. *Chem Ind-London*, 18-20 (2007).

36   Zangwill, A. & Vvedensky, D. D. Novel growth mechanism of epitaxial graphene on metals. *Nano Lett* **11**, 2092-2095, doi:10.1021/nl2006005 (2011).

37   Sprinkle, M. *et al.* Scalable templated growth of graphene nanoribbons on SiC. *Nat Nanotechnol* **5**, 727-731, doi:10.1038/nnano.2010.192 nnano.2010.192 [pii] (2010).

38   Zhou, Y. H. *et al.* A Universal Method to Produce Low-Work Function Electrodes for Organic Electronics. *Science* **336**, 327-332, doi:DOI 10.1126/science.1218829 (2012).

39   Pang, H., Lu, Q. & Gao, F. Graphene oxide induced growth of one-dimensional fusiform zirconia nanostructures for highly selective capture of phosphopeptides. *Chem Commun (Camb)* **47**, 11772-11774, doi:10.1039/c1cc14618a (2011).

40   Ruiz, O. N. *et al.* Graphene oxide: a nonspecific enhancer of cellular growth. *Acs Nano* **5**, 8100-8107, doi:10.1021/nn202699t (2011).

41   Majumdar, D., Baskey, M. & Saha, S. K. Epitaxial growth of crystalline polyaniline on reduced graphene oxide. *Macromol Rapid Commun* **32**, 1277-1283, doi:10.1002/marc.201100292 (2011).

42   Cao, X. *et al.* Graphene oxide as a carbon source for controlled growth of carbon nanowires. *Small* **7**, 1199-1202, doi:10.1002/smll.201100071 (2011).

43   Xu, Z. P. & Xue, K. Engineering graphene by oxidation: a first-principles study. *Nanotechnology* **21**, doi:Artn 045704 Doi 10.1088/0957-4484/21/4/045704 (2010).

44   Gomez-Navarro, C. *et al.* Atomic Structure of Reduced Graphene Oxide. *Nano Lett* **10**, 1144-1148, doi:Doi 10.1021/Nl9031617 (2010).

45   Liu, L. *et al.* Graphene oxidation: thickness-dependent etching and strong chemical doping. *Nano Lett* **8**, 1965-1970, doi:10.1021/nl0808684 (2008).

46   Robinson, J. T., Perkins, F. K., Snow, E. S., Wei, Z. & Sheehan, P. E. Reduced Graphene Oxide Molecular Sensors. *Nano Letters* **8**, 3137-3140, doi:10.1021/nl8013007 (2008).

47   Gomez-Navarro, C. *et al.* Electronic transport properties of individual chemically reduced graphene oxide sheets. *Nano Lett* **7**, 3499-3503, doi:Doi 10.1021/Nl072090c (2007).

48   Li, X. *et al.* Large-Area Synthesis of High-Quality and Uniform Graphene Films on Copper Foils. *Science* **324**, 1312-1314 (2009).

49   Li, X., Cai, W., Colombo, L. & Ruoff, R. S. Evolution of graphene growth on Ni and Cu by carbon isotope labeling. *Nano Lett* **9**, 4268-4272, doi:10.1021/nl902515k (2009).

50   Li, Q. *et al.* Growth of Adlayer Graphene on Cu Studied by Carbon Isotope Labeling. *Nano Lett*, doi:10.1021/nl303879k (2013).

51   Wu, Y. *et al.* Growth mechanism and controlled synthesis of AB-stacked bilayer graphene on Cu-Ni alloy foils. *Acs Nano* **6**, 7731-7738, doi:10.1021/nn301689m (2012).

52   Zhang, B. *et al.* Low-temperature chemical vapor deposition growth of graphene from toluene on electropolished copper foils. *Acs Nano* **6**, 2471-2476, doi:10.1021/nn204827h (2012).

53   Ji, H. *et al.* Graphene growth using a solid carbon feedstock and hydrogen. *Acs Nano* **5**, 7656-7661, doi:10.1021/nn202802x (2011).

54   Wassei, J. K. & Kaner, R. B. Oh, the Places You'll Go with Graphene. *Acc Chem Res*, doi:10.1021/ar300184v (2013).

55   Bae, S. *et al.* Roll-to-roll production of 30-inch graphene films for transparent electrodes. *Nature Nanotechnology* **5**, 574-578, doi:10.1038/nnano.2010.132 (2010).

56   Hecht, D. S., Hu, L. B. & Irvin, G. Emerging Transparent Electrodes Based on Thin Films of Carbon Nanotubes, Graphene, and Metallic Nanostructures. *Advanced Materials* **23**, 1482-1513, doi:10.1002/adma.201003188 (2011).

57   Choe, M. *et al.* Efficient bulk-heterojunction photovoltaic cells with transparent multi-layer graphene electrodes. *Org. Electron.* **11**, 1864-1869, doi:10.1016/j.orgel.2010.08.018 (2010).

58   Park, H., Rowehl, J. A., Kim, K. K., Bulovic, V. & Kong, J. Doped graphene electrodes for organic solar cells. *Nanotechnology* **21**, doi:505204 10.1088/0957-4484/21/50/505204 (2010).

59   Wu, J. B. *et al.* Organic Light-Emitting Diodes on Solution-Processed Graphene Transparent Electrodes. *Acs Nano* **4**, 43-48, doi:10.1021/nn900728d (2010).

60   Kim, S. R., Parvez, M. K. & Chhowalla, M. UV-reduction of graphene oxide and its application as an interfacial layer to reduce the back-transport reactions in dye-sensitized solar cells. *Chem. Phys. Lett.* **483**, 124-127, doi:10.1016/j.cplett.2009.10.066 (2009).

61   Ma, H., Yip, H. L., Huang, F. & Jen, A. K. Y. Interface Engineering for Organic Electronics. *Adv. Funct. Mater.* **20**, 1371-1388, doi:10.1002/adfm.200902236 (2010).

62   Candelise, C., Winskel, M. & Gross, R. Implications for CdTe and CIGS technologies production costs of indium and tellurium scarcity. *Prog Photovoltaics* **20**, 816-831, doi:Doi 10.1002/Pip.2216 (2012).

63   Gramling, C. Indium prices on the rise. *Geotimes* **52**, 16-16 (2007).

64   Novoselov, K. S. *et al.* Detection of individual gas molecules adsorbed on graphene. *Nature materials* **6**, 652-655, doi:Doi 10.1038/Nmat1967 (2007).

65   Ghosh, A., Late, D. J., Panchakarla, L. S., Govindaraj, A. & Rao, C. N. R. NO2 and humidity sensing characteristics of few-layer graphenes. *J. Exp. Nanosci.* **4**, 313-322, doi:10.1080/17458080903115379 (2009).

66   Fowler, J. D. *et al.* Practical Chemical Sensors from Chemically Derived Graphene. *Acs Nano* **3**, 301-306, doi:10.1021/nn800593m (2009).

67   Sojoudi, H., Baltazar, J., Henderson, C. & Graham, S. Impact of post-growth thermal annealing and environmental exposure on the unintentional doping of CVD graphene films. *J Vac Sci Technol B* **30**, doi:Artn 041213 Doi 10.1116/1.4731472 (2012).

68   Malard, L. M., Pimenta, M. A., Dresselhaus, G. & Dresselhaus, M. S. Raman spectroscopy in graphene. *Phys Rep* **473**, 51-87, doi:DOI 10.1016/j.physrep.2009.02.003 (2009).

69   Ryu, S. *et al.* Atmospheric Oxygen Binding and Hole Doping in Deformed Graphene on a SiO(2) Substrate. *Nano Lett* **10**, 4944-4951, doi:Doi 10.1021/Nl1029607 (2010).

70   Liu, H., Liu, Y. & Zhu, D. Chemical doping of graphene. *J Mater Chem* **21**, 3335-3345 (2011).

71   Lin, Y.-C., Lin, C.-Y. & Chiu, P.-W. *Controllable graphene N-doping with ammonia plasma*. Vol. 96 (AIP, 2010).

72   Wei, D. *et al.* Synthesis of N-doped graphene by chemical vapor deposition and its electrical properties. *Nano Lett* **9**, 1752-1758, doi:10.1021/nl803279t (2009).

73   Traversi, F., Russo, V. & Sordan, R. Integrated complementary graphene inverter. *Applied Physics Letters* **94**, doi:223312 10.1063/1.3148342 (2009).

74   Stander, N., Huard, B. & Goldhaber-Gordon, D. Evidence for Klein Tunneling in Graphene p-n Junctions. *Phys Rev Lett* **102**, doi:Artn 026807 Doi 10.1103/Physrevlett.102.026807 (2009).

75   Katsnelson, M. I., Novoselov, K. S. & Geim, A. K. Chiral tunnelling and the Klein paradox in graphene. *Nat Phys* **2**, 620-625, doi:Doi 10.1038/Nphys384 (2006).

76   Cheianov, V. V., Fal'ko, V. & Altshuler, B. L. The focusing of electron flow and a Veselago lens in graphene p-n junctions. *Science* **315**, 1252-1255, doi:DOI 10.1126/science.1138020 (2007).

77   Chiu, H. Y., Perebeinos, V., Lin, Y. M. & Avouris, P. Controllable p-n Junction Formation in Mono layer Graphene Using Electrostatic Substrate Engineering. *Nano Lett* **10**, 4634-4639, doi:Doi 10.1021/Nl102756r (2010).

78   Yu, T. H., Liang, C. W., Kim, C. D. & Yu, B. Local electrical stress-induced doping and formation of monolayer graphene P-N junction. *Appl Phys Lett* **98**, doi:Artn 243105 Doi 10.1063/1.3593131 (2011).

79   Iqbal, M. Z., Siddique, S., Iqbal, M. W. & Eom, J. Formation of p-n junction with stable p-doping in graphene field effect transistors using deep UV irradiation. *Journal of Materials Chemistry C* **1**, 3078-3083, doi:10.1039/c3tc30232f (2013).

80   Kim, Y. D. *et al.* Focused-laser-enabled p-n junctions in graphene field-effect transistors. *Acs Nano* **7**, 5850-5857, doi:10.1021/nn402354j (2013).

81   Cheng, H. C., Shiue, R. J., Tsai, C. C., Wang, W. H. & Chen, Y. T. High-Quality Graphene p-n Junctions via Resist-free Fabrication and Solution-Based Noncovalent Functionalization. *Acs Nano* **5**, 2051-2059, doi:Doi 10.1021/Nn103221v (2011).

82   Brenner, K. & Murali, R. Single step, complementary doping of graphene. *Appl Phys Lett* **96**, doi:Artn 063104 Doi 10.1063/1.3308482 (2010).

CHAPTER 2

FACILE FORMATION OF GRAPHENE P-N JUNCTIONS USING APTES

Monolithic and patterned aminopropyltriethoxysilane (APTES) layers are used to create n-doped graphene, graphene p-n junctions, and FET devices containing p-n junctions in the device channel through transfer of CVD graphene onto APTES coated substrates. APTES doping is shown to not result in introduction of defects. I-V measurements of FET devices containing patterned APTES layers show it is possible to control the position of the two current minima (two Dirac points) in the ambipolar p-n junction.

2.1   Introduction

Graphene, a two-dimensional sp^2 hybridized carbon lattice that is also the fundamental building block of graphite, has attracted significant interest recently due to its distinctive electrical and mechanical properties,[1,2] including its nearly linear energy dispersion relation that results in electric field induced generation of electrons and holes which travel as massless Dirac fermions with high velocities.[3-5] Carrier mobilities in pristine graphene have been estimated to be as large as 200,000 cm^2/Vs, which is several orders-of-magnitude larger than crystalline silicon and superior to other organic semiconductors. These electrical properties have spurred research directed at modifying graphene for use in a variety of electronic, optoelectronic, and sensor technologies.[1,6]

In its pristine state, graphene is metallic.[5] Although graphene may be useful as a conductor, much of the current interest is in utilizing it in a semiconducting form. Therefore, introduction and control of the bandgap is crucial. For example, substitution of carbon atoms in the graphene lattice with atoms such as nitrogen has been shown to open a bandgap.[7,8] In addition, substrate induced band-gap opening[9] and lateral confinement of charge carriers to a quasi-one-dimensional (1D) have been shown to create an energy gap near the charge neutrality point.[10]

A second and equally important challenge is to develop methods for controllably doping graphene to allow for adjustment of the work function of graphene. [11] Doping of graphene has been achieved primarily through electrostatic gating[12], through chemical interactions[13], and through intercalation.[11,14,15] Replacement of carbon atoms in the graphene lattice has also been shown to modulate the carrier types and concentrations in the material to allow for p- and n-type doping, and fabrication of field effect transistors

(FETs) based on such substitutionally-doped graphene has been achieved.[11] N-doped graphene has also been created through chemical vapor deposition (CVD) of graphene from carbonaceous precursors containing ammonia (NH_3) as a nitrogen-doping source during the deposition.[16] Similar results have also been achieved using pyridine as both the carbon and nitrogen source for CVD of graphene.[17] Most graphene samples obtained in these ways are composed of multilayer films with significant numbers of defects that reduce carrier mobilities significantly. N^+ ion irradiation of graphene followed by annealing in ammonia and nitrogen environments has also been used to modulate doping concentration in graphene flakes.[18] Alternatively, exposure of graphene to ammonia plasma has been shown to produce n-type doping.[19] In both studies where post-treatment of graphene in nitrogen containing environments was used, the result has been relatively high defect levels in the doped graphene. Therefore, due to both the complexity and the lack of control of some of these doping processes, along with the resulting high defect levels reported for many of these doping techniques, this study has focused on developing a low temperature, scalable technique for doping graphene with minimal introduction of defects.

It is well known that the properties of graphene are sensitive to the surfaces and materials with which graphene is in contact. It has been shown that adsorbates on the graphene surface can act as dopants.[20,21] A common example is that adventitious oxygen can serve as a strong p-type dopant.[22] Charge transfer from such adsorbates has been used to fabricate p-n junctions,[23-25] but the position of such junctions has been essentially random, and the dopant concentrations have not been well controlled. While such adsorbate-surface interactions make graphene potentially attractive as a sensor platform,

such methods are less suitable for doping graphene in devices because of the difficulty in controlling the doping and the general lack of stability of such adsorbate layers. Surface interactions of graphene monolayers with self assembled monolayers (SAMs) on SiO_2 substrates have also been recently studied.[26-29] While it has been observed that such monolayers can dope graphene, there has thus far been no implementation and use of SAMs to controllably dope and form p-n junctions in graphene. Most of the studies reported so far on formation of controlled p-n junctions have instead used multiple gates or electrostatic substrate engineering.[12,30-33]

In the work reported here, a facile and low temperature approach to fabricate p-n junctions on large area CVD-grown graphene has been utilized to build simple graphene FET devices containing p-n junctions in their channel. Standard lithographic methods were used to pattern a graphene FET channel containing a thin layer of aminopropyltriethoxysilane (APTES) in selected regions of the channel. Early studies suggest that amine groups can donate their lone pairs of electrons to graphene, increasing the electron carrier density and inducing n-doping in graphene.[27,29,34-36] In the process presented in this work, the intrinsically p-doped CVD graphene obtained as a result of the particular transfer process[20] utilized to deposit graphene onto the FET devices provides the basis for the p-doping required to form a p-n junction in combination with APTES layers. Upon heating the device under an inert atmosphere, the intrinsically p-doped graphene is de-doped in a controlled manner, resulting in a dopant concentration profile that leads to formation of a p-n junction. X-ray photoelectron spectroscopy (XPS) and micro-Raman spectroscopy studies confirm that the doped graphene is defect-free and that the dopant concentrations are modulated by the APTES concentration on the substrate as well as the

concentration of the adsorbed molecules and atmospheric dopants on the graphene. To the best of our knowledge, this is the first time that SAMs have been used to fabricate a p-n junction that allows an overall control of the dopants in the junction. In addition, since the dopant layer is pre-fabricated and pre-patterned before transfer of the graphene to the device substrate, the graphene is never subsequently exposed to photoresist and other or treatments that would otherwise be required to fabricate dopant profiles, thus allowing for control of the graphene electrical properties.

2.2   Experimental Section

Back-gated CVD graphene field effect transistors were fabricated using standard lithography and metallization techniques in conjunction with a solution-based self-assembled monolayer coating technique and a solution based transfer of CVD grown graphene. A highly p-doped Si wafer was used as a gate, with a 300 nm thick thermally grown silicon dioxide layer as the gate dielectric. For the APTES layer deposition, the substrate was first cleaned and pre-treated by UV ozone for 15 min in order to produce a hydroxyl-terminated substrate, known to react efficiently with silane-coupling agents such as APTES. The substrate was immediately immersed in a 1%(v/v) solution of APTES in anhydrous toluene for three hours. The substrate was removed, sonicated for 15 min in pure toluene, and dried under flowing nitrogen. Deposition was confirmed by contact angle measurements using a VCA 2000 goniometry system,by x-ray photoelectron spectroscopy (XPS), and by XPS mapping acquired using a Thermo K-Alpha XPS (Thermoscientific) operating under ultra-high vacuum conditions with an Al Kα micro-focused monochromator.For work function measurements, Ultraviolet Photo-electron

Spectroscopy , (UPS) was performed in a Kratos AxisDLD Ultra spectrometer (using He I excitation source) at base pressure 10^{-8} Torr with the Fermi energy (E_F) calibrated using an atomically clean silver sample. All samples were in electronic equilibrium with the spectrometer via a metallic clip on the graphene and characterizations were performed at normal takeoff angle (90° relative to detector).

The SAM coated surface contained a high density of molecules that predominantly existed as free amines (i.e. non-hydrogen bonded) as characterized by x-ray photoelectron spectroscopy (XPS).[37,38] The APTES coated surface had a measured contact angle with deionized (DI) water of ~ 60°,[39] as compared to <10° contact angle measured immediately after the UV ozone cleaning treatment, indicative of coupling of the APTES monolayer to the surface. Finally, CVD grown graphene was transferred on top of the pre-made FET device structures containing either patterned APTES coated channels (i.e. ones not fully covered in APTES due to prepatterning of the channel with photoresist prior to APTES deposition) or fully APTES coated channels. The devices were immediately transferred to a nitrogen-purged glovebox. In addition to the FET devices, two types of control samples were also fabricated for collection of reference of XPS and UPS data and Raman spectra. One control sample consisted of CVD graphene transferred onto the cleaned SiO_2 coated silicon substrate containing no APTES, and one control sample contained an unpatterned, continuous APTES film.

CVD graphene was prepared following standard literature procedures.[40] Graphene was synthesized on 25 μm thick Cu foil (Alfa Aesar, item No. 14482, cut to 1 in by 1 in squares) in a low pressure $Ar/H_2/CH_4$ environment at 1000 °C.[40] PMMA (MicroChem 950 PMMA Series) was then spun cast from an organic solution (9% solution in anisole, spin

coated at 1500 rpm for 1 min) onto the as-grown graphene coated Cu samples and baked (180 °C for 5 to 10 minutes) to form an approximately 500 nm thick film that served as an auxiliary support material for handling and transferring the graphene films. The Cu foil was treated overnight with a 30 wt% $FeCl_3$ aqueous solution to completely remove copper. The resulting bi-layer PMMA-graphene samples were treated with 10 wt% HCl solution for 10 min, followed deionized (DI) water several times to remove bound contaminants. Raman spectroscopy using a 532 nm laser excitation wavelength was performed in order to verify the presence of graphene and characterize its quality.

2.3   Results and Discussion

Figure 2-1 shows the XPS survey spectra for: (1) the APTES-treated graphene FET devices in areas containing the APTES layer (labeled 'Graphene/APTES'), (2) graphene FET devices in regions not containing the APTES layer (labeled 'Graphene'), and (3) a control sample containing only the APTES layer on an SiO_2 coated silicon substrate (labeled 'APTES'). These XPS survey scan spectra were collected over the binding energy (B.E.) range from 0-800 eV with a step size of 1 eV and a spot size of 400 μm. The clear presence of the N1s peak in **Figure 2-1A** for the Graphene/APTES and APTES samples (and lack of such a peak in the Graphene sample) supports the conclusion that the APTES SAMs were successfully deposited onto selected regions of the SiO_2 substrate in these samples. The N1s high resolution spectrum (**Figure 2-1E**) for regions containing APTES can be deconvoluted and fit with two peaks centered at 400 eV (representing 77% of the total N1s peak area) and 401.9 eV (representing 23% of the total N1s peak area), which can be assigned to free amine ($-NH_2$) and either a protonated ($-NH_3^+$) or hydrogen bonded

amine, respectively.[38,41] The small amount of the nitrogen XPS signal assigned to the peak at 401.9 eV is likely due to protonated amine that results from the graphene transfer process (e.g. from exposure to acid). **Figure 2-1B** shows the chemical shifts in the high resolution C1s spectra for: (1) regions of the FET device sample where graphene exists with no underlying APTES layer (black), (2) regions of the FET device sample where the graphene exists with an underlying APTES layer (red), and (3) a control sample with only the APTES layer deposited onto a silicon dioxide coated silicon substrate (green). We observe that for the APTES control sample the C1s peak maximum occurs with a binding energy of 285.3 eV. The shift in the C1s peak binding energy in the case of the APTES layer away from that for simple hydrocarbons (i.e. simple hydrocarbon C1s peak locations are approximately 284.5 eV) is attributed to the inductive effect of N atoms present in the APTES layer,[42] in accord with previously reported data.[28] The C1s peak for graphene on the oxide surface, at a binding energy of 284.5 eV, is typical of graphene. The C1s peak in the graphene samples deposited onto the APTES coated oxide films (Graphene/APTES) reaches its maximum at a binding energy of 285.1 eV and appears to be the result of the superposition of the graphene and APTES C1s XPS spectra.

 Figure 2-1C shows the UPS spectra for: (1) Graphene and (2) Graphene/APTES, before and after annealing at 200 °C for 4 hours. The secondary electron edge occurs at the binding energy corresponding to the deepest of the energy levels that can be excited with the radiation employed. Hence, the work function Φ (energy difference between the Fermi and vacuum level) can be calculated from equation (1),[43]

$$\Phi = 21.22 - BE_{SEE} \tag{1}$$

where BE_{SEE} is the binding energy at the secondary electron cutoff. The work function of graphene and graphene/APTES were determined to be 4.71±0.08 eV and 4.45±0.05 eV before anneal, and 4.57± 0.02 eV and 4.26±0.12 eV after anneal, respectively. The change in the work function after anneal is attributed to the removal of external doping from impurities that can be incorporated into the graphene film during the synthesis and transfer process.[20,44] The work function of the graphene/APTES sample is ~0.2 eV lower than that of the graphene sample. This has been attributed to the lone pair electrons in the nitrogen in the amine SAMs, given that in the case of NH_3 molecules, DFT calculations have shown that there is a small charge transfer to the graphene,[45] which would explain the raising of the Fermi level from the Dirac point (n-doping).[28,34,46] This doping is further supported by Raman spectroscopy and electrical data discussed later (see **Figures 2-2 and 2-3**).
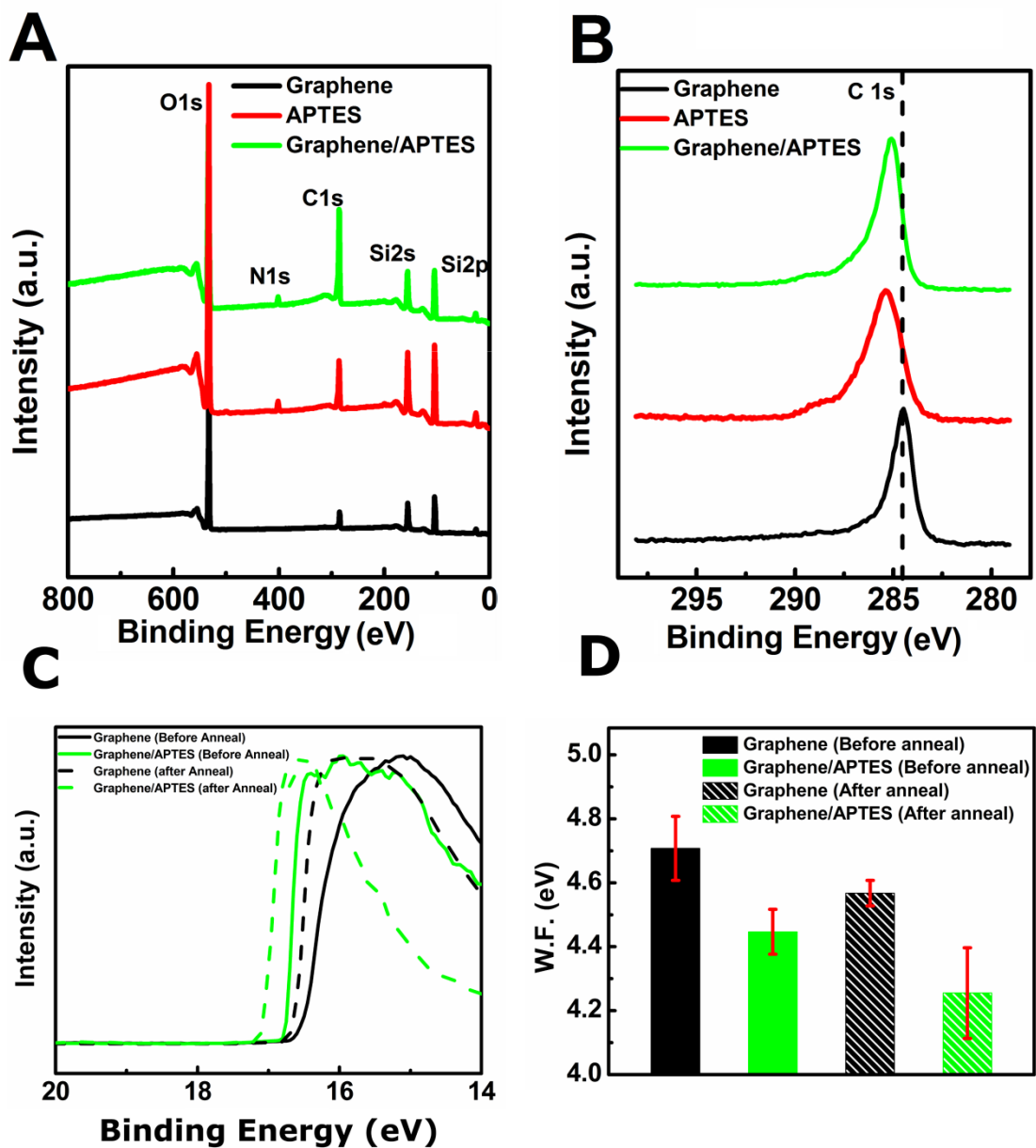
Figure 2-1: XPS spectra representing a (A) survey scan and the (B) C1s binding energy region for three types of samples: (black line) graphene on SiO_2, (red line) APTES layer on SiO_2, (green line) graphene on APTES coated SiO_2.(C) UPS spectra for Graphene (black) and Graphene/APTES (green), before and after anneal. (D) UPS-determined work functions. (E) XPS spectra representing N 1s binding energy for graphene/ SiO_2 (black) and graphene /SAMs (red). All data were normalized to the largest intensity within each spectrum.

E

Intensity (au)

Legend:
- Graphene
- Graphene+APTES
- Free-amine fit
- Protonated amine fit
- Fit envelope

Bidding Energy (eV)
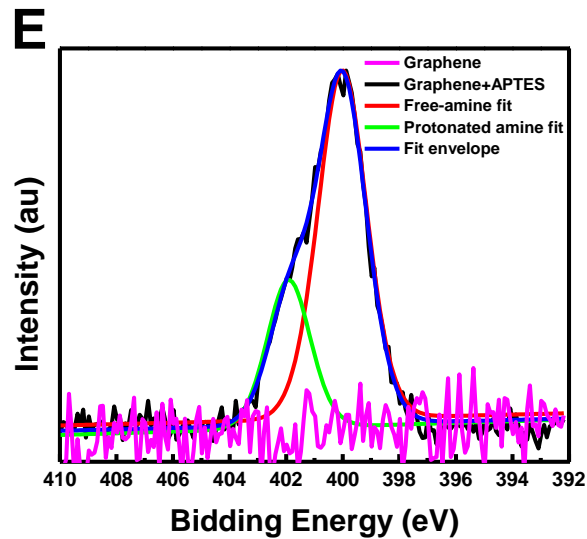
Figure 2-1 Continued

Raman spectroscopy and microscopy measurements (Horiba HR800 µRaman system) were also used to characterize the resulting graphene and graphene devices. Raman spectroscopy was utilized to investigate the quality of the graphene and its doping state by examining the D, G, and 2D bands and their positions. All spectra were excited with visible (532 nm) laser light and collected in a backscattering configuration with a laser power below 0.5 mW to reduce laser-induced heating.[21] A 50X objective lens was used to focus the laser on the graphene samples during the Raman measurements. The samples were placed inside an environmentally controlled microscope stage with heating, vacuum, and gas delivery capability (Linkam TS 1500) for in-situ Raman measurements. The thermal stage was mounted onto an X-Y-Z micropositioning stage to control focusing and the measurement position. A quartz window was used to allow optical access to the sample

while a vacuum pump was used to evacuate the sample chamber to a pressure of ~1 mTorr. The drift of the laser spot on the graphene due to thermal expansion was minimized before all measurements. The sample was heated to 200 °C and held at that temperature 5-90 min to allow for desorption of atmospheric adsorbed p-dopants such as oxygen and water. Raman spectra were acquired at multiple locations before and after heating and cooling to verify reproducibility. The Raman peaks corresponding to the D, G, and 2D Raman peaks in graphene were fit with Gauss-Lorentzian curve fits to determine their peak position, line width, and intensity. The as-grown graphene films utilized in this work and the graphene transferred onto the APTES layers all showed prominent graphitic (G and 2D) bands with no detectable defect peak (D) (see **Figure 2-2A** - full spectra). The high 2D over G band intensity ratio I_{2D}/I_G and low full width at half maximum (FWHM) of the 2D band are indicative of a monolayer graphene film.[40] A critical observation is that no appearance of or increase in the D band was observed during any of the transfer or annealing steps. This indicates that successful doping, as will be shown later, of the graphene monolayer without damage to the carbon lattice structure was achieved. [28,47]

Figure 2-2B-D shows the G band position, the B band full width at half maximum (FWHM), and the 2D to G band intensity ratio (I_{2D}/I_G) as a function of annealing time for both graphene transferred onto a surface region not containing APTES layer and a surface region containing the APTES layer. For graphene transferred onto APTES, the largest value of the G peak position (~1590.2 cm^{-1}), the smallest value of full width half maximum of the G peak (FWHM ~36.1 cm^{-1}), and the smallest value of the I_{2D}/I_G (~1.8) ratio were all measured before thermal annealing at 200 ºC. After annealing for 5 min at 200 ºC, the smallest value for the G peak position (~1585.7 cm^{-1}), the largest G peak FWHM (~21.1

cm^{-1}), and the largest I_{2D}/I_G ratio (~2.5) were all characteristic of de-doped graphene[21].

Longer heat treatments at 200 ºC resulted in an increase in the G peak position (~1586.5

cm^{-1}), a decrease in the FWHM (G) (~19 cm^{-1}) and a decrease in the I_{2D}/I_G ratio (~2.4).

These results are in agreement with the observations by Ferrari and coworkers that

implicate n- doping of the graphene monolayer.[48] For samples transferred onto a substrate

region without APTES, a decrease in the G peak position (from 1591 cm^{-1} to 1588 cm^{-1})

and a broadening of the G peak (FWHM increased from 18 cm^{-1} to 23 cm^{-1}) were observed,

indicative that de-doping of the graphene has occurred due to thermal desorption of

adsorbed dopants on the graphene surface.[48] (see **Figure 2-2B**)
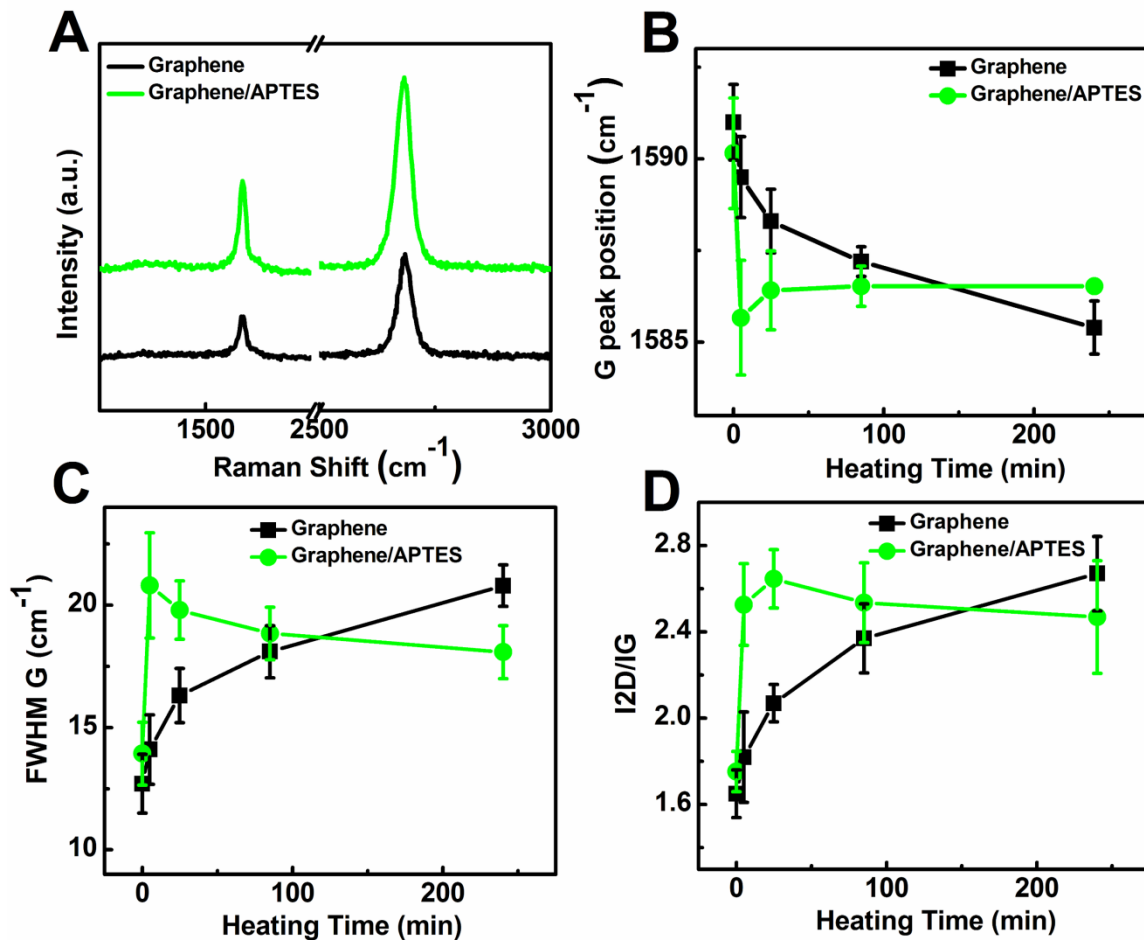
Figure 2-2: Full Raman spectra for two samples: (black line) graphene on SiO₂ and (green line) graphene on APTES coated SiO₂. (B) G band peak position for the samples shown in 2A as a function of heating time at 200 °C. (C) FWHM of the G band for the samples shown in 2A as a function of heating time at 200 °C. (D) Ratio of 2D vs. G band peak intensity for the samples shown in 2A as a function of heating time at 200 °C.

Electrical transport properties in graphene FET devices were made in three configurations: (1) FET devices with graphene transferred directly onto SiO_2 coated channels without APTES surface treatment, (2) FET devices with graphene transferred directly onto SiO_2 coated channels covered completely with the APTES surface treatment, and (3) FET devices with graphene transferred directly onto SiO_2 coated channels partially coated in a pattern-wise manner with APTES. Electrical measurements, including I-V curves, were made using a probe station configured with a HP 4156 semiconductor parameter analyzer maintained under an inert atmosphere. Measurements were performed on both as-made devices and after heating in the inert atmosphere to verify both the thermal desorption induced de-doping of the graphene and n-type doping of the graphene in the presence of APTES.

All devices, both with and without APTES, demonstrated p-doped characteristics in their as-made state, due presumably to adsorbed species on the graphene surface resulting from the CVD graphene transfer process [see **figure 2-3A-B**].[47,49,50] As the devices were annealed at 200 °C under the inert nitrogen environment, adsorbed p-dopants were removed, leading to pristine graphene with a charge neutrality point at approximately zero volts.[44,49] Attempts were also made to de-dope the devices in high-vacuum (10^{-8} torr) combined with in-situ electrical transport measurements (for up to 7 days), but no significant de-doping or shift of the neutrality point was observed in these cases (**Figure 2-3**). For graphene FET devices made using APTES coating the complete FET channel, as the sample is heated at 200 °C, the charge neutrality point is observed to gradually shift to lower voltages with increasing annealing time. For the APTES treated devices, the n-type doping characteristics were observed to stabilize after approximately 3 hours of heat

treatment at 200 °C, with the charge neutrality point (CNP) stabilizing at ~ -26 V. The electron concentration (*n*) of the APTES-treated graphene after annealing was approximately 2×10^{12} cm^{-2}, as calculated using equation 2,[44,51]

$$n = C_gV_{np}/e \qquad (2)$$

where $C_g = 115$ aF/μm^2,[52] e is the charge of the electron, and V_{np} is the voltage at the charge neutrality point. The electron concentration (n) is related to the energy position of the Dirac point by the equation,[53]

$$E_D=\hbar\upsilon_F(\pi n)^{-1/2} \qquad (3)$$

where υ_F is the Fermi velocity of graphene (1.1×10^{-6} ms^{-1}).[26] The calculated energy position of the Dirac point is 0.18 eV after anneal, which correlates well with the shift of the graphene work function from the control (~0.2 eV, **Figure 2-1**).

The field-effect mobility for both of the devices was ~ 434±100 cm^2/Vs (hole and electron mobility), extracted using equation 4,[6]

$$\mu= L_{ch}g_m/W_{ch}V_{ds}C_{ox} \qquad (4)$$

where μ= mobility, L_{ch}= 2000 μm, g_m= dI_D/dV_{GS} , W_{ch}= 50 μm , V_{DS}= 0.1 V and C_g= 115 aF/μm^2. This result indicates that the APTES layer was able to dope the graphene in the FET device without otherwise affecting or degrading its mobility as compared to devices

made without the doping layer. This is consistent with previous studies that have indicated that contact of graphene with self-assembled monolayers has not significantly affected their mobilities as compared to graphene in contact with substrates not containing the SAMs.[13,27,29]
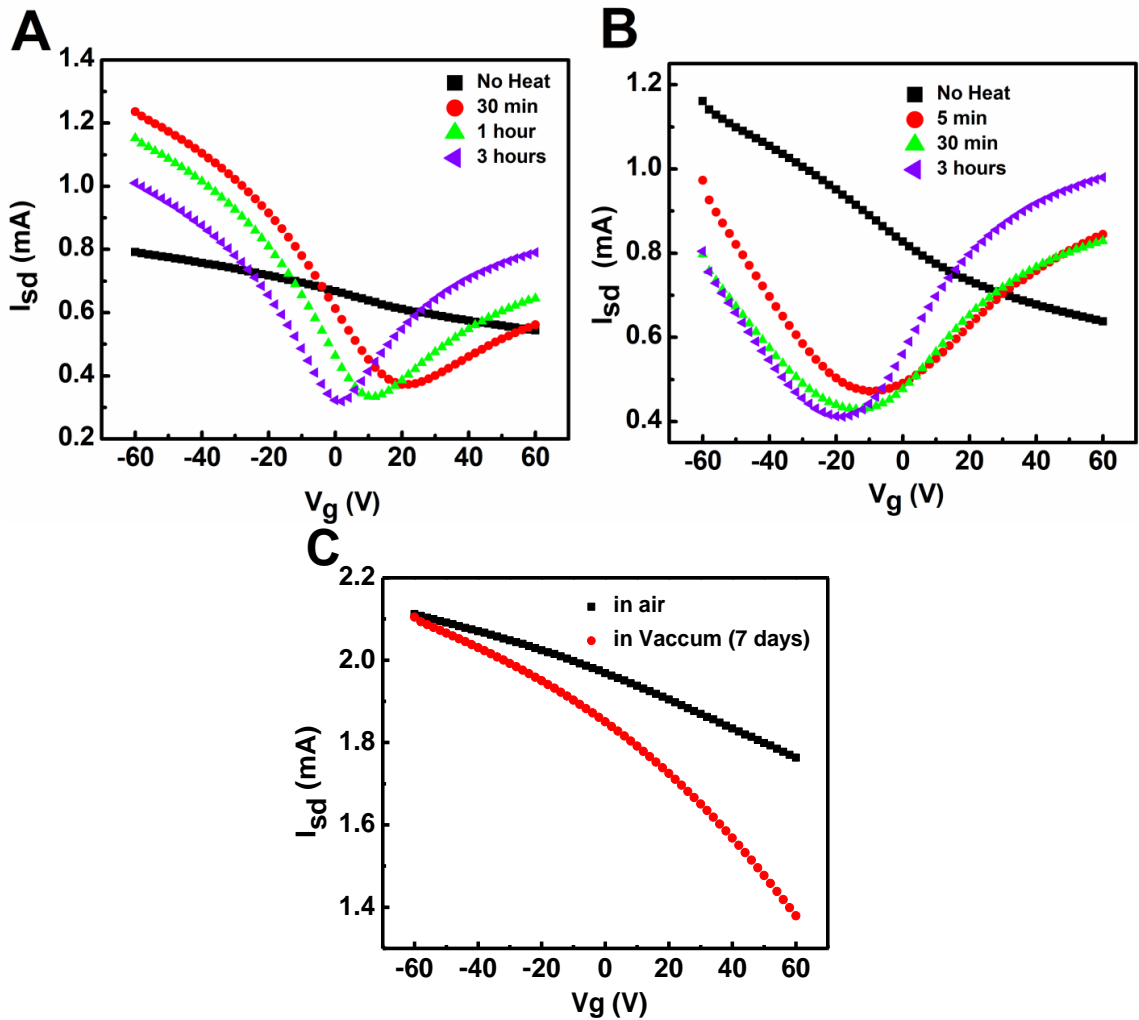
Figure 2-3: Source-drain current versus gate voltage for different device heating times at 200 °C for simple graphene FET devices fabricated using a simple (A) SiO₂ gate dielectric and (B) an APTES coated gate dielectric. (C) Source-drain current versus gate voltage as a function of pump down time for a graphene/APTES FET device.

Back-gated graphene-based p-n junction with patterned p-n regions in the FET channel were fabricated and measured following the same basic process described above. **Figure 2-4A** illustrates the fabrication steps involved in making the patterned p-n junctions in the FET channel devices. After lithography and deposition processes (i.e. typical lift-off procedures) were used to form the gold electrodes on the 300 nm thick SiO_2 gate dielectric films on highly p-doped silicon wafers, half of each of the channels in the FET devices were patterned with photoresist and hard baked. The device samples were then treated with APTES using the same solution processing sequence described earlier to deposit APTES in the half of each device channel that was not protected by hard-baked photoresist. The photoresist was removed by placing the devices in N-methylpyrrolidone (NMP) for 1 hour, followed by further sonication in acetone and inspection by optical microscopy to ensure removal of all photoresist.

The resulting patterned APTES layers were verified by XPS mapping as illustrated in **Figure 2-4B**. XPS mapping was performed using a 30 μm spot size with a step size of 28 μm, and a Gaussian smoothing algorithm was applied to the raw data. The signal associated with 399.5 eV binding energy was used for mapping the N1s spectra. The figure shows a well defined boundary between areas of the substrate coated with the APTES layer and those without. Further analysis of the position of these boundaries with respect to the location and intensity of peaks in the XPS originating from the gold source and drain contacts confirm that the lithographic alignment was sufficient to locate these p-n junctions in the FET channels. C1s mapping using a binding energy centered at 285 eV was also performed. Again, a well defined boundary is observed in the patterned APTES samples,

with the strongest C1s signal corresponding to regions containing the strongest N1s signal as well, consistent with the formation of a well defined patterned APTES layer.

Electrical measurements were performed on the fabricated CVD graphene devices containing the patterned APTES in the device channels by probing the devices under inert atmosphere using a method similar to that described previously. As expected, as-made devices exhibited a heavily doped p-type characteristic (**Figure 2-4C**) due presumably to doping from adsorbed species. The two expected current minima region for the devices in the as-made state were located at sufficiently large positive gate potentials to preclude measurement without breakdown of the device dielectric. After annealing at 200 °C for only 5 min, two minima in the I_{sd}-V_g data were clearly observed, corresponding to two Dirac points as a result of desorption of p-dopants. For V_g larger than approximately +35 V in this device, the device channel was effectively in a n/n+ doping configuration where both regions of the channel were p-doped, but the region of the channel that does not contain the APTES layer was more heavily p-doped. For V_g of approximately 0 V to +35 V, the formation of a p-n junction in the device channel was observed. For V_g less than 0 V, the device channel existed in a p+/p doping configuration where the regions of the channel containing the APTES layer were more heavily n-doped. After 30 min of annealing at 200 °C, the device channel was n/n+ doped for V_g larger than +15 V, p-n doped for Vg between -10 V and +15V, and p/p+ doped for Vg less than -10V. These behaved roughly symmetrically in terms of electrical response around Vg=0 V. Further annealing led to additional shifts of the Vg range over which a p-n junction doping profile existed in the device channel to more negative Vg. It was also possible during these measurements to demonstrate the unique ambipolar character of the devices. Switching of

the source-drain bias voltage from positive to negative values showed no rectifying behavior as would be characteristic of an ambipolar device.[12,54]

In addition to using this strategy of patterning the amine layer to introduce controlled modulation of the doping profile in the device channel, it is also of course possible to modulate the amount of free amine on the substrate by changing the time or solution concentration conditions used to deposit the amine. This modulation of the amount of APTES on the dielectric surface can in turn be used to modulate the doping level in the devices. To demonstrate this, the APTES deposition time was varied between 1 and 7 hours for devices made with the unpatternd APTES layer covering the entire device channel. **Figure 2-4E** shows the carrier concentration measured in the graphene devices along with the nitrogen to silicon ratio (N/Si) obtained by XPS in each of these samples as a function of APTES deposition time. Clearly the carrier concentration is observed to scale roughly with APTES deposition time over the range of APTES deposition times measured. One would expect this behavior to saturate once a sufficiently dense and thick enough APTES layer is formed such that no further electronic influence on the graphene film is created by further deposition of APTES. Carrier concentrations in excess of 4.5×10^{12} cm^{-2} were observed in the devices measured, corresponding to a CNP change above -60 V (**Figure 2-4**). This ability to control the n-doping characteristics of the device surface, i.e. through modulation of the density of APTES deposited (e.g. by controlling deposition time or solution concentration) on the gate dielectric, can be easily combined with the patterned p-n junction fabrication techniques to allow for full control of the position of the charge neutrality points in the I-V characteristics of the resulting FET devices. This unique p-n junction behavior of graphene, in contrast with the traditional rectifying behavior of

conventional semiconductors, allows the development of graphene-based bipolar devices which have been demonstrated to display new and exciting phenomena such as Klein tunneling, [30,31,33] and produce lensing effects for coherent electrons, i.e. so called Veselago lensing.[55] Our simple method for producing patterned doping profiles in graphene films and devices facilitates the study of such phenomena since it allows precise and independent control over the characteristics of the FET I-V curves as compared to the more limited control possible with electrostatic substrate engineering,[12] and other fabrication techniques. [24,25,31,33,56]
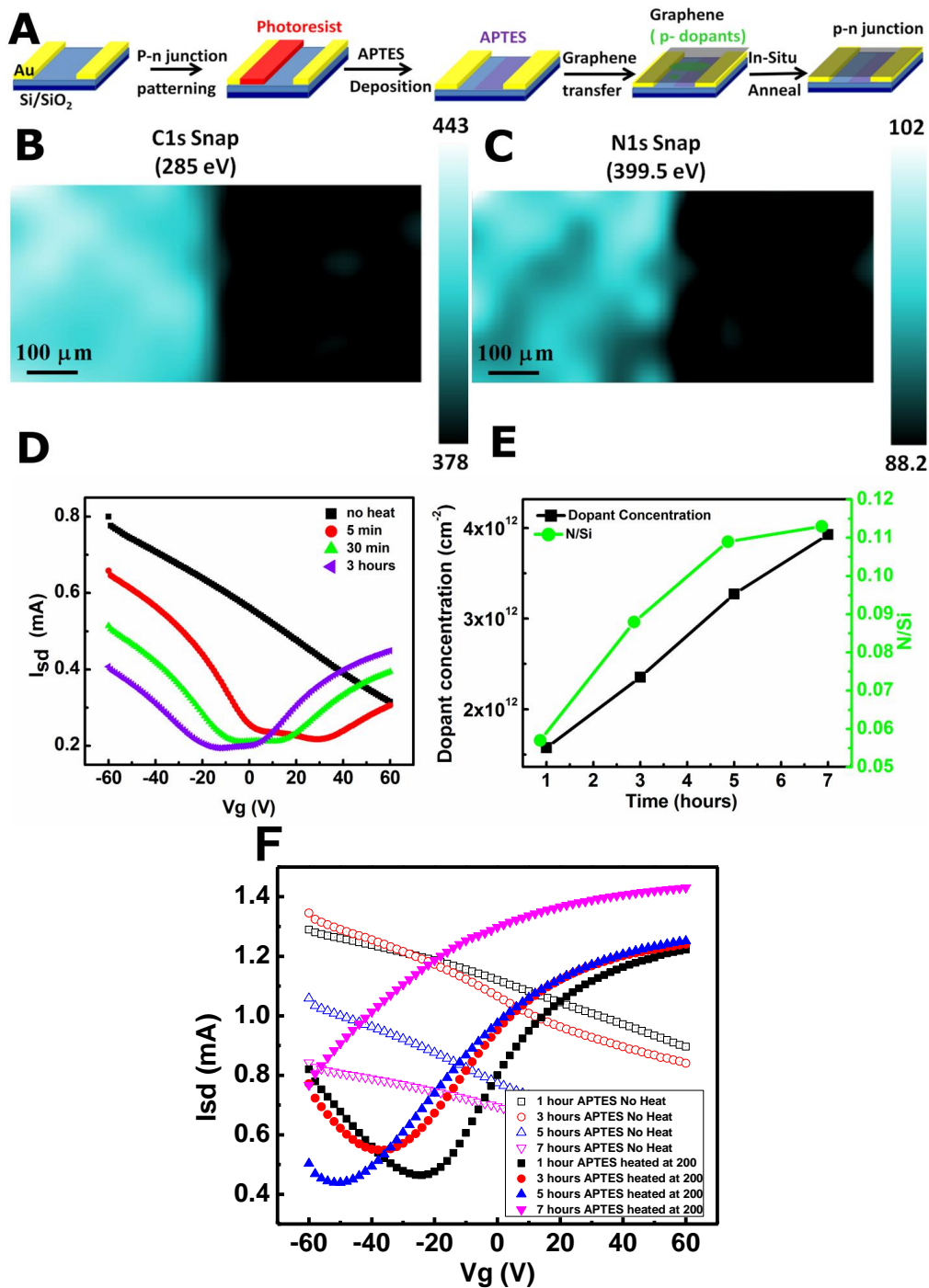
Figure 2-4: Schematic showing the process used to fabricate the graphene p-n junction. XPS mapping of the graphene p-n junction for the (B) C1s intensity at a binding energy of ~ 285 eV (C) N 1s intensity at a binding energy of 399.9 eV. (D) Source-drain current versus gate voltage as a function of heating times at 200 °C for a graphene p-n junction. (E) Dopant concentration and Nitrogen/silicon (N/Si) ratio versus APTES deposition time. (F) Source-drain current versus gate voltage heated at 200 °C as a function of APTES time deposition for a simple's graphene/APTES FET.

2.4   Conclusions

The use of a self-assembled covalent APTES monolayer has been demostrated to n-dope graphene, controlling the resulting doping level in graphene FET devices depending upon the amount of APTES deposited onto the FET gate dielectric surface. Production of FET devices with patterned p- and n-doped regions through lithographic patterning of such APTES layers using the combination of control of APTES deposition and patterning to tune the I-V characteristics of graphene FET devices was done. It has also been shown that use of such APTES doping schemes does not degrade the resulting graphene electronic properties as has been problematic in previously reported doping procedures due to introduction of defects into the graphene layer. Overall, the methods described here allow for facile, controllable, and low temperature fabrication of graphene p-n junctions.

2.5   References

1   Geim, A. K. Graphene: Status and Prospects. *Science* **324**, 1530-1534, doi:DOI 10.1126/science.1158877 (2009).

2   Geim, A. K. & Novoselov, K. S. The rise of graphene. *Nat Mater* **6**, 183-191, doi:10.1038/nmat1849 (2007).

3   Ohta, T., Bostwick, A., Seyller, T., Horn, K. & Rotenberg, E. Controlling the electronic structure of bilayer graphene. *Science* **313**, 951-954, doi:DOI 10.1126/science.1130681 (2006).

4   Du, X., Skachko, I., Barker, A. & Andrei, E. Y. Approaching ballistic transport in suspended graphene. *Nat Nanotechnol* **3**, 491-495, doi:10.1038/nnano.2008.199 (2008).

5   Novoselov, K. S. *et al.* Electric Field Effect in Atomically Thin Carbon Films. *Science* **306**, 666-669 (2004).

6   Schwierz, F. Graphene transistors. *Nat Nano* **5**, 487-496 (2010).

7   Usachov, D. *et al.* Nitrogen-Doped Graphene: Efficient Growth, Structure, and Electronic Properties. *Nano Lett* **11**, 5401-5407, doi:Doi 10.1021/Nl2031037 (2011).

8   Zhao, L. Y. *et al.* Visualizing Individual Nitrogen Dopants in Monolayer Graphene. *Science* **333**, 999-1003, doi:DOI 10.1126/science.1208759 (2011).

9   Zhou, S. Y. *et al.* Substrate-induced bandgap opening in epitaxial graphene. *Nat Mater* **6**, 770-775, doi:10.1038/nmat2003 (2007).

10   Han, M. Y., Ozyilmaz, B., Zhang, Y. B. & Kim, P. Energy band-gap engineering of graphene nanoribbons. *Phys Rev Lett* **98**, doi:Artn 206805 Doi 10.1103/Physrevlett.98.206805 (2007).

11   Liu, H., Liu, Y. & Zhu, D. Chemical doping of graphene. *J Mater Chem* **21**, 3335-3345 (2011).

12   Chiu, H. Y., Perebeinos, V., Lin, Y. M. & Avouris, P. Controllable p-n Junction Formation in Mono layer Graphene Using Electrostatic Substrate Engineering. *Nano Lett* **10**, 4634-4639, doi:Doi 10.1021/Nl102756r (2010).

13   Farmer, D. B., Lin, Y. M., Afzali-Ardakani, A. & Avouris, P. Behavior of a chemically doped graphene junction. *Appl Phys Lett* **94**, doi:Artn 213106 Doi 10.1063/1.3142865 (2009).

14   Dai, H. J. *et al.* N-Doping of Graphene Through Electrothermal Reactions with Ammonia. *Science* **324**, 768-771, doi:10.1126/science.1170335 (2009).

15   Ast, C. R., Gierz, I., Riedl, C., Starke, U. & Kern, K. Atomic Hole Doping of Graphene. *Nano Lett* **8**, 4603-4607, doi:Doi 10.1021/Nl802996s (2008).

16   Wei, D. *et al.* Synthesis of N-doped graphene by chemical vapor deposition and its electrical properties. *Nano Lett* **9**, 1752-1758, doi:10.1021/nl803279t (2009).

17   Jin, Z., Yao, J., Kittrell, C. & Tour, J. M. Large-scale growth and characterizations of nitrogen-doped monolayer graphene sheets. *ACS Nano* **5**, 4112-4117, doi:10.1021/nn200766e (2011).

18   Guo, B. *et al.* Controllable N-Doping of Graphene. *Nano Lett*, doi:10.1021/nl103079j (2010).

19   Lin, Y.-C., Lin, C.-Y. & Chiu, P.-W. *Controllable graphene N-doping with ammonia plasma*. Vol. 96 (AIP, 2010).

20   Pirkle, A. *et al.* The effect of chemical residues on the physical and electrical properties of chemical vapor deposited graphene transferred to SiO(2). *Appl Phys Lett* **99**, doi:Artn 122108 Doi 10.1063/1.3643444 (2011).

21   Ni, Z. H. *et al.* The effect of vacuum annealing on graphene. *Journal of Raman Spectroscopy* **41**, 479-483, doi:10.1002/jrs.2485 (2010).

22   Ryu, S. *et al.* Atmospheric Oxygen Binding and Hole Doping in Deformed Graphene on a SiO(2) Substrate. *Nano Lett* **10**, 4944-4951, doi:Doi 10.1021/Nl1029607 (2010).

23   Brenner, K. & Murali, R. In situ doping of graphene by exfoliation in a nitrogen ambient. *Appl Phys Lett* **98**, doi:Artn 113115 Doi 10.1063/1.3562018 (2011).

24   Lohmann, T., von Klitzing, K. & Smet, J. H. Four-Terminal Magneto-Transport in Graphene p-n Junctions Created by Spatially Selective Doping. *Nano Lett* **9**, 1973-1979, doi:Doi 10.1021/Nl900203n (2009).

25   Peters, E. C., Lee, E. J. H., Burghard, M. & Kern, K. Gate dependent photocurrents at a graphene p-n junction. *Appl Phys Lett* **97**, doi:Artn 193102 Doi 10.1063/1.3505926 (2010).

26   Park, J. *et al.* Work-Function Engineering of Graphene Electrodes by Self-Assembled Monolayers for High-Performance Organic Field-Effect Transistors. *J Phys Chem Lett* **2**, 841-845, doi:Doi 10.1021/Jz200265w (2011).

27   Wang, R. *et al.* Control of Carrier Type and Density in Exfoliated Graphene by Interface Engineering. *Acs Nano* **5**, 408-412, doi:10.1021/nn102236x (2010).

28   Yokota, K., Takai, K. & Enoki, T. Carrier Control of Graphene Driven by the Proximity Effect of Functionalized Self-assembled Monolayers. *Nano Lett*, doi:10.1021/nl201607t (2011).

29   Yan, Z. *et al.* Controlled Modulation of Electronic Properties of Graphene by Self-Assembled Monolayers on SiO(2) Substrates. *ACS Nano* **5**, 1535-1540, doi:Doi 10.1021/Nn1034845 (2011).

30   Williams, J. R., DiCarlo, L. & Marcus, C. M. Quantum hall effect in a gate-controlled p-n junction of graphene. *Science* **317**, 638-641, doi:DOI 10.1126/science.1144657 (2007).

31   Young, A. F. & Kim, P. Quantum interference and Klein tunnelling in graphene heterojunctions. *Nat Phys* **5**, 222-226, doi:Doi 10.1038/Nphys1198 (2009).

32   Velasco, J. *et al.* Probing charging and localization in the quantum Hall regime by graphene p-n-p junctions. *Phys Rev B* **81**, doi:Artn 121407 Doi 10.1103/Physrevb.81.121407 (2010).

33   Stander, N., Huard, B. & Goldhaber-Gordon, D. Evidence for Klein Tunneling in Graphene p-n Junctions. *Phys Rev Lett* **102**, doi:Artn 026807 Doi 10.1103/Physrevlett.102.026807 (2009).

34   Kobayashi, S. *et al.* Control of carrier density by self-assembled monolayers in organic field-effect transistors. *Nat Mater* **3**, 317-322, doi:10.1038/nmat1105 (2004).

35   Shim, M., Javey, A., Kam, N. W. S. & Dai, H. J. Polymer functionalization for air-stable n-type carbon nanotube field-effect transistors. *J Am Chem Soc* **123**, 11512-11513, doi:Doi 10.1021/Ja0169670 (2001).

36   Kong, J. & Dai, H. J. Full and modulated chemical gating of individual carbon nanotubes by organic amine compounds. *J Phys Chem B* **105**, 2890-2893 (2001).

37   Lee, S. H. *et al.* Photooxidation of Amine-Terminated Self-Assembled Monolayers on Gold. *J Phys Chem C* **114**, 10512-10519, doi:Doi 10.1021/Jp101426h (2010).

38   Hooper, A. E., Werho, D., Hopson, T. & Palmer, O. Evaluation of amine- and amide-terminated self-assembled monolayers as 'Molecular glues' for Au and SiO2 substrates. *Surface and Interface Analysis* **31**, 809-814, doi:10.1002/sia.1125 (2001).

39   Heremans, P., Janssen, D., De Palma, R., Verlaak, S. & Dehaen, W. Static solvent contact angle measurements, surface free energy and wettability determination of various self-assembled monolayers on silicon dioxide. *Thin Solid Films* **515**, 1433-1438, doi:Doi 10.1016/J.Tsf.2006.04.006 (2006).

40   Li, X. *et al.* Large-Area Synthesis of High-Quality and Uniform Graphene Films on Copper Foils. *Science* **324**, 1312-1314 (2009).

41   Kowalczyk, D., Slomkowski, S., Chehimi, M. M. & Delamar, M. Adsorption of aminopropyltriethoxy silane on quartz: An XPS and contact angle measurements study. *Int J Adhes Adhes* **16**, 227-232 (1996).

42   Chirakul, P., Perez-Luna, V. H., Lopez, G. P. & Hampton, P. D. Self-assembled monolayers of amine-terminated thiols. *Abstr Pap Am Chem S* **217**, U668-U668 (1999).

43   Ishii, H., Sugiyama, K., Ito, E. & Seki, K. Energy level alignment and interfacial electronic structures at organic/metal and organic/organic interfaces (vol 11, pg 605, 1999). *Adv Mater* **11**, 972-972 (1999).

44   Shen, Z. X. *et al.* The effect of vacuum annealing on graphene. *Journal of Raman Spectroscopy* **41**, 479-483, doi:Doi 10.1002/Jrs.2485 (2010).

45   Leenaerts, O., Partoens, B. & Peeters, F. M. Adsorption of small molecules on graphene. *Microelectron J* **40**, 860-862, doi:DOI 10.1016/j.mejo.2008.11.022 (2009).

46   Wang, X. M., Xu, J. B., Wang, C. L., Du, J. & Xie, W. G. High-Performance Graphene Devices on SiO2/Si Substrate Modified by Highly Ordered Self-Assembled Monolayers. *Adv Mater* **23**, 2464-+, doi:DOI 10.1002/adma.201100476 (2011).

47   Novoselov, K. S. *et al.* Detection of individual gas molecules adsorbed on graphene. *Nat Mater* **6**, 652-655, doi:Doi 10.1038/Nmat1967 (2007).

48   Das, A. *et al.* Monitoring dopants by Raman scattering in an electrochemically top-gated graphene transistor. *Nat Nano* **3**, 210-215, doi:http://www.nature.com/nnano/journal/v3/n4/suppinfo/nnano.2008.67_S1.html (2008).

49   Szafranek, B. N., Schall, D., Otto, M., Neumaier, D. & Kurz, H. High On/Off Ratios in Bilayer Graphene Field Effect Transistors Realized by Surface Dopants. *Nano Lett* **11**, 2640-2643, doi:10.1021/nl200631m (2011).

50   Novoselov, K. S. *et al.* fake. *Science* **306**, 666-669, doi:10.1126/science.1102896 (2004).

51   Nourbakhsh, A. *et al.* Tuning the Fermi Level of SiO(2)-Supported Single-Layer Graphene by Thermal Annealing. *J Phys Chem C* **114**, 6894-6900, doi:Doi 10.1021/Jp910085n (2010).

52   Joselevich, E., Tsivion, D., Schvartzman, M., Popovitz-Biro, R. & von Huth, P. Guided Growth of Millimeter-Long Horizontal Nanowires with Controlled Orientations. *Science* **333**, 1003-1007, doi:Doi 10.1126/Science.1208455 (2011).

53   Zhang, Y. B. *et al.* Giant phonon-induced conductance in scanning tunnelling spectroscopy of gate-tunable graphene. *Nat Phys* **4**, 627-630, doi:Doi 10.1038/Nphys1022 (2008).

54   Cheng, H. C., Shiue, R. J., Tsai, C. C., Wang, W. H. & Chen, Y. T. High-Quality Graphene p-n Junctions via Resist-free Fabrication and Solution-Based Noncovalent Functionalization. *Acs Nano* **5**, 2051-2059, doi:Doi 10.1021/Nn103221v (2011).

55   Cheianov, V. V., Fal'ko, V. & Altshuler, B. L. The focusing of electron flow and a Veselago lens in graphene p-n junctions. *Science* **315**, 1252-1255, doi:DOI 10.1126/science.1138020 (2007).

56   Brenner, K. & Murali, R. Single step, complementary doping of graphene. *Appl Phys Lett* **96**, doi:Artn 063104 Doi 10.1063/1.3308482 (2010).

CHAPTER 3

CREATING GRAPHENE P-N JUNCTIONS USING SELF-ASSEMBLED MONOLAYERS

3-Aminopropyltriethoxysilane (APTES) and 1H,1H,2H,2H-Perfluorooctyltriethoxysilane (PFES) were used to modify the interface between transferred CVD graphene films and its supporting dielectric to create n-type and p-type graphene, respectively. A graphene p-n junction was obtained by patterning both modifiers on the same dielectric and verified through the creation of a field effect transistor (FET). Characteristic I-V curves indicate the presence of two separate Dirac points which confirms an energy separation of neutrality points within the complementary regions. This method minimizes doping-induced defects and results in thermally stable graphene p-n junctions for temperatures up to 200°C.

3.1   Introduction

Graphene has exhibited some unique properties that have made it of interest to the scientific community for use as an electronic material. These properties include an unusual band structure that makes it a gapless semiconductor, linear energy-momentum relation near the Dirac point, and extraordinarily high carrier mobilities.[1-3] Due to the zero-gap in single-layer graphene, both carrier type and concentration can be controlled through an electrostatic gate, making graphene a promising material for semiconductor applications.[2,4] This electrostatic gating allows the development of graphene-based bipolar devices where a junction between hole-rich and electron-rich regions, or a p-n junction, can be formed.[5,6] Graphene p-n junctions have already displayed new and exciting phenomena such as Klein tunneling, where electrons traveling perpendicular to the junction experience zero resistance[7] and fractional quantum Hall transport.[6] Such junctions are predicted to produce lensing effects for coherent electrons, so called Veselago lensing, where diverging electron waves are refocused by the junction.[8] Most graphene junctions to date have been fabricated using multiple electrostatic gates,[6] electrical stress-induced doping,[9,10] chemical treatment by gas exposure,[11] chemical modifications on top of the graphene,[12-14] and modification of the substrate by changing the local electrostatic potential in the vicinity of one of the contacts.[15] However, current methods for electrostatic gating require a number of fabrication steps that may not be easily scalable in industry level and are usually expensive. In addition, chemical doping on top of graphene can degrade the carrier mobility in the device through the introduction of defects and impurities in the graphene. In addition,

physisorbed dopant molecules are not stable and may desorb resulting in changes in the electronic properties of the graphene.

Here, we utilize a low temperature controllable method to fabricate p-n junctions in graphene by modifying the interface between graphene and its support substrate with self-assembled monolayers (SAMs). SAMs have been extensively used to enhance the mobility of organic thin film transistors and to eliminate the Schottky barrier at the metal semiconductor interface.[16-19] They have been recently used to modify graphene and dielectric interfaces by reducing charged impurity scattering and the effects of environmentally induced doping on graphene,[20,21] and to control charge carrier and concentration to create n- and p-type graphene field effect transistors (FETs).[22-25] Unlike chemical doping, this method uses SAMs that covalently bond to the substrate rather than graphene resulting thermally stable doping and unlike electrostatic gating, independent of dielectric material and thickness.

3-Aminopropyltriethoxysilane (APTES) and 1H,1H,2H,2H-Perfluorooctyltriethoxysilane (PFES) were used to modify the interface between transferred layers of CVD graphene and its supporting dielectric to create n- and p- type graphene, respectively. APTES contains an amine functional group with a basic nitrogen atom having a lone electron pair. The electron-rich amine group donates an electron to the carbon atoms in graphene, causing N-doping. In contrast, fluorine is a well-known electron acceptor. Thus, adding a layer of PFES results in the transfer of an electron from the graphene creating p-type graphene. The purpose of the silane group is to create a strong covalent bond to the oxide dielectric support such as SiO_2, thereby anchoring the APTES and PFES which induces thermal stability of the modified interface and the doped graphene

layer. By patterning adjacent regions of APTES and PFES, p-n junctions in the graphene were created.

3.2   Experimental Section

The fabrication process of the graphene p-n junction is schematically illustrated in **Figure 3-1**. First, the source and drain contacts (gold 50 nm thick) were defined using a conventional electron-beam lithography and lift-off processes on a highly p-doped Si substrate with a 300 nm thick SiO_2 layer to create back gated field effect transistor structures. The resulted channel size is 25 μm by 25 μm. Another set of devices were fabricated with a channel size of 10 μm by 10 μm. Prior to APTES deposition, the substrate was first pre-treated by UV ozone for 15 min in order to produce a hydroxyl-terminated substrate that reacts with the silane coupling agent. Immediately afterwards, the substrate was immersed in a 0.1 %(v/v) solution of anhydrous toluene and 3-aminopropyltrietoxysilane (APTES) for 3 hours, producing a free-amine rich substrate with a contact angle of ~ 60°. Next, half of the channel in the FET device was patterned with photoresist. After development, the other half of the channel was treated with UV-Ozone for 15 minutes to remove the exposed APTES and produce a hydroxyl-terminated surface. Next, the device was treated for one hour with 10 microliters of PFES dissolved in 10 ml of toluene 1 %(v/v). The measured contact angle for PFES-treated substrate was c.a. 110°. Finally, the resist was removed to expose the APTES coated region prior to transfer of graphene on top of the SAMs coated SiO_2. Monolayer graphene was grown on a 25 μm thick sheet of Cu foil (Alfa Aesar, item No. 14482) in a low pressure environment

using chemical vapor deposition (CVD) and transferred to the device through a similar method explained in literature.[8]
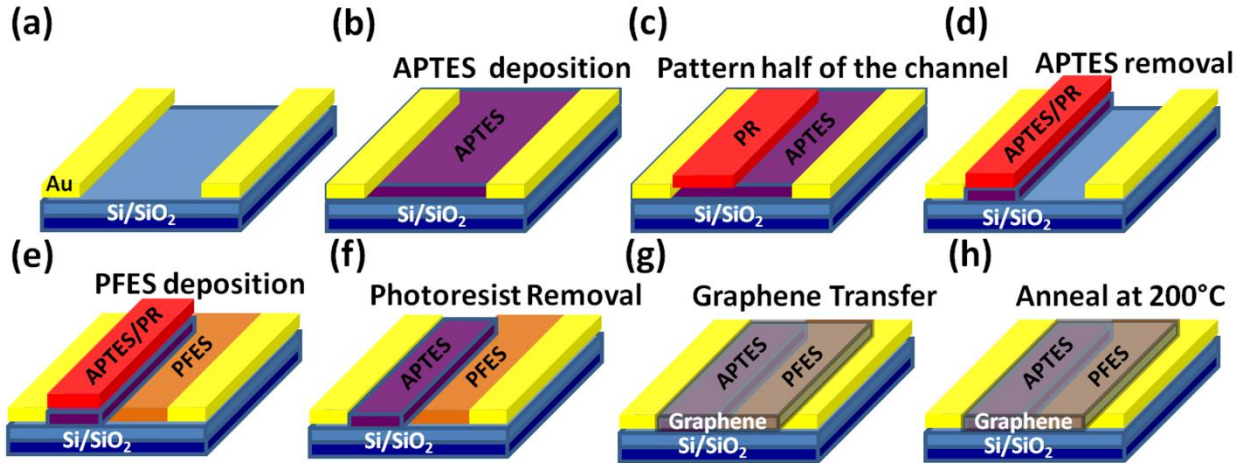
Figure 3-1: **Schematic of the graphene p-n junction fabrication steps.**

3.3   Results and Discussion

X-ray photoelectron spectroscopy was employed to identify the surface functionalization present on the SiO_2 on each side of the channel to confirm the presence of APTES and PFES. XPS data were acquired using a spectrophotometer (VG Scientific ESCALAB 210) with an $K\alpha$ X-ray source ($h\upsilon = 1486.68$ eV). The survey scan spectra were collected at the binding energy (B.E.) of 0-1300 eV with a step size of 1 eV at a pass energy of 200 eV and a spot size of 400 μm. **Figure 3-2A** shows survey scan spectra randomly collected from as-transferred graphene, functionalized with APTES, and with PFES. The scan showed the most prominent peaks to be C1s and O1s on all spectra. The appearance of a N1s peak centered at 400.1 eV and a F1s peak centered at 689.3 eV in the

survey spectra confirms the presence of APTES and PFES underneath the graphene, respectively. High resolution XPS spectra of the C1s binding energy was also acquired over 282-293 eV with a step size of 0.1 eV and 50 eV pass energy. The appearance of a shoulder and a shift in the C1s peak position of functionalized graphene also verified the presence of APTES and PFES on the substrate [see **Figure 3-2B**]. To ensure the presence and formation of the patterned SAMs on the channel, XPS mapping was utilized [see **Figure 3-2C-E**]. XPS mapping was performed using a 30 micron spot size with a step size of 28 microns, and a Gaussian smoothing algorithm (Thermo scientific) was applied to the raw data. **Figure 3-2C** shows the intensity of the N1s map with a well defined boundary that indicates the presence of amine only on half of the channel. Similarly, the F1s map indicates the presence of fluorine in the other half of the channel [see **Figure 3-2D**]. For the core level C1s mapping, a binding energy centered at 285.3 eV was selected.
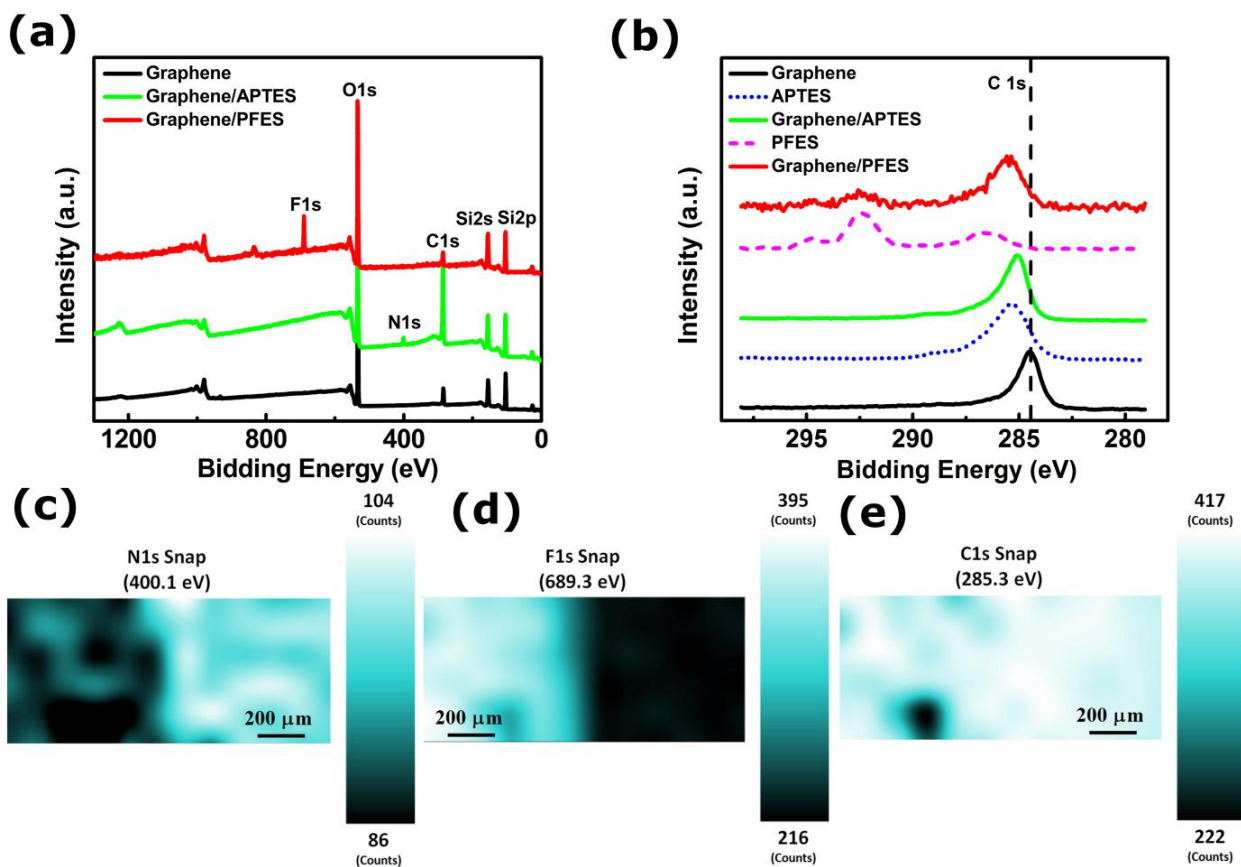
Figure 3-2: XPS spectra representing (a) Survey scan and (b) Core level C1s binding energy for graphene/SiO₂ (black), graphene/PFES/SiO₂ (red) and Graphene/APTES/SiO₂ (green). XPS mapping of a graphene p-n junction. (c) C1s binding energy centered at 285.3 eV.(d) N1s binding energy centered at 400.1 eV and (e) F1s binding energy centered at 689.3 eV.

It is well known that environmentally-induced water vapor and oxygen bound to the graphene are electron acceptors[26] that play an important role in the unintentional p-doping of graphene films. This unintentional doping of the graphene had to be removed in order to fully reveal the effects of the APTES and PFES on the graphene. To remove this unintentional doping effect, the samples were heat treated under nitrogen atmosphere to unmask the intentional doping effects of the APTES and the PFES underlying layer.[27] To this end, the samples were cycled between room temperature and 200ºC from 5-180 minutes while in-situ Raman spectroscopy was utilized at room temperature to investigate the quality of the graphene and its doping state by examining the D, G, and 2D bands and their positions. All spectra were excited with visible (532 nm) laser light and collected in the backscattering configuration. The samples were placed inside an environmentally controlled microscope stage with heating, vacuum, and gas delivery capability (Linkam TS 1500) for in-situ Raman measurements. The sample was heated up to 200°C under nitrogen atmosphere and held between 5-180 min to allow for desorption of atmospheric p-dopants bonded to the sample. Raman measurements were performed before and after annealing at nitrogen atmosphere. **Figure 3-3A** shows the Raman spectra of as-transferred, APTES treated, and PFES treated graphene after 3 hours of annealing at 200°C. The difference in the G and 2D peak width, position, and their intensity ratio for each sample is indicative of various doping states. A critical observation is that no increase on the D band was observed during any of the annealing steps; hence successful doping of the graphene monolayer without significant damage to the lattice structure was achieved.[28,29] Monitoring of the G peak position with increase in heating time, its full width at half maximum FWHM(G), and intensity ratio of 2D over G peak (I_{2D}/I_G) reveal the changes in electronic state of various

devices. **Figure 3-3B** shows a decrease in the G peak position of as-transferred graphene after annealing for only 5 minutes. Further annealing resulted in a greater decrease in the peak position, leading to 1588 cm^{-1} after 3 hours of annealing. This indicates the de-doping process induced by the removal of the environmentally induced dopants through annealing.[30] **Figures 3-3C** and **3-3D** show an increase in FWHM(G) from 17 to 23 and I_{2D}/I_G from 1.685 to 1.7, respectively. These confirm the removal of atmospheric p-dopant, leading to de-doped graphene after 3 hours of heat treatment. The G peak position of as-transferred graphene functionalized with APTES was 1590 cm^{-1}, and FWHM (G) was 14 cm^{-1}. These are lower than the corresponding values for graphene without functionalization with APTES and are indicative of a reduction in p-doping state. This change in the G peak position is due to competing effects between n-doping induced by APTES and p-doping by water vapor and oxygen. Similar to as-transferred graphene, heat treatment for 5 minutes resulted in the removal of p-dopants, leading to a decrease in G peak position down to 1585.5 cm^{-1}, an increase in FWHM(G) to 21 and I_{2D}/I_G to 2.65. These values are similar to those measured for de-doped graphene. However, further heat treatment resulted in the removal of additional p-dopants, causing the n-doping effect to become dominant. This led to an increase in the G peak position to 1586.5 cm^{-1} and a decrease in FWHM(G) to 20 and I_{2D}/I_G to 2.3, which is in accord with observed Raman characteristics for n-doped graphene.[32]

The trend in Raman characteristics for PFES functionalized graphene is similar to that obtained with as-transferred graphene. A heavily p-doped characteristic before heat treatment is due to the presence of both PFES and atmospheric dopants from water vapor and oxygen. However, removal of atmospheric dopants by heat treatment for 3 hours

results in lowering the p-doping level in the graphene with a 7 cm^{-1} decrease in the G peak position, 6 cm^{-1} increase in FWHM(G), and 0.7 increase in I_{2D}/I_G. The shift in the position of the G peak is indicative of induced doping by SAMs without a change in the structure of graphene.
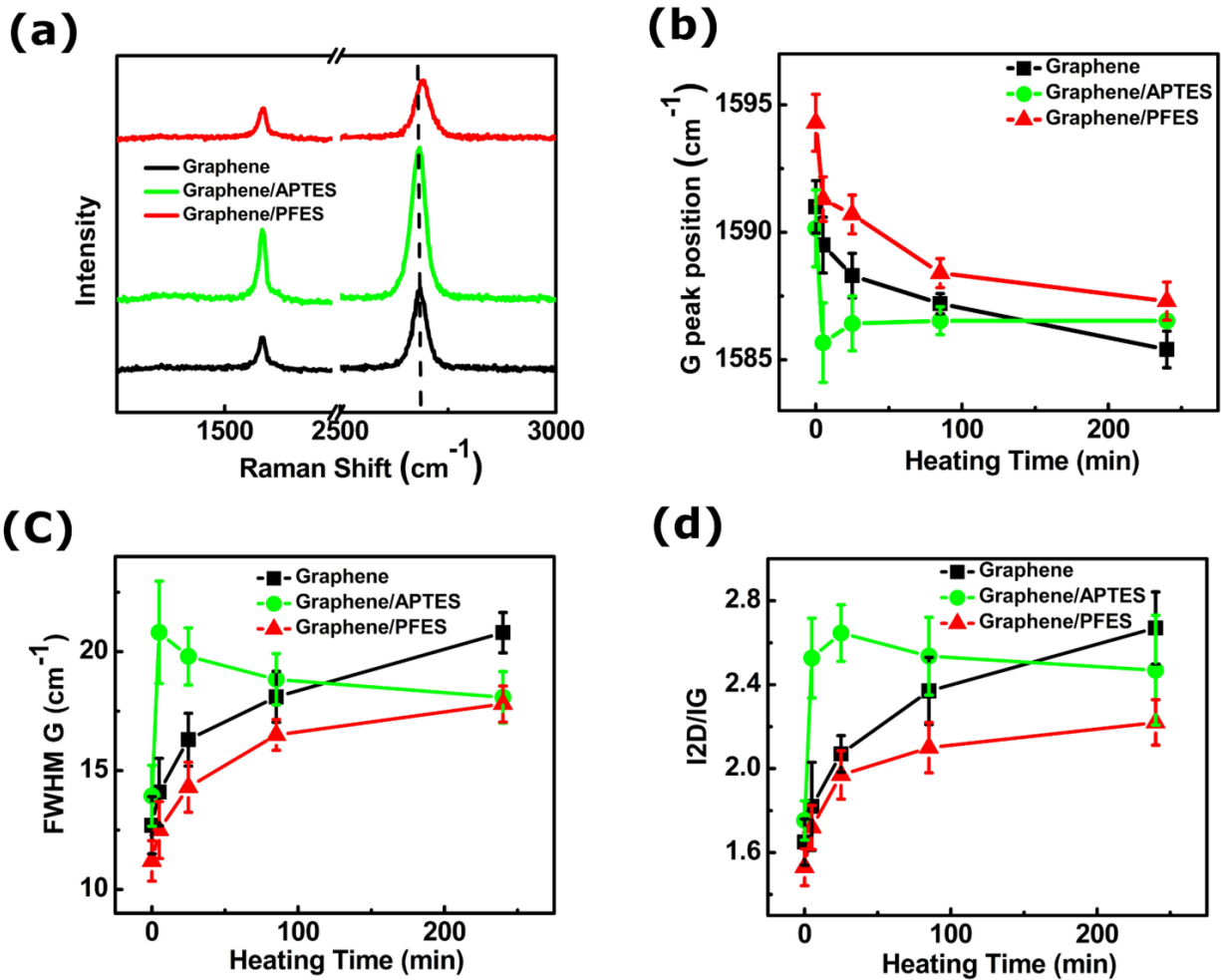
Figure 3-3: (a) Raman spectra of graphene/SiO$_2$(black), grapheen/APTES/SiO$_2$(green), and graphene/PFES/SiO$_2$(red) after being heated at 200 °C under nitrogen atmosphere for 3 hours. (b)-(d) G peaks position, FWHM (G), and I$_{2D}$/I$_G$ as a function of heating time under nitrogen atmosphere for graphene/SiO$_2$, graphene/APTES/SiO$_2$, and

To further demonstrate the n-type and p-type characteristics induced by APTES and PFES in graphene, back-gated FET devices were fabricated as shown in **Figure 3-1**. Here, the difference is that the device were only treated with APTES or PFES. Another set of devices were fabricated without SAMs as control devices. Transport in the APTES- and PFES-treated graphene devices as well as the devices without SAMs was measured using a probe station equipped with a HP 4156 semiconductor parameter analyzer under a nitrogen atmosphere [see **Figure 3-4A**]. It is noteworthy that these measurements were performed after heat treatment of the devices up to 200°C under the nitrogen atmosphere to remove dominant p-dopants from air exposure and transfer process of CVD graphene in order to unmask the intentional doping effect induced by SAMs. The charge neutrality point for graphene without SAMs was around zero volts after 3 hours of heat treatment, indicative of de-doped graphene as shown in **Figure 3-4A**. It is important to note that further annealing for up to 7 days did not cause a change in the neutrality point in graphene device. This is in contrast with the observed n-type characteristic of graphene due to annealing in a nitrogen atmosphere as we saw no evidence of n-type doping in these samples.[12] For the APTES treated device, n-doping characteristics were observed with the charge neutrality point (CNP) stably forming at c.a. -30 V after 3 hours of heat treatment at 200°C. On the other hand, for PFES treated device, p-type behavior was observed with charge neutrality point stabilizing at c.a. 20 V after 3 hours of annealing at the same environment. Source-drain current values, I_{sd}, in the devices with the same channel size did not experience a significant change after being treated with APTES or PFES. Several APTES and PFES-treated devices were fabricated and similar results were obtained for each set of devices. **Figure 3-4B** demonstrates the I_{sd}-V_{sd} output characterization for

66

graphene, graphene/APTES, and graphene/PFES at variable back-gate voltages (V_g). The linear I_{sd}-V_{sd} behavior in all devices indicate the lack of significant Schottky barriers and good ohmic contact at the Au-graphene interface. For graphene devices without SAMs, at any given value for V_{ds}, I_{ds} is minimum for V_g=0 volts, indicative of de-doped graphene. This change in the I_{ds} at any given values for V_{ds} is observed at V_g= 20 V and V_g= -30 V for graphene/PFES and graphene/APTES indicative of p- and n-doping, respectively. Unlike the sample without SAMs, intentional doping by APTES and PFES was shown to be thermally stable, as there was no change in the neutrality point after removal of the atmospheric dopants via thermal annealing in nitrogen. The electron and hole concentration of the APTES and PFES-treated graphene after annealing was approximately 2.16 ± 0.08 $\times10^{12}$ cm^{-2} and 1.44 ± 0.1 $\times10^{12}$ cm^{-2}, respectively. These values were calculated using the equation, $n = C_g V_{np}/e$,[31,32] where C_g = 115 aF/μm^2,[33] e is the charge of the electron and V_{np} is the voltage at the charge neutrality point. Both electron and hole field-effect mobilities for graphene, graphene/APTES, and graphene/PFES were shown in Table 1. The electron and hole mobilities for graphene devices without SAMs are of the same order of magnitude. These values are extracted using the relation $\mu_{FE} = L_{ch}g_m/W_{ch}V_{ds}C_{ox}$,[34] where L_{ch}= 25 μm, g_m=dI_{ds}/dV_g, W_{ch}= 25 μm , V_{ds}= 0.1 V and C_{ox}=115 aF/μm^2,[33] indicating that the SAMs has no effect on the mobility of graphene devices.[23,35,36] The slight difference in the mobility and the minimum current of APTES and PFES-treated devices can be due to the differences in the transferred graphene that has origins in varying grain size or transfer process of CVD graphene.

Electrical data measurements were performed on fabricated p-n junctions in a nitrogen atmosphere using a method similar to that explained earlier [see **Figure 3-4C**]. As-

fabricated devices indicated p-type characteristics due to excess amount of atmospheric dopants [not shown in figure]. After annealing at 200 °C a shift in the charge neutrality point to lower values was observed that indicated removal of atmospheric dopants. This annealing provides control of the position of the junction until the neutrality point for the p- side of the channel is reached. When the annealing time increased to 4 hours, two Dirac points (peaks) were seen in the I-V curve: one located at $V_{np} \sim 20$ V and the other at $V_{np} \sim -20$ V. **Figure 3-4B** shows an I-V characteristic curve of the device after being annealed overnight showing two separate Dirac points, which indicates an energy separation of neutrality points within the complementary regions. A drain voltage sweeping from $V_{ds}=-1$ V to $V_{ds}=1$ V were performed and I_{ds} were plotted for various V_g values [see **Figure 3-4D**]. For a given V_{ds}, an increase in V_g from 20 to 60 V results in an increase in I_{ds} indicative of p-type characteristic and a decrease in V_g from 20 to -20 V cause an increase in I_{ds} demonstrating n-type characteristic in a single p-n junction device. Unlike conventional semiconductor p-n junction, I_{ds}-V_{ds} curve does not show rectifying behavior. This is due to the chirality of the massless Dirac fermions of graphene, the backscattering by a potantial barrier is suppressed for the carriers in graphene (Klein Tunneling).[7] The amount of free amine and fluorine available on the substrate can be tuned by varying the APTES and PFES deposition time to fully control the transport behavior of the fabricated p-n junction.
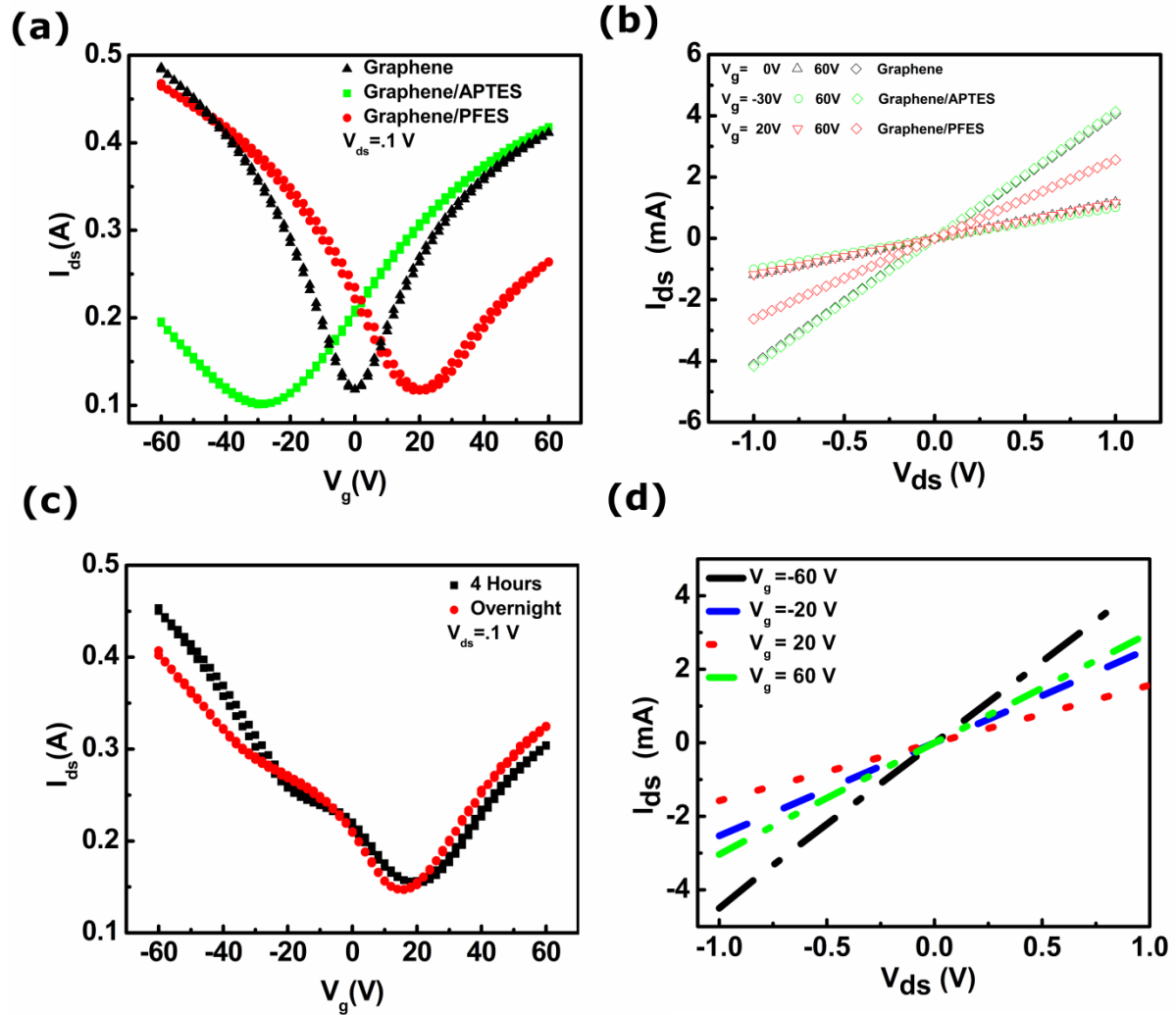
Figure 3-4: (a) Drain-source current versus gate voltage for graphene/SiO$_2$(black), graphene/APTES/SiO$_2$(green) and graphene/ PTES/SiO$_2$(red) after being heated at 200 ^{o}C for 3 hours under nitrogen environment. (b) I$_{ds}$-V$_{ds}$ characteristic of the graphene, graphene/APTES, and graphene/PFES devices at different gate voltages. (c) Drain-source current versus gate voltage as a function of heating time for a graphene p-n junction. (d) I$_{ds}$-V$_{ds}$ characteristic of the graphene p-n junction at

3.4   Conclusions

In summary, we utilized APTES and PFES to induce n- and p-type characteristics in graphene without altering its structure. These SAMs bond to the substrate and are thermally stable. Simultaneous use of these groups in a FET device results in formation of two separate Dirac points, as indicative of a graphene p-n junction. Variation in the duration of substrate functionalizing with these SAMs and heat treatment period results in p-n junctions with controlled position and height.

3.5   References

1   Du, X., Skachko, I., Barker, A. & Andrei, E. Y. Approaching ballistic transport in suspended graphene. *Nat Nanotechnol* **3**, 491-495, doi:10.1038/nnano.2008.199 (2008).

2   Novoselov, K. S. *et al.* Electric Field Effect in Atomically Thin Carbon Films. *Science* **306**, 666-669 (2004).

3   Novoselov, K. S. *et al.* Two-dimensional Gas of Massless Dirac Fermions in Graphene. *Nature* **438**, 197-200, doi:10.1038/nature04233 (2005).

4   Ohta, T., Bostwick, A., Seyller, T., Horn, K. & Rotenberg, E. Controlling the electronic structure of bilayer graphene. *Science* **313**, 951-954, doi:10.1126/science.1130681 (2006).

5   Abanin, D. A. & Levitov, L. S. Quantized transport in graphene p-n junctions in a magnetic field. *Science* **317**, 641-643, doi:10.1126/science.1144672 (2007).

6   Williams, J. R., DiCarlo, L. & Marcus, C. M. Quantum hall effect in a gate-controlled p-n junction of graphene. *Science* **317**, 638-641, doi:DOI 10.1126/science.1144657 (2007).

7   Katsnelson, M. I., Novoselov, K. S. & Geim, A. K. Chiral tunnelling and the Klein paradox in graphene. *Nat Phys* **2**, 620-625, doi:Doi 10.1038/Nphys384 (2006).

8   Cheianov, V. V., Fal'ko, V. & Altshuler, B. L. The focusing of electron flow and a Veselago lens in graphene p-n junctions. *Science* **315**, 1252-1255, doi:10.1126/science.1138020 (2007).

9   Yu, T. H., Liang, C. W., Kim, C. D. & Yu, B. Local electrical stress-induced doping and formation of monolayer graphene P-N junction. *Appl Phys Lett* **98**, doi:Artn 243105 Doi 10.1063/1.3593131 (2011).

10   Rao, G., Freitag, M., Chiu, H. Y., Sundaram, R. S. & Avouris, P. Raman and Photocurrent Imaging of Electrical Stress-Induced p-n Junctions in Graphene. *Acs Nano* **5**, 5848-5854, doi:10.1021/nn201611r (2011).

11   Lohmann, T., von Klitzing, K. & Smet, J. H. Four-Terminal Magneto-Transport in Graphene p-n Junctions Created by Spatially Selective Doping. *Nano Letters* **9**, 1973-1979, doi:10.1021/nl900203n (2009).

12   Brenner, K. & Murali, R. Single step, complementary doping of graphene. *Applied Physics Letters* **96**, doi:063104 10.1063/1.3308482 (2010).

13   Peters, E. C., Lee, E. J. H., Burghard, M. & Kern, K. Gate dependent photocurrents at a graphene p-n junction. *Appl Phys Lett* **97**, doi:Artn 193102 Doi 10.1063/1.3505926 (2010).

14   Farmer, D. B., Lin, Y.-M., Afzali-Ardakani, A. & Avouris, P. Behavior of a chemically doped graphene junction. *Applied Physics Letters* **94**, doi:213106 10.1063/1.3142865 (2009).

15   Chiu, H.-Y., Perebeinos, V., Lin, Y.-M. & Avouris, P. Controllable p-n Junction Formation in Mono layer Graphene Using Electrostatic Substrate Engineering. *Nano Letters* **10**, 4634-4639, doi:10.1021/nl102756r (2010).

16   Kobayashi, S. *et al.* Control of carrier density by self-assembled monolayers in organic field-effect transistors. *Nat Mater* **3**, 317-322, doi:10.1038/nmat1105 (2004).

17   Ito, Y. *et al.* Crystalline Ultrasmooth Self-Assembled Monolayers of Alkylsilanes for Organic Field-Effect Transistors. *Journal of the American Chemical Society* **131**, 9396-9404, doi:10.1021/ja9029957 (2009).

18   Pernstich, K. P. *et al.* Threshold voltage shift in organic field effect transistors by dipole monolayers on the gate insulator. *J. Appl. Phys.* **96**, 6431-6438, doi:10.1063/1.1810205 (2004).

19   Vosgueritchian, M., LeMieux, M. C., Dodge, D. & Bao, Z. N. Effect of Surface Chemistry on Electronic Properties of Carbon Nanotube Network Thin Film Transistors. *Acs Nano* **4**, 6137-6145, doi:10.1021/nn1012226 (2010).

20   Liu, Z. H., Bol, A. A. & Haensch, W. Large-Scale Graphene Transistors with Enhanced Performance and Reliability Based on Interface Engineering by Phenylsilane Self-Assembled Monolayers. *Nano Letters* **11**, 523-528, doi:10.1021/nl1033842 (2011).

21   Park, J. *et al.* Work-Function Engineering of Graphene Electrodes by Self-Assembled Monolayers for High-Performance Organic Field-Effect Transistors. *J Phys Chem Lett* **2**, 841-845, doi:Doi 10.1021/Jz200265w (2011).

22   Wang, R. *et al.* Control of Carrier Type and Density in Exfoliated Graphene by Interface Engineering. *Acs Nano* **5**, 408-412, doi:10.1021/nn102236x (2011).

23   Yan, Z. *et al.* Controlled Modulation of Electronic Properties of Graphene by Self-Assembled Monolayers on SiO(2) Substrates. *Acs Nano* **5**, 1535-1540, doi:10.1021/nn1034845 (2011).

24   Shin, W. C., Seo, S. & Cho, B. J. Highly air-stable electrical performance of graphene field effect transistors by interface engineering with amorphous fluoropolymer. *Applied Physics Letters* **98**, doi:153505 10.1063/1.3578396 (2011).

25   Wang, X. M., Xu, J. B., Wang, C. L., Du, J. & Xie, W. G. High-Performance Graphene Devices on SiO(2)/Si Substrate Modified by Highly Ordered Self-Assembled Monolayers. *Advanced Materials* **23**, 2464-+, doi:10.1002/adma.201100476 (2011).

26   Schedin, F. *et al.* Detection of individual gas molecules adsorbed on graphene. *Nature Materials* **6**, 652-655, doi:10.1038/nmat1967 (2007).

27   Ni, Z. H. *et al.* The effect of vacuum annealing on graphene. *Journal of Raman Spectroscopy* **41**, 479-483, doi:10.1002/jrs.2485 (2010).

28   Novoselov, K. S. *et al.* Detection of individual gas molecules adsorbed on graphene. *Nat Mater* **6**, 652-655, doi:Doi 10.1038/Nmat1967 (2007).

29   Yokota, K., Takai, K. & Enoki, T. Carrier Control of Graphene Driven by the Proximity Effect of Functionalized Self-assembled Monolayers. *Nano Lett*, doi:10.1021/nl201607t (2011).

30   DasA *et al.* Monitoring dopants by Raman scattering in an electrochemically top-gated graphene transistor. *Nat Nano* **3**, 210-215, doi:http://www.nature.com/nnano/journal/v3/n4/suppinfo/nnano.2008.67_S1.html (2008).

31   Shen, Z. X. *et al.* The effect of vacuum annealing on graphene. *J Raman Spectrosc* **41**, 479-483, doi:Doi 10.1002/Jrs.2485 (2010).

32   Nourbakhsh, A. *et al.* Tuning the Fermi Level of SiO(2)-Supported Single-Layer Graphene by Thermal Annealing. *J Phys Chem C* **114**, 6894-6900, doi:Doi 10.1021/Jp910085n (2010).

33   Joselevich, E., Tsivion, D., Schvartzman, M., Popovitz-Biro, R. & von Huth, P. Guided Growth of Millimeter-Long Horizontal Nanowires with Controlled Orientations. *Science* **333**, 1003-1007, doi:Doi 10.1126/Science.1208455 (2011).

34   Schwierz, F. Graphene transistors. *Nat Nano* **5**, 487-496 (2010).

35   Farmer, D. B., Lin, Y. M., Afzali-Ardakani, A. & Avouris, P. Behavior of a chemically doped graphene junction. *Appl Phys Lett* **94**, doi:Artn 213106 Doi 10.1063/1.3142865 (2009).

36   Wang, R. *et al.* Control of Carrier Type and Density in Exfoliated Graphene by Interface Engineering. *Acs Nano* **5**, 408-412, doi:10.1021/nn102236x (2010).

CHAPTER 4

PHOTOCHEMICAL DOPING AND TUNING OF THE WORK FUNCTION AND DIRAC POINT IN GRAPHENE USING PHOTOACID AND PHOTOBASE GENERATORS

This work demonstrates that photochemical doping of CVD-grown graphene can be easily achieved using photoacid (PAG) and photobase (PBG) generators such as triphenylsulfonium perfluoro-1-butanesufonate (TPS-Nf) and 2-nitrobenzyl N-cyclohexylcarbamate (NBC). The TPS-Nf ionic onium salt photoacid generator does not noticeably dope or alter the electrical properties of graphene when coated onto the graphene surface but is very effective at inducing p-doping of graphene upon exposure of the PAG coated graphene sample. Likewise, the neutral NBC photobase generator does not significantly affect the electrical properties of graphene when coated, but upon exposure to ultraviolet light produces a free-amine, which induces n-doping of the graphene. Electrical measurements show that the doping concentration can be modulated by controlling the deep ultraviolet (DUV) light exposure dose delivered to the sample. The interaction between both dopants and graphene was also investigated via Raman spectroscopy, X-ray photoelectron spectroscopy (XPS) and ultraviolet photoelectron spectroscopy (UPS). The photochemical doping process is able to tune the work function of the single layer graphene samples used in this work from 3.4 eV to 5.3 eV. Finally a p-n junction was fabricated and analyzed via XPS mapping and electrical measurements, showing that it is possible to control the position of the two current minima (two Dirac points) in the ambipolar p-n junction.

4.1   Introduction

Graphene, a two-dimensional sp^2 hybridized carbon lattice, has attracted significant interest due to its distinctive electrical and mechanical properties[1-4] including its high charge carrier mobility, transparency, mechanical strength and flexibility[5]. These properties have spurred research directed at modifying graphene for use in a variety of electronic, optoelectronic, and sensor technologies.[6-8] Therefore graphene may play an important role in providing an alternative to current materials (for example, indium tin oxide -ITO, or silicon) in a variety of applications, such as transparent electrodes[9-12] (which are critical elements for numerous devices such as displays, OLEDs, photovoltaic devices) [1,13] in which ground breaking performances by graphene based devices have already been shown.[14,15]

Tailoring the electronic properties of graphene without inducing structural defects is necessary in order to fully achieve its potential for variety of electronics applications.[6,7,16] Intentional doping of graphene (by charge or electron transfer) allows tuning of the work function of graphene without introducing large numbers of defects. A variety of doping techniques have been explored, primarily through electrostatic gating,[17] chemical interactions,[18] and intercalation[19].[20] Replacement of carbon atoms with atoms of other elements in the graphene lattice has also been shown to modulate the carrier types and concentrations in graphene to allow for p- and n-type doping; however, these methods induce structural defects in the graphene which results in a degradation in the electronic properties of doped films made using by methods.[18] Doping of graphene through charge-transfer interactions[21,22] has been shown to be an effective method to modify the electronic structure without interfering with the integrity of the sp^2 lattice.

Different types of dopants have been used, including gases,[23] metals,[10,24] polymers,[25] organic compounds and metal-organic compounds.[18,19,26,27] Nevertheless, most of these dopants and processes suffer from one or more of the following deficiencies: lack of scalability, failure to provide access to large dopant concentrations, limited air stability, or that they irreversibly dope the graphene upon contact, preventing modulation and tuning of doping during post-processing. Furthermore, careful control of dopant concentrations, including the ability to selectively and locally modulate doping level (e.g. via photopatterning) and thus the transport behavior from neutral to p-doped or n-doped in an area-selective manner could be very useful for a variety of applications such as circuits and sensors.[6,7,28]

We have previously reported several methods for doping graphene using both self-assembled monolayers (SAMs) and dip-coated films.[19,29,30] In addition, other work has shown that deposition of graphene on a substrate with pre-patterned SAMs leads to doping of graphene in a spatially controlled manner.[29] In all such cases, there was no simple method for tuning the doping level after a particular graphene device was assembled. For example, in the case of the SAM doping, the doping level is controlled by the density of SAM molecule deposition on the substrate surface when the SAM coating is made.

Photo-induced doping of graphene hence presents itself as a potentially attractive process since it would allow for facile spatial control of the doping using conventional lithography tools, opening the door to using graphene both as the semiconductor and as contacts in devices. Photochemical dopant strategies reported in the literature for graphene; however, required large exposure times and yielded very small changes in the neutrality point.[24,31-37]

The goal of the work reported here was to demonstrate a method whereby a latent dopant could be deposited in contact with the graphene film and subsequently modulated using external stimuli to tune the doping level in the graphene and also thereby its work function. Ultimately, we sought to demonstrate that such doping activation could be achieved in a pattern-wise manner. In thinking about possible methods for achieving these goals, we decided to borrow lessons from the extensive work done by our group in semiconductor lithography and photoresist technology.[38-41] This study has focused on developing an on-demand photochemical method for doping of graphene using photoacid (PAG) and photobase (PBG) generators. Specifically, this paper reports on examples of both PAG (triphenylsulfonium perfluoro-1-butanesufonate, TPS-Nf) and PBG (2-nitrobenzyl *N*-cyclohexylcarbamate, NBC) to easily dope graphene, and the observation that such doping can be controlled in an area-selective manner using traditional lithographic exposure tools. Electrical measurements confirm that before exposure, the graphene maintains its pristine electrical properties after being coated with the PAG and PBG compounds and that by modulating the deep ultraviolet (DUV) light exposure dose delivered to the films, the doping concentration for both the p and n-dopants can be controlled. Raman spectroscopy, XPS and UPS were used to characterize graphene samples doped using this strategy. Significantly, it is shown from UPS that this doping technique yields a work function modulation from 3.4 eV to 5.3 eV in single layer graphene. Finally, using TPS-Nf a p-n junction was fabricated and analyzed via XPS mapping and electrical measurements, demonstrating that it is possible to control the position of the two current minima (two neutrality points) in the ambipolar p-n junction with such dopants.

4.2 Experimental Section

4.2.1 Graphene Growth

CVD graphene was obtained following standard literature procedures.[42] Graphene was synthesized on 25 μm thick Cu foil (Alfa Aesar, item No. 14482, cut into 1 x 1 in squares) in a low pressure $Ar/H_2/CH_4$ environment at 1000 °C.[42] PMMA (MicroChem 950 PMMA Series) was spun cast from an organic solution (9% solution by weight in anisole, spin coated at 1500 rpm for 1 min) onto the as-grown graphene coated Cu samples and baked (180 °C for 10 minutes) to form an approximately 500 nm thick film that served as an auxiliary support material for handling and transferring the graphene films. The sample was treated overnight with a 30 wt% $FeCl_3$ aqueous solution to remove the copper foil. The resulting bi-layer PMMA-graphene samples were treated with 10 wt% HCl solution for 10 min, followed by deionized (DI) water several times to remove bound contaminants. The PMMA-graphene bilayers were then placed onto SiO_2 coated Si substrate with the graphene face in contact with the SiO_2 surface. The PMMA carrier film was then removed by immersing the substrate film stack in fresh acetone up to 5 times for 30 min each time. Finally the graphene/SiO_2/Si stacks were annealed at 200 °C under an inert nitrogen or argon atmosphere for 10 min. The samples were then analyzed by Raman and XPS to ensure the successful removal of the copper and PMMA films and the presence of clean mono-layer graphene films.

4.2.2 Device fabrication, doping procedure and electrical measurements

A highly p-doped Si wafer was as the substrate for field effect device fabrication since it could be easily used as a common gate for all devices. A 300 nm thick thermal silicon dioxide layer grown on the p-doped Si wafers was used as the gate dielectric. The Si/SiO$_2$ substrate was cleaned by piranha solution and pre-treated by UV ozone for 15 min. Next, lithography and deposition processes (i.e. typical lift-off procedures) were used to form the gold electrodes (3 nm thick chromium adhesion layer first deposited onto the SiO$_2$ followed by a 50nm thick gold layer for electrode fabrication, where width =50 μm and length=2000 μm) on the 300 nm thick SiO$_2$ gate dielectric. Monolayer graphene was transferred to these pre-fabricated electrode devices using the procedure described earlier. For n-doping, samples were coated with NBC via spin casting (1000 rpm for 1 min) using a 2% v/v solution of NBC in anhydrous toluene. For p-doping the samples were coated with TPS-Tf via spin casting (1000 rpm for 1 min) using a 2% v/v solution of TPS-Nf in anhydrous ethanol. The samples were exposed using a handheld DUV light (Model UVGL-25: 4 watt UV lamp, wavelength 254 nm) for a time period varying from (10 s to 10 min). Once the electrode devices were fabricated, all the sample preparations beginning with the graphene transfer were performed inside of a glovebox in a controlled environment. Electrical measurements, including I-V curves, were made using a probe station configured with a HP 4156 semiconductor parameter analyzer maintained under an inert atmosphere in the glovebox as well. A control sample containing only graphene that was exposed to DUV was also analyzed to confirm that any changes in the neutrality point are in fact a result of the dopants (**Figure 4-1**).
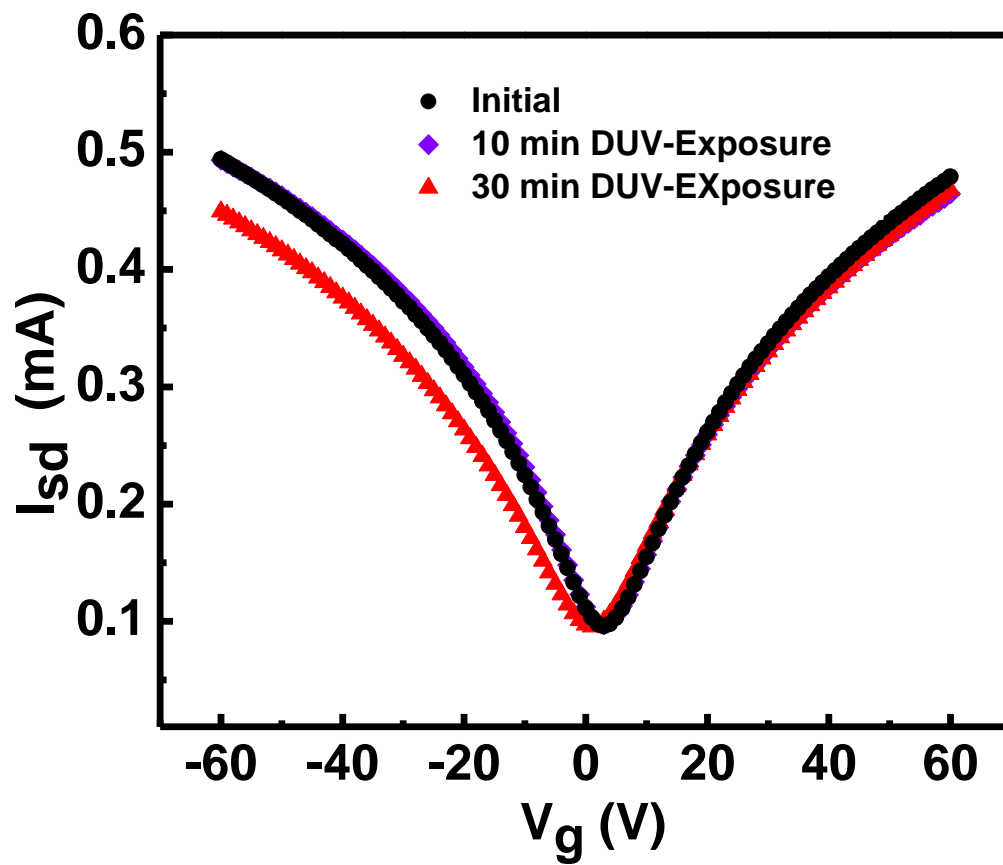
Figure 4-1: Source-drain current versus gate voltage for simple graphene FET devices initial, after 10 min DUV exposure and 30 min DUV exposure.

For p-n junction fabrication, 50 nm thick gold electrodes (3 nm thick chromium was used for adhesion, width = 5000μm, length= 10000μm) were evaporated through a shadow mask onto a clean, graphene transferred, 300 nm thick SiO_2 gate dielectric films on highly p-doped silicon wafers. TPS-Nf was spin-coated following the same conditions mentioned above; half of each of the channels in the FET devices were covered with a shadow mask, exposed to DUV light and measured following the same basic process described above.

4.2.3   Surface Characterization and UV/Visible Spectroscopy

Transfers from the glovebox into the photoelectron spectrometer were done under N_2 atmosphere using a Kratos air-sensitive transporter 39-322 that couples into the transfer chamber of a Kratos Axis Ultra^{DLD} XPS/UPS system under positive N_2 pressure. All samples were in electronic equilibrium with the spectrometer via a metallic clip on the graphene and characterizations were performed at normal take-off angle. XPS using monochromatic Al Kα line was performed at a base pressure of 10^{-9} Torr with the Fermi level calibrated using atomically clean silver. Spot size was *ca.* 700 μm. Survey XPS scans were run at 160 eV pass energy and high resolution scans typically at 20 eV pass energy and 100 meV steps, while UPS spectra were acquired at 5 eV pass energy and 0.05 eV step size with the aperture and iris set to 55 μm . Calibration of spectra was done with the Si 2p peak set to BE = 104.9 eV, same as that of the treated graphene (10 min) on SiO_2. XPS mapping was acquired using a Thermo K-Alpha XPS (Thermoscientific) operating under ultra-high vacuum conditions with an Al Kα micro-focused monochromator and a 30 μm spot size. Raman spectroscopy and microscopy measurements were performed using a

Horiba HR800 μRaman system without exposure to air[43]. All spectra were excited with visible (532 nm) laser light and collected in a backscattering configuration with a laser power below 0.5 mW to reduce laser-induced heating and were acquired at multiple locations to verify reproducibility. All the peaks were fitted with Gauss-Lorentzian curve fits to determine their peak position, line width, and intensity.

UV/Visible spectroscopy was acquired in an Agilent Cary 5000 UV/Vis spectrometer for 0.5 cm radius spots (under air). Glass was used as the sample and reference to calibrate the 100%T, and 0%T was calibrated by blocking the sample light path. CVD graphene was transferred to the same type of glass slides and annealed in the glovebox at 200°C before treatment.

4.3   Results and Discussion

Photoacid generator (PAG) and photobase generator (PBG) compounds have been extensively studied and utilized on semiconductor microlithography. In this study, we chose TPS-Nf and NBC due to their high solubility in common solvents, ambient stability, and efficient photochemical reactivity.[44] It was anticipated that PAG compounds such as TPS-Nf could be used to p-dope graphene while PBG compounds such as NBC could be used to achieve n-doping. As illustrated in **Figure 4-2A**, TPS-Nf generates an acid (proton) upon DUV irradiation due to decomposition of the triphenylsulfonium chromophore. [45] The generated proton is then responsible for p-doping of the graphene layer, lowering the Fermi energy level (i.e. shifting farther from the vacuum level, and thereby increasing the work function) (**Figure 4-2C**).[46]   In the case of the photobase generator NBC, the *o*-nitrobenzyl chromophore follows a known intramolecular rearrangement resulting in the

formation of a photochemically liberated free-amine under DUV irradiation (**Figure 4-2B**).[44] This free-amine has a lone pair of electrons which we believe are responsible for n-doping of graphene as previously demonstrated in our earlier APTES SAM studies.[29,30] Density functional theory (DFT) calculations have shown that for NH_3 molecules, there is a small charge transfer to the graphene.[47] This would explain the increase of the Fermi level from the Dirac point (i.e. n-doping).[30,48-50]
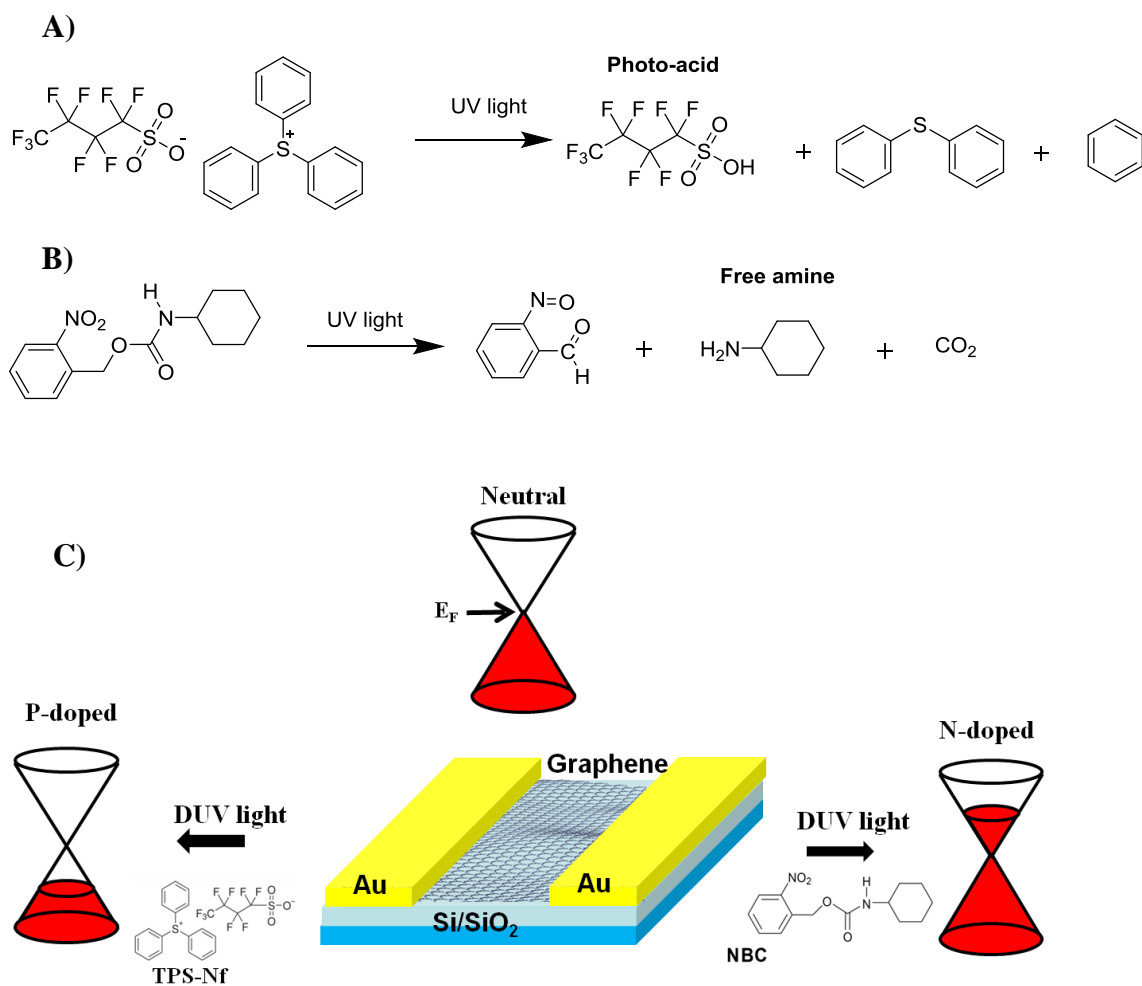
Figure 4-2: Schematic of reaction pathways for A) TPS-Nf and B) NBC. C) Schematic representation of p- and n-doping of graphene field effect transistor (FET) by TPS-Nf and NBC respectively, with associated changes to the graphene Fermi Energy level.

Figure 4-2C shows a simple scheme of a FET device with graphene coated with TPS-Nf or NBC as well as the photochemical induced Fermi energy changes upon exposure of the device. To determine the applicability of our proposed approach, graphene/TPS-Nf and graphene/NBC samples were fabricated using chemical vapor deposition (CVD) grown monolayer graphene transferred onto a 300 nm SiO_2/Si wafer using a common method described elsewhere[29,42] and annealed under an inert atmosphere to remove ambient and transfer process residues[43,51] (i.e. graphene layers that are here after referred as "as-transferred"). For the TPS-Nf treated sample, a 2% solution of TPS-Nf (Sigma Aldrich) dissolved in anhydrous ethanol was spin cast under inert atmosphere onto the as-transferred graphene. For the NBC treated sample, a 2% solution of NBC (Midori Kagaku Co.) dissolved in anhydrous toluene was spin cast in a similar fashion onto as-transferred graphene samples.

Raman spectroscopy was utilized to investigate the quality of the graphene and its doping state by examining the D, G, and 2D bands and their respective peak positions. The "as-transferred" graphene films utilized in this work showed prominent graphitic (G and 2D) (see **Figure 4-4A** - full spectra) bands with a minimal defect peak (D) (see **Figure 4-3**). The high 2D over G band intensity ratio (I_{2D}/I_G) and low full width at half maximum (FWHM) of the 2D band are indicative of monolayer graphene films.[42]
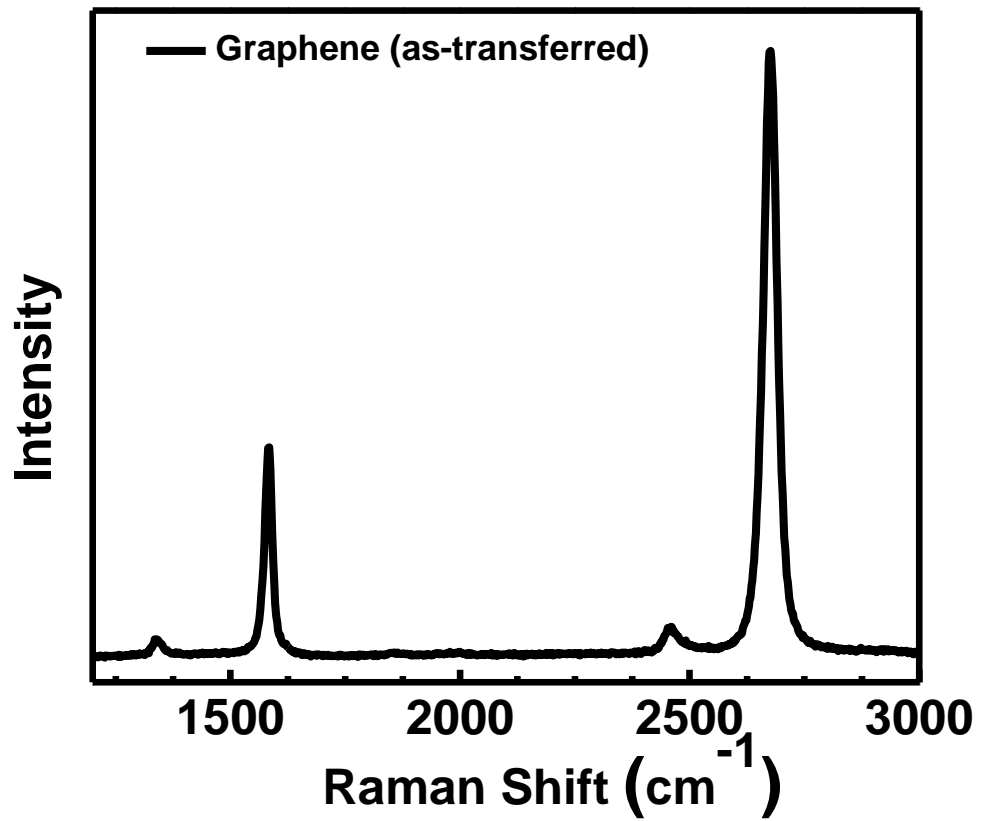
Figure 4-3: Full Raman spectra of graphene as made on SiO₂ (black line).

Figure 4-4B-D shows the G band position, the G band full width at half maximum (FWHM), the 2D band position and the 2D to G band intensity ratio (I_{2D}/I_G) for as-transferred graphene, after spin coating the TPS-Nf and NBC dopants (hereafter referred as "unexposed") and finally after DUV exposure (5 min exposure for TPS-Nf and 10 min exposure for NBC). For the graphene/TPS-Nf treated sample, the as-transferred and unexposed peak positions remain mostly constant : G peak position of ~1585 cm^{-1}, full width half maximum of the G peak (FWHM) ~20 cm^{-1}, 2D peak position of ~2677 cm^{-1} and I_{2D}/I_G ratio of ~3.2, which indicates that prior to exposure, no significant doping is induced into the graphene by coating of the TPS-Nf onium salt photoacid generator. After exposure however, a clear change in the Raman peak positions and their relative intensities for the sample coated with TPS-Nf PAG is observed: An upshift on the G peak position to ~1608.6 cm^{-1}, a decrease on the FWHM of G peak to ~11.3 cm^{-1}, a upshift in the 2D peak position of ~2690 cm^{-1} and a decrease on the I_{2D}/I_G ratio to ~0.76, which clearly indicates p-doping of the graphene.[25,52] Similarly, for the NBC treated sample, the same behavior is observed where prior to exposure the peak positions remain constant when comparing the as-transferred graphene both coated and not coated with NBC: G peak position of ~1585 cm^{-1}, FWHM of the G peak ~20 cm^{-1}, 2D peak position of ~2675 cm^{-1} and I_{2D}/I_G ratio ~3.2. After exposure, again the graphene sample coated with the NBC PBG exhibits clear changes in the peak positions and their intensity ratios: An upshift in the G peak position to~1596 cm^{-1}, a decrease on the G peak FWHM to~16 cm^{-1}, a upshift on the 2D peak position to~2678 cm^{-1} and a decrease of the I_{2D}/I_G ratio to ~2, clearly indicates n-doping of the graphene[53]. Both of these results obtained by Raman spectroscopy are in clear agreement with the observations by Ferrari and coworkers on n and p-doping of

electrochemically top-gated graphene transistor[53] and is further supported by the UPS/XPS

and electrical data discussed below.
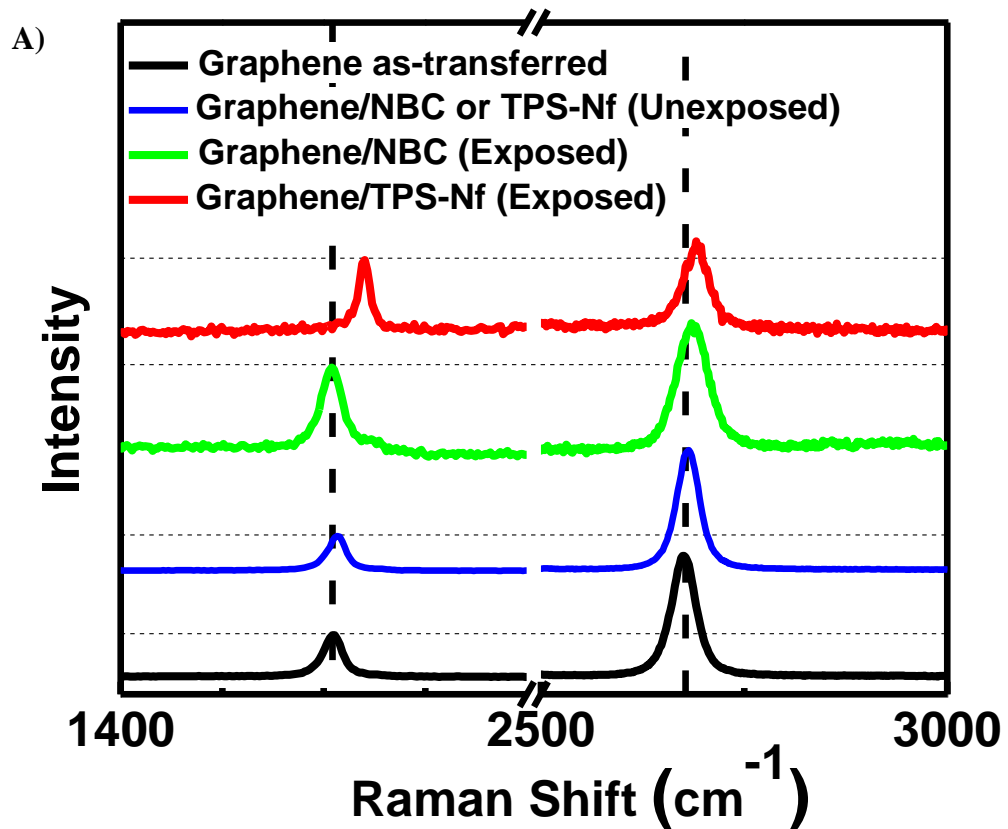
Figure 4-4: (A) Full Raman spectra for four samples on SiO_2: graphene as-transferred (black line), Graphene/NBC or Graphene/TPS-Nf unexposed (since both yielded the same spectra with no significant changes as compared to the initial graphene spectra) (blue line), Graphene/NBC after exposure (green line) and Graphene/TPS-Nf after exposure (red line). **(B)** G band peak position, **(C)** 2D band peak position, **(D)** FWHM of the G band and **(E)** ratio of the 2D band peak intensity over G band peak intensities for the samples initially (as-transferred), unexposed and finally after exposure.

B)

C)

D)

E)
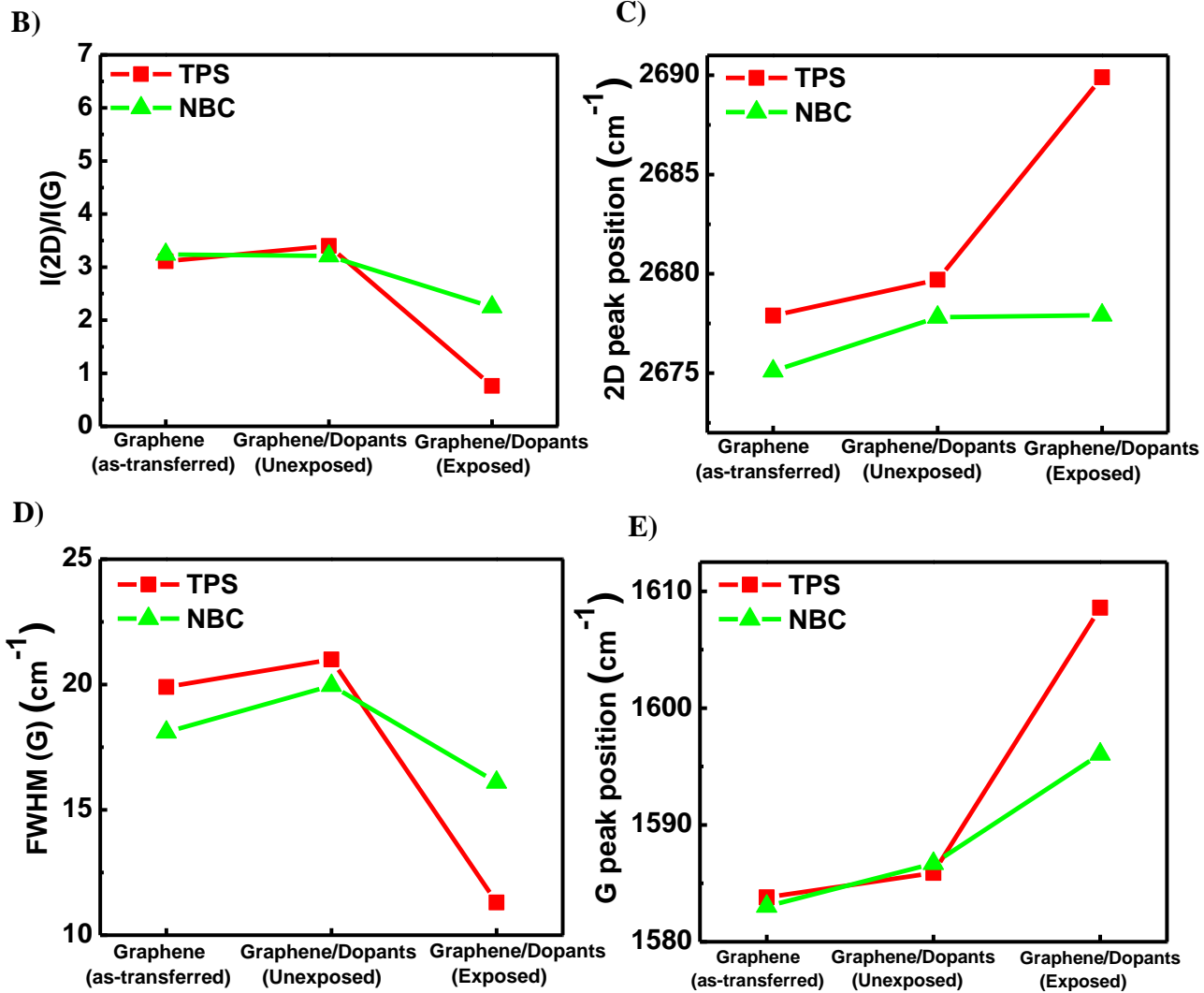
Figure 4-4 Continued

90

The p- and n-doping effect of TPS-Nf and NBC respectively, were also evaluated by UV photoelectron Spectroscopy (UPS). **Figure 4-5A** shows the UPS spectra for (1) TPS-Nf and (2) NBC: as-transferred, unexposed and finally after exposure (5 and 10 min for TPS-Nf and NBC respectively). The work function Φ (energy difference between the Fermi and vacuum level) can be calculated from equation (1),[54] since the secondary electron edge occurs at the binding energy corresponding to the deepest of the energy levels that can be excited with the radiation employed.

$$\Phi = 21.22 - BE_{SEE} \tag{1}$$

where BE_{SEE} is the binding energy at the secondary electron cutoff. The work function of the as-transferred graphene, unexposed graphene/TPS-Nf and graphene/TPS-Nf after exposure were determined to be 3.82±0.1 eV, 3.97±0.1eV and 5.29± 0.09 eV, respectively (**Figure 4-5B**). These values are in good agreement with the results obtained from the Raman spectrum where no significant changes were observed in the unexposed graphene/TPS-Nf film as compared to the as-transferred graphene, while after DUV light exposure the graphene exhibits significant p-doping. Using equation (2), the electron concentration (n) was calculated since it is related to the energy position of the Dirac point by the equation,[55]

$$E_D = \hbar v_F (\pi n)^{-1/2} \tag{2}$$

where v_F is the Fermi velocity of graphene (1.1×10^{-6} ms^{-1}).[56] The calculated doping concentration was approximately 1.2×10^{14} cm^{-2}, which is the highest doping level reported to date for photochemically p-doped graphene and is comparable to the results obtained from other doping techniques. [31-35,57-59]

Similarly, for NBC, the work function for as-transferred graphene, unexposed graphene/NBC and exposed graphene/NBC were determined to be 3.80±0.07 eV, 3.77±0.11 and 3.38± 0.18 eV, respectively, using equation (1) (**Figure 4-5B**). Once again, no significant change was observed in the graphene samples prior to the DUV exposure. Similarly, using equation (2), the electron concentration (n) was found to be 1.1×10^{13} cm^{-2} after exposure.
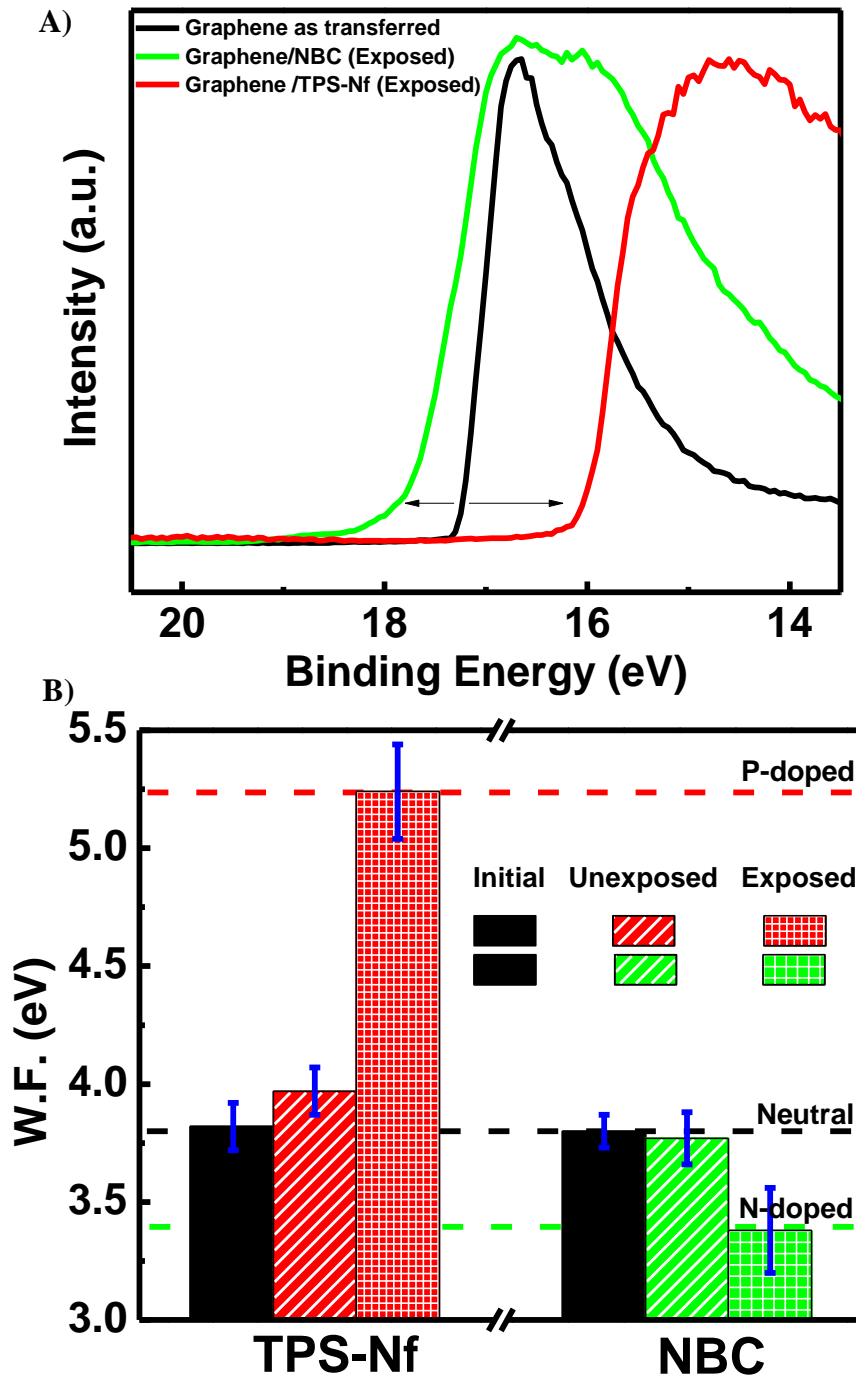
Figure 4-5: (A) UPS spectra for Graphene as-transferred (black), Graphene/TPS-Nf exposed (red) and Graphene/NBC exposed (green), **(B)** UPS-determined work functions.

Doping of graphene induced by surface electron transfer can further be examined and confirmed by X-ray photoelectron spectroscopy (XPS) measurements. **Figure 4-6A** shows the chemical shifts in the high resolution C1s spectra for: (1) as-transferred graphene (black), (2) exposed graphene/TPS-Nf (red) and (3) exposed graphene/NBC (green). It is observed that for the bare graphene sample, the C1s peak maximum occurs with a binding energy (BE) of 284.9 eV as expected.[43,60] For the graphene/TPS-Nf sample, upon on DUV exposure, the C1s peak of graphene shifts to lower binding energy from 284.9 eV to 284.2 eV which is expected for a p-doped sample.[25] For the graphene/NBC sample, the C1s peak has contributions from graphene and the dopant, with an overall maximum shift to higher binding energy from 284.9 eV to 285.9 eV.[28] This is presumably the result of both the BE of the dopant C 1s and the n-doping of graphene by the free-amine present in the NBC layer,[28,61] in accord with previously reported data.[48] It is important to notice that, for the unexposed samples, no shift on the binding energy of the C1s peak was observed (**Figure 4-6B**), in agreement with the UPS and Raman results. N1s, S2s and S2p high-resolution spectra for each sample were also collected and the results are presented in **Figure 4-6 C, D** and **E**. These clearly show that after exposure both molecules undergo the expected photo-reaction: (1) the NBC case shows the emergence of the free amine peak at ~401 eV in the N1s spectra [62] and (2) the TPS-Nf case shows the appearance of the peak at ~227.5 eV in the S2s spectra that is attributed to the rearrangement of the sulfur center in the TPS salt after the photoacid generation.[63] These results further support our statement concerning p–type and n-type doping observed for TPS-Nf and NBC coated graphene films.
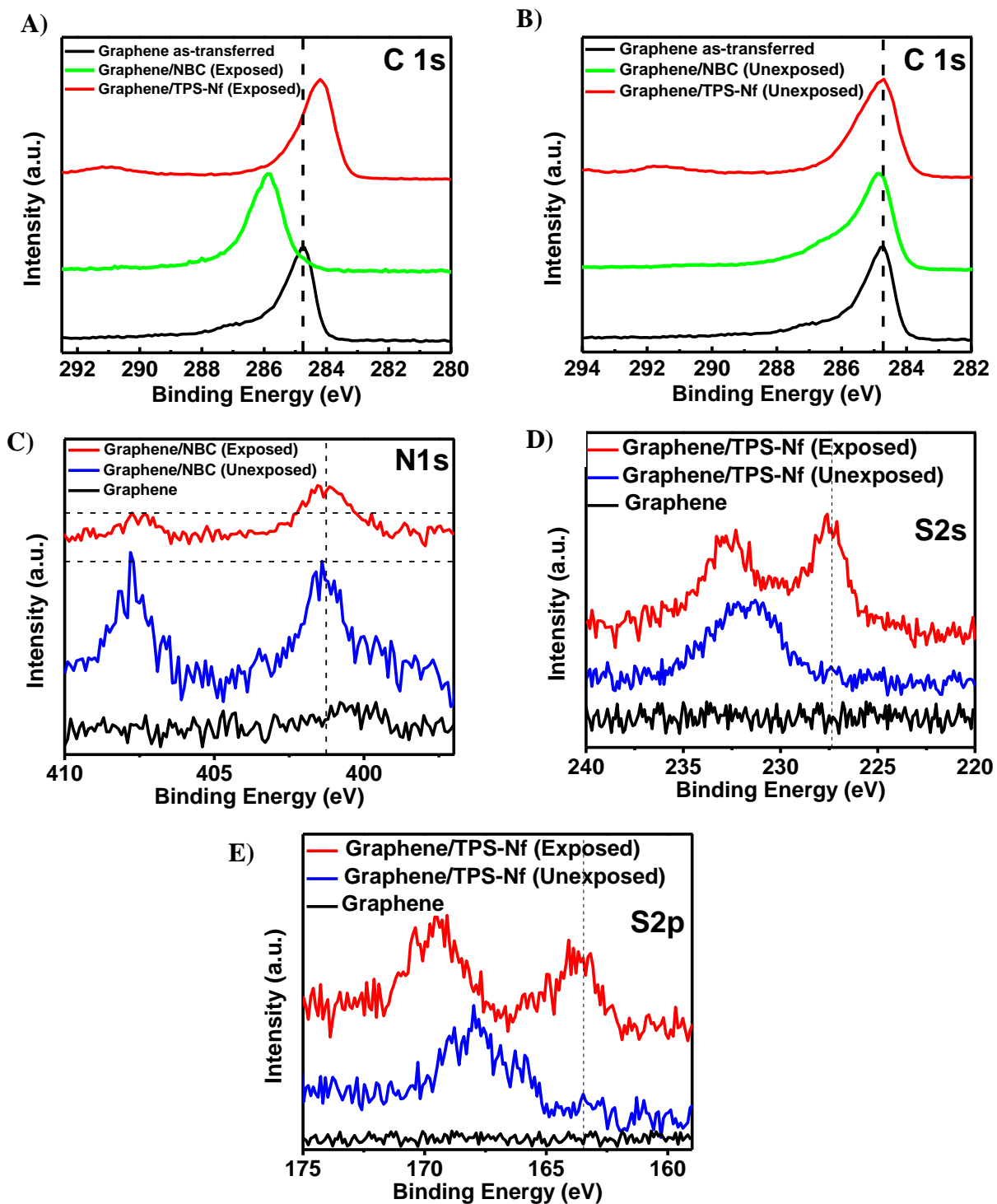
Figure 4-6: High resolution XPS spectra representing the (A) C1s (Samples after exposure) (B) C1s (Unexposed samples) binding energy region for three types of samples: graphene as-transferred (black line), graphene/TPS-Nf (red line) and graphene/NBC (green line) on SiO$_2$. High resolution XPS spectra for (C) N1s , (D) S2s and (E) S2p. All data were normalized to the largest intensity within each spectrum.

Once evidence of doping using photochemically activated PAG and PBG compounds was obtained, the next step was to quantify the effect of such doping strategies on the electrical properties of graphene. In order to test the electrical transport properties of graphene that has been modified using such photochemically activated dopants, back-gated graphene field effect transistors (GFET) were fabricated using standard lithography and metallization techniques reported previously.[29,30]

Figure 4-7 shows the resulting drain current (I_d) versus the gate voltage (V_g) for TPS-Nf and NBC coated graphene films. For the bare, as-transferred graphene, all devices demonstrated a charge neutrality point (V_{NP}) of approximately zero volts as a result of the careful washing in multiple acetone baths followed by a 30 min anneal at 200 °C under a nitrogen environment to remove any adsorbed p-dopants from the transfer process of the CVD graphene.[43] The annealing time and temperature were controlled carefully in order to avoid n-doping as previously reported.[64] For the GFET devices made using TPS-Nf (**Figure 4-7A**), a shift in the neutrality point of ~ -15 V was observed in unexposed films, which is attributed to ethanol exposure during the TPS-NF coating process as shown in our control experiment. **Figure 4-7C** shows that a drop of ~ -15 V in the neutrality point was observed for a graphene sample dipped in ethanol and immediately dried with nitrogen, which clearly demonstrates solvent induced n-doping similar to that observed in the TPS-Nf coating case.

Upon exposure of the TPS-Nf coated graphene film devices, the charge neutrality point is observed to gradually shift to higher voltages as would be expected for increasing levels of p-doping with increasing exposure time and generation of additional photoacid. At 5 s exposure, the neutrality point shifts to ~10 V; at 15 s, the neutrality point stabilized

at ~48 V; for 30 s it is above 60 V and after 5 min, the charge neutrality point is so far

beyond 100 V that it is difficult to resolve with the available measurement techniques. The

hole concentration (n) of the TPS-Nf treated graphene after annealing was calculated from

the V_{NP} using equation 3,[65,66]

$$n = C_G V_{NP}/e \qquad\qquad\qquad (3)$$

where C_G = 115 aF/μm^2, [52] e is the charge of the electron, and V_{NP} is the voltage at the

charge neutrality point. Hole concentrations were calculated to be approximately 7.19 ×

10^{11} cm^{-2} and 3.45 × 10^{12} cm^{-2} for the 5 s and 15 s exposure respectively (i.e. these were

the only cases where the neutrality point could be precisely measured because of the

voltage limitations of the probe measurement system used). The electron concentration (n)

is related to the energy position of the Dirac point by equation (2), hence the calculated

energy position of the Dirac point, were approximately 0.11 eV and 0.24 eV after 5 and

15 s exposure respectively.

Figure 4-7B shows the electrical response for the GFET devices made using NBC.

In the unexposed state, little shift in the neutrality point is observed. This lack of a shift in

the neutrality point is indicative of a lack of chemical doping of the graphene by NBC or

the toluene solvent used to coat it onto the GFET device (**Figure 4-7D**). This is consistent

with earlier observations made in the Raman spectroscopy and UPS data. Upon exposure

of the NBC-coated GFET, the charge neutrality point is observed to gradually shift to lower

voltages with increasing exposure time and generation of larger amounts of photobase. At

5 min, the neutrality point stabilizes at ~-36 V and after 10 min, the charge neutrality point

is far above 60 V which is the maximum amount of voltage that can be applied to the device using the tool configuration. The electron concentration (n) of the NBC-treated graphene after annealing is approximately 2.58×10^{12} cm^{-2} for the 5 min exposure as calculated using equation (2) and the energy position of the Dirac point is approximately 0.20 eV as calculated from equation (3). One of the reasons NBC requires a higher exposure time than TPS-Nf (10 sec versus 5 min) in order to observe a change in the doping concentration, rises from the fact that the quantum yield (Q) (the ratio of product molecules, photoacid for TPS-Nf or photobase for NBC, to absorbed photons), for TPS-Nf is approximately five times higher than NBC (0.52 versus 0.1).[44,45] Nevertheless the electrical measurements are in agreement with the Raman, UPS and XPS results which clearly indicate that prior to exposure, there is little effect on the V_{NP} for graphene and that after exposure both TPS-Nf and NBC p- and n-dope respectively.

Using equation (3), the expected V_{NP} was calculated for both TPS-Nf and NBC photoinduced doping from the work function values determined via UPS on exposed graphene/TPS-Nf and graphene/NBC samples. The estimated neutrality point positions were 148 V for NBC (10 min exposure) and 1700 V for TPS-Nf. These estimates were in general agreement with the GFET electrical measurements since the neutrality point for both exposure times was far above 100 V (**Figure 4.7**). An increase in device current magnitude (at Vg=0) of 3 to 5 times was also observed, which also indicated that the conductivity of the device was being improved in a similar manner (**Figure 4.7**). In this case, such changes were achieved while maintaining film transmittance above ~70% for both dopants (**Figure 4-8A**). Experiments are underway that focus on improving and optimizing such parameters which are sought in a variety of applications[7]. Air stability

for the samples prior to exposure was also tested (**Figure 4-8B** and **C**) and slight to no decrease on the neutrality point was observed in the graphene-coated samples, in contrast to the bare graphene exposed to air (**Figure 4-8D**). This shows that the PAG and PBG dopant precursor layers can protect the graphene quality until they are exposed to generate the desired doping, unlike other doping techniques that require further annealing in order to remove such atmospheric dopants[18,28,29]. It is important to mention that after DUV light exposure, subsequent air exposure did not generate the desired doping, thus a protective layer or packaging should be used in the devices after DUV exposure or handled under an inert atmosphere.
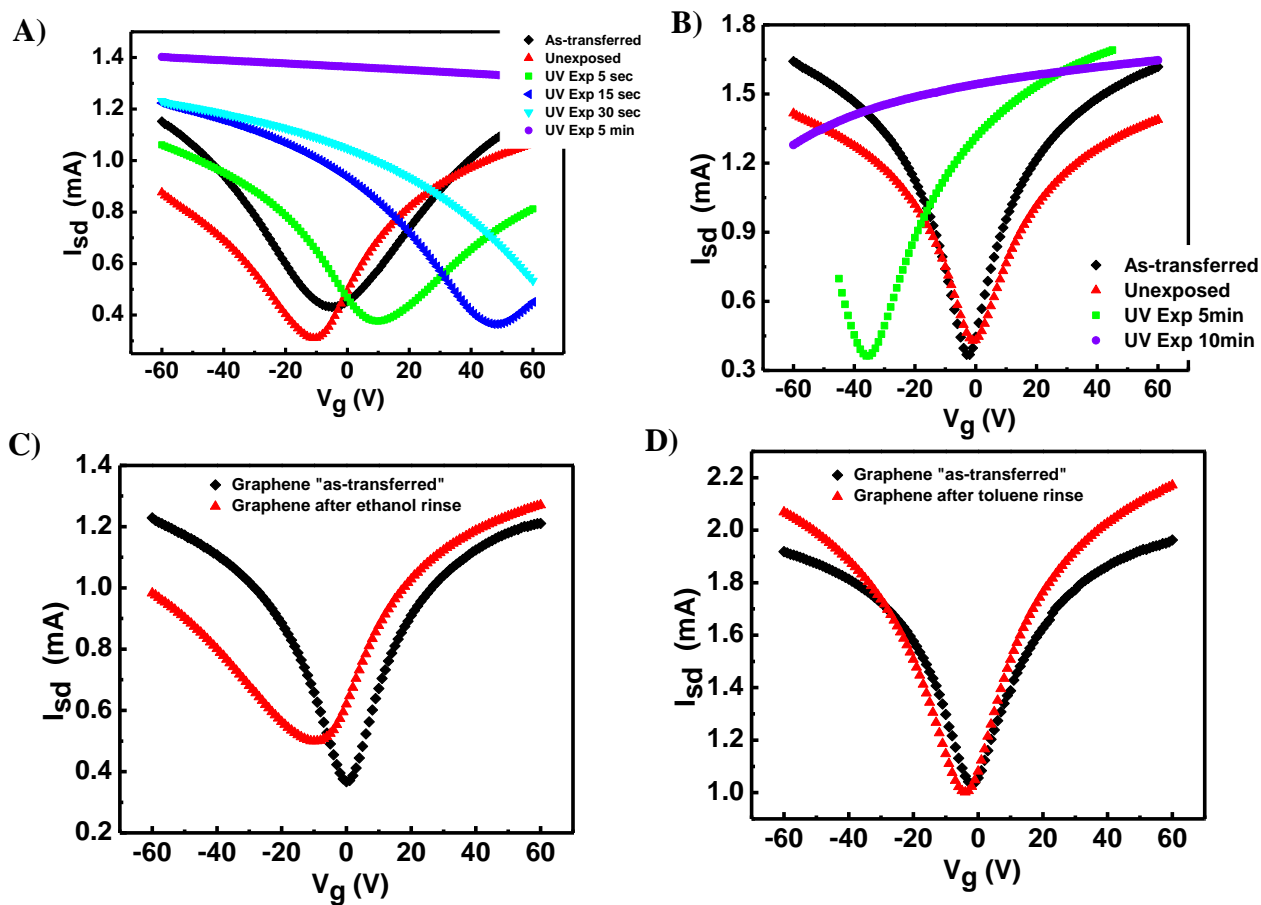
Figure 4-7: Source-drain current versus gate voltage for a simple graphene FET device for (A) graphene/TPS-Nf, (B) graphene/NBC. (Vsd=.1V). Graphene FET devices initial, and after (C) ethanol rinse and (D) toluene rinse.
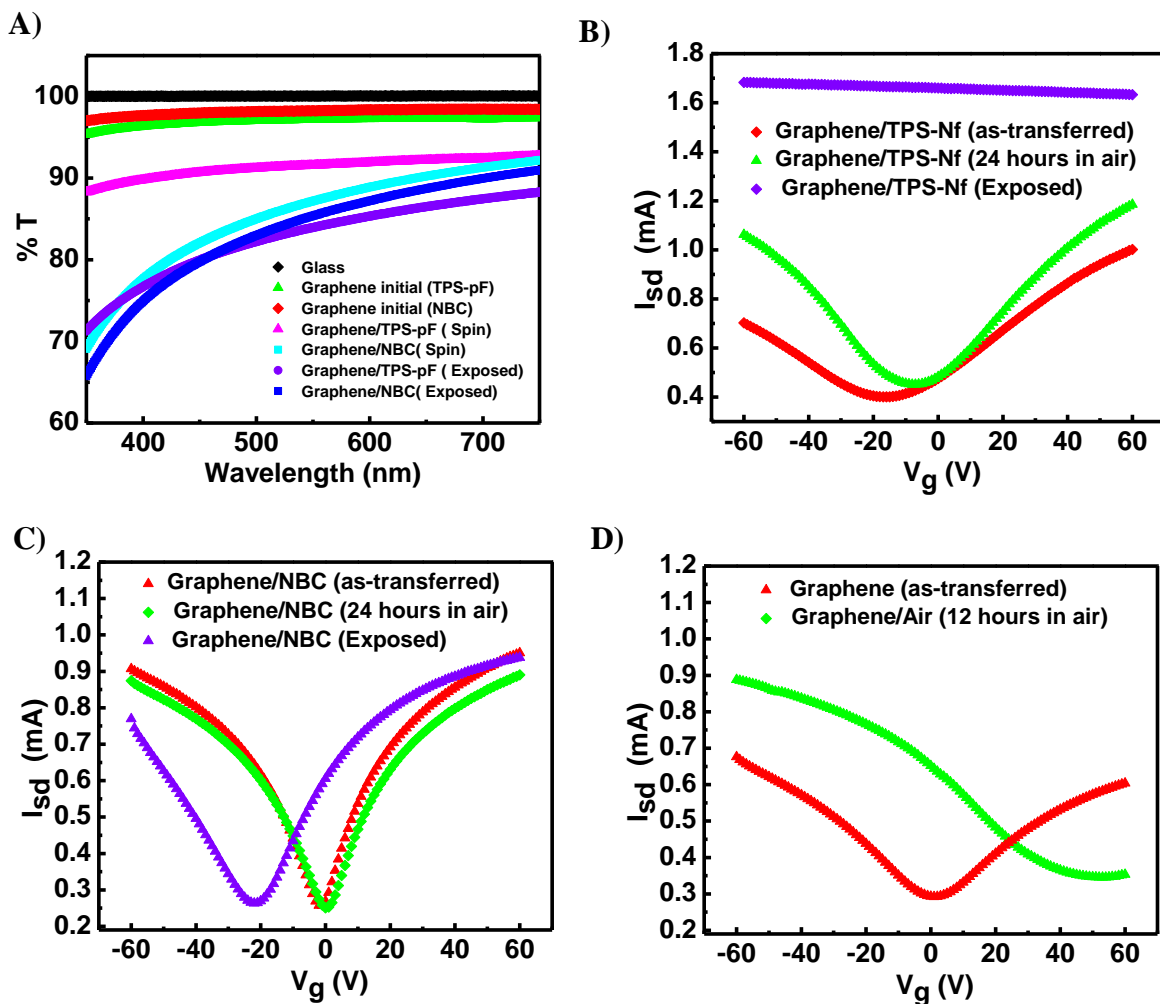
Figure 4-8: (A) UV/Vis spectroscopy for graphene on glass. The black line represents the control sample (black), as-made graphene (green line used for TPS-Nf and red line used for NBC), Graphene spin coated with TPS-Nf (pink curve-Graphene/TPS-Nf), Graphene spin coated with NBC (light blue-graphene/NBC), graphene spin coated with TPS-Nf exposed to DUV light (purple curve-graphene/TPS-Nf) and graphene spin coated with NBC exposed to DUV light (dark blue curve-graphene/NBC). (B) Source-drain current versus gate voltage for simple graphene FET devices after spin coating with TPS-Nf (red curve-Graphene/TPS-Nf), graphene spin coated with TPS-Nf 24 hours in air (green curve-Graphene/TPS-Nf), graphene spin coated with TPS-Nf exposed to DUV light (purple curve-Graphene/TPS-Nf). (C) Source-drain current versus gate voltage for simple graphene FET devices after spin coating with NBC (red curve-graphene/NBC), graphene spin coated with NBC after 24 hours in air (green curve-graphene/NBC), graphene spin coated with NBC exposed to DUV light (purple curve-graphene/NBC). (D) Source-drain current versus gate voltage for simple graphene FET devices as- transferred (red curve-graphene), graphene exposed to air for 12 hour (green curve-graphene/Air).

In order to demonstrate the ability to develop an area-selected pattern-wise doping, back-gated graphene-based p-n junction with patterned p-n regions in the FET channel were fabricated using TPS-Nf as dopant and were measured following the same basic process described above. First, 50 nm thick gold electrodes were evaporated through a shadow mask onto a clean, graphene transferred, 300 nm thick SiO_2 gate dielectric films on highly p-doped silicon wafers. Next, half of each of the channels in the FET devices were covered with a shadow mask and exposed to DUV light (**Figure 4-9A**).

The area selectivity of the chemical conversion of the PAG dopant precursor in the patterned FET device was confirmed by XPS mapping of the FET as illustrated in **Figure 4-9B**. The signal at a binding energy of 163 eV was used for mapping the S2p spectra, which is associated with the exposed TPS-Nf as discussed earlier (**Figure 4-6**). The figure shows a well defined boundary in the S2p spectral map of the FET, as quantified by the signal intensity at 163 eV over the area of the device, between areas of the substrate that were exposed to DUV light and those left unexposed. C1s mapping of the photopatterned FET devices was also accomplished as quantified by the signal intensity at a binding energy of 284 eV, which again corresponds to p-doped graphene (**Figure 4-6**). Again, a well-defined boundary in the doping of the FET channel was observed, with the exposed regions of the FET channel showing clear signs of p-doping. Furthermore, the areas of the FET device exhibiting the most intense C1s signal at 284 eV which is indicative of p-doping, were perfectly correlated with the areas of the device exhibiting the strongest S2p signal that is indicative of the production of the photoacid as well. All of these results are consistent with the formation of a well defined photopatterned p-doped region that is the

result of exposure induced production of photoacid dopant in selected portions of the FET channel.

Electrical measurements were performed on the fabricated CVD graphene devices containing the photopatterned TPS-Nf dopant precursor coatings. The devices were probed under inert atmosphere using a method similar to that described earlier. As expected, the unexposed sample exhibited a slight n-type characteristic due to the solvent (**Figure 4-9C** and **Figure 4-7**) processing with only a single obvious neutrality point. For devices with a 5 second ultraviolet exposure through the shadow mask on the device channel, two minima in the Isd-Vg data were clearly observed, corresponding to two neutrality points as would be expected from a p-n junction,[17,30,37] which in this case is formed by the photochemically created p-type doped region in the slightly n-type device layer. For devices with a 15 sec masked ultraviolet exposure of the channel, again two minima are clearly observed in the Isd-Vg data and additionally the positive Vg neutrality point shifts to more positive values as would be consistent with higher doping levels that result from further photoacid generation during the longer exposure. It is important to notice that the position of the neutrality points in the p-n junction are in agreement with the expected position obtained and discussed earlier from the blanket film exposure experiments (~ 12 V and 50 V for 5 sec and 15 sec exposure respectively of TPS-Nf coated graphene samples) and that little change is observed in the position of the Dirac point corresponding to the unexposed slightly n-type region. It was also possible during these measurements to demonstrate the unique ambipolar character of the devices. Switching of the source-drain bias voltage from positive to negative values showed no rectifying behavior as would be characteristic of an ambipolar device.[17,67] This unique p-n junction behavior of graphene,

103

in contrast with the traditional rectifying behavior of conventional semiconductors, allows the development of graphene-based bipolar devices which have been demonstrated to display new and exciting phenomena such as Klein tunneling,[68-70] and produce lensing effects for coherent electrons, i.e. so called Veselago lensing.[71] Our simple method for producing patterned doping profiles in graphene films and devices facilitates the study of such phenomena and possibly enables the use of graphene for a variety of applications such as circuits and sensors, since it allows precise, simple and independent control over the work function and doping properties of graphene, as compared to the more limited and difficult control possible with electrostatic substrate engineering,[17] and other fabrication techniques[68,69,72-74]
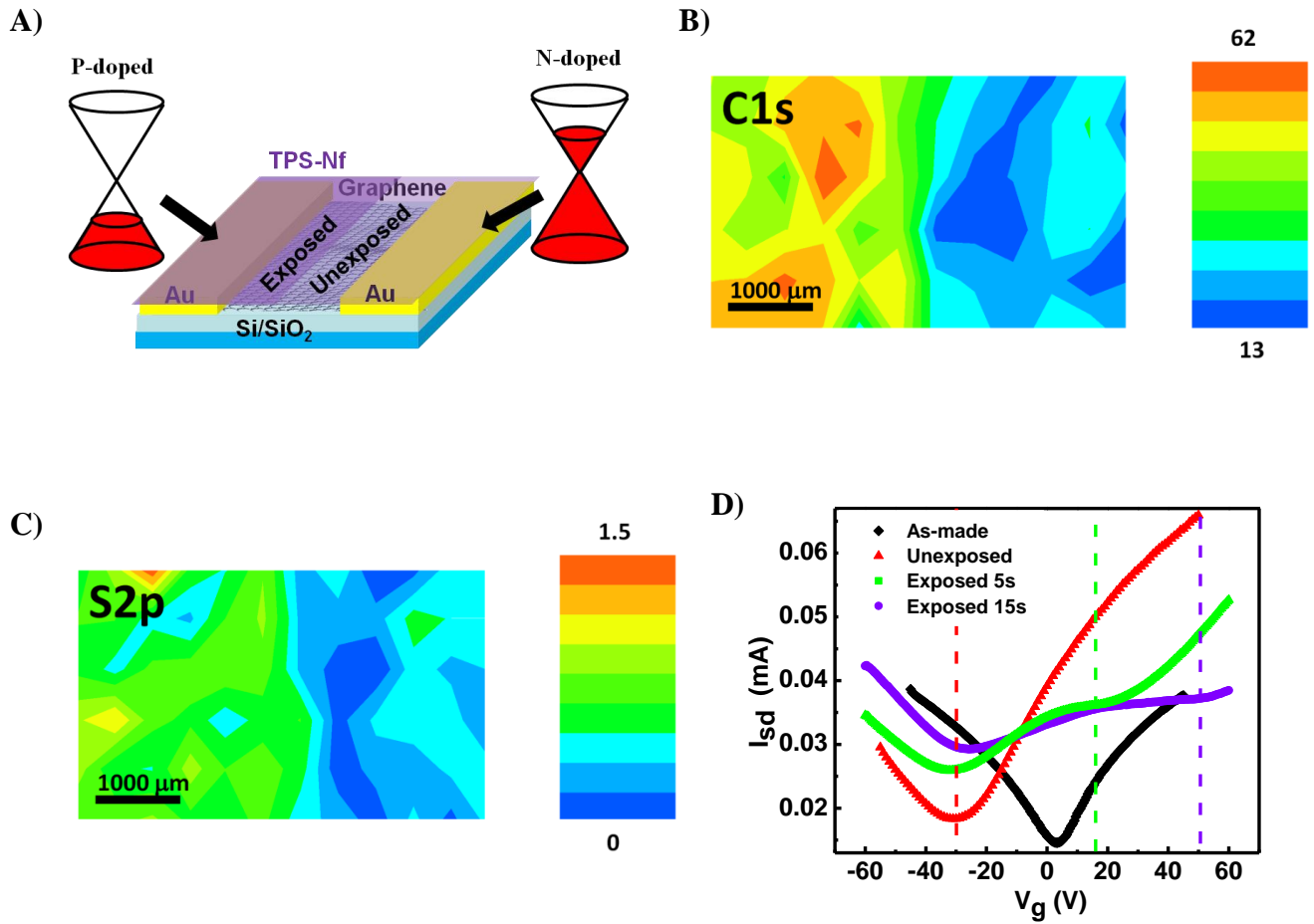
Figure 4-9: **(A) Schematic showing the fabricate graphene/TPS-Nf p-n junction. XPS mapping of the graphene p-n junction for the (B) C1s intensity at a binding energy of ~ 284 eV (C) S2p intensity at a binding energy of ~163 eV. (D) Source-drain current versus gate voltage as a function of exposure time for a graphene p-n junction (Vsd=5V).**

4.4   Conclusions

In the work reported here, we have developed an on-demand photochemical method for doping of graphene using triphenylsulfonium perfluoro-1-butanesufonate (TPS-Nf) and 2-nitrobenzyl *N*-cyclohexylcarbamate (NBC) photoacid and photobase generators. Both compounds can be used to easily dope graphene and such doping can be controlled in an area-selective manner using traditional lithographic exposure techniques and tools. Electrical measurements and XPS confirm that before exposure, graphene coated with either TPS-Nf or NBC maintains its pristine electrical properties, and that by modulating the deep ultraviolet (DUV) light exposure dose delivered to the films, the doping concentration for both p and n-type doping can be easily modulated and controlled. This doping technique yields a possible work function modulation from 3.4 eV to 5.3 eV in single layer graphene. Area-selective doping and modification of an existing graphene FET device are demonstrated through photochemical formation of a p-n junction in a pre-fabricated graphene FET device coated with TPS-Nf and exposed in a pattern-wise manner. The exposure is masked in such a way that the p-n junction is formed in the middle of the graphene FET device channel. Measurements of the I-V characteristics of the photochemically doped FET device show the expected two current minima (i.e. two Dirac or neutrality points) for an ambipolar p-n junction in graphene. Our simple method for producing patterned doping profiles in graphene films and devices opens up a variety of new possibilities for forming complex doping profiles in a simple manner in graphene, and can enable rapid testing of concepts for graphene devices involving controlled work function tuning, complex doping profiles and simple post-fabrication tuning of devices.

4.5   References

1   Geim, A. K. Graphene: Status and Prospects. *Science* **324**, 1530-1534, doi:DOI 10.1126/science.1158877 (2009).

2   Novoselov, K. S. *et al.* Electric Field Effect in Atomically Thin Carbon Films. *Science* **306**, 666-669 (2004).

3   Pati, S. K., Enoki, T. & Rao, C. N. R. *Graphene and its fascinating attributes.* (World Scientific, 2011).

4   Castro Neto, A. H., Guinea, F., Peres, N. M. R., Novoselov, K. S. & Geim, A. K. The electronic properties of graphene. *Rev Mod Phys* **81**, 109-162, doi:DOI 10.1103/RevModPhys.81.109 (2009).

5   Geim, A. K. & Novoselov, K. S. The rise of graphene. *Nat Mater* **6**, 183-191, doi:10.1038/nmat1849 (2007).

6   Jo, G. *et al.* The application of graphene as electrodes in electrical and optical devices. *Nanotechnology* **23**, doi:Artn 112001 Doi 10.1088/0957-4484/23/11/112001 (2012).

7   Novoselov, K. S. *et al.* A roadmap for graphene. *Nature* **490**, 192-200, doi:10.1038/nature11458 nature11458 [pii] (2012).

8   Wassei, J. K. & Kaner, R. B. Oh, the Places You'll Go with Graphene. *Acc Chem Res*, doi:10.1021/ar300184v (2013).

9   Kasry, A., Kuroda, M. A., Martyna, G. J., Tulevski, G. S. & Bol, A. A. Chemical doping of large-area stacked graphene films for use as transparent, conducting electrodes. *Acs Nano* **4**, 3839-3844, doi:10.1021/nn100508g (2010).

10   Shi, Y. *et al.* Work function engineering of graphene electrode via chemical doping. *Acs Nano* **4**, 2689-2694, doi:10.1021/nn1005478 (2010).

11   Kim, K. S. *et al.* Large-scale pattern growth of graphene films for stretchable transparent electrodes. *Nature* **457**, 706-710, doi:10.1038/nature07719 nature07719 [pii] (2009).

12   Liu, Z. K. *et al.* The Application of Highly Doped Single-Layer Graphene as the Top Electrodes of Semitransparent Organic Solar Cells. *Acs Nano* **6**, 810-818, doi:Doi 10.1021/Nn204675r (2012).

13   Schwierz, F. Graphene transistors. *Nat Nano* **5**, 487-496 (2010).

14   Lin, Y. M. *et al.* 100-GHz Transistors from Wafer-Scale Epitaxial Graphene. *Science* **327**, 662-662, doi:DOI 10.1126/science.1184289 (2010).

15   Han, T. H. *et al.* Extremely efficient flexible organic light-emitting diodes with modified graphene anode. *Nat Photonics* **6**, 105-110, doi:Doi 10.1038/Nphoton.2011.318 (2012).

16   Georgakilas, V. *et al.* Functionalization of Graphene: Covalent and Non-Covalent Approaches, Derivatives and Applications. *Chemical Reviews* **112**, 6156-6214, doi:Doi 10.1021/Cr3000412 (2012).

17   Chiu, H. Y., Perebeinos, V., Lin, Y. M. & Avouris, P. Controllable p-n Junction Formation in Mono layer Graphene Using Electrostatic Substrate Engineering. *Nano Lett* **10**, 4634-4639, doi:Doi 10.1021/Nl102756r (2010).

18   Liu, H., Liu, Y. & Zhu, D. Chemical doping of graphene. *J Mater Chem* **21**, 3335-3345 (2011).

19   Paniagua, S. A. *et al.* Production of heavily n- and p-doped CVD graphene with solution-processed redox-active metal-organic species. *Materials Horizonts* (2013).

20   Usachov, D. *et al.* Nitrogen-Doped Graphene: Efficient Growth, Structure, and Electronic Properties. *Nano Lett* **11**, 5401-5407, doi:Doi 10.1021/Nl2031037 (2011).

21   Nistor, R. A., Newns, D. M. & Martyna, G. J. The Role of Chemistry in Graphene Doping for Carbon-Based Electronics. *Acs Nano* **5**, 3096-3103, doi:Doi 10.1021/Nn200225f (2011).

22   Chen, W., Qi, D. C., Gao, X. Y. & Wee, A. T. S. Surface transfer doping of semiconductors. *Prog Surf Sci* **84**, 279-321, doi:DOI 10.1016/j.progsurf.2009.06.002 (2009).

23   Lin, Y.-C., Lin, C.-Y. & Chiu, P.-W. *Controllable graphene N-doping with ammonia plasma*. Vol. 96 (AIP, 2010).

24   Huh, S., Park, J., Kim, K. S., Hong, B. H. & Bin Kim, S. Selective n-Type Doping of Graphene by Photo-patterned Gold Nanoparticles. *Acs Nano* **5**, 3639-3644, doi:Doi 10.1021/Nn1035203 (2011).

25   Lee, W. H. *et al.* Simultaneous Transfer and Doping of CVD-Grown Graphene by Fluoropolymer for Transparent Conductive Films on Plastic. *Acs Nano* **6**, 1284-1290, doi:Doi 10.1021/Nn203998j (2012).

26   Farmer, D. B. *et al.* Chemical doping and electron-hole conduction asymmetry in graphene devices. *Nano Lett* **9**, 388-392, doi:10.1021/nl803214a (2009).

27   Wang, R. *et al.* Control of Carrier Type and Density in Exfoliated Graphene by Interface Engineering. *Acs Nano* **5**, 408-412, doi:10.1021/nn102236x (2010).

28   Wei, P. *et al.* Tuning the Dirac Point in CVD-Grown Graphene through Solution Processed n-Type Doping with 2-(2-Methoxyphenyl)-1,3-dimethyl-2,3-dihydro-1H-benzoimidazole. *Nano Lett* **13**, 1890-1897, doi:10.1021/nl303410g (2013).

29   Baltazar, J. *et al.* Facile Formation of Graphene P-N Junctions Using Self-Assembled Monolayers. *J Phys Chem C* **116**, 19095-19103, doi:Doi 10.1021/Jp3045737 (2012).

30   Sojoudi, H., Baltazar, J., Tolbert, L. M., Henderson, C. L. & Graham, S. Creating Graphene p-n Junctions Using Self-Assembled Monolayers. *Acs Appl Mater Inter* **4**, 4781-4786, doi:Doi 10.1021/Am301138v (2012).

31   Shashikala, H. B. M., Nicolas, C. I. & Wang, X. Q. Tunable Doping in Graphene by Light-Switchable Molecules. *J Phys Chem C* **116**, 26102-26105, doi:Doi 10.1021/Jp311269c (2012).

32   Jang, A. R. *et al.* Reversibly Light-Modulated Dirac Point of Graphene Functionalized with Spiropyran. *Acs Nano* **6**, 9207-9213, doi:Doi 10.1021/Nn303539y (2012).

33   Peimyoo, N. *et al.* Photocontrolled Molecular Structural Transition and Doping in Graphene. *Acs Nano* **6**, 8878-8886, doi:Doi 10.1021/Nn302876w (2012).

34   Luo, Z. T., Pinto, N. J., Davila, Y. & Johnson, A. T. C. Controlled doping of graphene using ultraviolet irradiation. *Appl Phys Lett* **100**, doi:Artn 253108 Doi 10.1063/1.4729828 (2012).

35   Kim, M., Safron, N. S., Huang, C. H., Arnold, M. S. & Gopalan, P. Light-Driven Reversible Modulation of Doping in Graphene. *Nano Lett* **12**, 182-187, doi:Doi 10.1021/Nl2032734 (2012).

36   Iqbal, M. Z., Siddique, S., Iqbal, M. W. & Eom, J. Formation of p-n junction with stable p-doping in graphene field effect transistors using deep UV irradiation. *Journal of Materials Chemistry C* **1**, 3078-3083, doi:10.1039/c3tc30232f (2013).

37   Kim, Y. D. *et al.* Focused-laser-enabled p-n junctions in graphene field-effect transistors. *Acs Nano* **7**, 5850-5857, doi:10.1021/nn402354j (2013).

38   Lawson, R. A., Tolbert, L. M. & Henderson, C. L. High sensitivity nonchemically amplified molecular resists based on photosensitive dissolution inhibitors. *J Vac Sci Technol B* **28**, C6s12-C16s18, doi:Doi 10.1116/1.3511790 (2010).

39   Lawson, R. A., Noga, D. E., Tolbert, L. M. & Henderson, C. L. Nonionic photoacid generator behavior under high-energy exposure sources. *J Micro-Nanolith Mem* **8**, doi:Artn 043010 Doi 10.1117/1.3259205 (2009).

40   Lawson, R. A., Lee, C. T., Tolbert, L. M. & Henderson, C. L. Effect of acid anion on the behavior of single component molecular resists incorporating ionic

photoacid generators. *Microelectron Eng* **86**, 738-740, doi:DOI 10.1016/j.mee.2008.11.043 (2009).

41   Lawson, R. A. *et al.* Molecular glass photoresists containing photoacid generator functionality: A route to a single molecule photoresist - art. no. 65191N. *Advances in Resist Materials and Processing Technology XXIV* **6519**, N5191-N5191, doi:Artn 65191n Doi 10.1117/12.712928 (2007).

42   Li, X. *et al.* Large-Area Synthesis of High-Quality and Uniform Graphene Films on Copper Foils. *Science* **324**, 1312-1314 (2009).

43   Sojoudi, H., Baltazar, J., Henderson, C. & Graham, S. Impact of post-growth thermal annealing and environmental exposure on the unintentional doping of CVD graphene films. *J Vac Sci Technol B* **30**, doi:Artn 041213 Doi 10.1116/1.4731472 (2012).

44   Crivello, J. V. & Dietliker, K. *Photoinitiators for Free Radical Cationic & Anionic Photopolymerisation*. 2 edn, Vol. 3 (John Wiley and Sons, 1998).

45   Tagawa, S., Nagahara, S., Iwamoto, T., Wakita, M. & Kozawa, T. Radiation and photochemistry of onium salt acid generators in chemically amplified resists. *Advances in Resist Technology and Processing Xvii, Pts 1 and 2* **3999**, 204-213, doi:Doi 10.1117/12.388304 (2000).

46   Kasry, A., Kuroda, M. A., Martyna, G. J., Tulevski, G. S. & Bol, A. A. Chemical Doping of Large-Area Stacked Graphene Films for Use as Transparent, Conducting Electrodes. *Acs Nano* **4**, 3839-3844, doi:Doi 10.1021/Nn100508g (2010).

47   Leenaerts, O., Partoens, B. & Peeters, F. M. Adsorption of small molecules on graphene. *Microelectron J* **40**, 860-862, doi:DOI 10.1016/j.mejo.2008.11.022 (2009).

48   Yokota, K., Takai, K. & Enoki, T. Carrier Control of Graphene Driven by the Proximity Effect of Functionalized Self-assembled Monolayers. *Nano Lett*, doi:10.1021/nl201607t (2011).

49   Wang, X. M., Xu, J. B., Wang, C. L., Du, J. & Xie, W. G. High-Performance Graphene Devices on SiO2/Si Substrate Modified by Highly Ordered Self-Assembled Monolayers. *Adv Mater* **23**, 2464-+, doi:DOI 10.1002/adma.201100476 (2011).

50   Kobayashi, S. *et al.* Control of carrier density by self-assembled monolayers in organic field-effect transistors. *Nat Mater* **3**, 317-322, doi:10.1038/nmat1105 (2004).

51   Ryu, S. *et al.* Atmospheric Oxygen Binding and Hole Doping in Deformed Graphene on a SiO(2) Substrate. *Nano Lett* **10**, 4944-4951, doi:Doi 10.1021/Nl1029607 (2010).

52   Das, A. *et al.* Monitoring dopants by Raman scattering in an electrochemically top-gated graphene transistor. *Nat Nanotechnol* **3**, 210-215, doi:DOI 10.1038/nnano.2008.67 (2008).

53   Das, A. *et al.* Monitoring dopants by Raman scattering in an electrochemically top-gated graphene transistor. *Nat Nano* **3**, 210-215, doi:http://www.nature.com/nnano/journal/v3/n4/suppinfo/nnano.2008.67_S1.html (2008).

54   Ishii, H., Sugiyama, K., Ito, E. & Seki, K. Energy level alignment and interfacial electronic structures at organic/metal and organic/organic interfaces (vol 11, pg 605, 1999). *Adv Mater* **11**, 972-972 (1999).

55   Zhang, Y. B. *et al.* Giant phonon-induced conductance in scanning tunnelling spectroscopy of gate-tunable graphene. *Nat Phys* **4**, 627-630, doi:Doi 10.1038/Nphys1022 (2008).

56   Park, J. *et al.* Work-Function Engineering of Graphene Electrodes by Self-Assembled Monolayers for High-Performance Organic Field-Effect Transistors. *J Phys Chem Lett* **2**, 841-845, doi:Doi 10.1021/Jz200265w (2011).

57   Chen, Z. Y. *et al.* Surface transfer hole doping of epitaxial graphene using MoO3 thin film. *Appl Phys Lett* **96**, doi:Artn 213104 Doi 10.1063/1.3441263 (2010).

58   Tongay, S. *et al.* Stable hole doping of graphene for low electrical resistance and high optical transparency. *Nanotechnology* **22**, doi:Artn 425701 Doi 10.1088/0957-4484/22/42/425701 (2011).

59   Qi, Y., Mazur, U. & Hipps, K. W. Charge transfer induced chemical reaction of tetracyano-p-quinodimethane adsorbed on graphene. *Rsc Adv* **2**, 10579-10584, doi:Doi 10.1039/C2ra21756b (2012).

60   Bae, S. *et al.* Roll-to-roll production of 30-inch graphene films for transparent electrodes. *Nat Nanotechnol* **5**, 574-578, doi:Doi 10.1038/Nnano.2010.132 (2010).

61   Chirakul, P., Perez-Luna, V. H., Lopez, G. P. & Hampton, P. D. Self-assembled monolayers of amine-terminated thiols. *Abstr Pap Am Chem S* **217**, U668-U668 (1999).

62   Yeh, W.-M., Lawson, R. A., Tolbert, L. M. & Henderson, C. L. Resist surface crosslinking using amine-based reactive rinses to mitagate pattern collapse in thin film lithography. *SPIE Proceedings* **8325**, 83251X-83251X, doi:10.1117/12.928876 (2012).

63   Kumada, T. *et al.* Study on the over-Top Coating Suppressing Surface Insoluble Layer Generation for Chemical Amplification Resist. *Advances in Resist Technology and Processing X* **1925**, 31-42, doi:Doi 10.1117/12.154764 (1993).

64   Brenner, K. & Murali, R. In situ doping of graphene by exfoliation in a nitrogen ambient. *Appl Phys Lett* **98**, doi:Artn 113115 Doi 10.1063/1.3562018 (2011).

65   Shen, Z. X. *et al.* The effect of vacuum annealing on graphene. *Journal of Raman Spectroscopy* **41**, 479-483, doi:Doi 10.1002/Jrs.2485 (2010).

66   Nourbakhsh, A. *et al.* Tuning the Fermi Level of SiO(2)-Supported Single-Layer Graphene by Thermal Annealing. *J Phys Chem C* **114**, 6894-6900, doi:Doi 10.1021/Jp910085n (2010).

67   Cheng, H. C., Shiue, R. J., Tsai, C. C., Wang, W. H. & Chen, Y. T. High-Quality Graphene p-n Junctions via Resist-free Fabrication and Solution-Based Noncovalent Functionalization. *Acs Nano* **5**, 2051-2059, doi:Doi 10.1021/Nn103221v (2011).

68   Stander, N., Huard, B. & Goldhaber-Gordon, D. Evidence for Klein Tunneling in Graphene p-n Junctions. *Phys Rev Lett* **102**, doi:Artn 026807 Doi 10.1103/Physrevlett.102.026807 (2009).

69   Young, A. F. & Kim, P. Quantum interference and Klein tunnelling in graphene heterojunctions. *Nat Phys* **5**, 222-226, doi:Doi 10.1038/Nphys1198 (2009).

70   Williams, J. R., DiCarlo, L. & Marcus, C. M. Quantum hall effect in a gate-controlled p-n junction of graphene. *Science* **317**, 638-641, doi:DOI 10.1126/science.1144657 (2007).

71   Cheianov, V. V., Fal'ko, V. & Altshuler, B. L. The focusing of electron flow and a Veselago lens in graphene p-n junctions. *Science* **315**, 1252-1255, doi:DOI 10.1126/science.1138020 (2007).

72   Brenner, K. & Murali, R. Single step, complementary doping of graphene. *Appl Phys Lett* **96**, doi:Artn 063104 Doi 10.1063/1.3308482 (2010).

73   Lohmann, T., von Klitzing, K. & Smet, J. H. Four-Terminal Magneto-Transport in Graphene p-n Junctions Created by Spatially Selective Doping. *Nano Lett* **9**, 1973-1979, doi:Doi 10.1021/Nl900203n (2009).

74   Peters, E. C., Lee, E. J. H., Burghard, M. & Kern, K. Gate dependent photocurrents at a graphene p-n junction. *Appl Phys Lett* **97**, doi:Artn 193102 Doi 10.1063/1.3505926 (2010).

CHAPTER 5

EXFOLIATION OF GRAPHENE SHEETS BY AN ELECTRON DONOR SURFACTANT

A novel macromolecular surfactant dicholesteryldithienothiophene (ChDTT) was synthesized and optimized for use in graphene exfoliation and dispersion. By simple sonication of expandable graphite in solutions containing ChDTT, graphene sheets with sizes exceeding 50 micrometers were observed and characterized by transmission electron microscopy (TEM), atomic force microscopy (AFM), electrical measurements, Raman and X-ray photoelectron (XPS) spectroscopies. The new surfactant is more efficient than poly(m-phenylenevinylene-co-2,5-dioctyloxy-p-phenylenevinylene) (PmPV), avoids use of polymeric materials, and can be removed at lower thermal treatment. Using this surfactant, graphene flakes can be extracted directly from HOPG or other graphitic sources without additional chemical treatment, producing larger flakes of higher quality.

5.1   Introduction

Production of single layer graphene (SLG), whose isolation was originally considered unrealistic[1], has attracted extensive recent scientific and technological interest.[2] Single layer graphene is a monolayer of sp^2-bonded carbon atoms tightly packed into a two-dimensional honeycomb lattice characterized by the benzene repeat unit and is the basic building block unit for many carbon allotropes with other dimensionality, e.g. carbon nanotubes (CNTs), fullerenes, and graphite. Depending upon the environment in which it is placed, single layer graphene has a number of fascinating electronic properties including ultra high electron mobility[3], ballistic transport[3], anomalous quantum Hall effects[4], and semiconducting properties[5]. These unusual electronic properties and interest in graphene are not however confined only to single layer graphene. While single layer graphene intrinsically has no bandgap, Zhang and coworkers reported that a bandgap exists in mechanically exfoliated bilayer graphene which is continuously tunable by independently varying the top and bottom gate voltage in a dual-gate field-effect transistor[6]. Also, bilayer graphene exhibits unconventional quantum Hall effect behavior.[7] For trilayer graphene, applying a perpendicular electric field results in band overlap, resulting in semimetal behavior.[8] The persistence of unusual electronic properties into multiple layer graphitic materials has led to a somewhat generalized definition of "multi-layer graphene" (MLG) as graphite containing fewer than ten layers.[1] Beyond this limit of 10 layers, the difference in band overlap between MLG and bulk graphite is less than 10% and the corresponding electronic properties are of less interest.[9]

Interest in and demand for graphene is also not limited to its electronic properties owing to its other unusual properties including extremely high surface area,[10] exceptional

mechanical elasticity,[11] high tensile stiffness and strength,[12] and high thermal conductivity.[13,14] With respect to these other properties and their application, again there is significant interest in MLG forms as well. As such, SLG and MLG hold significant technological promise in a variety of areas including electronics,[13,15,16] energy storage,[16,17] sensors,[18,19] and composites[20].

Although a number of different methods have been reported for preparation of SLG and MLG in the past few years, including mechanical exfoliation[13], solvent-based exfoliation[21], surfactant mediated liquid exfoliation[22], and Hummers' method[23]; nevertheless mechanical exfoliation is still one of the most commonly used methods for production of research quantities of SLG due to its simplicity and its ability to reliably produce single layer graphene.[13] However, production of significant quantities and large areas of SLG and MLG are not practical using such mechanical techniques. Instead, large scale graphene production can be divided into two general categories: epitaxial growth by chemical methods, such as chemical vapor deposition (CVD)[24,25] or SiC annealing[26]; and chemical exfoliation from graphitic sources in the liquid phase[21,27,28]. CVD and SiC annealing routes have the demonstrated advantage of being able to produce large areas of continuous graphene with good control over the number of graphene layers. However, CVD and SiC methods suffer from a number of problems including complexity, cost, and hazards of the controlled environment, high temperature reactor systems required for such methods. In contrast, liquid phase exfoliation routes to production of graphene offer the potential for production of large volumes of graphene under generally inexpensive and comparatively benign conditions.

One of the first reported liquid phase exfoliation routes to production of graphene, often referred to as Hummers' method, which involves the oxidation and exfoliation of a graphitic source material (e.g. graphite) to form suspended graphite oxide (GO) dispersions followed by reduction of the GO to form graphene.[29,30] From a solution processing point of view, GO is an ideal intermediate for graphene exfoliation since its negatively charged surface not only allows graphene oxide sheets to be readily dispersed in water but also stabilizes the individual GO sheets from re-aggregation due to electrostatic repulsion. Also, casting of GO from water can allow for formation of well controlled, continuous, and uniform films of graphene. However, the oxidation of graphene inherently induces unrecoverable defects into the graphene lattice that result in degradation of its electronic properties[31-35] and to a lesser degree reduction in mechanical and thermal properties of graphene.[36]. For example, the mobility of pristine mechanically exfoliated graphene has been reported to be as large 12,000 cm^2/Vs and higher[37,38] while the mobility of reduced GO is generally in the range of 2 to 200 cm^2/Vs.[31] To avoid the poor conductivity resulting from the interruption of the graphene sp^2 structure inherent in GO reduction methods, several liquid phase methods involving direct exfoliation of graphene from graphite materials using ultrasonic agitation have also been developed and reported. By matching the surface energy between solvent and graphene, single layer graphene flakes have been successfully exfoliated into different solvents such as N-methylpyrrolidone (NMP) and hexafluorobenzene (C_6F_6) in conjunction with ultrasonic energy.[21,39,40] However, such simple solvent exfoliation routes exhibit a number of limitations including production of very small flakes (~100 nm in diameter and smaller), low concentrations of graphene flakes in solution, and poor solution stability. In order to ameliorate many of these problems with

simple solution exfoliation, the use of surfactants to enhance the exfoliation of graphene into solvents via sonication has also been explored. [41-49] Ionized surfactants[27,50,51] and macromolecules[5,52] such as polymers have also been used to exfoliate and stabilize pristine or chemically functionalized[28,53] graphene flake suspensions by means of surface charge repulsion or steric destabilization. In fact, the use of appropriate surfactants can allow for the direct exfoliation of graphene into normally incompatible solvents such as water.[27] The use of surfactants and macromolecules in the exfoliation and solution stabilization process introduces additional complications ranging from the effect of the presence of the surfactant on the graphene on its properties [41,46] to the potential need for simple and efficient removal of the surfactant that does not damage the graphene [41,45]. Liquid phase methods are suitable for various processes, including chemical modification, impregnation, mixing, casting, and spin-coating. A solution phase differentiation method which can separate graphene with controlled thickness has also been recently reported[50]. Combined with various deposition techniques, e.g. dielectrophoresis[54] or Langmuir-Blodgett[53] films, liquid phase exfoliation enables the fabrication of graphene arrays with monodispersed thickness.

In common to all these techniques is the very small size (~100 nm) of the flakes, even with thicker MLG. For solvent assisted exfoliation, the exfoliation capability is also low.[55] To avoid these problems, macromolecules, notably polymers[56-58] and biomolecules[59-61] (such as DNA and peptides), have been intensively employed to isolate CNT. The π-conjugated polymer backbone or DNA non-covalently attaches to the nanotube surface through $\pi-\pi$ stacking, which preserves the electrical and optical properties of the CNT. Conversely, charge transfer between surfactant and CNT improves

the exfoliation capability. Unlike for CNT, the solubilization of graphene by biomolecules not yet been successful.[55] Graphene has recently been exfoliated using the same polymer used in a CNT system, poly(m-phenylenevinylene-co-2,5-dioctyloxy-p-phenylenevinylene) (PmPV),[5] however removal of such polymer is not achieved easily as we discuss it later in this paper.

Therefore, here we present a novel macromolecular surfactant dicholesteryldithienothiophene (ChDTT) synthesized and optimized for use in graphene exfoliation and dispersion. By simple sonication of expandable graphite in solutions containing ChDTT, graphene sheets with sizes exceeding 50 micrometers were observed and characterized by transmission electron microscopy (TEM), atomic force microscopy (AFM), electrical measurements, Raman spectroscopy and X-ray photoelectron Spectroscopy (XPS).

Transmission electron microscopy (TEM) and atomic force microscopy (AFM) analysis, revealed the presence of large size, multi-layer graphene sheets with a high level of exfoliation in ChDTT-containing solution. Raman spectroscopy confirmed that the ultra-large graphene sheet (50 μm) was as thin as 3-5 layers. X-ray photoelectron (XPS) spectroscopy also indicated that ChDTT could be totally removed by thermal treatment, leaving defect free and very slightly oxidized graphene flakes, which is not possible in the PmPV system. Furthermore, the new surfactant is more efficient than poly(m-phenylenevinylene-co-2,5-dioctyloxy-p-phenylenevinylene) (PmPV), avoids use of polymeric materials, and can be removed at lower thermal treatment. Using this surfactant, graphene flakes can be extracted directly from HOPG or other graphitic sources without

additional chemical or mechanical, producing larger flakes of higher quality compared to reduced graphene oxide.

5.2   Experimental Section

The graphite intercalation compound (GIC) was first expanded by thermal shock. The procedure is described as follows: First, commercially available "expandable graphite" (NYACOL NYAGRAPH 351), was quickly heated to 1000°C for 1 min under forming gas. The resulting black expanded graphite powder was dispersed in a 1,2-dichloroethane (DCE) solution of ChDTT or PmPV (0.1mg/mL). The solution was ultrasonicated for 30 min and centrifuged under 14K RPM for 10 min. The clear supernatant, containing flakes of single or multi-layer graphene, was collected for further analysis. Characterization methods included Raman spectroscopy (Renaishaw 2000, 488nm), X-ray photoelectron spectroscopy (XPS, Thermo-K Alpha), atomic force microscopy (AFM, Agilent picoplus system), transmission electron microscopy (TEM, JEOL 100CX II, 100kV), scanning electron microscopy (SEM, Zeiss Gemini Ultra-60), thermogravity analysis (TGA, Texas Instrument Q500), and UV-Vis spectrometer.

Back-gated graphene field effect transistors were fabricated using a combination of photolithography and electron-beam lithography as well as metallization techniques (**Figure 5.1**). A UV ozone treated highly p-doped Si wafer was used as a gate, with a 300 nm thick thermally grown silicon dioxide layer as the gate dielectric .Lithography and deposition processes (i.e. typical lift-off procedures) were used to form the gold alignment marks (to aid on the selection of the graphene flakes of interested) on the 300 nm thick SiO_2 gate dielectric films. Next, the surfactant exfoliated flakes were dropped casted on the fabricated substrate and inspected via raman spectroscopy (**Figure 5.2**) in order to

119

select potential few layers graphene flake. Next electron-beam lithography was used to define the souce and drain electrodes, followed by gold deposition (i.e. lift-off). Electrical measurements, including I-V curves, were made using a probe station configured with a HP 4156 semiconductor parameter analyzer maintained under an inert atmosphere. Measurements were performed on both as-made devices and after heating in the inert atmosphere to remove most of the DTT surfactant.
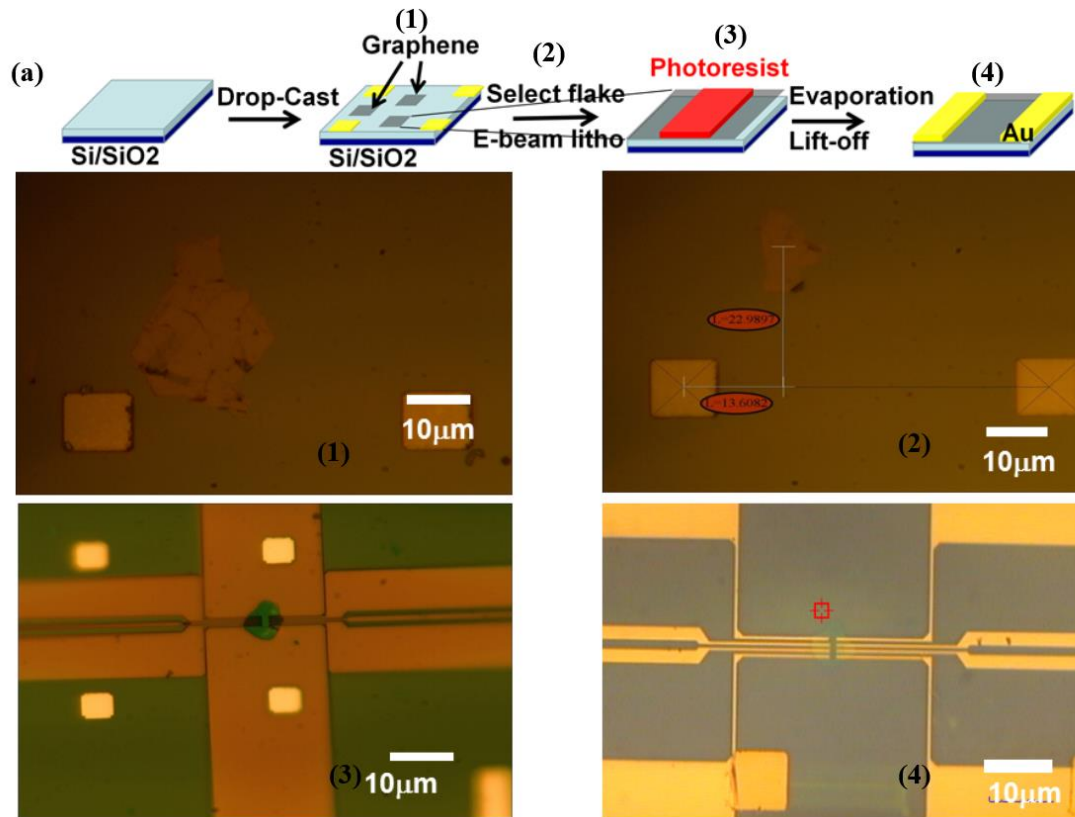
Figure 5.1. (A) Schematic showing the process used to fabricate the graphene FET device and Optical Image of each fabrication step.
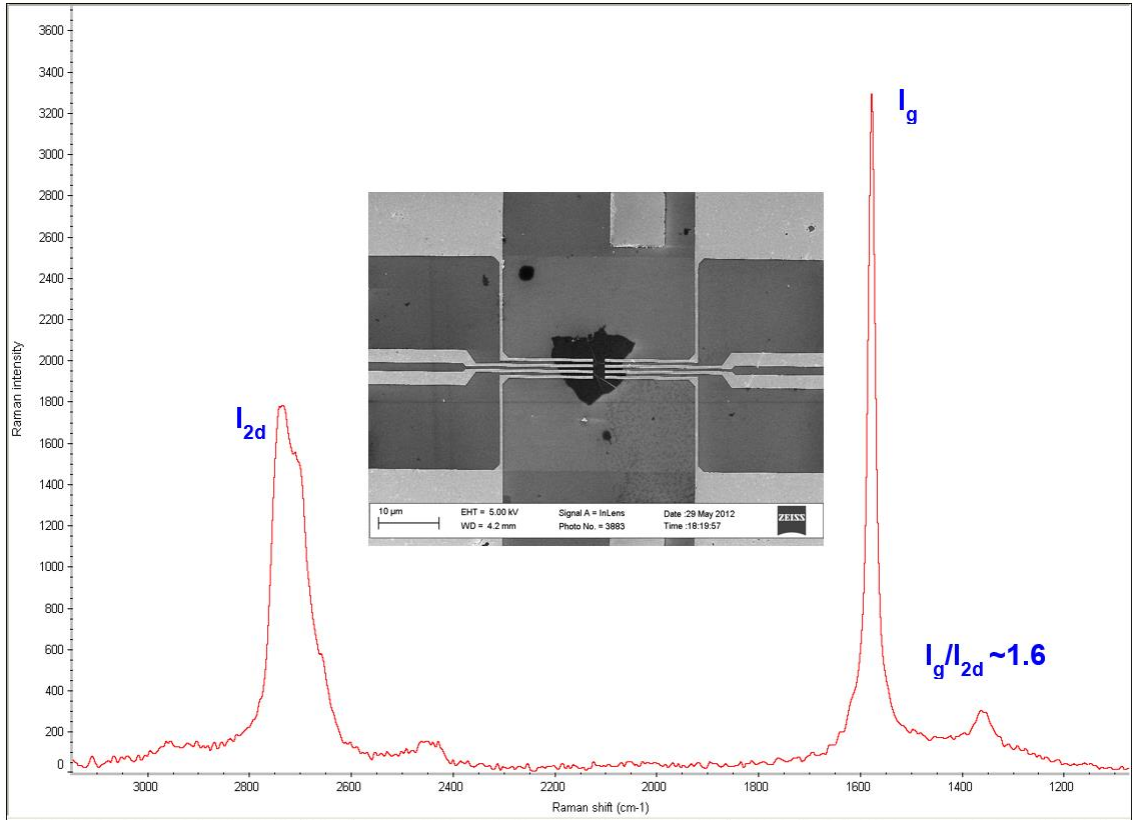
Figure 5.2. (a) Raman Spectroscopy of the graphene layer used to fabricate the graphene FET device . Insert shows the SEM image of the fabricated device.

5.3   Results and Discussion

Our new macromolecular surfactant (**Figure 5.3**), dicholesteryldithienothiophene (ChDTT) consists of a central π-conjugated core, i.e. DTT, which can adsorb on graphene surface through charge-transfer interaction, and cholesteryl side chains (**Figure 5.4A**). Such groups, which are widely distributed components of surfactants in nature, were incorporated into DTT to provide both solubility and nonbonding interactions. Recently, Janowska and coworkers has reported that large size graphene flakes (average about 10 µm) can be synthesized in water or ammonia by a series of sonication and microwave treatments[51]. However, graphene oxidation (in water) or nitrogen doping (in ammonia) still cannot be avoided. Using their procedure as a model, we investigated whether the material in **Figure 5.4** was indeed graphene and if it could be used to make, first, graphene flakes and, then, uniform sheets. For comparison purposes, another popular macromolecular surfactant. PmPV, known to disperse CNT and graphene by π−π stacking between π-conjugated backbone and the aromatic surface, has also been synthesized.

To prove our idea that the DTT core plays the same role in our newly designed ChDTT system, UV-Vis spectroscopy was used to monitor the absorption change for both ChDTT and PmPV after the surfactant-graphite interaction. A 2 mg portion of thermal expanded graphite was added to 0.01mM ChDTT/DCE solution. After stirring for 90 minutes, the mixture was filtered through a 0.2 µm PTFE filter to remove unchanged graphite. Unlike ultrasonication, mild stirring did not exfoliate expanded graphite. **Figure 5.4B** displays the UV-Vis spectra of a ChDTT/DCE solution before and after graphite immersion. It shows an absorption decrease, indicating a decrease in ChDTT concentration according to the Beer's law. Under higher concentrations and reaction times (20 mg

123

expanded graphite and 16 hour stir), the absorption peaks between 300 to 400 nm disappear

(line c in **Figure 5.4B**), implying that ChDTT molecules were adsorbed on the expanded

graphite surface and removed from solution. Similar absorption changes in the PmPV/DCE

system are described in **Figure 5.4C**. These results suggest that the dispersion mechanism

of ChDTT is similar to that of PmPV, involving charge transfer between surfactant and

graphene, which we believe aid the exfoliation of graphite during ultrasonication.
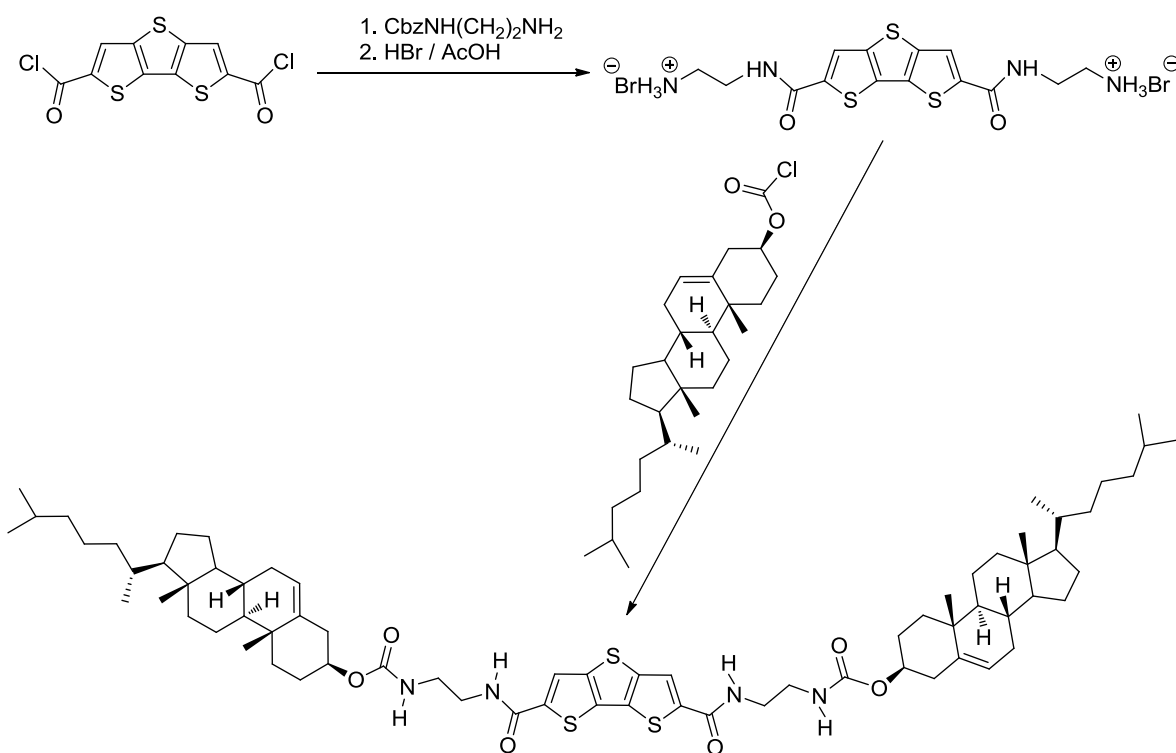
Figure 5.3: The synthesis route of Dicholesteryl-dithienothiophene (ChDTT)

(a)

Bulk Graphite in solution of
dicarboxylic dithienothiophene

Formation of charge transfer
complex and pi-pi stacking

(b)

(c)
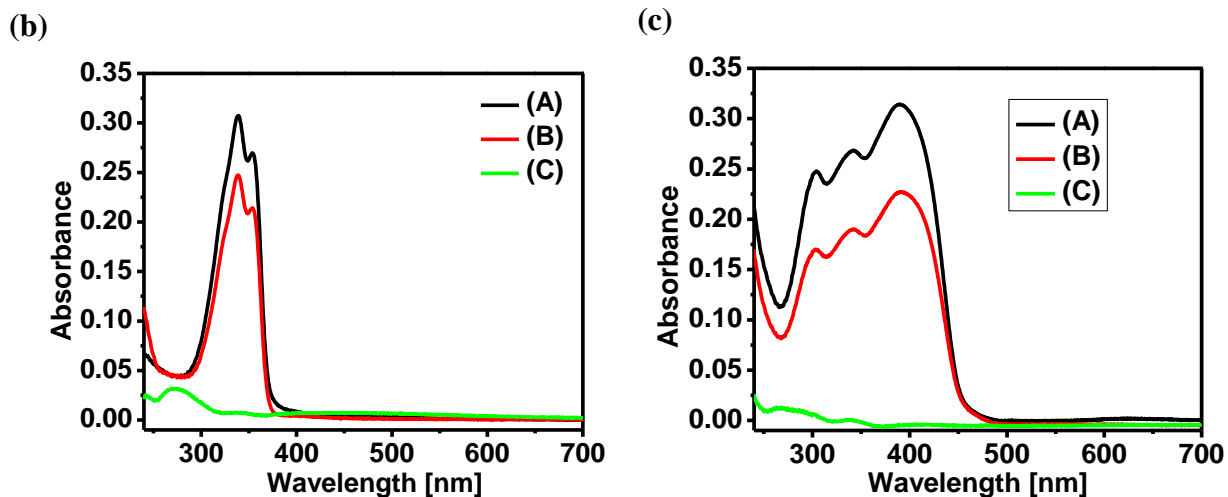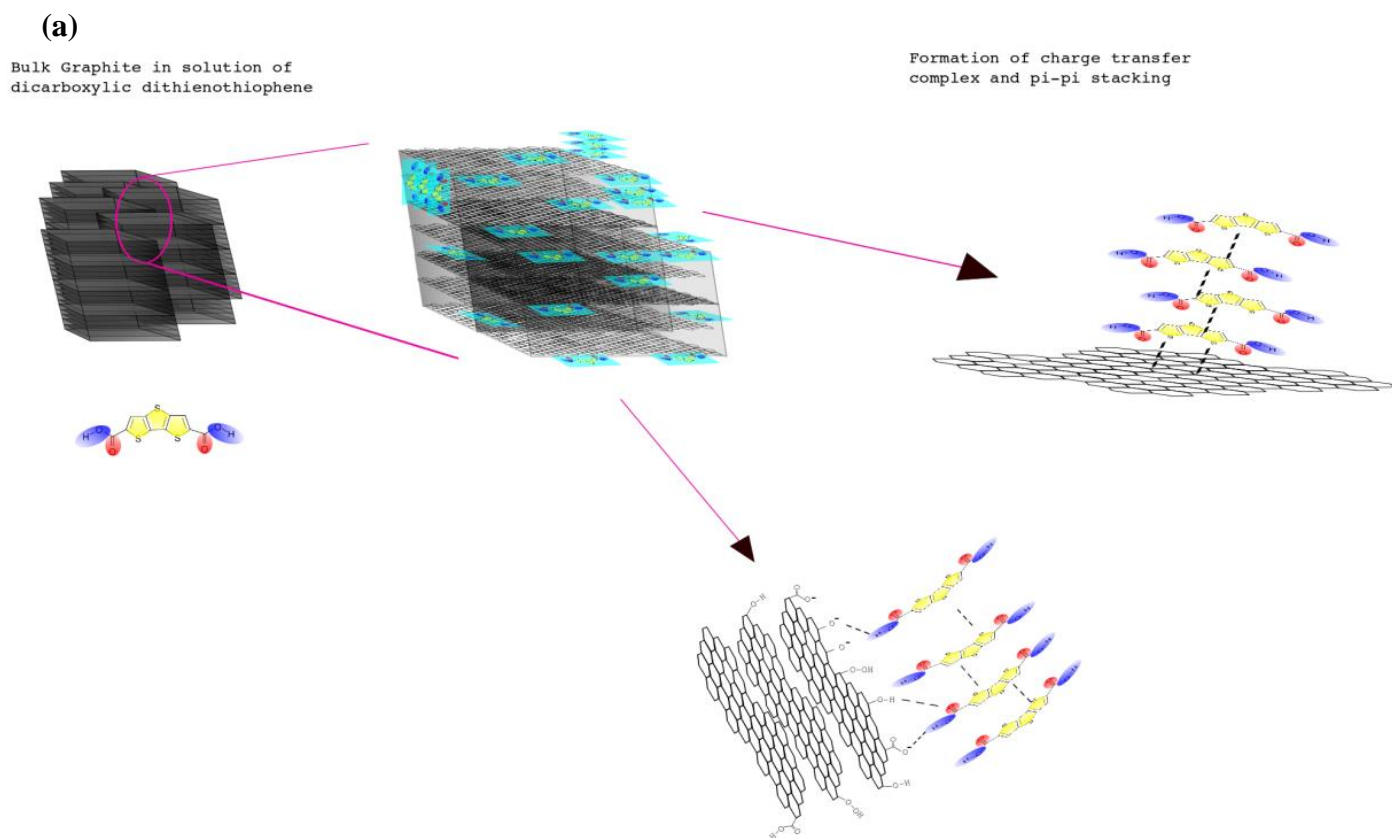
Figure 5.4. (a) Schematic of ChDTT and Graphite interactions, leading to exfoliation of few layer graphene. (b) Absorption spectra of: A) ChDTT in 1,2-DCE, 0.01 mM solution; B) After addition of 2mg expandable carbon to the mother solution (as described in A)) and stirring for 90 min at rt; C) After addition of 20 mg expandable carbon and stirring for 16 h at rt. The spectra were normalized at the baseline. (c) Absorption spectra of: A) Poly(m-henylenevinylene-co-2,5-dioctyloxy-p-phenylenevinylene) (PmPV) in 1,2-DCE, 0.027 mM solution; B) After addition of 2 mg expandable carbon to the mother solution and stirring for 90 min at rt; C) After addition of 20 mg expandable carbon and stirring for 16 h at rt.

In order to characterize the number of layers in our MLG, Raman spectrometry was used to probe single graphene flakes made by ChDTT exfoliation. Graphene flakes were deposited on a silicon wafer with 300 nm thermal oxide by drop casting. The sample was then heated to 400 ˚C in air to remove the surfactant (the choice of removal temperature is discussed below). The significant contrast between SiO_2 background and graphene flakes makes individual thin sheets visible under the 50X optical microscope, and a well aligned 2 μm laser beam with 488 nm wavelength was able to focus on a specific spot.

Graphitic carbon materials display three fingerprints in Raman spectra: the G (Graphite) band at ~ 1580 cm^{-1}, the 2D band (or G' band) at ~2700 cm^{-1}, and the disordered D (defect) band at ~1350 cm^{-1}. The evolution of the Raman spectra from graphite to MLG to single-layer graphene under different laser wavelengths has been intensively studied[62]. For visible Raman spectra (488 nm and 514 nm), both the intensity ratio of the 2D band to G band (I_G/I_{2D}) and the shape of 2D band are layer-sensitive[63-65]. With a 488 nm laser and 300 nm SiO_2, the I_G/I_{2D} ratio has specific value of 2.1, 1.49, 1.14, 0.74, and 0.24 for 5, 4, 3, 2, and 1 layer graphene, respectively.[63] Moreover, the 2D band is a single Lorentzian peak for single layer graphene, while the same peak for double layer graphene deconvolves into 4 Lorentzian peaks, which can be explained by the double-resonant model for graphene[62]. With an increase of layers, at least 6 Lorentzians to fit tri-layer graphene and 3 Lorentzians for MLG over 4 layers must be used[66]. Further increases in layers leads to a significant increase of the relative intensity of the highest energy peak until it reaches the limit of bulk graphite. For graphite itself, the 2D band is assigned to 2 convolved peaks with approximately 1/4 and 1/2 the height of the G peak, respectively.

To characterize the precise thickness of our ultra-large graphene flakes, sheets of ~7μm, 20 μm, and 50 μm diameter were probed with HOPG for comparison. **Figure 5.5A** shows the wide range Raman spectra (1000 cm^{-1} ~ 3000 cm^{-1}) of these flakes. From the intensity ratio (I_G/I_{2D}), we can estimate: (1) the 50 μm flake (I_G/I_{2D}=2.18) is approximately 5 layers, (2) the 20 μm flake (I_G/I_{2D}=1.5) is approximately 4 layers, and (3) the 7μm flake (I_G/I_{2D}=1.16). The 2D band deconvolution shown in **Figure 5.5B** can provide further information about the layer number. For 50 μm and 20 μm flakes, the 2D band shows a typical MLG shape (intensity at higher wave number is slightly stronger) and can be fit with 3 Lorentzian peaks. Again, the intensity of the highest energy peak for the 50 μm flake is stronger than for the 20 μm flake and much weaker than that HOPG. Combined with the I_G/I_{2D} ratio, this demonstrates that they are 5-layer and 4-layer graphene flakes. For the 7 μm flake, the special 2D band shape can only be fit with at least 6 Lorentzians in agreement with the literature.[63] Together with the I_G/I_{2D} ratio, this also coincides with the features of 3 layer graphene. It should be noted that no defect band (~1350 cm^{-1}) can be found in either of these flakes, implying that no structure disorder was introduced during our processes. Multiple flakes were analyzed via Raman Spectroscopy, de-convoluted and a flake size distribution was plotted in **Figure 5.6**. We can estimated that most of the flakes obtained with from ChDTT exfoliation are in between 10-20 microns (long axis dimension) with 4-5 layer and 2-5 microns (long axis dimension) with 3-4 layers. It is important to mention that for ChDTT a larger number of graphene flakes were observed in comparison with the PmPV (on 50 by 50 microns optical microscopy image) with demonstrated that not only larger and few layer graphene are obtained by ChDTT but also ChDTT is an overall better efficienct exfoliation surfactant than PmPV.

(a)

(b)
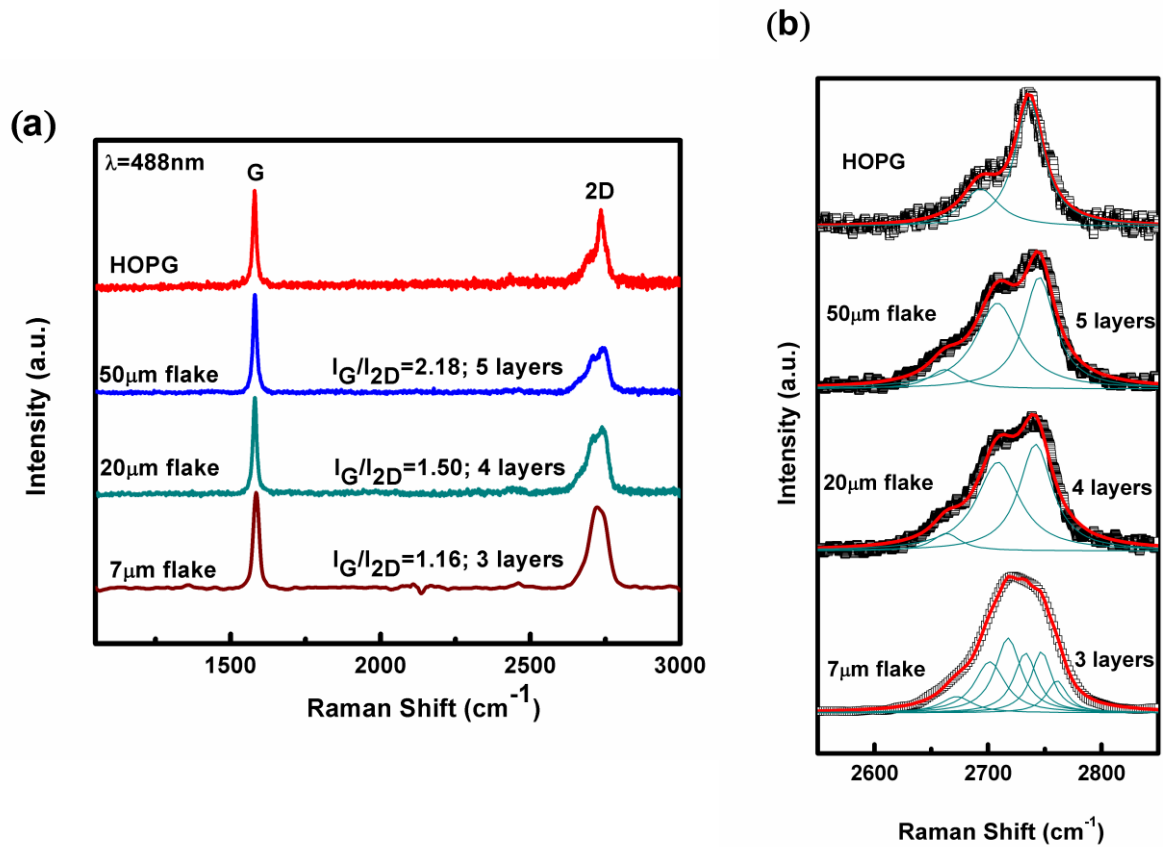
Figure 5.5. Raman spectra for HOPG and ChDTT exfoliated graphene flakes with approximately 50μm, 20μm, and 7μm in size.. b) The deconvolution of 2D band of Raman spectra in (a). Black squares are experimental measurement. Red solid lines are fitting results.
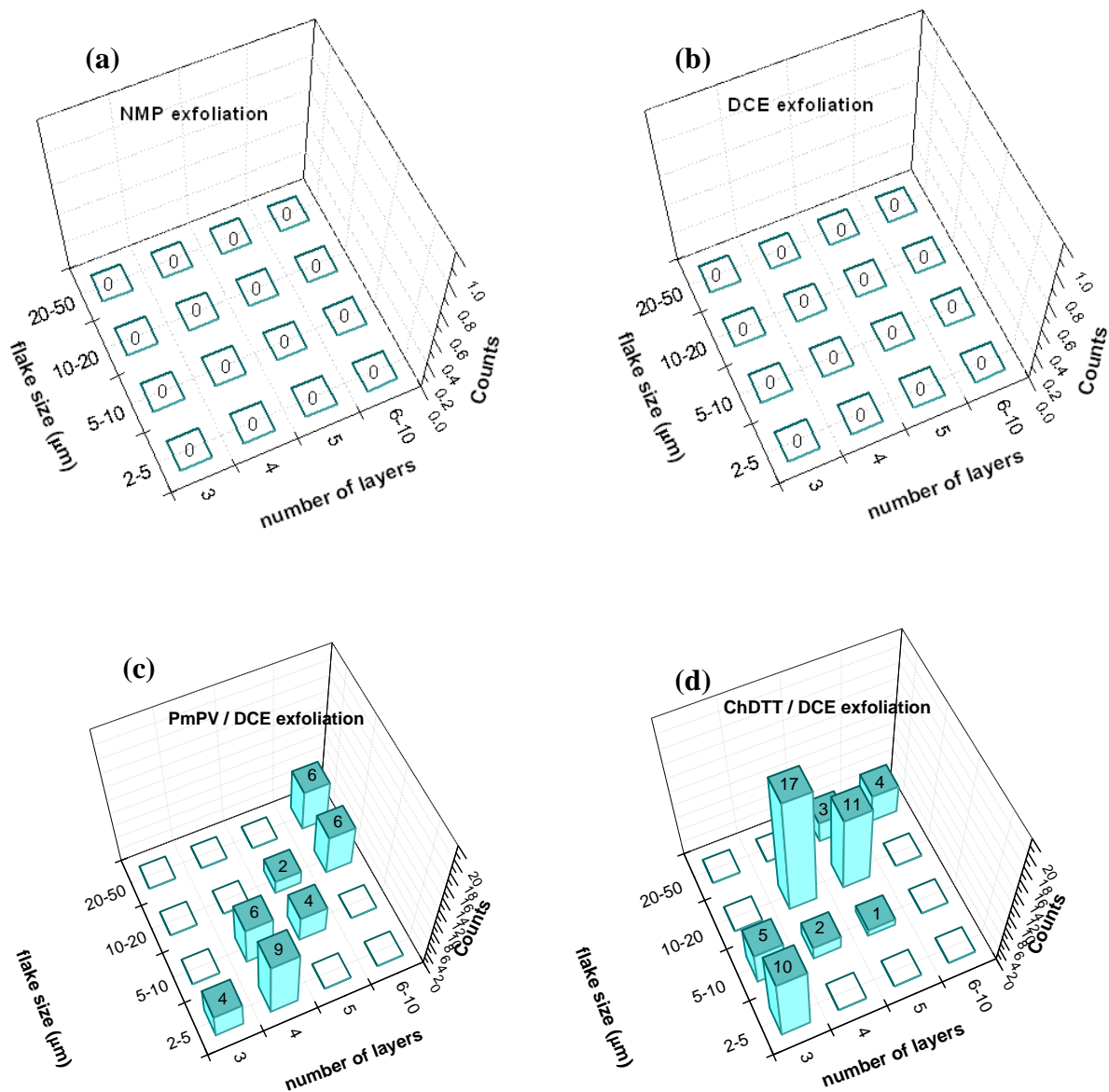
Figure 5.6. Statically yield for exfoliation of graphite by (a) NMP, (b) DCE (c) PmPV/DCE and (d) ChDTT obtained via Raman Spectroscopy of different samples at a 50 by 50 microns magnification. It is important to notice that PmPV yielded less total number of flakes on the same optical microscopy window.

Transmission electron microscopy (TEM) was used to directly investigate the state of graphene flakes remaining dispersed in the solution. One drop of sonicated and centrifuged ChDTT/EG supernatant was applied on a lacy-carbon TEM grid, dried, and analyzed without further treatment. In addition to flakes of several μm, ultra-large graphene sheets (over 20 μm) were frequently found. **Figure 5.7A** and **5.7B** shows a combination of these two types of graphene flakes: one edge of an ultra-large graphene sheet with several small embedded pieces. It is well known that the surface tension of graphene flake preparations is not high enough to support a high aspect ratio (20μm across vs. few atomic layers thick) ,[51] hence folded edges and crumples are always observed in these large flakes. In addition, significant particle formation suggests ChDTT residues, which were not removed. To characterize the thickness and uniformity of ultra-large flakes, small aperture selective-area electron diffraction (SAED) was probed at different area of this sample. **Figure 5.7C** show SAED patterns from two specific spots in **Figure 5.7A** and labeled with Miller-Bravais (hkil) indices. They both clearly demonstrate a single set of hexagonal patterns without superimposed shifting diffraction, indicating no stacked MLG layers with twisting angles at these spots. **Figure 5.7C** shows stronger {2110} peaks, demonstrating multilayer (3-5) with Bernal AB stacking. We note that no border is observed in this type of ultra-large MLG, which suggests that this is a single continuous MLG sheet. It is reported that the ultra-large MLG sheet was always made up of smaller individual graphene flakes with an obvious boundary[51]. We believe this is the first graphene sheet of this size, chemical exfoliated in single piece. Selected HRTEM images of regular flakes are also shown in **Figure 5.7D** and **5.7E** confirming the observation from Raman Spectroscopy and SAED, that our sample is composed of 3-5 layers graphene flakes.
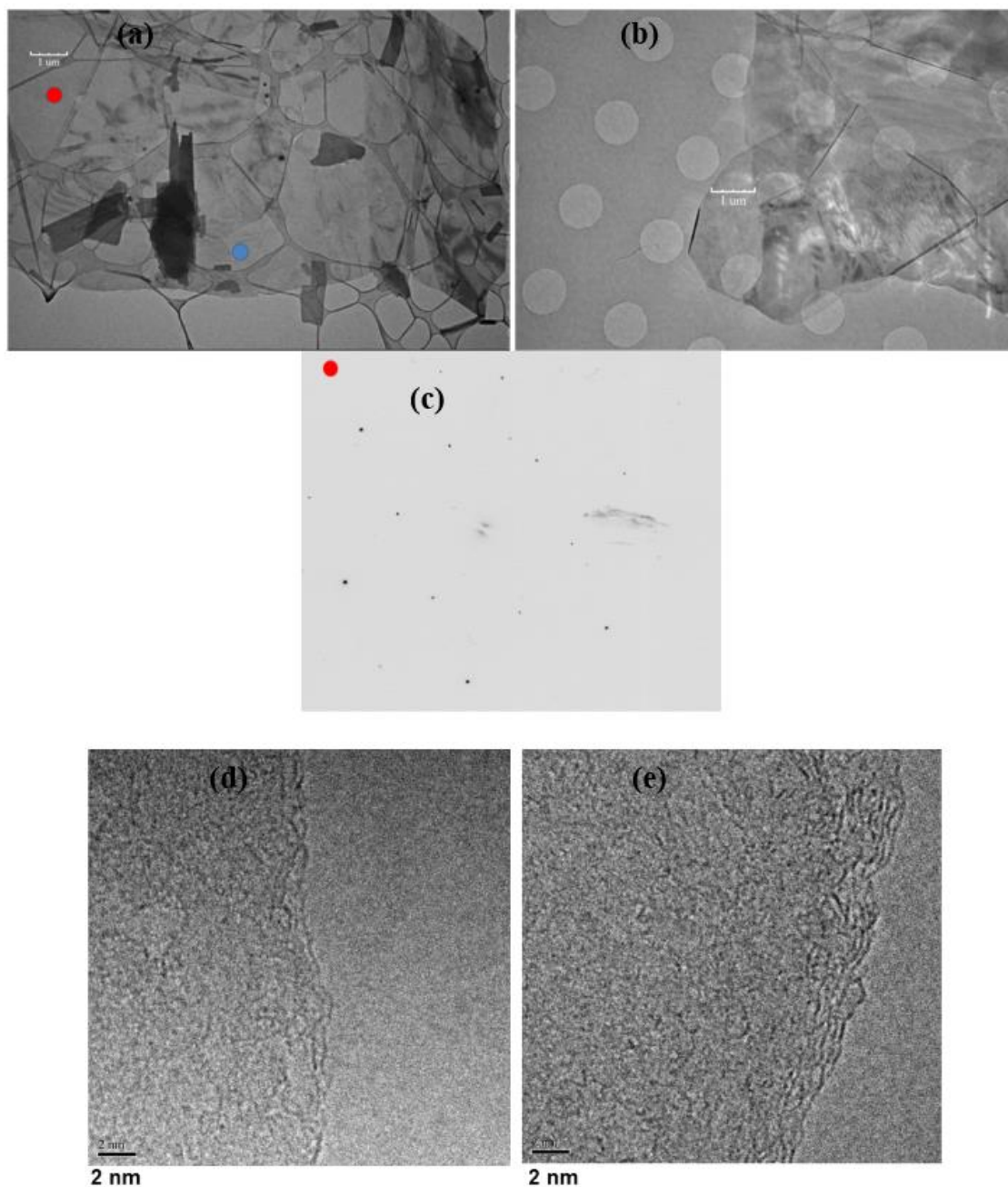
Figure 5.7: a) and b) TEM image of one edge of as-synthesized ultra-large graphene sheet with size > 20μm. The graphene sheet is folded with several small size graphene sheets embedded in it. c) Selective-area electron diffraction (SAED) patterns in (a) show that it contains different number of layers (from single layer to few layers) at different part. d) and e) Selected HRTEM images of regular flakes are also shown in a) and b) showing that our sample is composed mostly of 3-5 layers graphene flakes.

Although it is suggested that macromolecular surfactants, such as PmPV and DNA, interact with CNT and graphene through π–π stacking, thoroughly removing surfactant is still essential due to the sensitivity of electronic properties to surface condition .[67] The challenge relates not only to the surfactant removal, but also the preservation of sp^2 carbon structure. For this reason, Li.et al. has attempted to remove PmPV using a two-step decomposition.[22] First, a PmPV/graphene cast SiO_2 sample was heated to 400°C in air to combust most of the polymer. To avoid the oxidation of graphene, a second-stage combustion with higher temperature (600°C) was performed under ultra-high vacuum.[22]

To realize the high-temperature decomposition behaviors of our ChDTT, thermal gravimetric analysis (TGA) was performed in both air and inert condition (argon) along with PmPV for comparison. **Figure 5.8A** shows the TGA results for both materials under both environments. For the first stage, ChDTT has about 35% remaining mass at 400°C, whereas PmPV retains 58% clearly showing that for PmPV we are left with close to 2/3 of surfactant while for ChDTT only ~1/3 is left on the samples ; furthermore, atomic force microscopy (AFM) images taken after equal thermal treatment still showed significant quantities of PmPV remaining (**Figure 5.9**).

An alternative method is a second-stage thermal treatment, involving high temperature heating under inert gas. The TGA curve of PmPV (in Ar) reveals remaining residue up to 1000°C (Fig. 4a). The AFM image also supports the conclusion that PmPV cannot be removed under these circumstances (**Figure 5.9**). Conversely, ChDTT was totally removed before 700°C. The AFM also shows a clean surface after 800°C rapid thermal processor (RTP) treatment (**Figure 5.9**) in agreement with the TGA data (**Figure 5.8a**).

XPS was performed to examine the carbon 1s (C1s) state (**Figure 5.8**). After deconvolution, it revealed only minor oxidation occurred (**Figure 5.8C**) as compared with the C1s XPS spectrum of the starting material, expanded graphite, shown in **Figure 5.8B** . The difference between starting material and product flakes implies that our process, including ChDTT exfoliation and thermal treatment, did not result in extensive oxidation. The insets of **Figure 5.8C** also show the high-resolution scans at N1s and S2p, (the two elements other than carbon in ChDTT) and no such elements were seen, further supporting the AFM results.

As we seek lower temperature removal techniques, 6M nitric acid was used for 1 hour to chemically decompose the surfactants. It is important to mention that nitric acid is known to effectively oxidize graphene,[68] which makes a reasonable assumption that solution exfoliated graphene flakes should have equal effect.

X-ray photoelectron spectroscopy (XPS) was then used to examine the carbon bonding state of nitric acid treated graphene (**Figure 5.8D**). Typically the graphene carbon 1s (C_{1s}) peak in the XPS spectrum is dominated by C-C bond scattering located at 284.5eV. In addition, 3 minor C1s components are assigned to C-O, C=O, and O=C-OH, with 1.5eV, 2.5eV, and 4eV shifts on the higher energy side[69]. As expected, the C1s XPS spectra of nitric acid treated samples show strong oxidation states in all C-O, C=O, and COOH bonding regimes. Thus the 2D carbon plane was extensively oxygenated, and the flakes tended toward graphene oxides. Nevertheless, AFM images showed a clean surface for ChDTT/graphene, but not for PmVP/graphene (**Figure 5.9**) reinforcing the idea that ChDTT is much easier to remove than PmVP.
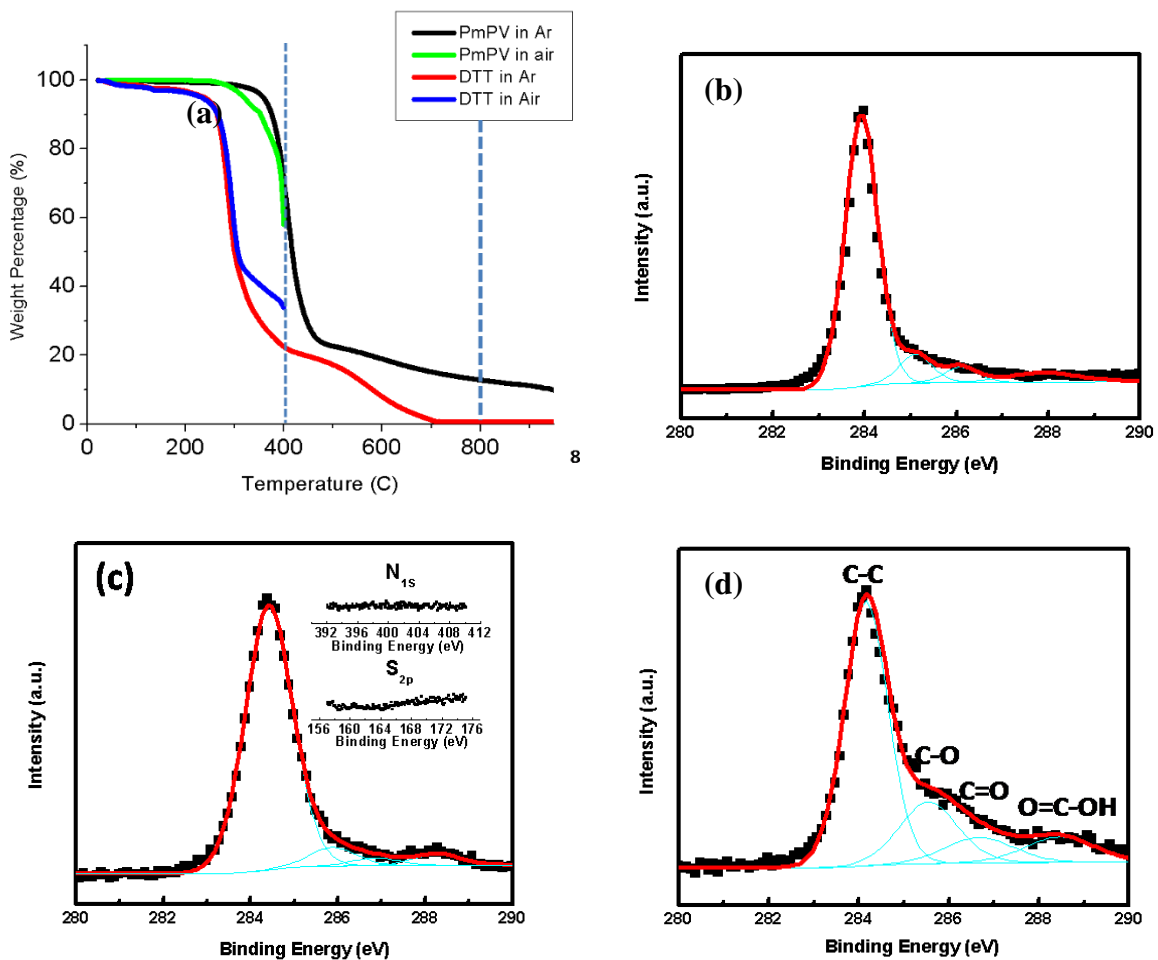
Figure 5.8. (a) TGA results for PmPV and ChDTT under various removal procedures results. **(b)** XPS high-resolution C1s peak for expanded graphite, **(c)** C1s peak for 800 C thermal treatment in forming gas **(d)** XPS high-resolution C1s peak after 6M nitric acid treatment for 1 hr. The Shirley background has been applied. All spectra are fitted with C-C peak at 284.4 eV, C-O peak at 285.9 eV, C=O peak at 286.9 eV, and COOH at 288.4 eV. Inset spectrum in (c) is the N1s and S2p peak
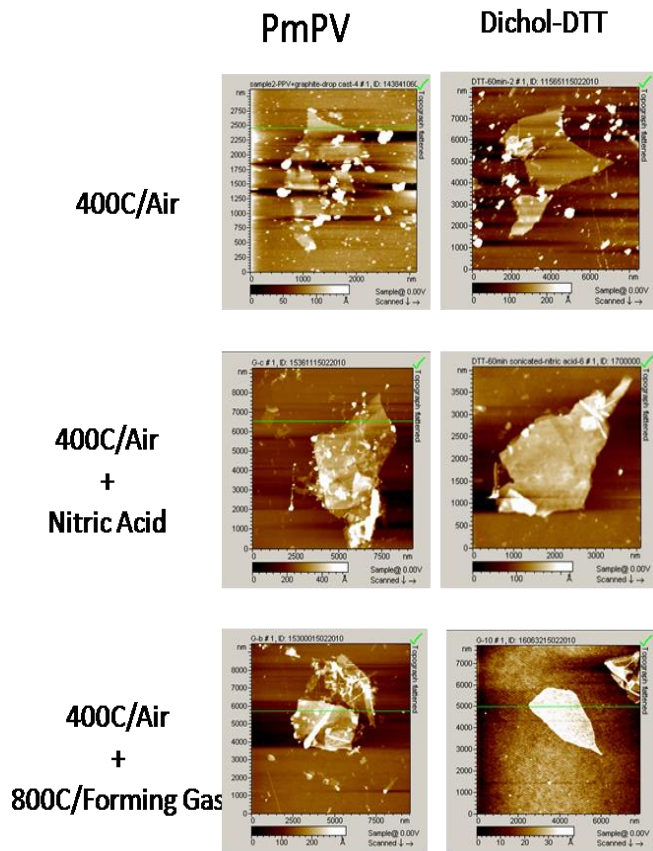
Figure 5.9. AFM analyses of ChDTT and PmPV after residues cleaned up by either thermal treatment or nitric acid treatment.

Electrical transport properties in graphene flake FET devices (**Figure 5.10**) were made in two configurations: (1) before ChDTT surfactant removal (2) after surfactant removal (both samples before measurements were annealed at 200°C under an inert atmosphere to remove any atmospheric dopants).[70] Prior to the surfactant removal, the FET device demonstrated p-doped characteristics in their as-made state, due presumably to adsorbed species (i.e. surfactant) on the graphene surface resulting from the exfoliation process (**Figure 5.10A**).[71-73] As the devices were annealed at 400 °C under air, to remove the DTT surfactant, adsorbed p-dopants were removed, leading to pristine graphene with a charge neutrality point at approximately zero volts (**Figure 5.10B**).[71,74]

The calculated field-effect mobility was $\sim 240 \pm 10$ cm^2/Vs (hole and electron mobility), extracted using equation 4,[75]

$$\mu = L_{ch}g_m/W_{ch}V_{ds}C_{ox} \tag{4}$$

where μ= mobility, L_{ch}= 2000 μm, g_m= dI_D/dV_{GS} , W_{ch}= 50 μm , V_{DS}= 0.1 V and C_g= 115 aF/μm^2. This result indicates that the graphene obtained from exfoliation demonstrated higher mobilities (up to 3 order of magnitude) values compared to graphene oxide reduction[32] since the flakes undergo little degradation.

(a)

(b)
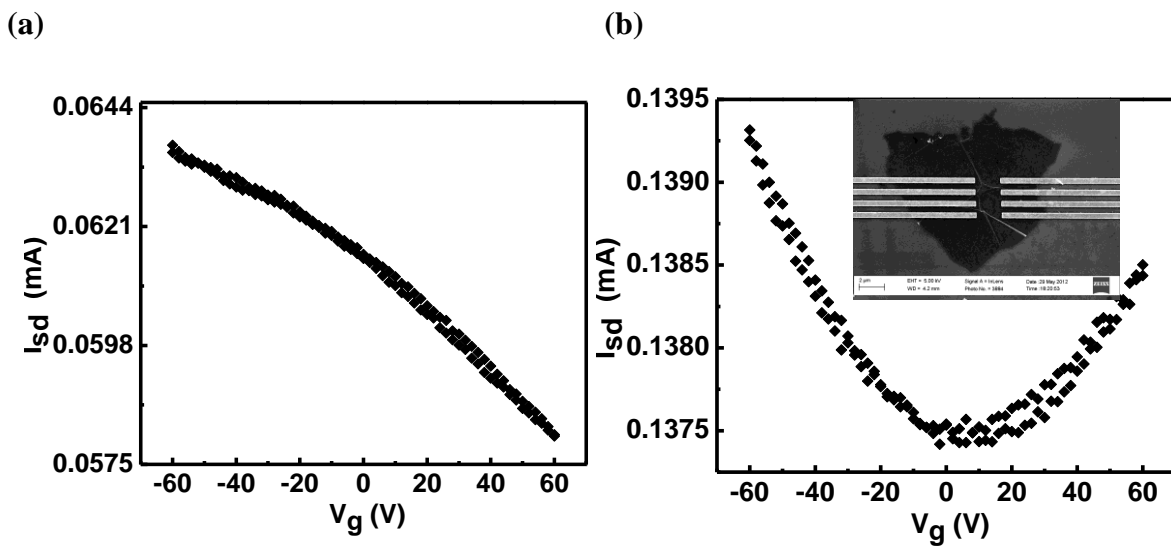
Figure 5.10. Source-drain current versus gate voltage for a graphene flake FET obtained via ChDTT exfoliation (a) before (b) and after surfactant removal. Insert shows the SEM image of the fabricated device.

5.4   Conclusions

A novel macromolecular surfactant dicholesteryldithienothiophene (ChDTT) was synthesized and optimized for use in graphene exfoliation and dispersion. By simple sonication of expandable graphite in solutions containing ChDTT, graphene sheets with sizes exceeding 50 micrometers were observed and characterized by transmission electron microscopy (TEM), atomic force microscopy (AFM), electrical measurements, Raman, and X-ray photoelectron (XPS) spectroscopy. The new surfactant is more efficient than poly(m-phenylenevinylene-co-2,5-dioctyloxy-p-phenylenevinylene) (PmPV), avoids use of polymeric materials, and can be cleanly removed by simple thermal treatment. Using this surfactant, graphene flakes can be extracted directly from HOPG or other graphitic sources without additional chemical, mechanical, or thermal treatment, producing larger flakes of higher quality.

5.5   References

1   Geim, A. K. & Novoselov, K. S. The rise of graphene. *Nature Materials* **6**, 183-191 (2007).

2   Novoselov, K. S. *et al.* A roadmap for graphene. *Nature* **490**, 192-200, doi:10.1038/nature11458 nature11458 [pii] (2012).

3   Novoselov, K. S. *et al.* Electric field effect in atomically thin carbon films. *Science* **306**, 666-669 (2004).

4   Zhang, Y. B., Tan, Y. W., Stormer, H. L. & Kim, P. Experimental observation of the quantum Hall effect and Berry's phase in graphene. *Nature* **438**, 201-204, doi:Doi 10.1038/Nature04235 (2005).

5   Li, X. L., Wang, X. R., Zhang, L., Lee, S. W. & Dai, H. J. Chemically derived, ultrasmooth graphene nanoribbon semiconductors. *Science* **319**, 1229-1232, doi:DOI 10.1126/science.1150878 (2008).

6   Zhang, Y. B. *et al.* Direct observation of a widely tunable bandgap in bilayer graphene. *Nature* **459**, 820-823, doi:Doi 10.1038/Nature08105 (2009).

7   Novoselov, K. S. *et al.* Unconventional quantum Hall effect and Berry's phase of 2 pi in bilayer graphene. *Nature Physics* **2**, 177-180, doi:Doi 10.1038/Nphys245 (2006).

8   Craciun, M. F. *et al.* Trilayer graphene is a semimetal with a gate-tunable band overlap. *Nature Nanotechnology* **4**, 383-388, doi:Doi 10.1038/Nnano.2009.89 (2009).

9   Partoens, B. & Peeters, F. M. From graphene to graphite: Electronic structure around the K point. *Physical Review B* **74**, -, doi:Artn 075404 Doi 10.1103/Physrevb.74.075404 (2006).

10   Peigney, A., Laurent, C., Flahaut, E., Bacsa, R. R. & Rousset, A. Specific surface area of carbon nanotubes and bundles of carbon nanotubes. *Carbon* **39**, 507-514, doi:Doi 10.1016/S0008-6223(00)00155-X (2001).

11   Lee, C., Wei, X. D., Kysar, J. W. & Hone, J. Measurement of the elastic properties and intrinsic strength of monolayer graphene. *Science* **321**, 385-388, doi:DOI 10.1126/science.1157996 (2008).

12   Xu, Z. P. Graphene Nano-Ribbons Under Tension. *J Comput Theor Nanos* **6**, 625-628, doi:DOI 10.1166/jctn.2009.1082 (2009).

13   Novoselov, K. S. *et al.* Electric field effect in atomically thin carbon films. *Science* **306**, 666-669, doi:DOI 10.1126/science.1102896 (2004).

14   Balandin, A. A. *et al.* Superior thermal conductivity of single-layer graphene. *Nano Lett* **8**, 902-907, doi:Doi 10.1021/Nl0731872 (2008).

15   Ilic, B. *et al.* Attogram detection using nanoelectromechanical oscillators. *J Appl Phys* **95**, 3694-3703, doi:Doi 10.1063/1.1650542 (2004).

16   Ghosh, S. *et al.* Extremely high thermal conductivity of graphene: Prospects for thermal management applications in nanoelectronic circuits. *Appl Phys Lett* **92**, doi:Artn 151911 Doi 10.1063/1.2907977 (2008).

17   Sen, D., Novoselov, K. S., Reis, P. M. & Buehler, M. J. Tearing Graphene Sheets From Adhesive Substrates Produces Tapered Nanoribbons. *Small* **6**, 1108-1116, doi:DOI 10.1002/smll.201000097 (2010).

18   Xu, Z. P. & Xue, K. Engineering graphene by oxidation: a first-principles study. *Nanotechnology* **21**, doi:Artn 045704 Doi 10.1088/0957-4484/21/4/045704 (2010).

19   Huang, J. Y. *et al.* In situ observation of graphene sublimation and multi-layer edge reconstructions. *P Natl Acad Sci USA* **106**, 10103-10108, doi:DOI 10.1073/pnas.0905193106 (2009).

20   Gomez-Navarro, C. *et al.* Atomic Structure of Reduced Graphene Oxide. *Nano Lett* **10**, 1144-1148, doi:Doi 10.1021/Nl9031617 (2010).

21   Hernandez, Y. *et al.* High-yield production of graphene by liquid-phase exfoliation of graphite. *Nat Nanotechnol* **3**, 563-568, doi:DOI 10.1038/nnano.2008.215 (2008).

22   Li, X., Wang, X., Zhang, L., Lee, S. & Dai, H. Chemically derived, ultrasmooth graphene nanoribbon semiconductors. *Science* **319**, 1229-1232, doi:10.1126/science.1150878 (2008).

23   Hummers, W. S. & Offeman, R. E. Preparation of Graphitic Oxide. *J Am Chem Soc* **80**, 1339-1339, doi:Doi 10.1021/Ja01539a017 (1958).

24   Kim, K. S. *et al.* Large-scale pattern growth of graphene films for stretchable transparent electrodes. *Nature* **457**, 706-710, doi:Doi 10.1038/Nature07719 (2009).

25   Reina, A. *et al.* Large Area, Few-Layer Graphene Films on Arbitrary Substrates by Chemical Vapor Deposition. *Nano Letters* **9**, 30-35, doi:Doi 10.1021/Nl801827v (2009).

26   Berger, C. *et al.* Electronic confinement and coherence in patterned epitaxial graphene. *Science* **312**, 1191-1196, doi:DOI 10.1126/science.1125925 (2006).

27   Lotya, M. *et al.* Liquid Phase Production of Graphene by Exfoliation of Graphite in Surfactant/Water Solutions. *J Am Chem Soc* **131**, 3611-3620, doi:Doi 10.1021/Ja807449u (2009).

28   Sun, Z. Z., Kohama, S., Zhang, Z. X., Lomeda, J. R. & Tour, J. M. Soluble graphene through edge-selective functionalization. *Nano Research* **3**, 117-125, doi:DOI 10.1007/s12274-010-1016-2 (2010).

29   Dikin, D. A. *et al.* Preparation and characterization of graphene oxide paper. *Nature* **448**, 457-460, doi:Doi 10.1038/Nature06016 (2007).

30   Li, D., Muller, M. B., Gilje, S., Kaner, R. B. & Wallace, G. G. Processable aqueous dispersions of graphene nanosheets. *Nature Nanotechnology* **3**, 101-105, doi:DOI 10.1038/nnano.2007.451 (2008).

31   Gomez-Navarro, C. *et al.* Electronic transport properties of individual chemically reduced graphene oxide sheets. *Nano Lett* **7**, 3499-3503, doi:Doi 10.1021/Nl072090c (2007).

32   Eda, G., Fanchini, G. & Chhowalla, M. Large-area ultrathin films of reduced graphene oxide as a transparent and flexible electronic material. *Nat Nano* **3**, 270-274, doi:http://www.nature.com/nnano/journal/v3/n5/suppinfo/nnano.2008.83_S1.html (2008).

33   Ruoff, R. Calling all chemists. *Nat Nanotechnol* **3**, 10-11, doi:DOI 10.1038/nnano.2007.432 (2008).

34   Sun, Z. Z., James, D. K. & Tour, J. M. Graphene Chemistry: Synthesis and Manipulation. *J Phys Chem Lett* **2**, 2425-2432, doi:Doi 10.1021/Jz201000a (2011).

35   Tung, V. C. *et al.* Low-Temperature Solution Processing of Graphene-Carbon Nanotube Hybrid Materials for High-Performance Transparent Conductors. *Nano Lett* **9**, 1949-1955, doi:Doi 10.1021/Nl9001525 (2009).

36   Jang, J. Y., Jeong, H. M. & Kim, B. K. Compatibilizing Effect of Graphite Oxide in Graphene/PMMA Nanocomposites. *Macromol Res* **17**, 626-628 (2009).

37   Geim, A. K. & Novoselov, K. S. The rise of graphene. *Nat Mater* **6**, 183-191, doi:10.1038/nmat1849 (2007).

38   Du, X., Skachko, I., Barker, A. & Andrei, E. Y. Approaching ballistic transport in suspended graphene. *Nat Nanotechnol* **3**, 491-495, doi:10.1038/nnano.2008.199 (2008).

39   Blake, P. *et al.* Graphene-based liquid crystal device. *Nano Letters* **8**, 1704-1708, doi:Doi 10.1021/Nl080649i (2008).

40   Bourlinos, A. B., Georgakilas, V., Zboril, R., Steriotis, T. A. & Stubos, A. K. Liquid-Phase Exfoliation of Graphite Towards Solubilized Graphenes. *Small* **5**, 1841-1845, doi:DOI 10.1002/smll.200900242 (2009).

41   Coleman, Lotya & others. High-Concentration Surfactant-Stabilized Graphene Dispersions. *ACS Nano* **4** (2010).

42   Liu, Guo & others. Water dispersible graphene noncovalently functionalized with tryptophan and its poly(vinyl alcohol) nanocomposite. *Composites: Part B* **42** (2011).

43   Coleman, Lotya & others. Liquid Phase Production of Graphene by Exfoliation of Graphite in Surfactant/Water Solutions. *Journal of the American Chemical Society* **131** (2009).

44   Strano, Blankschtein & others. Bi- and trilayer graphene solutions. *Nature Nanotechnology* **6** (2011).

45   Hersam & Green. Solution Phase Production of Graphene with Controlled Thickness via Density Differentiation. *Nano Letters* **9** (2009).

46   Ger, Pu & others. Dispersion of graphene in aqueous solutions with different types of surfactants and the production of graphene films by spray or drop coating. *Journal of the Taiwan Institute of Chemical Engineers* **43** (2012).

47   Ger, Pu & others. Production of few-layer graphene by supercritical CO2 exfoliation of graphite. *Materials Letters* **63** (2009).

48   Ferrari, Hasan & others. Solution-phase esfoliation of graphite for ultrafast photonics. *Physica Status Solidi B: Basic Solid State Physics* **247** (2010).

49   Hou, Hao, Qian & Zhang. Aqueous dispersions of TCNQ-anion-stabilized graphene sheets. *Chem. Comm.*, 6576 (2008).

50   Green, A. A. & Hersam, M. C. Solution Phase Production of Graphene with Controlled Thickness via Density Differentiation. *Nano Letters* **9**, 4031-4036, doi:Doi 10.1021/Nl902200b (2009).

51   Janowska, I. *et al.* Microwave synthesis of large few-layer graphene sheets in aqueous solution of ammonia. *Nano Research* **3**, 126-137, doi:DOI 10.1007/s12274-010-1017-1 (2010).

52   Bourlinos, A. B. *et al.* Aqueous-phase exfoliation of graphite in the presence of polyvinylpyrrolidone for the production of water-soluble graphenes. *Solid State Communications* **149**, 2172-2176, doi:DOI 10.1016/j.ssc.2009.09.018 (2009).

53   Li, X. L. *et al.* Highly conducting graphene sheets and Langmuir-Blodgett films. *Nature Nanotechnology* **3**, 538-542, doi:DOI 10.1038/nnano.2008.210 (2008).

54   Vijayaraghavan, A. *et al.* Dielectrophoretic Assembly of High-Density Arrays of Individual Graphene Devices for Rapid Screening. *Acs Nano* **3**, 1729-1734, doi:Doi 10.1021/Nn900288d (2009).

55   Coleman, J. N. Liquid-Phase Exfoliation of Nanotubes and Graphene. *Advanced Functional Materials* **19**, 3680-3695, doi:DOI 10.1002/adfm.200901640 (2009).

56   Dalton, A. B. *et al.* Selective interaction of a semiconjugated organic polymer with single-wall nanotubes. *Journal of Physical Chemistry B* **104**, 10012-10016, doi:Doi 10.1021/Jp002857o (2000).

57   Murphy, R. *et al.* High-yield, nondestructive purification and quantification method for multiwalled carbon nanotubes. *Journal of Physical Chemistry B* **106**, 3087-3091, doi:Doi 10.1021/Jp0132836 (2002).

58   Cadek, M. *et al.* Reinforcement of polymers with carbon nanotubes: The role of nanotube surface area. *Nano Letters* **4**, 353-356, doi:Doi 10.1021/Nl035009o (2004).

59   Zheng, M. *et al.* Structure-based carbon nanotube sorting by sequence-dependent DNA assembly. *Science* **302**, 1545-1548 (2003).

60   Nakashima, N., Okuzono, S., Murakami, H., Nakai, T. & Yoshikawa, K. DNA dissolves single-walled carbon nanotubes in water. *Chemistry Letters* **32**, 456-457, doi:Doi 10.1246/Cl.2003.456 (2003).

61   Gigliotti, B., Sakizzie, B., Bethune, D. S., Shelby, R. M. & Cha, J. N. Sequence-independent helical wrapping of singles-walled carbon nanotubes by long genomic DNA. *Nano Letters* **6**, 159-164, doi:Doi 10.1021/Nl0518775 (2006).

62   Ferrari, A. C. *et al.* Raman spectrum of graphene and graphene layers. *Physical Review Letters* **97**, -, doi:Artn 187401 Doi 10.1103/Physrevlett.97.187401 (2006).

63   Calizo, I., Bejenari, I., Rahman, M., Liu, G. & Balandin, A. A. Ultraviolet Raman microscopy of single and multilayer graphene. *Journal of Applied Physics* **106**, -, doi:Artn 043509 Doi 10.1063/1.3197065 (2009).

64   Calizo, I., Balandin, A. A., Bao, W., Miao, F. & Lau, C. N. Temperature dependence of the Raman spectra of graphene and graphene multilayers. *Nano Letters* **7**, 2645-2649, doi:Doi 10.1021/Nl071033g (2007).

65   Haluska, M. *et al.* Investigation of the shift of Raman modes of graphene flakes. *Physica Status Solidi B-Basic Solid State Physics* **244**, 4143-4146, doi:DOI 10.1002/pssb.200776202 (2007).

66   Malard, L. M., Pimenta, M. A., Dresselhaus, G. & Dresselhaus, M. S. Raman spectroscopy in graphene. *Phys Rep* **473**, 51-87, doi:DOI 10.1016/j.physrep.2009.02.003 (2009).

67   Dong, X. C., Shi, Y. M., Chen, P., Ling, Q. D. & Huang, W. Aromatic Molecules Doping in Single-Layer Graphene Probed by Raman Spectroscopy and

Electrostatic Force Microscopy. *Jpn J Appl Phys* **49**, doi:Artn 01ah04 Doi 10.1143/Jjap.49.01ah04 (2010).

68   Kasry, A., Kuroda, M. A., Martyna, G. J., Tulevski, G. S. & Bol, A. A. Chemical doping of large-area stacked graphene films for use as transparent, conducting electrodes. *Acs Nano* **4**, 3839-3844, doi:10.1021/nn100508g (2010).

69   Yang, D. *et al.* Chemical analysis of graphene oxide films after heat and chemical treatments by X-ray photoelectron and Micro-Raman spectroscopy. *Carbon* **47**, 145-152, doi:DOI 10.1016/j.carbon.2008.09.045 (2009).

70   Sojoudi, H., Baltazar, J., Henderson, C. & Graham, S. Impact of post-growth thermal annealing and environmental exposure on the unintentional doping of CVD graphene films. *J Vac Sci Technol B* **30**, doi:Artn 041213 Doi 10.1116/1.4731472 (2012).

71   Szafranek, B. N., Schall, D., Otto, M., Neumaier, D. & Kurz, H. High On/Off Ratios in Bilayer Graphene Field Effect Transistors Realized by Surface Dopants. *Nano Lett* **11**, 2640-2643, doi:10.1021/nl200631m (2011).

72   Novoselov, K. S. *et al.* fake. *Science* **306**, 666-669, doi:10.1126/science.1102896 (2004).

73   Novoselov, K. S. *et al.* Detection of individual gas molecules adsorbed on graphene. *Nat Mater* **6**, 652-655, doi:Doi 10.1038/Nmat1967 (2007).

74   Shen, Z. X. *et al.* The effect of vacuum annealing on graphene. *Journal of Raman Spectroscopy* **41**, 479-483, doi:Doi 10.1002/Jrs.2485 (2010).

75   Schwierz, F. Graphene transistors. *Nat Nano* **5**, 487-496 (2010).

CHAPTER 6

EXPLORING SURFACE DIELS-ALDER ADDUCTS ON SILICA AS A CONTROLLABLE CARBON PRECURSOR FOR PRISTINE GRAPHENE

A dienophile-modified SiO_2 surface served as a platform for Diels-Alder mediated attachment of anthracene and 9,9'-bianthryl. The resulting monolayers were investigated by x-ray photoelectron spectroscopy (XPS) and directly used as precursor for graphene, as verified by Raman spectroscopy. 9,9'-bianthryl adduct yield the best quality graphene, which is attributed to the higher carbon precursor availability and compared to anthracene adduct and the maleimide dienophile. This study opens the door towards rationale direct growth of graphene on surface reaction mediated by copper catalyst.

6.1   Introduction

The electronic properties of graphene continue to spur applications in electronics, chemical sensors, biological sensors, filters, and nanocomposites.[1-5] Chemical vapour deposition (CVD) of graphene has become one of the most studied growth technique with methane as the dominant feedstock.[6-8] There has been multiple studies done on copper foil/nickel using alternative carbon precursors,[9-13] however there has been no success using evaporated copper on a dielectric surface such as SiO_2 (which is a critical component for a variety of semiconductor devices) with covalently attached monolayers or other attached chemical moieties.[12] One of the reasons for such lack of success is the fact that contrary to nickel where the growth of graphene occurs from carbon dissolution,[7] in copper the growth is mainly via surface reaction.[7] Hence, carefully designed precursors as well as carbon delivery methods have to be investigated. Furthermore, the ability to assemble polyaromatic hydrocarbons (PAHs) monolayers on surfaces and further processing such prefabricated moieties into electronic materials (such as graphene) is thus a tantalizing prospect which we now implement in the context of a Diels-Alder reaction.

A great deal of research has already been conducted on attachment of aromatics on surfaces by capturing dienes with suitable dienophile, and vice-versa.[14-22] However, previous surface modifications relied on multistep syntheses in order to modify the dienes with the desired anchoring groups, as well as to assure the formation of highly ordered arrangements on a surface.[23,24] To date, there have been no efforts towards the conversion of Diels-Alder adducts into graphene. Previous studies have focused on conversion of transferred carbon nano-membranes obtained from cross-linked aromatic self-assembled monolayers to produce nano-crystalline graphene,[25] an imperfect source for graphitic

applications. We report here the use of organized organic molecular systems, which can undergo consolidation leading to electronically active materials. The Diels-Alder (DA) reaction is a workhorse for such transformations, since the forward 4+2 condensation is chemically reversible and occurs with high yields under relatively mild conditions. One clear advantage of using Diels-Alder adducts is avoiding flammable carbon sources such as methane;[6] furthermore, since we can easily choose which PAH to use, we have a control on the amount of carbon used for graphitization.[26] We selected anthracene and Bianthryl since both aromatic compounds are very soluble in common solvents, well studied dienes and allows us to easily double the amount of carbon available in the surface, enabling an adjustable source for release and control of the carbon precursor and thus, the synthesized graphene layers.[26]

6.2   Experimental Section

For Our approach is illustrated by Scheme 1: maleimide was chosen as the dienophile core of our scheme since it can be easily functionalized, including introduction of functional groups to allow for attachment to various metals (a thiol terminated maleimide was synthesized and is currently being investigated) and silicon. It produces DA adducts with various dienes, including PAHs, in high chemical yields and with good desired stability.

Although the goal of this work was the surface Diels-Alder reaction of maleimide and anthracene/ bianthryl, a model solution reaction between N-dodecylmaleimide (maleimide-C12) and bianthryl /anthracene was performed in preparative scale and the resulting Diels-Alder adduct carefully analyzed. A reaction between excess N-

dodecylmaleimide (maleimide-C12) and anthracene produced mono Diels-Alder adducts, with central benzene ring cycloaddition as characterized by NMR (see S.I). Unlike anthracene, 9,9'-bianthryl undergoes peripheral rather than central benzene ring cycloaddition, producing a quantitative mixture of mono and bis Diels-Alder adducts (see S.I).

Both the anthracene reaction product and the bis adduct product from the Bianthryl were subjected to thermogravimetric analysis (TGA) which revealed molecular integrity up to 250 °C before the first onset of mass loss (**Figure 6.1**). For the anthracene Diels-Alder adduct, 100% mass loss is observe, beginning at approximately 250 °C. This loss corresponds to the sublimation of the whole adduct, therefore no reverse Diels-Alder (rDA) reaction is observed. For Bianthryl Diels-Alder adduct, the 60% mass loss that begins at approximately 250 °C corresponds to a loss of two molecules of N-dodecylmaleimide, consistent with the reverse Diels-Alder (rDA) reaction. A second distinct mass loss occurs at an onset temperature of ca. 320 °C, and corresponds to sublimation of 9,9'-bianthryl, as supported by a separate TGA analysis of pure 9,9'-bianthryl. It is worth noting that the mass loss in the case of the DA adduct was incomplete and the remaining residue, 3-4% of the initial mass, suggests that high molecular weight, non-volatile carbonaceous species have formed. Such high molecular weight species are presumably the result of cross-condensation of reactive species arising from the retro Diels-Alder process. We note, parenthetically, that similar condensation products were observed during pyrolysis of pentacene.[27-30]
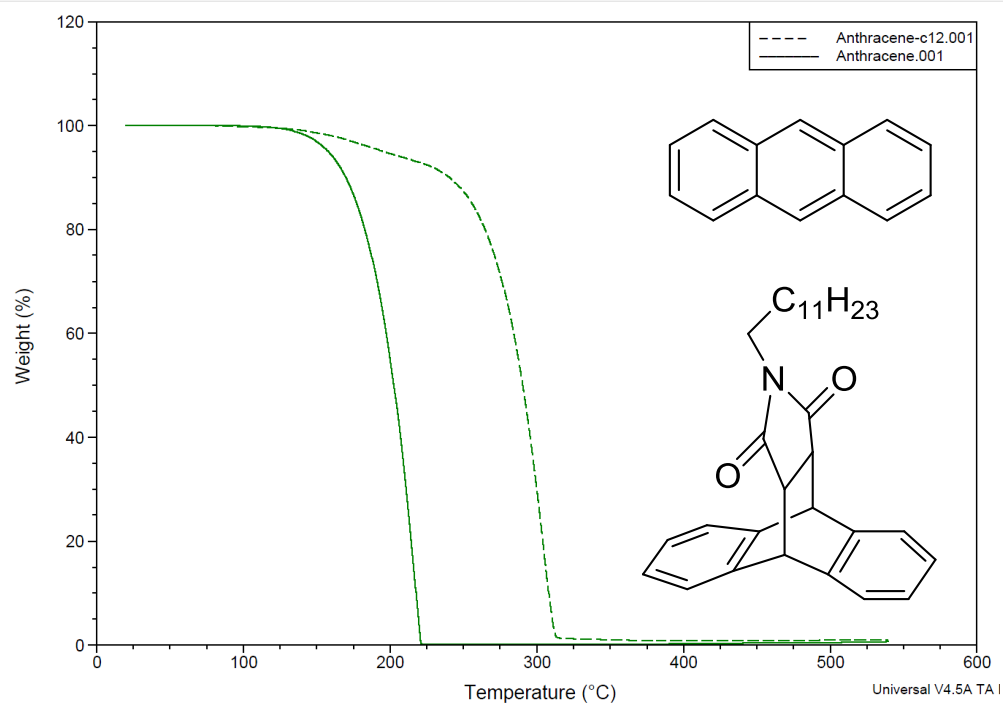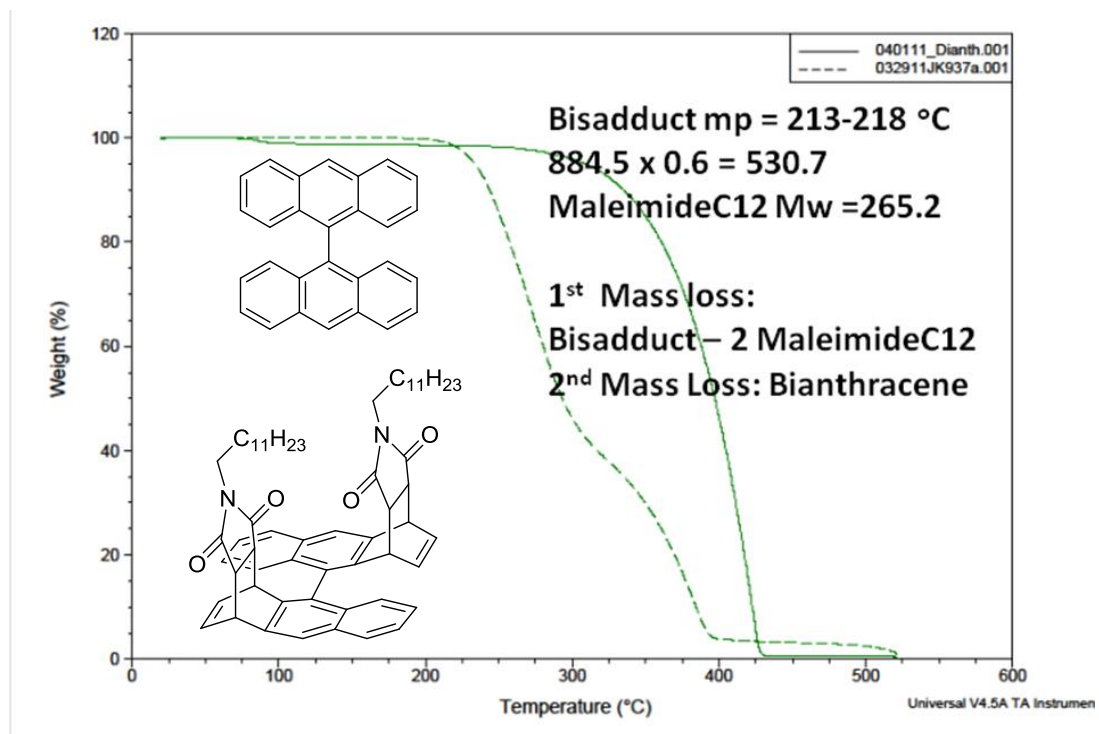
Figure 6.1: 1- Thermogravimetric analysis (TGA) for the Diels-Alder bisadduct of (Top) 9,9'-Bianthryl and Maleimide-C12 and (Bottom) Anthracene and Maleimide-C12. Legend -Broken line: the adduct, Solid line: 9,9'-bianthryl/anthracene.

The synthesis and surface reaction of 3-(triethoxysilyl)propyl maleimide (MPES) is illustrated in Scheme 1. The surface anchoring 3-(triethoxysilyl)propylmaleimide was synthesized according to the literature[31,32] from 3-(triethoxysilyl)propylamine and maleic anhydride in the presence of $ZnBr_2$ and hexamethyldisilazane. For monolayer fabrication, a silicon wafer was cleaned and pre-treated by UV ozone in order to produce a hydroxyl-terminated surface, immediately followed by immersion of the substrate in a 1% (v/v) solution of MPES in anhydrous toluene for three hours. The substrate was removed from solution, sonicated in pure toluene, and dried under flowing nitrogen. The deposition of the covalent attached monolayers was confirmed by contact angle measurements using a VCA 2000 goniometry system. The MPES-coated surface had a contact angle with deionised (DI) water of ca. 45° as compared to <10° contact angle measured immediately after ozone treatment of native SiO_2 on Si. In order to perform the cycloaddition, the MPES-coated substrates were immersed in a solution of either anthracene or 9,9'-bianthryl in xylene for 24 hours at 140 °C, cleaned by thorough rinsing, and characterized by X-ray photoelectron spectroscopy (XPS).
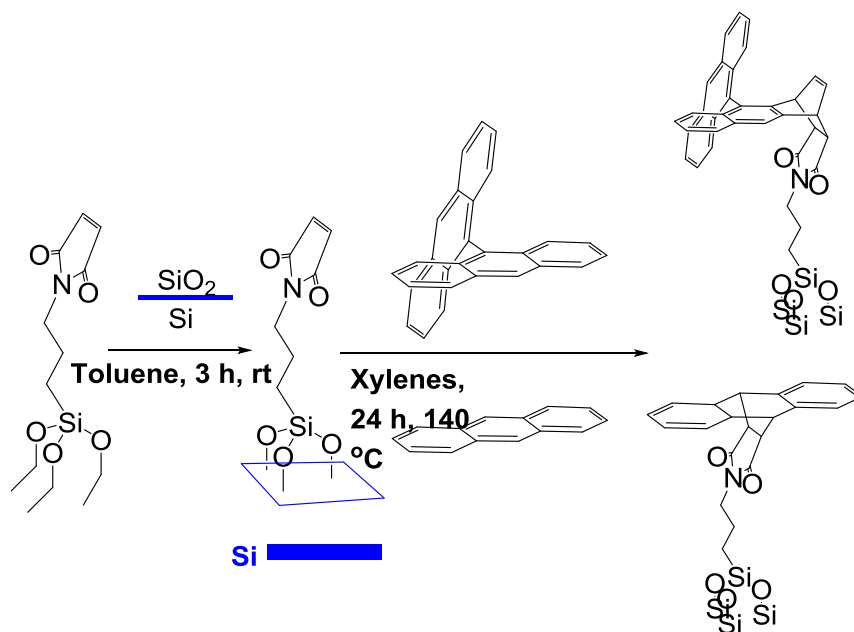
Scheme 1. (a) Reaction scheme of a silicon oxide surface with maleimide and 9,9'-bianthryl/anthracene attachment via [4+2] cycloaddition.

6.3   Results and Discussion

Figure 6.2A shows XPS survey spectra for: (1) control SiO_2 substrate (labelled 'SiO$_2$'), (2) the MPES-treated substrate containing the maleimide layer (labelled 'MPES'), (3) anthracene treated MPES substrate (labelled 'A-MPES') and (4) 9,9'-bianthryl treated MPES substrate (labelled 'B-MPES'). The presence of the N1s peak in **Figure 6.2A** for the MPES, A-MPES and the B-MPES samples (and lack of N1s peak in the control sample) supports the conclusion that the MPES moieties were successfully produced in the SiO_2 substrate. The N1s high-resolution spectrum (**Appendix 1- Figure A5**) for regions containing MPES, A-MPES and B-MPES was well described by a fit using a single Gaussian peak centered at 401.9 eV which is commonly assigned to the amide N1s in maleimide.[14,33] **Figure 6.2B** shows the chemical shifts in the high resolution C1s spectra for an MPES-coated, an A-MPES-coated and a B-MPES-coated SiO_2 substrate. We observe that for the MPES sample the C1s peak can be fit with two Gaussian peaks centered at 286 eV (representing ~77% of the total C1s peak area) and 289 eV (representing ~23% of the total C1s peak area), which we assign to carbons involved in C-C and N-C=O bonds, respectively, confirming the presence of the maleimide on the surface.[20] For the A-MPES, we can again fit with two Gaussian peaks centered at 286 eV (representing ~90% of the total C1s peak area) and 289 eV (representing ~10% of the total C1s peak area), which we assign to carbons involved in C-C and N-C=O bonds respectively, clearly indicating an increase in C-C bonding, indicative of anthracene attachment. B-MPES sample, the C1s peak can be reasonably well fit with a single Gaussian peak centered at 286 eV, which we assign to carbons involved in C-C bonds. This may be somewhat surprising at first glance, given the fact that the maleimide moiety still remains on the surface, and in fact a small
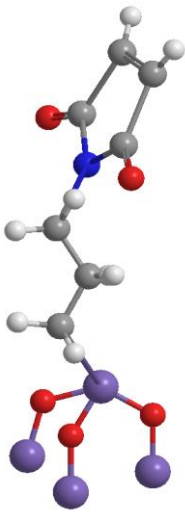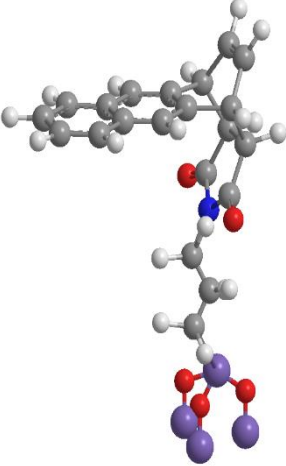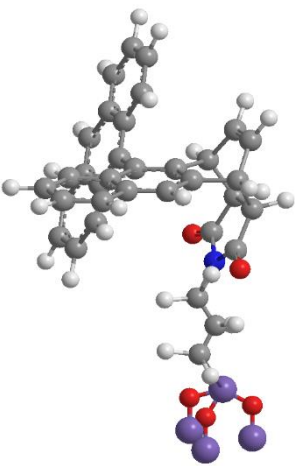
shoulder peak can be assigned at 289 eV, corresponding to carbons in the maleimide N-C=O bond, to improve the peak fit slightly. The overwhelming magnitude though of the carbon in C-C bonds as compared to N-C=O bonds supports the formation of the 9,9'-bianthryl adduct on the maleimide monolayer and its presence on the surface compared with the MPES and A-MPES samples.

Table 6.1 shows the C/N ratio expected and the obtained experimental via XPS analyses for each samples. The expected ratios were 7:1, 21:1 and 35:1, while the experimental values were 7.44± 1, 17.9±4 and 36.2± 7 for MPES, A-MPES and B-MPES respectively. This clearly shows that all the maleimide sites on the surface reacted with our PAH's and the Bianthryl sample provides a higher amount of carbon available on the surface compared to MPES and A-MPES samples (Appendix 1 has total percentage amount for each element on each sample).

A

B
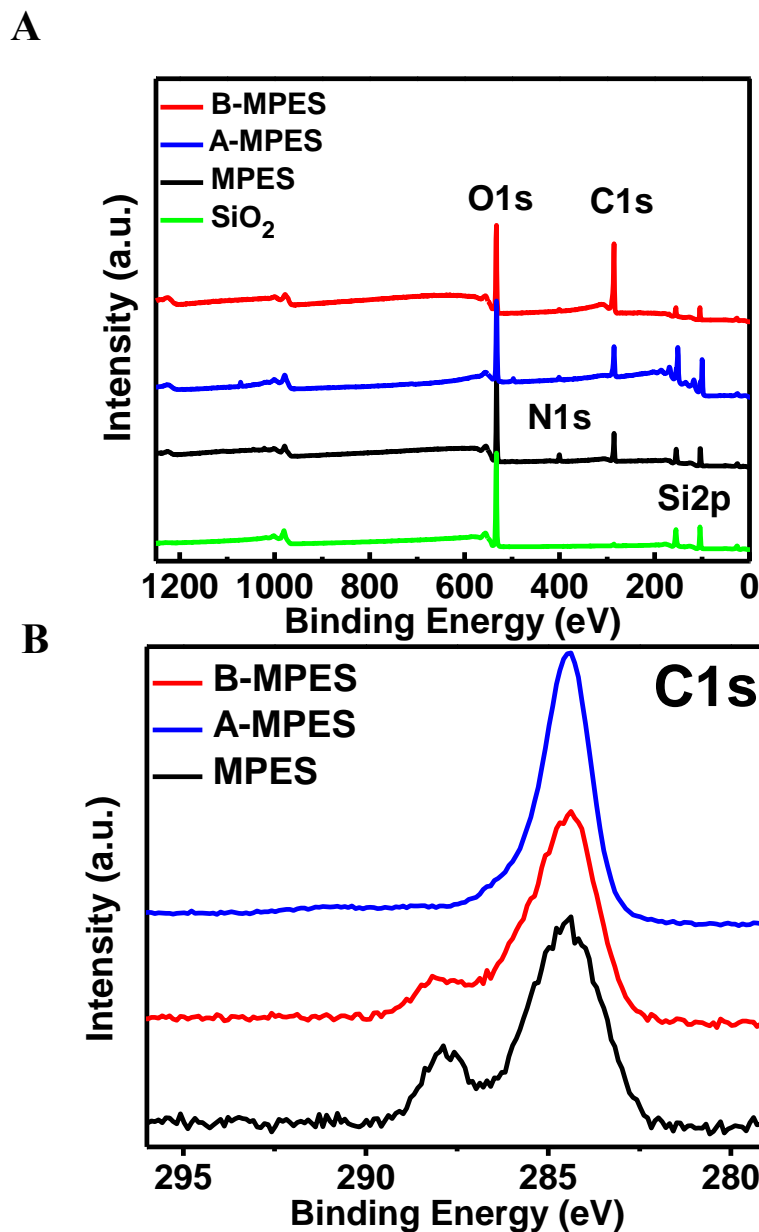
Figure 6.2. (a) XPS spectra representing survey scan for three types of samples: (green line) graphene on SiO₂, (black line) MPES layer covalently attached to SiO₂, (blue line) Anthracene/MPES DA adduct and (red line) 9,9'-Bianthryl/MPES DA adduct coated SiO₂. (b) High resolution XPS spectra for C1s for (black line) MPES layer covalently attached to SiO₂, (blue line) Anthracene/MPES DA adduct and (red line) 9,9'-Bianthryl/MPES DA adduct coated SiO₂.(All the data was normalized to the highest intensity).

Table 6.1 C/N ratio expected and obtained experimental via XPS analyses for: MPES, A-MPES and B-MPES

Structure			
	MPES	A-MPES	B-MPES

	Expected	Experimental	Expected	Experimental	Expected	Experimental
C/N At. %	7:1	7.4:1	21:1	21.3:1	35:1	36.2:1

Next, conversion of such adducts into 2-D sheets of graphene was investigated: the MPES, A-MPES and B-MPES-coated substrates were coated with Cu (300 nm) using an electron beam evaporator, followed by annealing in a tube furnace in argon/hydrogen environment at 1000 °C (see Appendix 1). It is important to mention that Cu was selected because of its ability to promote catalytic surface graphitization, instead of

We investigated the quality of the graphene layers obtained by such means by examining the D, G, and 2D bands and their positions in the Raman spectra. The signals corresponding to the D (~1300 cm^{-1}), G (~1590 cm^{-1}), and 2D (~2700 cm^{-1}) Raman frequencies in the obtained graphene were fit with Gauss-Lorentzian curve fits to determine their peak position, line width, and intensity. For the MPES and the A-MPES samples, the

Raman collected at the SiO$_2$ surface of where the Cu dewetted, we observed a D and G band as well as a broad 2D band (3), characteristic of defective graphene[11,34] which is consistent with what has been observed for graphitization of other materials to graphene on silicon oxide surfaces.[25,35] and no graphitic signal were observed on the surface of the dewetted copper. For the B-MPES-grown at 1000 °C, the Raman collected at the SiO$_2$ surface of where the Cu dewetted, we observed a D and G band as well as a broad 2D band (3), characteristic of defective graphene,[11,34] however on the surface of the dewetted copper, graphene films showed prominent graphitic (G and 2D) bands with no detectable defect peak (D) as well as the G* peak at (~2450 cm^{-1})[36] (**Figure 6.3**). The high 2D over G band intensity ratio of 2.67 and a low full width at half maximum (FWHM) of the 2D band at ca. 36 cm^{-1} are indicative of a monolayer graphene film[6] (**Appendix 1- Figure A6**). Furthermore, by varying the temperature to 900 °C no copper evaporation occured and no signals corresponding to the D (~1300 cm^{-1}), G (~1590 cm^{-1}), and 2D (~2700 cm^{-1}) Raman frequencies were observed. These results indicate that during the graphitization process, de-wetting and evaporation of Cu took place due to the high temperature and the low pressure (~1500 mTorr) inside the chamber. Cu evaporation from the surface results in the release of the 9,9'-bianthryl, possible via rDA, from the MPES monolayer to react at the Cu surface leading to graphene formation at the top surface of the de-wetted Cu (see the inset picture on **Figure 6.3**). Again, it is important to mention that the Raman collected at the SiO$_2$ surface of where the Cu dewetted, we observed a D and G band as well as a broad 2D band (3), characteristic of defective graphene[11,34] which is consistent with what has been observed for graphitization of other materials to graphene on silicon oxide surfaces.[25,35]

Given the very limited solubility of carbon in Cu,[7] the fact that graphene growth occurred on top of a Cu film with a carbon source embedded underneath and produced graphene superior to that obtained directly on the substrate surface may seem puzzling. Li and co-workers have shown, however, that methane transport occurs through Cu layers in both directions, due to the presence of grain boundaries in Cu CVD applications.[34] They have identified a few layer graphene in those voids in their graphene growth experiments, hence proving that the reaction can take place at any active site of Cu, not only on extended flat surfaces. Accordingly, in our experiments we observe the best quality graphene on top of the Cu in the case of B-MPES. As illustrated in **Figure 6.3** inset, in addition to grain boundaries, we observe metal dewetting and formation of voids in the Cu layer. One conceivable mechanism for graphene formation is that the DA adducts confined to space between Cu metal and SiO_2 decompose, liberating bianthryl.[28,37,38] Bianthryl or the active species resulting from rDA can oligomerize, possibly through the intervention of catalytic Cu, analogous to an earlier report for gold,[18,21] and consolidate into graphene (**Figure 6.4**). On the other hand, for the MPES, A-MPES (which can't undergo rDA, **Figure 6.1**). We observed a D and G band as well as a broad 2D band (3), characteristic of defective graphene[11,34] hence we can conclude that there is not enough carbon available for graphitization, therefore only defective graphitic structures are formed. Control samples containing only SiO_2 coated with Cu, did not yield any graphitic like signal, indicating that the copper by itself is insufficient to produce graphene. Rather, by utilizing this designed carbon precursor, we are able to control both the carbon release and surface graphitization, consistent with previous reports.[11,34]

Recent studies suggest that at these high temperatures the aromatic structures remain intact [16] reinforcing once again the experimental observations (**Figure 6.3**) and our hypothesis that the underlying growth mechanism mainly involves surface–mediated nucleation processes of dehydrogeneation and formation of charge transfer complexes between PAHs and metal surfaces,[21,39] nevertheless it will be very challenging to provide experimental proof and further studies will be necessary.
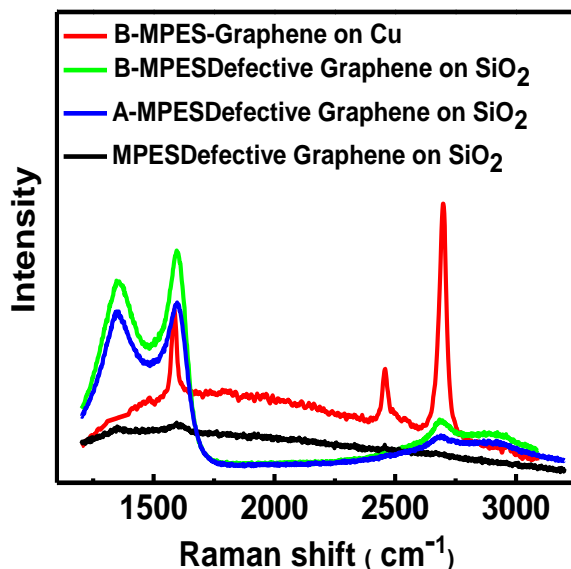
Figure 6.3. Full Raman spectra for: MPES (black line), A-MPES (blue line) and B-MPES (red and green) on Cu-coated SiO$_2$ and annealed in a tube furnace in argon/hydrogen environment at 1000 ºC. Inset: Optical image (30 by 40 microns) of surface after growth.

Figure 6.4. Surface reaction pathway for conversion of Diels-Alder adduct to graphene.

6.4   Conclusions

In summary, we have developed a convenient method of producing defect-free monolayer graphene by Cu-catalyzed conversion of 9,9'-bianthryl precursor released from a monolayer of its Diels-Alder adduct with maleimide immobilized on silicon dioxide surfaces. We are exploring other analogous graphene precursors as well as more convenient substrates.

6.5   References

1   Novoselov, K. S. *et al.* Electric Field Effect in Atomically Thin Carbon Films. *Science* **306**, 666-669 (2004).

2   Schwierz, F. Graphene transistors. *Nat Nano* **5**, 487-496 (2010).

3   Sarkar, S., Bekyarova, E. & Haddon, R. C. Chemistry at the Dirac Point: Diels-Alder Reactivity of Graphene. *Accounts Chem Res* **45**, 673-682, doi:Doi 10.1021/Ar200302g (2012).

4   Novoselov, K. S. *et al.* A roadmap for graphene. *Nature* **490**, 192-200, doi:10.1038/nature11458 nature11458 [pii] (2012).

5   Geim, A. K. & Novoselov, K. S. The rise of graphene. *Nat Mater* **6**, 183-191, doi:10.1038/nmat1849 (2007).

6   Li, X. *et al.* Large-Area Synthesis of High-Quality and Uniform Graphene Films on Copper Foils. *Science* **324**, 1312-1314 (2009).

7   Li, X., Cai, W., Colombo, L. & Ruoff, R. S. Evolution of graphene growth on Ni and Cu by carbon isotope labeling. *Nano Lett* **9**, 4268-4272, doi:10.1021/nl902515k (2009).

8   Ruoff, R. Calling all chemists. *Nat Nanotechnol* **3**, 10-11, doi:DOI 10.1038/nnano.2007.432 (2008).

9   Zhang, B. *et al.* Low-temperature chemical vapor deposition growth of graphene from toluene on electropolished copper foils. *Acs Nano* **6**, 2471-2476, doi:10.1021/nn204827h (2012).

10   Ji, H. *et al.* Graphene growth using a solid carbon feedstock and hydrogen. *Acs Nano* **5**, 7656-7661, doi:10.1021/nn202802x (2011).

11   Peng, Z., Yan, Z., Sun, Z. & Tour, J. M. Direct growth of bilayer graphene on SiO(2) substrates by carbon diffusion through nickel. *Acs Nano* **5**, 8241-8247, doi:10.1021/nn202923y (2011).

12   Yan, Z. *et al.* Growth of bilayer graphene on insulating substrates. *Acs Nano* **5**, 8187-8192, doi:10.1021/nn202829y (2011).

13   Ruan, G., Sun, Z., Peng, Z. & Tour, J. M. Growth of graphene from food, insects, and waste. *Acs Nano* **5**, 7601-7607, doi:10.1021/nn202625c (2011).

14   Sun, G. G. *et al.* Infrared spectroscopic ellipsometry (IRSE) and X-ray photoelectron spectroscopy (XPS) monitoring the preparation of maleimide-functionalized surfaces: from Au towards Si (111). *Surface and Interface Analysis* **43**, 1203-1210, doi:Doi 10.1002/Sia.3699 (2011).

15   Briggs, J. B. & Miller, G. P. [60]Fullerene-acene chemistry: a review. *Cr Chim* **9**, 916-927, doi:DOI 10.1016/j.crci.2005.11.014 (2006).

16   Ray, D. *et al.* Direct formation of fullerene monolayers using [4+2] Diels-Alder cycloaddition. *Chem Commun (Camb)* **47**, 2547-2549, doi:10.1039/c0cc04899b (2011).

17   Gherghel, L., Kubel, C., Lieser, G., Rader, H. J. & Müllen, K. Pyrolysis in the mesophase: a chemist's approach toward preparing carbon nano- and microparticles. *J Am Chem Soc* **124**, 13130-13138 (2002).

18   Talirz, L. *et al.* Termini of Bottom-Up Fabricated Graphene Nanoribbons. *J Am Chem Soc* **135**, 2060-2063, doi:10.1021/ja311099k (2013).

19   Engel, T. & Kickelbick, G. Thermoreversible Reactions on Inorganic Nanoparticle Surfaces: Diels–Alder Reactions on Sterically Crowded Surfaces. *Chem Mater* **25**, 149-157, doi:10.1021/cm303049k (2012).

20   Lee, J. K. *et al.* In-plane enyne metathesis and subsequent Diels-Alder reactions on self-assembled monolayers. *Langmuir* **21**, 10311-10315, doi:Doi 10.1021/La051680s (2005).

21   Cai, J. *et al.* Atomically precise bottom-up fabrication of graphene nanoribbons. *Nature* **466**, 470-473, doi:10.1038/nature09211 (2010).

22   Fort, E. H. & Scott, L. T. Carbon nanotubes from short hydrocarbon templates. Energy analysis of the Diels-Alder cycloaddition/rearomatization growth strategy. *J Mater Chem* **21**, 1373-1381, doi:Doi 10.1039/C0jm02517h (2011).

23   Arumugam, S. & Popik, V. V. Patterned Surface Derivatization Using Diels-Alder Photoclick Reaction. *J Am Chem Soc* **133**, 15730-15736, doi:Doi 10.1021/Ja205652m (2011).

24   Kaper, H., Grandjean, A., Weidenthaler, C., Schuth, F. & Goettmann, F. Surface Diels-Alder Reactions as an Effective Method to Synthesize Functional Carbon Materials. *Chem-Eur J* **18**, 4099-4106, doi:DOI 10.1002/chem.201102718 (2012).

25   Turchanin, A. *et al.* Conversion of Self-Assembled Monolayers into Nanocrystalline Graphene: Structure and Electric Transport. *Acs Nano* **5**, 3896-3904, doi:10.1021/nn200297n (2011).

26   Shin, H. J. *et al.* Transfer-free growth of few-layer graphene by self-assembled monolayers. *Adv Mater* **23**, 4392-4397, doi:10.1002/adma.201102526 (2011).

27   Ishii, Y., Song, H. Y., Kato, H., Takatori, M. & Kawasaki, S. Facile bottom-up synthesis of graphene nanofragments and nanoribbons by thermal polymerization of pentacenes. *Nanoscale* **4**, 6553-6561, doi:Doi 10.1039/C2nr31893h (2012).

28   Northrop, B. H., Norton, J. E. & Houk, K. N. On the mechanism of peripentacene formation from pentacene: Computational studies of a prototype for graphene formation from smaller acenes. *J Am Chem Soc* **129**, 6536-6546, doi:Doi 10.1021/Ja070392a (2007).

29   Roberson, L. B. *et al.* Pentacene disproportionation during sublimation for field-effect transistors. *J Am Chem Soc* **127**, 3069-3075, doi:Doi 10.1021/Ja044586r (2005).

30   Ishii, Y., Sakashita, T., Kawasaki, S., Kato, H. & Takatori, M. Fusing Treatment of Pentacenes: Toward Giant Graphene-Like Molecule. *Mater Express* **1**, 36-42, doi:DOI 10.1166/mex.2011.1005 (2011).

31   Hergenrother, W. L., Lin, C. J. & Chen, Y. Rubber compositions containing non-sulfur silica coupling agents bound to diene rubbers and component for tires. *U.S. Pat. Appl. Publ.* (03 Jun 2010).

32   Peng, L. *et al.* A fluorescence "turn-on" ensemble for acetylcholinesterase activity assay and inhibitor screening. *Org Lett* **11**, 4014-4017, doi:10.1021/ol9016723 (2009).

33   Yeh, W.-M., Lawson, R. A., Tolbert, L. M. & Henderson, C. L. Resist surface crosslinking using amine-based reactive rinses to mitagate pattern collapse in thin film lithography. *SPIE Proceedings* **8325**, 83251X-83251X, doi:10.1117/12.928876 (2012).

34   Su, C. Y. *et al.* Direct formation of wafer scale graphene thin layers on insulating substrates by chemical vapor deposition. *Nano Lett* **11**, 3612-3616, doi:10.1021/nl201362n (2011).

35   Bi, H., Sun, S. R., Huang, F. Q., Xie, X. M. & Jiang, M. H. Direct growth of few-layer graphene films on SiO2 substrates and their photovoltaic applications. *J Mater Chem* **22**, 411-416, doi:Doi 10.1039/C1jm14778a (2012).

36   Malard, L. M., Pimenta, M. A., Dresselhaus, G. & Dresselhaus, M. S. Raman spectroscopy in graphene. *Phys Rep* **473**, 51-87, doi:DOI 10.1016/j.physrep.2009.02.003 (2009).

37   Beno, B. R., Wilsey, S. & Houk, K. N. The C7H10 Potential Energy Landscape:‚Äâ Concerted Transition States and Diradical Intermediates for the Retro-Diels‚áíAlder Reaction and [1,3] Sigmatropic Shifts of Norbornene. *Journal of the American Chemical Society* **121**, 4816-4826, doi:10.1021/ja9818250 (1999).

38   Firestone, R. A. The diradical mechanism for 1,3-dipolar cycloadditions and related thermal pericyclic reactions. *Tetrahedron* **33**, 3009-3039, doi:http://dx.doi.org/10.1016/0040-4020(77)80448-1 (1977).

39   Wan, X. *et al.* High-Quality Large-Area Graphene from Dehydrogenated Polycyclic Aromatic Hydrocarbons. *Chem Mater* **24**, 3906-3915, doi:Doi 10.1021/Cm301993z (2012).

CHAPTER 7

TOWARDS A LOW TEMPERATURE GRAPHENE GROWTH USING NON-FLAMMABLE PRECURSORS

This chapter discusses synthesis of graphene at lower temperatures using a variety of carbon precursors and forming gas (3% H_2 and 97% N_2 or Ar) in order to make the overall process safer and cost effective. Chemical Vapor Deposition (CVD) experiments were performed under vacuum in the range of 25 mTorr to 1 Torr successfully producing good quality graphene. Attempts at growing graphene at 600 ^{o}C from the same carbon sources only formed amorphous carbon (ultra high vacuum experiments with benzene were also performed and yielded no graphene, only amorphous carbon). These results point to the fact that more careful studies should be conducted in order to understand the mechanism and the conditions necessary for low temperature graphene growth. The work was completed within the Tolbert and Henderson labs. Data analysis was equally shared between the two collaborating groups.

7.1   Introduction

Several methods have been developed for the synthesis of graphene since it was first isolated.[1,2] As mentioned in the introduction, mechanical exfoliation[1,3] still remains the best method for the production of small quantities of high quality graphene but due to the nature of the process, this method is not attractive for industry due to the lack of scalability.[5] Epitaxial growth from SiC suffers from the need of expensive SiC single crystals wafers[6] and the need for high temperatures and vacuum conditions.[5,7] Reduction of graphene oxide (rGO)[8] and liquid exfoliation of graphite[9,10] offer large volume processing but the low quality (of rGO) and size of the graphene flakes produced (liquid exfoliation) are still an issue that needs to be resolved[11,12] as previously mention.

Therefore, we focused on the synthesis of graphene by Chemical Vapor Deposition (CVD) on metal substrates[13-17], specifically copper. Most of the work in the literature use hydrogen as the carrier gas, methane as the carbon source and , if high quality graphene is desired, the use of ultra high or high vacuum and temperature close to ~1000 °C is required (with some examples of low temperature growth).[14,18-21]

The main objective of this work was to understand the synthesis of graphene at low temperatures by CVD, novel precursors (obtained commercially or synthesized by the Tolbert lab), without the need of dangerous concentrations of hydrogen (bellow the flammability limit, hence under 4%) and, if possible, under moderate vacuum.

It should be noted that two techniques were used for graphene growth, namely, evaporation of the carbon source into the heating chamber (CVD) containing the copper substrate and pyrolysis of the carbon source previously spin-coated on a metal substrate. These two different approaches for the synthesis of graphene were performed in order to compare the results from both methods, but no variation was observed. Furthermore, five different variables have to be taken into consideration during growth:

a) **Temperature**: Needed in order to (i) anneal the metal substrate (900 ^{o}C-1000 ^{o}C), (ii) grow graphene on the metal substrate (300 ^{o}C to 1000 ^{o}C), and (iii) evaporate the carbon source into the system.

b) **Vacuum**: Needed in order to grow good quality graphene. Reports in the literature vary from the use of ultrahigh[20] to moderate[4,32,33] vacuum systems.

c) **Gas carrier:** In this particular case, we wanted to avoid flammable concentration of hydrogen, therefore; forming gas (3% H_2 and 97% N_2 or Ar) was used.

d) **Metal substrate**: Graphene has been shown to grow in a variety of metal substrates, but we chose copper since the growth mechanism is via surface reaction, allowing us to compare our results with the literature.[4,22]

e) **Carbon source**: We chose some of the reported literature precursors[4] as well as some synthesized by the Tolbert lab as listed in the next section.

7.2 Experimental Section

All liquid and solid carbon materials from commercial sources were used as received. TGA traces were obtained with a TGAQ500 (TGA was used to assist in identifying the temperature range at which the carbon source could be introduced into the furnace hot zone.) Raman sprectum were recorded with a Nicolet Almega XR Raman spectrometer. Graphene was grown on 25 μm thick copper foils (Alfa Aesar item No. 46365 cut into 1 cm^2 squares) in a hot furnace consisting of a 46 mm ID fused silica tube heated in a Thermolyne F21100 tube furnace (**Figure 7.1** Shows the schematic for the setup used). The general growth processes are as follow:

(1) Load the fused silica tube with the copper foil on a fused silica boat;

(2) Evacuate under vacuum to 20 mTorr, back fill with forming gas (H_2/N_2 or H_2/Ar) to 1 Torr (5 cycles);

(3) Refill with forming gas (25 sccm, ~1 Torr);

(4) Let pressure reach 20 mTorr or 1 Torr (25 sccm);

(5) Heat furnace to 1000 °C and maintain for 30 min;

(6) Add solid carbon source for a desired period of time;

(7) Cool furnace to room temperature.
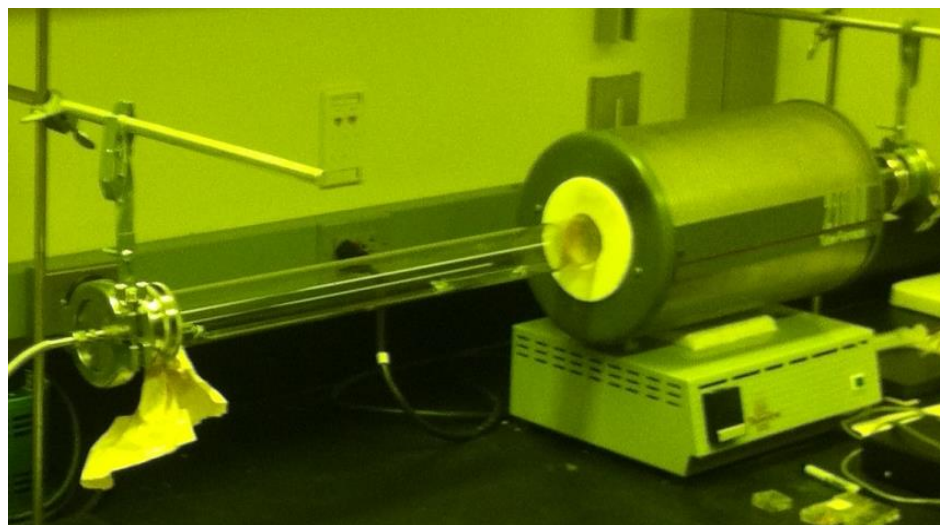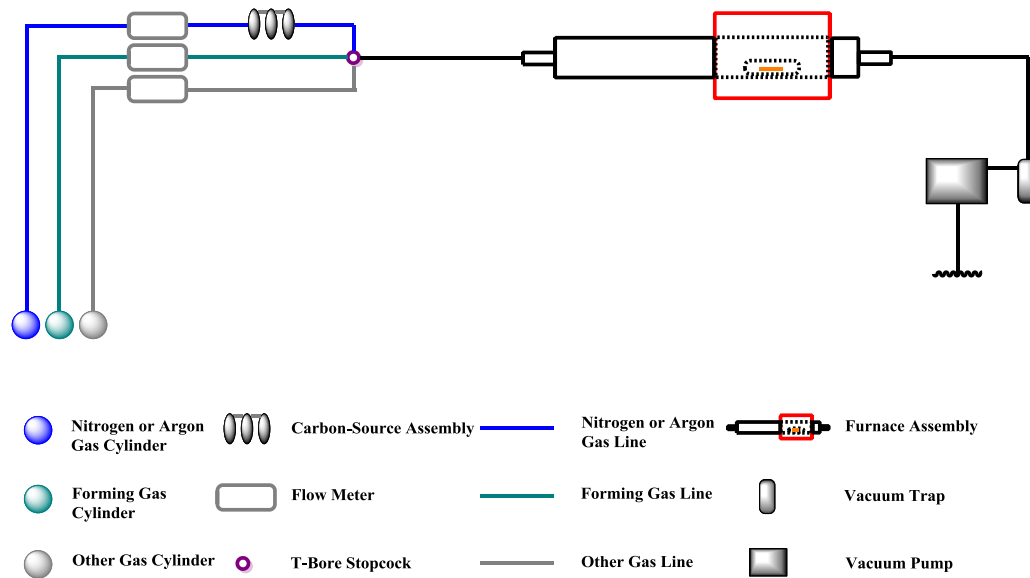
Figure 7.1 Schematic of the CVD setup for graphene growth and optical image of set-up.

As mentioned before, there were three different ways to expose the carbon precursor to the metal substrate.

1) Spin-coating a copper foil with a solution of the carbon source of choice and pyrolyse it at 600 ºC or 1000 ºC for 10 minutes under vacuum (20 mTorr) or with forming gas flow (1 Torr). The sample was then removed from the hot zone to cool down as fast as possible (**Table 7.1** entries 3, 4, 6, 7, 11, and 15 for 1000 ºC experiments and **Table 7.2** entries 4, 5, 11, 14, and 15 for 600 ºC experiments).

2) Annealing a copper sample for 30 minutes at 1000 ºC under forming gas while a second copper sample (previously spin-coated with a solution of the carbon source of choice) was held outside of the furnace hot zone. The spin-coated sample would be introduced into the hot zone under vacuum (20 mTorr) or forming gas flow (1 Torr), held inside the hot zone for ten minutes and then allowed to cool at room temperature (**Table 7.1** entries 5, 8, 9, 12, and 16). In the case of low temperature experiments, the temperature would be lowered to 600 ºC after the copper foil had been annealed at 1000 ºC (**Table 7.2** entries 6, 7, 12, 16, and 17).

3) Annealing a copper sample for 30 minutes at 1000 ºC under forming gas. The carbon source would then be evaporated into the chamber for a period of ten minutes under vacuum (20 mTorr) or forming gas flow (1 Torr) at which time the copper would be allowed to cool to room temperature (**Table 7.1** entries 10, 13, and 14). In the case of low temperature experiments, the temperature was lowered to 600 ºC after the copper foil had been annealed at 1000 ºC (**Table 7.2** entries 3, 8, 9, 10, 13, 18, and 19).

Ultra-high vacuum experiments were performed following the procedure described in the literature[23-25] using the equipment in Prof. Filler's lab (optical image of set-up below, Figure 7.2).
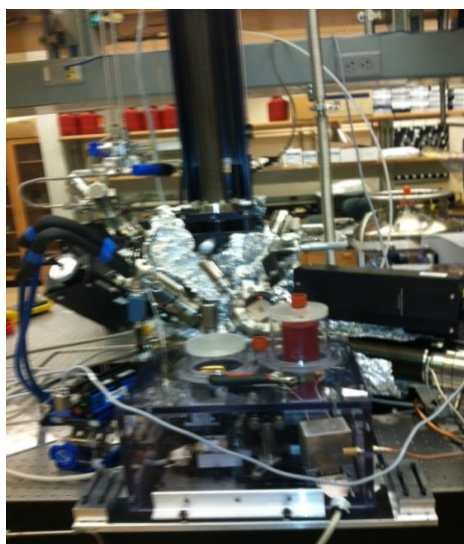
A-UHV system
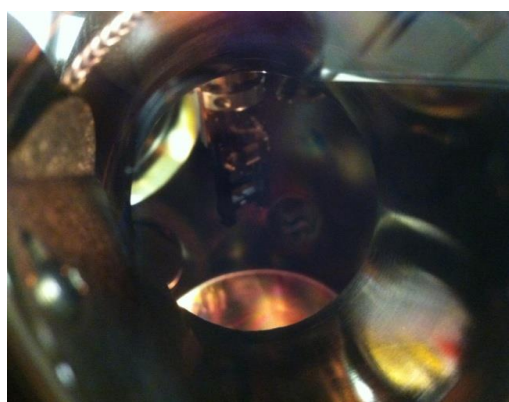
B- Sample Holder

C- Liquid Precursors

Figure 7.2 Optical image of UHV set-up in Prof.'s Filler lab.

7.3   Results and Discussion

Graphene was grown on copper substrates following the method described in the experimental protocol section. Several solid carbon sources were used including poly(methyl methacrylate) (PMMA) (**1)** and coronene (**2)** along with materials synthesized in the Tolbert laboratory (3-7, see **Figure 7.3** for complete list of chemicals). PMMA[4] and coronene[20,28] were chosen in order to duplicate reports in the literature, where graphene was successfully grown from these materials at 1000 ºC and 550 ºC, respectively. By attempting to reproduce their results with our setup, a procedure was developed for the growth of graphene by other carbon sources.

Single layer graphene was successfully grown on copper foil from different carbon sources at a temperature of 1000 ºC (**Table 7.1**). In contrast to the literature where single layer graphene was grown with hydrogen concentration of about 10%[4], our samples were formed under forming gas with hydrogen concentrations of only 3%.

1

2

3

4

5

6

7

8

9
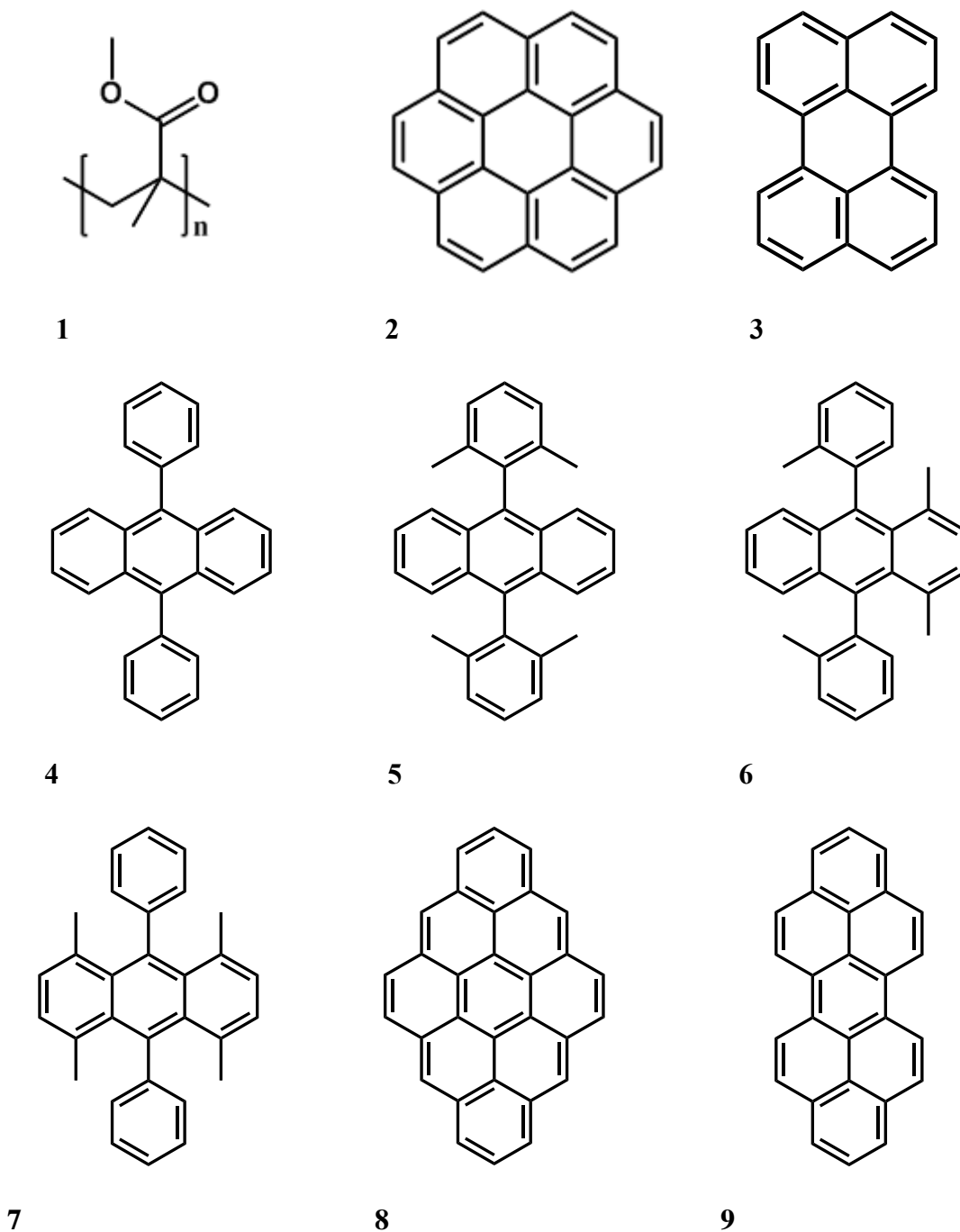
Figure 7.3 Molecular structures of (1) Poly(methyl methacrylate), (2) coronene, (3) Perylene, (4) 9,10-diphenylanthracene, (5) 9,10-bis(2,6-dimethylphenyl)anthracene, (6) 1,4-dimethyl-9,10-di-o-tolylanthracene, (7) 1,4,5,8-tetramethyl-9,10-diphenyl anthracene, (8) dibenzo[*bc,kl*]coronene and (9) dibenzo[*cd,lm*]perylene. Molecules 1 to 3 were purchased from Sigma-Aldrich, while 4-9 were synthesized by Dr. Juan Vargas (Tolbert lab).

Table 7.1 Single layer graphene grown on copper foil at different pressures and from different carbon sources.

Run	Substrate	Temp. (ºC)	Pressure (mTorr)	Gas	Growth Time (min)	Carbon Source	Graphene Layers
1	Copper	1000	20	H_2/Ar	10	-	-
2	Copper	1000	1000	H_2/Ar	10	-	-
3	Copper	1000	20	H_2/Ar	10	1^1	Single
4	Copper	1000	1000	H_2/Ar	10	1^1	Single
5	Copper	1000	1000	H_2/Ar	10	1^2	Single
6	Copper	1000	20	H_2/Ar	10	6^1	Single
7	Copper	1000	1000	H_2/Ar	10	6^1	Single
8	Copper	1000	20	H_2/Ar	10	6^2	Single
9	Copper	1000	1000	H_2/Ar	10	6^2	Single
10	Copper	1000	1000	H_2/Ar	10	6^3	Single
11	Copper	1000	1000	H_2/Ar	10	2^1	Single
12	Copper	1000	1000	H_2/Ar	10	2^2	Single
13	Copper	1000	1000	H_2/Ar	10	2^3	Single
14	Copper	1000	1000	H_2/Ar	10	3^3	single
15	Copper	1000	20	H_2/Ar	10	4^1	Single
16	Copper	1000	20	H_2/Ar	10	4^2	Single

[1]Carbon source spin-coated onto the copper substrate and introduced in this way into the hot zone held at 1000 ºC. [2]Carbon source spin-coated onto copper foil and introduced into the furnace held at 1000 ºC after a second uncoated copper foil had been annealed under forming gas for a period of 30 min. at 1000 ºC. Introduction of spin-coated sample was done under vacuum (20 mTorr) or with forming gas flow (1 Torr). [3]The carbon source was evaporated into the hot zone containing uncoated copper foil held at 1000 ºC for 30 minutes under vacuum and forming gas flow

Comparison of the Raman sprectum from graphene samples reported in the literature[4] (**Figure 7.4**) and those produced from our experiments (**Figure 7.5**, where PMMA was used as the carbon source), show that the quality of the graphene produced in our setup is similar to that reported in the literature. [4] The lack of a D peak at ~1360 cm^{-1} shows the formations of defect-free graphene at least in the domain where the measurements are taken. Furthermore, the G peak at 1590 cm^{-1} and a sharp 2D peak at 2720 cm$^{-1,}$ are both in agreement with single layer graphene. This representative spectrum for single layer graphene was observed in all samples prepared from different carbon sources under our growth conditions (**Table 7.1**).
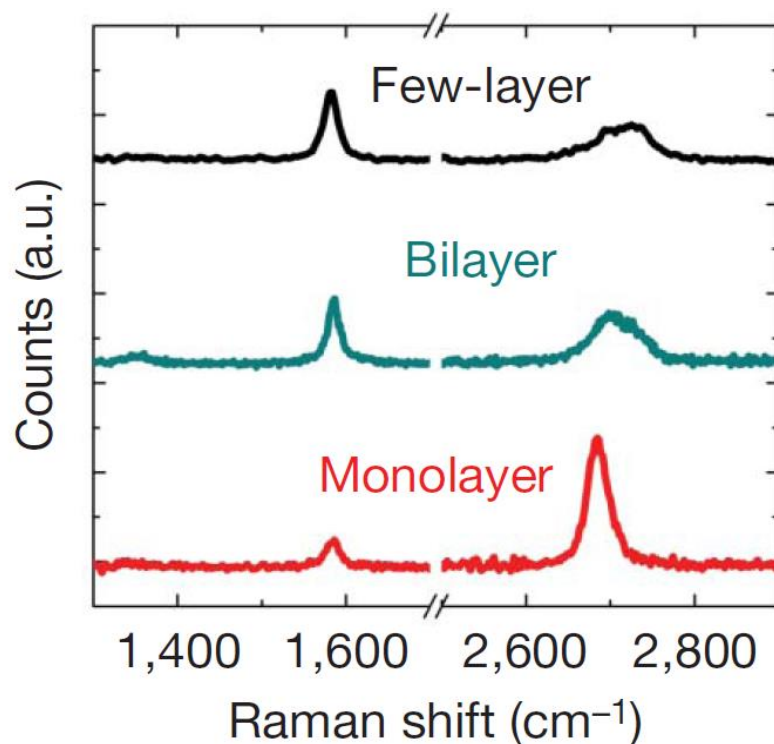
Figure 7.4 Controllable growth of pristine PMMA-derived graphene films. Difference in Raman sprectum from PMMA-derived graphene samples with controllable thicknesses derived from different flow rates of H_2.[4]
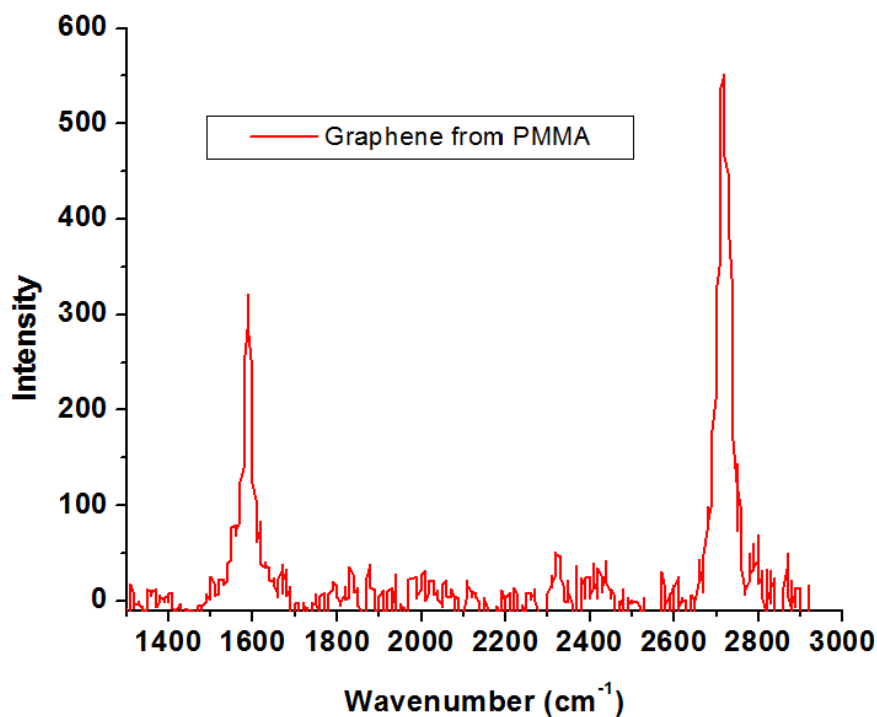
Figure 7.5 Raman spectrum of graphene grown from PMMA (1) at 1000 °C

The use of a variety of PAH as carbon precursors, from coronene[20] to (6) 1,4-dimethyl-9,10-di-o-tolylanthracene, was chosen with the hypothesis that by using carbon sources with molecular structures that closely resemble that of graphene, we should be able to grow grapheme at lower temperatures.

As with the previous experiments, coronene (**2**) was chosen as a carbon source in order to reproduce the results by the Xu group. [20] By reproducing their results with our setup, a procedure was developed for the growth of graphene by other carbon sources at low temperatures. It should be noted that the Xu group used ultra high vacuum (UHV) and higher concentrations of hydrogen (20%) in their experiments. Our system on the other hand had a maximum vacuum of 20 mTorr.

All experiments conducted under the conditions stated earlier in the experimental protocol failed to produce graphene at temperatures of 600 ºC (**Figure 7.6** and **Table 7.2**) and resulted in the formation of only amorphous carbon. The literature[20] reports the growth of graphene from coronene (**2**) at 10^{-6} to 10^{-7} Torr and annealing of the copper foil at 1000 ºC in 20% hydrogen and 80% Argon flow. One could argue that the use of forming gas with concentrations of 3% hydrogen and 97% Argon might not be sufficient for the annealing and activation of the metal substrate and subsequent formation of graphene; but the successful growth of graphene at 1000 ºC from different carbon sources under concentrations of 3% hydrogen and 97% Argon point to the contrary (**Table 7.1**). On the other hand, all our attempts at growing graphene at 600 ºC were done under a maximum vacuum of 20 mTorr. The possible effect of the vacuum change on the graphene growth is still a matter of debate. At the end, the failure to grow graphene at a temperature of 600 ºC might be due to any of these changes or to a combination of both. These experimental

results are suggestive of the importance of hydrogen and vacuum for the synthesis of graphene at low temperatures from solid carbon sources, for which more studies will be required.
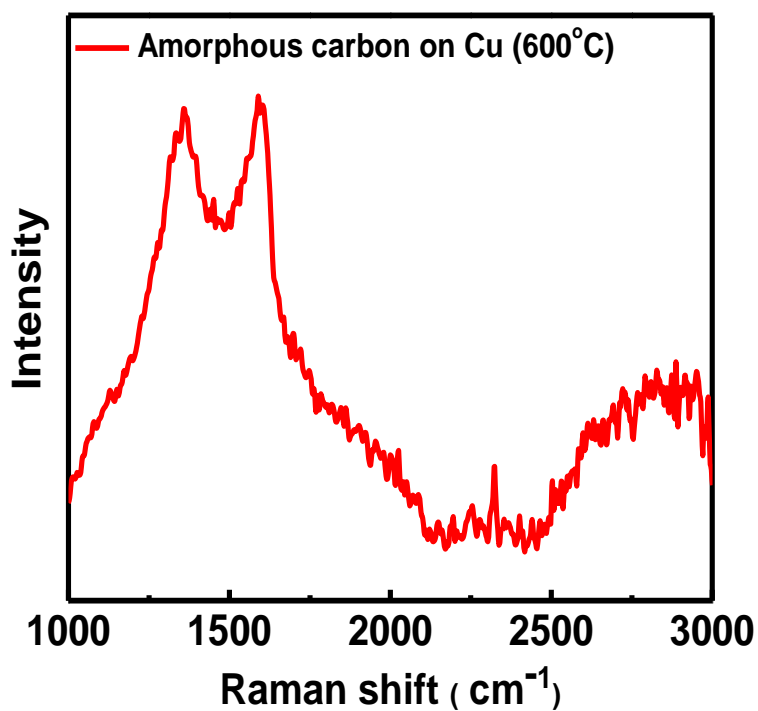
Figure 7.6 Raman spectrum of amorphous carbon grown from coronene (run 14 on table 9.2) at 600 ºC . Similar results were observed for all the other precursors in table 9.2 .

Table 7.2 Results from experiments of graphene growth on copper foil at 600 ºC at different pressures and from different carbon sources.

Run	Substrate	Temp. (ºC)	Pressure (mTorr)	Gas	Growth Time (min)	Carbon Source	Graphene Layers
1	Copper	600	20	H_2/Ar	10	-	-
2	Copper	600	1000	H_2/Ar	10	-	-
3	Copper	600	20	H_2/Ar	10	6^3	Amorphous
4	Copper	600	20	H_2/Ar	10	6^1	Amorphous
5	Copper	600	1000	H_2/Ar	10	6^1	Amorphous
6	Copper	600	20	H_2/Ar	10	6^2	Amorphous
7	Copper	600	1000	H_2/Ar	10	6^2	Amorphous
8	Copper	600	20	H_2/Ar	10	9^3	Amorphous
9	Copper	600	1000	H_2/Ar	10	6^3	Amorphous
10	Copper	600	1000	H_2/Ar	10	5^3	Amorphous
11	Copper	600	1000	H_2/Ar	10	8^1	Amorphous
12	Copper	600	20	H_2/Ar	10	8^2	Amorphous
13	Copper	600	20	H_2/Ar	10	8^3	Amorphous
14	Copper	600	20	H_2/Ar	10	2^1	Amorphous
15	Copper	600	1000	H_2/Ar	10	2^1	Amorphous
16	Copper	600	20	H_2/Ar	10	2^2	Amorphous
17	Copper	600	1000	H_2/Ar	10	2^2	Amorphous
18	Copper	600	20	H_2/Ar	10	2^3	Amorphous
19	Copper	600	1000	H_2/Ar	10	2^3	Amorphous

[1] Carbon source spin-coated onto the copper substrate and introduced in this way into the hot zone held at 600 ºC under vacuum (20 mTorr) or under forming gas flow (1 Torr). [2] Carbon source spin-coated onto copper foil and introduced into the furnace held at 600 ºC under vacuum (20 mTorr) or forming gas flow (1 Torr) after a second uncoated copper foil inside the furnace had been annealed under forming gas for a period of 30 min. at 1000 ºC. [3] The carbon source was evaporated into the hot zone containing uncoated copper foil held at 600 ºC. The copper foil had been annealed previously at 1000 ºC for 30 minutes under vacuum (20 mTorr) or forming gas flow (1 Torr).

We would like to make a final note that we also attempted to reproduce the work by Li et al., where benzene was used as precursor for low-temperature growth on copper foil.[20] The same procedure as described in the paper was used: An uncoated copper foil was placed inside the furnace ,using a quartz boat, and annealed under forming gas for a period of 30 min. at 1000 °C. Benzene was placed in a separate boat and introduced into the furnace held at the desired growth temperature, under vacuum (20 mTorr) or forming gas flow (1 Torr).

We first attempted the growth at 1000 °C and, as in the previous experiments at 1000 °C (**Table 7.1**), graphene was obtained (**Figure 7.5**). When the temperature was reduced to 600 °C the experimental protocol failed to produce graphene and resulted in the formation of only amorphous carbon (**Figure 7.6**). The paper[21] also claims that using PMMA, graphene was obtained as low as 400 °C, which we also attempted without success.

Could the actual graphene growth be happening at the pre-anneal step of 1000 °C and not at the "actual growth" temperature? From our literature research, all the papers that report low-temperature growth do indeed perform the pre-anneal at 1000 °C,[14,18,19,21] [14,20,21] hence we believe a more detailed study is needed.

7.4   Conclusions

In conclusion, our experiments show that good quality graphene can be grown from commercially available and synthesized materials. It seems that any carbon source regardless of the molecular structure will grow graphene at temperatures of 1000 ^{o}C and under vacuum. This is in accordance with literature reports, where good quality graphene has been grown from a number of carbon sources at this temperature. [22,26]

Attempts to grow graphene at lower temperature (600 ^{o}C) failed, producing only amorphous carbon on the copper substrate.. The failure of our setup to reproduce the work from the literature does not allow us to draw a conclusion indicating that our carbon sources do not grow graphene at this temperature. The fact that higher concentrations of hydrogen were not used in our setup might be enough cause to prevent the formation of graphene at these temperatures; nevertheless some reports presented in the literature should be re-evaluated in order to ensure reproducibility by the scientific community.

Moreover, careful studies should be performed in order to understand the mechanism and the conditions necessary for low temperature graphene growth. If possible, growth conditions that do not require the pre-anneal step at 1000 ^{o}C should be investigated since by performing a pre-anneal step (at 1000 ^{o}C), we are removing the point of having a low temperature process.

7.5　References

1　Novoselov, K. S. *et al.* Electric field effect in atomically thin carbon films. *Science* **306**, 666-669, doi:DOI 10.1126/science.1102896 (2004).

2　Geim, A. K. & Novoselov, K. S. The rise of graphene. *Nat Mater* **6**, 183-191, doi:10.1038/nmat1849 (2007).

3　Wassei, J. K. & Kaner, R. B. Oh, the Places You'll Go with Graphene. *Acc Chem Res*, doi:10.1021/ar300184v (2013).

4　Sun, Z. *et al.* Growth of graphene from solid carbon sources. *Nature* **468**, 549-552, doi:http://www.nature.com/nature/journal/v468/n7323/abs/nature09579.html#supplementary-information (2010).

5　Novoselov, K. S. *et al.* A roadmap for graphene. *Nature* **490**, 192-200, doi:10.1038/nature11458 nature11458 [pii] (2012).

6　Berger, C. *et al.* Ultrathin Epitaxial Graphite:‚Äâ 2D Electron Gas Properties and a Route toward Graphene-based Nanoelectronics. *The Journal of Physical Chemistry B* **108**, 19912-19916, doi:10.1021/jp040650f (2004).

7　Seyller, T. *et al.* Epitaxial graphene: a new material. *Phys Status Solidi B* **245**, 1436-1446, doi:DOI 10.1002/pssb.200844143 (2008).

8　Eda, G., Fanchini, G. & Chhowalla, M. Large-area ultrathin films of reduced graphene oxide as a transparent and flexible electronic material. *Nat Nano* **3**, 270-274, doi:http://www.nature.com/nnano/journal/v3/n5/suppinfo/nnano.2008.83_S1.html (2008).

9　Lotya, M. *et al.* Liquid Phase Production of Graphene by Exfoliation of Graphite in Surfactant/Water Solutions. *J Am Chem Soc* **131**, 3611-3620, doi:Doi 10.1021/Ja807449u (2009).

10　Hernandez, Y. *et al.* High-yield production of graphene by liquid-phase exfoliation of graphite. *Nat Nanotechnol* **3**, 563-568, doi:DOI 10.1038/nnano.2008.215 (2008).

11　Coleman, J. N. Liquid Exfoliation of Defect-Free Graphene. *Accounts Chem Res* **46**, 14-22, doi:Doi 10.1021/Ar300009f (2013).

12　Royall, S. Calling all chemists. *Chem Ind-London*, 18-20 (2007).

13　Li, Q. *et al.* Growth of Adlayer Graphene on Cu Studied by Carbon Isotope Labeling. *Nano Lett*, doi:10.1021/nl303879k (2013).

14   Zhang, B. *et al.* Low-temperature chemical vapor deposition growth of graphene from toluene on electropolished copper foils. *Acs Nano* **6**, 2471-2476, doi:10.1021/nn204827h (2012).

15   Ji, H. *et al.* Graphene growth using a solid carbon feedstock and hydrogen. *Acs Nano* **5**, 7656-7661, doi:10.1021/nn202802x (2011).

16   Li, X. *et al.* Large-Area Synthesis of High-Quality and Uniform Graphene Films on Copper Foils. *Science* **324**, 1312-1314 (2009).

17   Li, X., Cai, W., Colombo, L. & Ruoff, R. S. Evolution of graphene growth on Ni and Cu by carbon isotope labeling. *Nano Lett* **9**, 4268-4272, doi:10.1021/nl902515k (2009).

18   Kim, Y. J. *et al.* Low-temperature growth and direct transfer of graphene-graphitic carbon films on flexible plastic substrates. *Nanotechnology* **23**, 344016 (2012).

19   Xue, Y. *et al.* Low temperature growth of highly nitrogen-doped single crystal graphene arrays by chemical vapor deposition. *J Am Chem Soc* **134**, 11060-11063, doi:10.1021/ja302483t (2012).

20   Wan, X. *et al.* High-Quality Large-Area Graphene from Dehydrogenated Polycyclic Aromatic Hydrocarbons. *Chem Mater* **24**, 3906-3915, doi:Doi 10.1021/Cm301993z (2012).

21   Li, Z. *et al.* Low-Temperature Growth of Graphene by Chemical Vapor Deposition Using Solid and Liquid Carbon Sources. *Acs Nano* **5**, 3385-3390, doi:10.1021/nn200854p (2011).

22   Ruan, G., Sun, Z., Peng, Z. & Tour, J. M. Growth of graphene from food, insects, and waste. *Acs Nano* **5**, 7601-7607, doi:10.1021/nn202625c (2011).

23   Shin, N. & Filler, M. A. Controlling Silicon Nanowire Growth Direction via Surface Chemistry. *Nano Lett* **12**, 2865-2870, doi:Doi 10.1021/Nl300461a (2012).

24   Chou, L. W. & Filler, M. A. Engineering Multimodal Localized Surface Plasmon Resonances in Silicon Nanowires. *Angew Chem Int Edit* **52**, 8079-8083, doi:DOI 10.1002/anie.201301468 (2013).

25   Chou, L. W., Shin, N., Sivaram, S. V. & Filler, M. A. Tunable Mid-Infrared Localized Surface Plasmon Resonances in Silicon Nanowires. *J Am Chem Soc* **134**, 16155-16158, doi:Doi 10.1021/Ja3075902 (2012).

26   Li, Z. *et al.* Low-temperature growth of graphene by chemical vapor deposition using solid and liquid carbon sources. *Acs Nano* **5**, 3385-3390, doi:10.1021/nn200854p (2011).

CHAPTER 8

SYNTHESIS OF GRAPHITIC NANORIBBONS (GNRS) VIA ENCAPSULATION IN SINGLE-WALLED ALUMINOSILICATE NANOTUBES

In this chapter the synthesis of graphitic nano-ribbons (GNRs) by encapsulation in single walled aluminosilicate nanotubes (AlSi-SWNT) will be discussed. Our experiments showed that GNRs encapsulated in SWNT can be synthesized using other types of nanotubes, i.e. aluminosilicate. These experiments also show that the synthesis can proceed at temperatures as low as 200 ^{o}C and since the Rama signals from the AlSi-SWNT do not interfere with those of the synthesized GNRs, allowing for an easier interpretation of the spectra. Varying the size of nanotubes as well as the use of other starting materials, either commercially available or synthesized, should be explored and in principle could provide for the synthesis of GNRs with different sizes (length, width and perhaps edge termination), which are of tremendous interest in order to tune the semiconductor properties of graphene. This work was completed within the Tolbert and Henderson labs. Data analysis was equally shared between the two collaborating groups.

8.1   Introduction

As discussed through the chapters, graphene has emerged as a material of extensive scientific interest due to its variety of interesting electronic and optical properties. For example, it is being considered as a material for use in the formation of future high speed electronics due to its potential for significantly higher carrier mobility as compared to silicon.[1,2]

In such microelectronic applications, much of the current work is focused on first finding methods for depositing graphene over large areas of a substrate, either by CVD on copper or high temperature growth of graphene on the surface of SiC wafers through evaporation of Si atoms. However, in its sheet form, graphene is semi-metallic (no band gap)[3,4] and thus is of little direct use in the formation of the active regions of semiconductor devices such as field effect transistors. Therefore, methods are required that can transform the graphene into a semiconducting form by introducing a band gap in the material.[5-8]

One method for producing such semiconducting graphene is to confine it into the form of ribbons that are on the order of a few tens of nanometers in width, since their electronic properties can be adjusted by changes on their width and molecular geometry.[7,9-17] Currently, the few published results of such graphene ribbons made from SiC derived graphene[18] have utilized lithography and plasma etching steps to produce these ribbons from larger sheets of graphene. Other methods include, cutting graphene sheets to ribbons by electron beam[19], unzipping of carbon nanotubes[7,20], by deposition and fusion reaction of hydrocarbons on metallic surfaces[21,22] and recently by encapsulation in single-walled carbon nanotubes (SWNTs).[23,24]

In his work, Talyzin *et al* used thermally induced fusion of perylene (**1**) (**Figure 8.1**) and coronene to form graphene nano-ribbons encapsulated in single-walled carbon nanotubes. [23,24] Hydrogen-terminated GNRs were synthesized at temperatures of 350 - 440

ºC from perylene (**1**) (with best results at 400 ºC) and with coronene (**2**) in the range of 470 - 530 ºC (with best results at 450 - 470 ºC). [23,24]

Overall, the main idea behind encapsulation is to impose geometrical restrictions on the alignment of the reacting molecules prior to thermal fusion and subsequent formation of GNRs. In this case, these geometrical restrictions are imposed by the use of SWNT as one-dimensional reactors for the insertion and fusion of polycyclic aromatic hydrocarbons.

The authors claim that the use of SWNT is critical for the formation of nano-ribbons, but little experimental evidence is provided. Furthermore, when characterized by Raman spectroscopy, the signals produced by the carbon nanotube, overlap with the Raman spectrum of the newly synthesized GNRs, hence making it difficult for characterization of such fabricated ribbons.[23] For this reason, we sought to look for other nanotubes systems that could provide similar geometrical restrictions to be used as a one-dimensional reactor and, if possible, without producing overlap in the Raman Spectroscopy signals.

Recently, Prof. Nair's group has investigated Dehydration, Dehydroxylation, and Rehydroxylation of Aluminosilicate single-walled nanotubes (AlSi-SWNTs), a synthetic version of the nanotubular mineral imogolite .[25-27] AlSi-SWNT are metal oxide nanotubes that are formed of a tubular aluminum(III) hydroxide layer on the outer surface with pendant silanol groups on the inner surface[26] (**Figure 8.1a and Figure 8.1b**).

We sought to use these nanotubes as our encapsulation system, since these nanotubes could provide the desired one-dimensional geometrical restrictions without the signal overlap on the Raman spectra caused by the carbon nanotubes. Furthermore, their size (~1 nm inner diameter) is close to the SWNT used by Talyzin *et al*, hence, allowing us to have a close comparison of our results with the literature.[23]
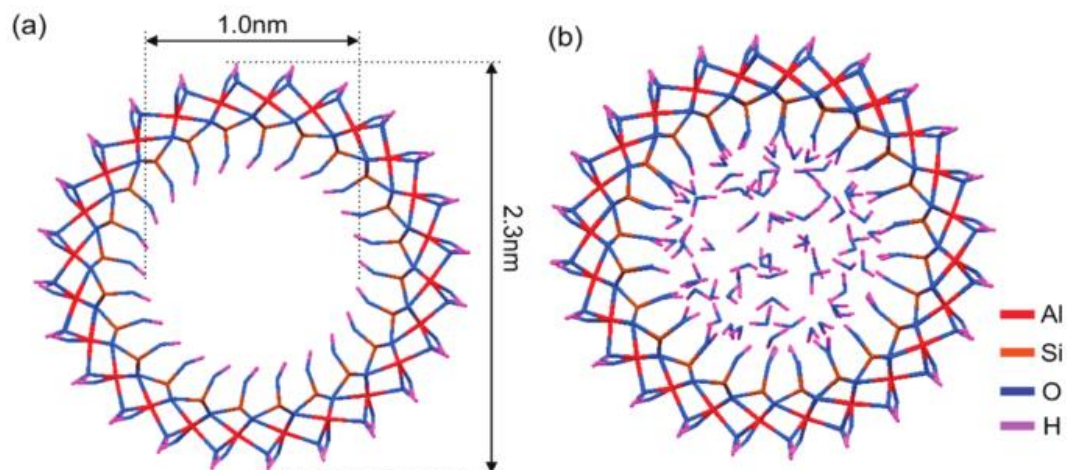
Figure 8.1 Aluminosilicate nanotubes (a) Cross-section of single-walled aluminosilicate nanotube. (b) Example of a model of the hydrated SWNT, with 14 wt% of water physisorbed in the SWNT at ambient conditions. [26]

8.2   Experimental Section

AlSi-SWNT were obtained from Dun-Yen Kan and the synthesis information can be found in the literature. [26] AlSi-SWNT (1 - 2 mg) were added to a glass ampoule and heated (150 °C) in a silicon bath for 1 – 2 hr under argon. Perylene (**1**) (20 mg, 79 μmol) was added to the glass ampoule. The reaction mixture was placed under argon flow for 30 minutes and then sealed under vacuum. The ampoule was heated in a Lindbergh furnace for 3 – 6 hours at 200, 250, and 300 °C. The reaction mixture was allowed to cool to r.t. and extracted with chloroform. Filtration afforded black aluminosilicate nanotubes. The nanotubes were further washed multiple times with chloroform and dried under argon.

Reactions were performed in a Blue M Lindberg tube furnace. Raman spectra were recorded with a Nicolet Almega XR Raman spectrometer using a 25 mW, 2.4 eV excitation

source (488 nm) through a 24 µM pinhole aperture and 100x objective.All spectra were excited with visible (488 nm) laser light and collected in a backscattering configuration with a laser power below 0.5 mW to reduce laser-induced heating and were acquired at multiple locations to verify reproducibility. All the peaks were fitted with Gauss-Lorentzian curve fits to determine their peak position, line width, and intensity.

TGA traces were obtained with a TGAQ500, NMR spectra were determined with a Varian Mercury Vx 300 spectrometer operating at 300 MHz for ^{1}H and at 75 MHz for ^{13}C, in deuterated solvents.

X-ray Photoelectron Spectroscopy (XPS) was acquired using a Thermo K-Alpha XPS (Thermoscientific) with a monochromatic Al Kα line, operating under ultra-high vacuum conditions and a 100 µm spot size. Survey XPS scans were obtained over the B.E. range (0-800 eV) with a step size of 1 eV and high resolution scans typically at 20 eV pass energy. Calibration of spectra was done with the Si2p peak set to Binding Energy (BE) = 104.9 eV. Sputter depth profiling was performed using an argon ion gun operating at 3000 eV.


1
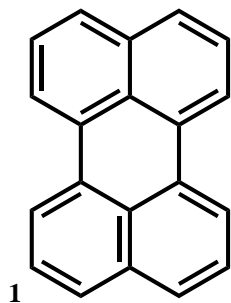
Figure 8.2 perylene (1)

8.3   Results and Discussion

As illustrated in **Figure 8.3**, we first analyzed the AlSi-SWNT and Perylene via Thermogravimetric Analysis (TGA). For the AlSi-SWNT (**Figure 8.3**), we observe a 15% loss in weight that we attribute to water. (cite Dun-yen). Annealing ~300°C we observe another 10 % drop in weight which is close to the reported decomposition temperature for such nantotubes. For the perylene (**Figure 8.3**) we observe a single drop at ~200°C , which is the expected temperature for Perylene sublimation.

We carefully followed the procedure from the literature and the Perylene/AlSi-SWNT precursors were annealed under an inner atmosphere. As illustrated in **Figure 8.4**, after annealing the precursors, a dark material (the GNR/AlSi-SWNT) was obtained: the remaining precursors (yellow) were dissolved in chloroform for NMR Spectroscopy (all the products dissolved in chloroform except the black materials/AlSi-SWNT) and the dark material analyzed via Raman Spectroscopy and XPS.
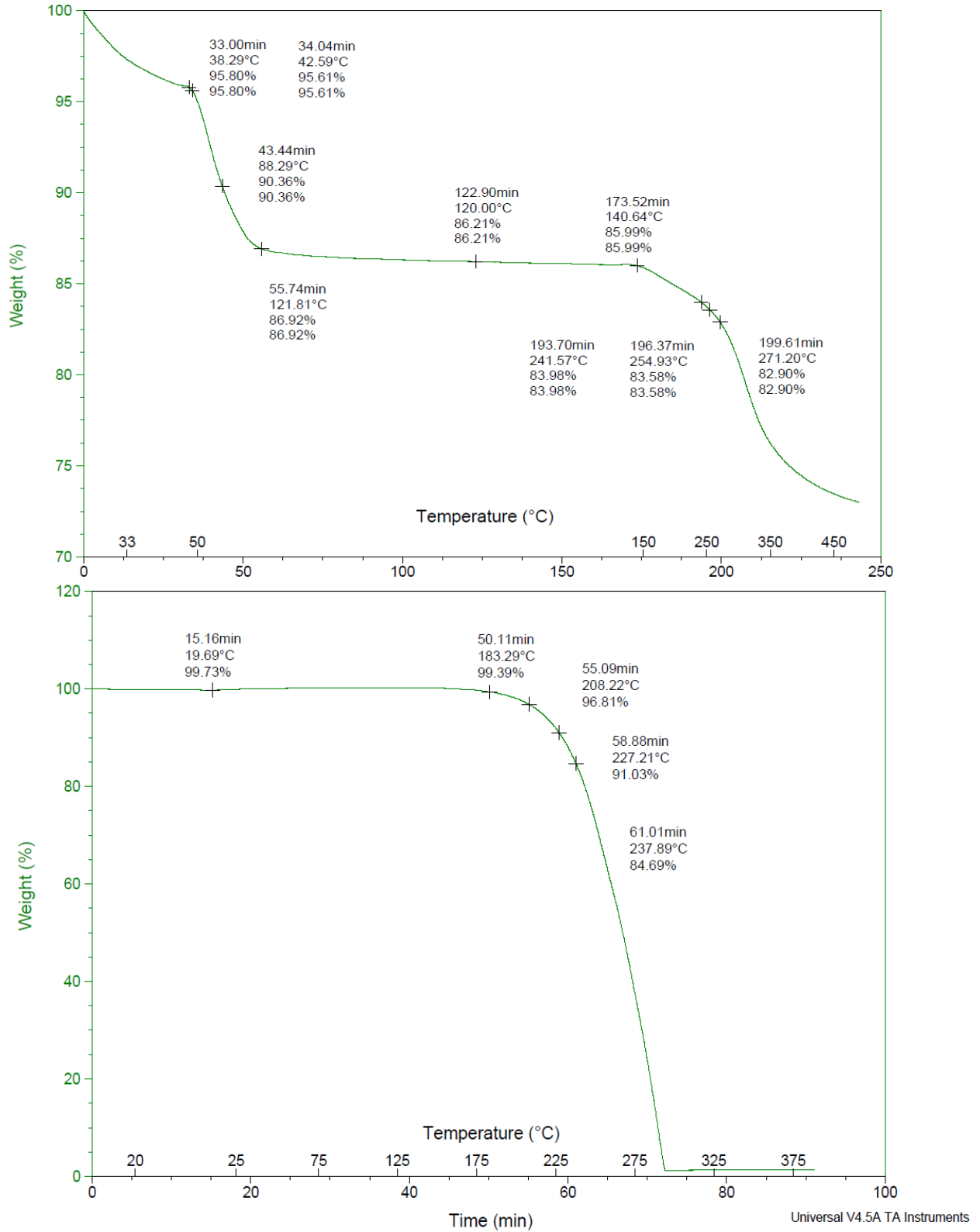
Figure 8.3 Thermogravimetric Analysis (TGA) of : (Top) AlSi-SWNT and (Bottom) Perylene.
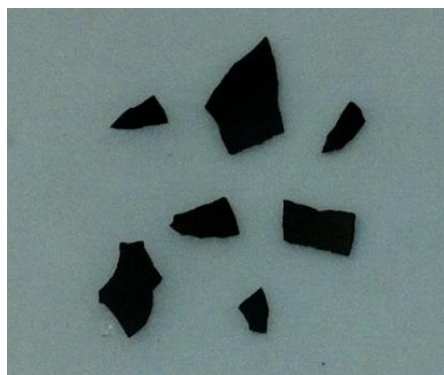
Figure 8.4 (Top) Reaction product recovered after annealing the precursors (Perylene and AlSi-SWNT). (Bottom left) Close up on the dark material obtained (the GNR/AlSi-SWNT). (Bottom right) Alumina silicate nanotubes (AlSi-SWNT) as-made.

Analysis of the NMR spectra of the remained precursors and the starting material (Perylene, **Figure 8.4**), yield identical spectra (**Figure 8.5**) which is in agreement with the TGA data, were at 200°C no changes in the weight percentage of the Perylene was observed, hence we can assume that no reaction occurred at such temperature.

Analysis of the Raman spectra of the AlSi-SWNT (**Figure 8.6**), perylene (**2**) (**Figure 8.7**), and the synthesized black material (**Figure 8.8**) points to the formation of GNR's. As expected, none of the peaks from the Raman spectrum of aluminosilicate nanotubes interfered with the Raman spectrum of the synthesized material (373cm-1 as expected for Al-Si bond) (**Figure 8.8**).

On Figure 9.8 we observe peaks at 1290 cm^{-1} ,1370 cm^{-1} and 1570 cm^{-1} which are   exactly as those reported for GNR previously described as polyperinaphthalene (**Figure 8.9** and **Figure 8.10**). Furthermore, polyperinaphthalene is the narrowest possible armchair graphitic nanoribbon, which in case of graphitization, would be the expected synthesis product of a GNR where perylene (**1**) is the starting material.[9,28-31] The Raman spectrum of the GNR's synthesized from perylene (**1**) (**Figure 8.8**) also shows peaks at 2670 cm^{-1}, 2930 cm^{-1}, and 3140 cm^{-1} which are consistent with C-H stretching, which possibly indicates that the material synthesized here are indeed hydrogen terminated as expected for the GNR's.[23,24]

We would like to mention that control experiments were performed by replacing the AlSi-SWNT with pieces of silicon coated with Aluminum oxide as well as bare silicon pieces, however no similar materials were obtained. Attempts to increase the temperature (i.e above 300°C) yielded amorphous carbon similar to those discussed in chapter 9 and chapter 6.

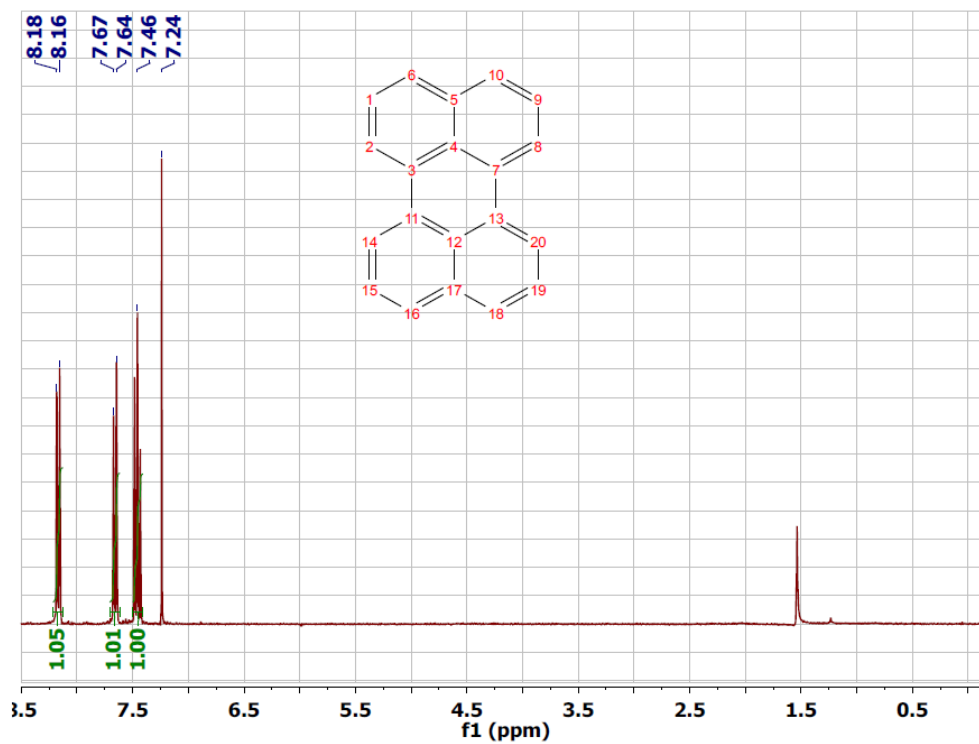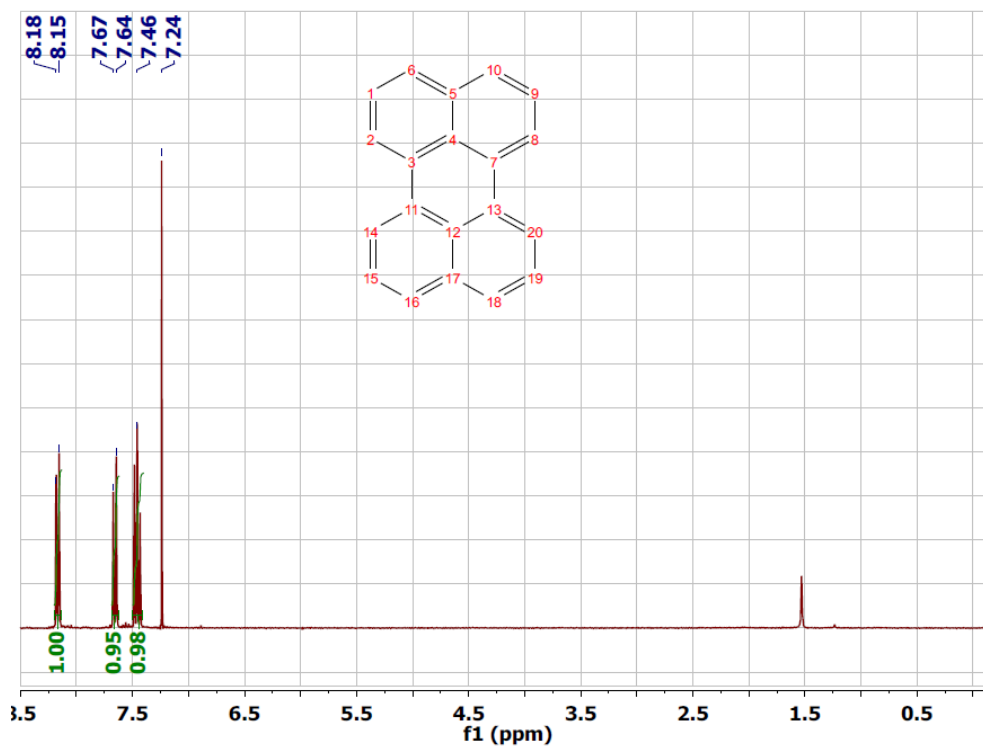**Figure 8.5** ^{1}H-NMR spectrum of: (Top) Perylene and (Bottom) the remained precursors after 200°C anneal. Both yield identical spectra.
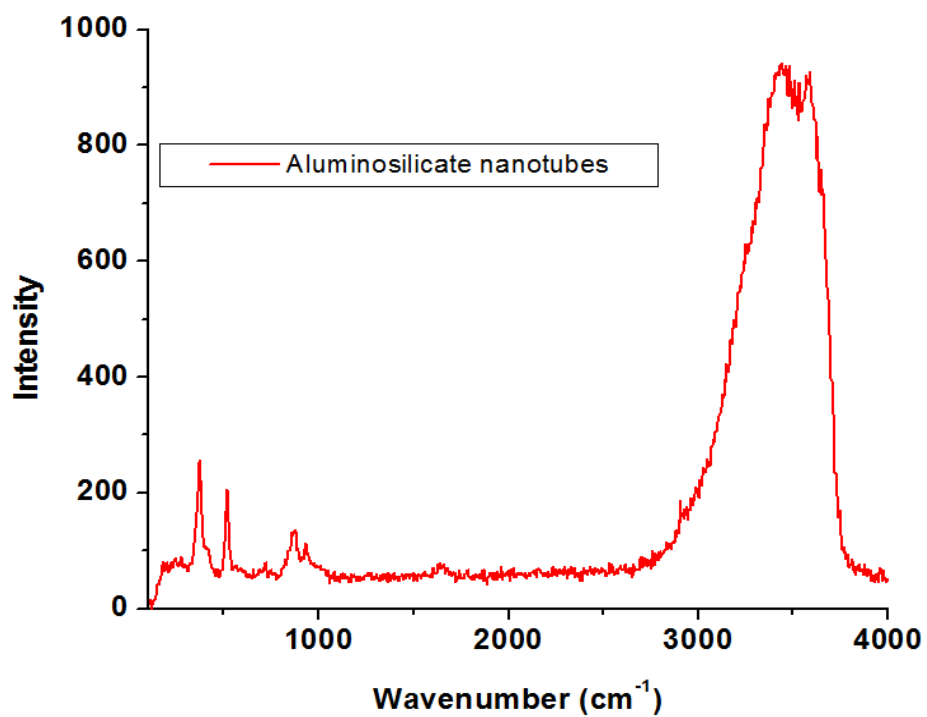
Figure 8.6 Raman spectrum of aluminosilicate nanotubes.
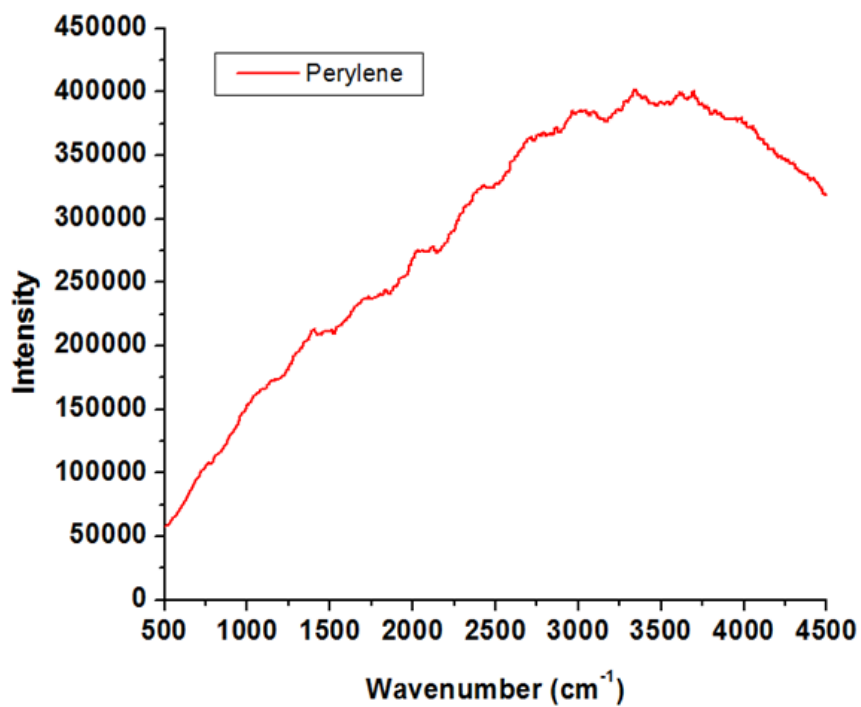
Figure 8.7 Raman spectrum of perylene (26).
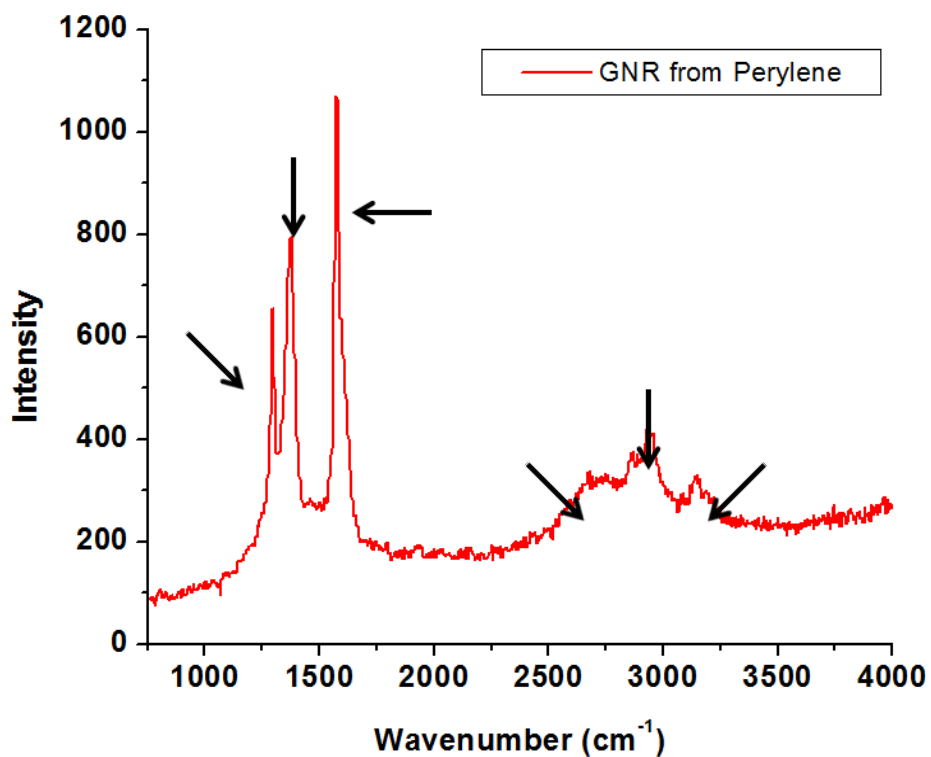
Figure 8.8 Raman spectrum of a graphitic nanoribbon (GNR) from perylene (1).
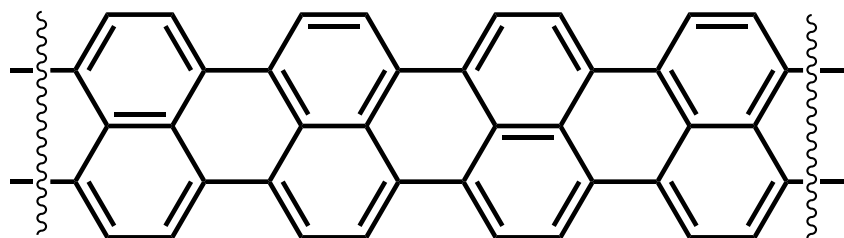
Figure 8.9 Polyperinaphthalene, the narrowest possible armchair nanoribbon.
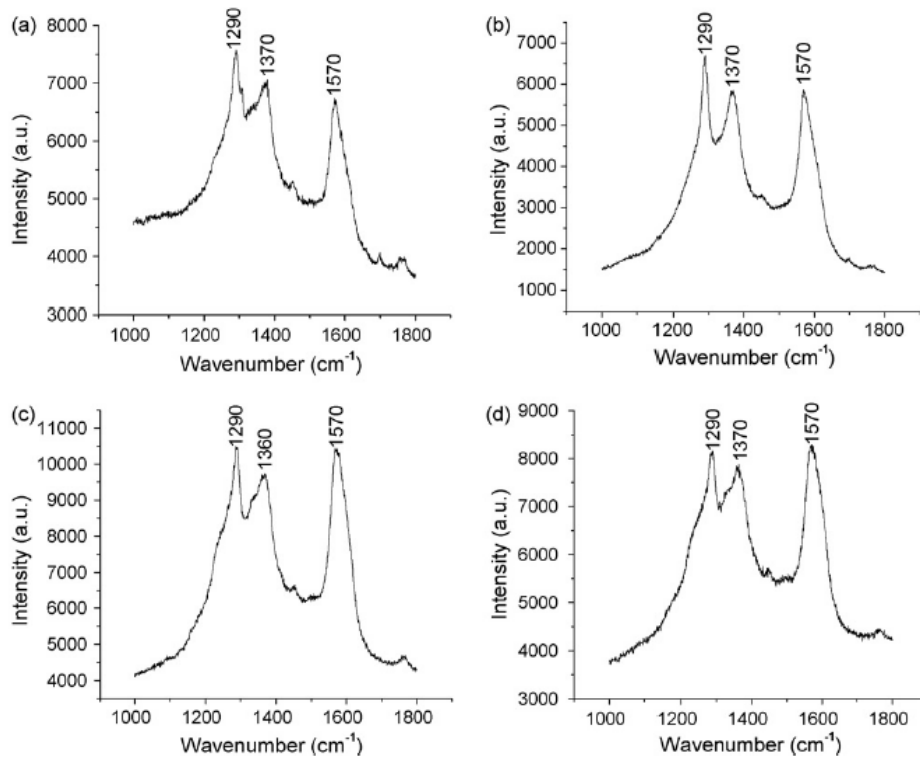
Figure 8.10 Typical micro-Raman spectra in the 1000–1800 cm^{-1} frequency range of PPN films on (a) aluminum, (b) steel, (c) silicon, and (d) ITO conducting glass. The weak feature at 1700 cm−1 in spectra (a) and (b) is from the room light.[28]

Carbon distribution through the obtained GNR's was confirmed through XPS and sputter argon ion etching. **Figure 8.11** shows the etch distribution profile for silicon (Si2p), carbon (C1s) , Oxygen (O1s) and Aluminum (Al2p) at the surface of the GNR's materials as a function of the sputter depth profiling time. Comparing the starting materials (AlSi-SWNT) carbon atomic percentage with the GNR's (AlSi/Perylene) we observe that we have 18 % and 28% respectively which would be expected for the surface. But as we etch into the material, the carbon atomic % for the GNR remains ~4 times higher (~1.6 % versus ~7%) which possibly points to the fact that the AlSi-SWNT are indeed filled with the GNR's. It is also possible that the carbon just penetrated throughout the structure, however more characterization and experimental studies will be necessary. We attempted to obtain HRTEM images of the synthesized ribbons , however we do not have such capabilities, nevertheless the data suggested that we have successfully encapsulated the GNR's into the AlSi-SWNT. Coronene studies are still underway and more analyzes/experiments are necessary to draw a final conclusion.

Atomic % Vs. Etching time
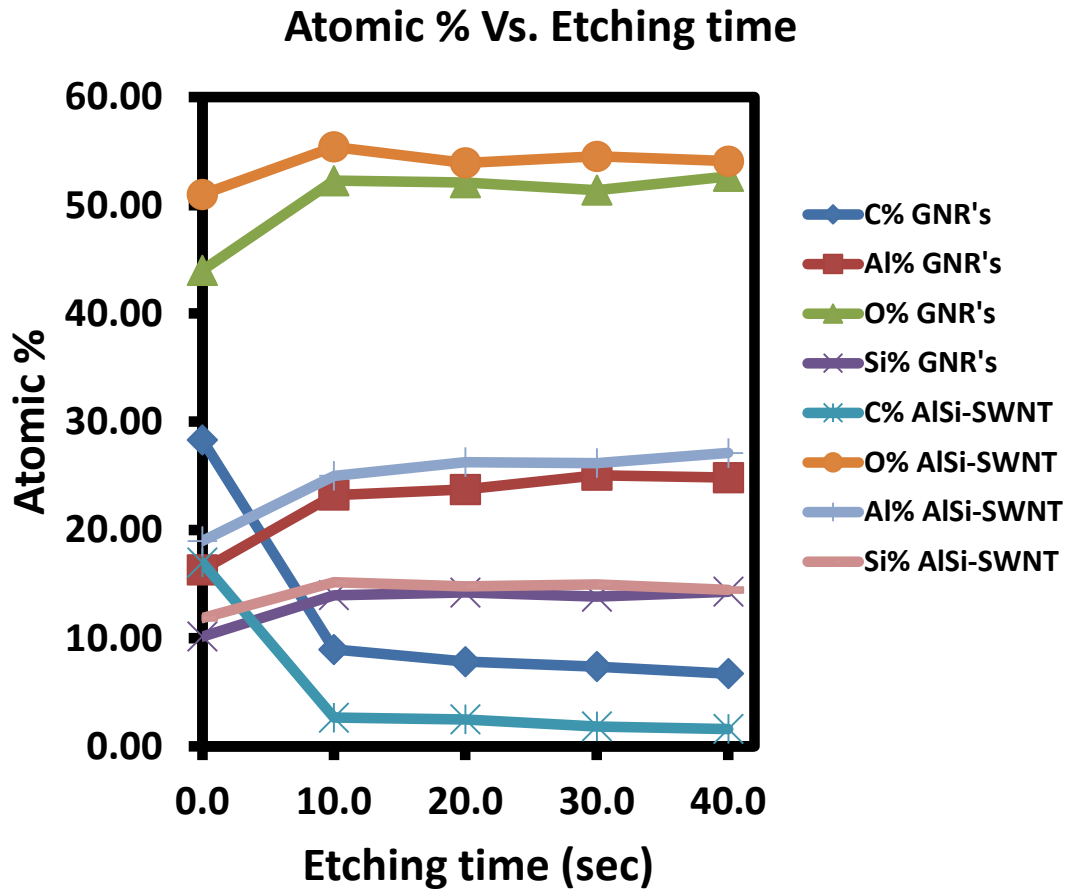
Figure 8.11 etch distribution profile for silicon (Si2p), carbon (C1s) , Oxygen (O1s) and Aluminum (Al2p) at the surface of the GNR's materials as a function of the sputter depth profiling time.

8.4   Conclusions

In summary, we have developed a convenient method of producing GNRs encapsulated in AlSi-SWNT, proving that such ribbons can be synthesized using other types of nanotubes, i.e. aluminosilicate. Another advantage that aluminosilicate nanotubes offer is the fact that the signals from its Raman spectrum do not interfere with those of the synthesized GNRs allowing in this way for an easier interpretation of the spectra. More experimental studies are necessary where the diameter/composition of the nanotubes are varied, as well as the use of other starting materials, either commercially available or synthesized since it might provide for the synthesis of GNRs of different shapes/sizes and open the door to the synthesis of GNRs at even lower temperatures than those reported here.

8.5   References

1   Geim, A. K. & Novoselov, K. S. The rise of graphene. *Nat Mater* **6**, 183-191, doi:10.1038/nmat1849 (2007).

2   Novoselov, K. S. *et al.* A roadmap for graphene. *Nature* **490**, 192-200, doi:10.1038/nature11458 nature11458 [pii] (2012).

3   Neto, A. H. C. & Guinea, F. Electron-phonon coupling and Raman spectroscopy in graphene. *Phys Rev B* **75**, doi:Artn 045404 Doi 10.1103/Physrevb.75.045404 (2007).

4   Castro Neto, A. H., Guinea, F., Peres, N. M. R., Novoselov, K. S. & Geim, A. K. The electronic properties of graphene. *Rev Mod Phys* **81**, 109-162, doi:DOI 10.1103/RevModPhys.81.109 (2009).

5   Han, M. Y., Ouml, zyilmaz, B., Zhang, Y. & Kim, P. Energy Band-Gap Engineering of Graphene Nanoribbons. *Phys Rev Lett* **98**, 206805 (2007).

6   Li, X., Wang, X., Zhang, L., Lee, S. & Dai, H. Chemically derived, ultrasmooth graphene nanoribbon semiconductors. *Science* **319**, 1229-1232, doi:10.1126/science.1150878 (2008).

7   Kosynkin, D. V. *et al.* Longitudinal unzipping of carbon nanotubes to form graphene nanoribbons. *Nature* **458**, 872-876, doi:10.1038/nature07872 (2009).

8   Jiao, L., Zhang, L., Wang, X., Diankov, G. & Dai, H. Narrow graphene nanoribbons from carbon nanotubes. *Nature* **458**, 877-880, doi:http://www.nature.com/nature/journal/v458/n7240/suppinfo/nature07919_S1.html (2009).

9   Yazyev, O. V. A Guide to the Design of Electronic Properties of Graphene Nanoribbons. *Accounts Chem Res* **46**, 2319-2328, doi:Doi 10.1021/Ar3001487 (2013).

10   James, D. K. & Tour, J. M. The Chemical Synthesis of Graphene Nanoribbons-A Tutorial Review. *Macromol Chem Phys* **213**, 1033-1050, doi:DOI 10.1002/macp.201200001 (2012).

11   Zhang, H. L., Zhang, C. Y. & Shi, D. D. A Review on Fabrication Methods of High-Quality Graphene Nanoribbons. *Adv Mater Res-Switz* **148-149**, 1737-1740, doi:DOI 10.4028/www.scientific.net/AMR.148-149.1737 (2011).

12   Jiao, L., Zhang, L., Wang, X., Diankov, G. & Dai, H. Narrow graphene nanoribbons from carbon nanotubes. *Nature* **458**, 877-880, doi:10.1038/nature07919 (2009).

13   Jiao, L., Wang, X., Diankov, G., Wang, H. & Dai, H. Facile synthesis of high-quality graphene nanoribbons. *Nat Nanotechnol* **5**, 321-325, doi:10.1038/nnano.2010.54 (2010).

14   Balandin, A. A. *et al.* Superior thermal conductivity of single-layer graphene. *Nano Lett* **8**, 902-907, doi:Doi 10.1021/Nl0731872 (2008).

15   Ritter, K. A. & Lyding, J. W. The influence of edge structure on the electronic properties of graphene quantum dots and nanoribbons. *Nat Mater* **8**, 235-242, doi:Doi 10.1038/Nmat2378 (2009).

16   Wakabayashi, K., Takane, Y. & Sigrist, M. Electronic transport properties and perfectly conducting channel of the disordered graphene nanoribbons. *Physics of Semiconductors* **1199**, 539-540 (2009).

17   Xu, Z. P. & Xue, K. Engineering graphene by oxidation: a first-principles study. *Nanotechnology* **21**, doi:Artn 045704 Doi 10.1088/0957-4484/21/4/045704 (2010).

18   Sprinkle, M. *et al.* Scalable templated growth of graphene nanoribbons on SiC. *Nat Nanotechnol* **5**, 727-731, doi:10.1038/nnano.2010.192 nnano.2010.192 [pii] (2010).

19   Jin, C. H., Lan, H. P., Peng, L. M., Suenaga, K. & Iijima, S. Deriving Carbon Atomic Chains from Graphene. *Phys Rev Lett* **102**, doi:Artn 205501 Doi 10.1103/Physrevlett.102.205501 (2009).

20   Sun, Z. Z., James, D. K. & Tour, J. M. Graphene Chemistry: Synthesis and Manipulation. *J Phys Chem Lett* **2**, 2425-2432, doi:Doi 10.1021/Jz201000a (2011).

21   Talirz, L. *et al.* Termini of Bottom-Up Fabricated Graphene Nanoribbons. *J Am Chem Soc* **135**, 2060-2063, doi:10.1021/ja311099k (2013).

22   Cai, J. M. *et al.* Atomically precise bottom-up fabrication of graphene nanoribbons. *Nature* **466**, 470-473 (2010).

23   Talyzin, A. V. *et al.* Synthesis of Graphene Nanoribbons Encapsulated in Single-Walled Carbon Nanotubes. *Nano Lett* **11**, 4352-4356, doi:Doi 10.1021/Nl2024678 (2011).

24   Chernov, A. I. *et al.* Optical Properties of Graphene Nanoribbons Encapsulated in Single-Walled Carbon Nanotubes. *Acs Nano* **7**, 6346-6353, doi:Doi 10.1021/Nn4024152 (2013).

25   Yucelen, G. I. *et al.* Formation of Single-Walled Aluminosilicate Nanotubes from Molecular Precursors and Curved Nanoscale Intermediates. *J Am Chem Soc* **133**, 5397-5412, doi:Doi 10.1021/Ja111055q (2011).

26   Kang, D. Y., Jones, C. W. & Nair, S. Dehydration, dehydroxylation, and rehydroxylation of single-walled aluminosilicate nanotubes. *Abstr Pap Am Chem S* **240** (2010).

27   Yucelen, G. I. *et al.* Shaping Single-Walled Metal Oxide Nanotubes from Precursors of Controlled Curvature. *Nano Lett* **12**, 827-832, doi:Doi 10.1021/Nl203880z (2012).

28   Yu, C., Wang, S. C., Sosnowski, M. & Iqbal, Z. Plasma-enhanced chemical vapor deposition of polyperinaphthalene thin films. *Synthetic Met* **158**, 425-429, doi:DOI 10.1016/j.synthmet.2008.03.004 (2008).

29   Mandal, B., Sarkar, S. & Sarkar, P. Energetics and electronic structure of encapsulated graphene nanoribbons in carbon nanotube. *J Phys Chem A* **117**, 8568-8575, doi:10.1021/jp4025359 (2013).

30   Kamo, H. *et al.* Formation of Poly-Peri-Naphthalene Thin-Film by Chemical-Vapor-Deposition. *Synthetic Met* **68**, 61-63, doi:Doi 10.1016/0379-6779(94)90147-3 (1994).

31   Murakami, M. & Yoshimura, S. Synthesis of Poly-Peri-Naphthalene by Vapor-Phase Polymerization - an Approach to a One-Dimensional Graphite. *J Chem Soc Chem Comm*, 1649-1650, doi:Doi 10.1039/C39840001649 (1984).

CHAPTER 9

CONCLUSIONS AND RECOMMENDATIONS

9.1 Conclusions

As faster, smaller, flexible and cheaper electronics are demanded, it is essential to improve current techniques and explore the development of new techniques in order to fully produce organic electronic materials suitable for device fabrication. In this dissertation, we explored the doping and synthesis of grapheme, all with the goal of improving current techniques and exploring the development of new processes that will broaden the application of graphene devices in research and industry, creating a path towards producing useful graphitic electronic materials.

The important findings of this dissertation are as follows:

➢ In chapter 2, the use of a self-assembled covalent APTES monolayer was demonstrated to n-dope graphene. Control of the resulting doping level in graphene FET devices was dependent upon the amount of APTES deposited onto the FET gate dielectric surface. FET devices were produced with patterned p- and n-doped regions, through lithographic patterning of such APTES layers using the combination of control of APTES deposition and patterning to tune the I-V characteristics of graphene FET devices. The use of such APTES doping schemes did not degrade the electronic properties of the resulting graphene, as had been problematic in previously reported doping procedures, which introduced defects into the graphene layer. Overall, the methods described here allowed for facile, controllable, and low temperature fabrication of graphene p-n junctions.

➢ In chapter 3, we again utilized APTES in conjunction with PFES to induce n- and p-type characteristics in graphene without altering its structure. These SAMs bound to the substrate and were thermally stable. Simultaneous use of these groups in a FET device resulted in formation of two separate Dirac points, as indicative of a graphene p-n junction. Variation in the duration of substrate functionalizing with these SAMs and heat treatment period resulted in p-n junctions with controlled position and height of the IV response curve.

➢ In chapter 4, we developed an on-demand photochemical method for doping of graphene using TPS-Nf and NBC photoacid and photobase generators, respectively. Both compounds could be used to easily dope graphene, and such doping could be controlled in an area-selective manner using traditional lithographic exposure techniques and tools. Electrical measurements and XPS confirmed that before exposure, graphene coated with either TPS-Nf or NBC maintained its pristine electrical properties, and that by modulating the deep ultraviolet (DUV) light dose delivered to the films, the doping concentration for both p and n-type doping could be easily modulated and controlled. This doping technique yielded a possible work function modulation from 3.4 eV to 5.3 eV in single layer graphene. Area-selective doping and modification of an existing graphene FET device were demonstrated through photochemical formation of a p-n junction in a pre-fabricated graphene FET device coated with TPS-Nf and exposed in a pattern-wise manner. The exposure was masked in such a way that

the p-n junction was formed in the middle of the graphene FET device channel. Measurements of the I-V characteristics of the photochemically doped FET device showed the expected two current minima (i.e. two Dirac or neutrality points) for an ambipolar p-n junction in graphene. Our simple method for producing patterned doping profiles in graphene films and devices opens up a variety of new possibilities for forming complex doping profiles in a simple manner in graphene, and can enable rapid testing of graphene device concepts involving controlled work function tuning, complex doping profiles and simple post-fabrication tuning of devices.

➢ In chapter 5, a novel macromolecular surfactant dicholesteryldithienothiophene (ChDTT) was synthesized and optimized for use in graphene exfoliation and dispersion. By simple sonication of expandable graphite in solutions containing ChDTT, graphene sheets with sizes exceeding 50 micrometers were observed and characterized by transmission electron microscopy (TEM), atomic force microscopy (AFM), electrical measurements, Raman, and X-ray photoelectron (XPS) spectroscopy. The new surfactant was more efficient than poly(m-phenylenevinylene-co-2,5-dioctyloxy-p-phenylenevinylene) (PmPV), avoided use of polymeric materials, and could be cleanly removed by simple thermal treatment. Using this surfactant, graphene flakes could be extracted directly from HOPG or other graphitic sources without additional chemical, mechanical, or thermal treatment, producing large flakes of high quality.

➢ In chapter 6, we developed a convenient method of producing defect-free monolayer graphene by Cu-catalyzed conversion of a 9,9'-bianthryl precursor released from a monolayer of its Diels-Alder adduct with maleimide immobilized on silicon dioxide surfaces. We are exploring other analogous graphene precursors as well as more convenient substrates.

➢ In chapter 7, our experiments shown that good quality graphene could be grown from commercially available and synthesized materials. It seems that any carbon source regardless of the molecular structure will grow graphene at temperatures of 1000 $^{\circ}$C and under vacuum. This is in accordance with literature reports, where good quality graphene has been grown from a number of carbon sources at this temperature. [22,26] Attempts to grow graphene at lower temperature (600 $^{\circ}$C) failed, producing only amorphous carbon on the copper substrate. The failure of our setup to reproduce the work from the literature did not allow us to draw a conclusion indicating that our carbon sources did not grow graphene at this temperature. The fact that higher concentrations of hydrogen were not used in our setup might be enough cause to prevent the formation of graphene at these temperatures; nevertheless, some reports presented in the literature should be re-evaluated in order to ensure reproducibility by the scientific community.

➢ In chapter 8, we developed a convenient method for producing GNRs encapsulated in AlSi-SWNT, proving that such ribbons could be synthesized using other types of nanotubes, i.e. aluminosilicate. Another advantage that aluminosilicate nanotubes offered is the fact that the signals from its Raman spectrum did not

interfere with those of the synthesized GNRs allowing in this way for an easier interpretation of the spectra and possible extraction.

Based on these experimental findings, the following recommendations for future work were derived:

9.2   Recommendations for Future Work

9.2.1   Doping of Graphene

We have developed techniques for controllably doping graphene through a simple chemical process using self-assembled monolayer compounds, photo-acid and photo-base generators (chapters 2-4), and we have demonstrated simple p-n junctions fabricated in this manner. Not discussed here, and in collaboration with Prof. Graham's group, we have studied an ultrathin layer of a polymer, polyethylenimine ethoxylated (PEIE), which is air-stable, is able to n-dope graphene and is able to induce a change in the work function above 1eV.

We have also collaborated with Prof Marder's lab and are currently developing a novel technique of doping via redox active species.[1] Here graphene has been n- and p-doped using solution-processed metal-organic complexes. Electrical measurements, photoemission spectroscopy, and Raman spectroscopy were used to characterize the doped films and to give insights into the changes. The work function decreased by as much as 1.3 eV with the n-dopant, with contributions from electron transfer and surface dipole, and the conductivity significantly increased (**Figure 9.2**).

Nevertheless, further studies are necessary, since with one's ability to control the work function of graphene and carrier concentrations, applications in electrode fabrication are a possibility.[2] Work by our group (in collaboration with Dr. Hua-Wei Chu) as well as in the literature,[3] has demonstrated that graphene based electrodes can improve the properties of organic semiconductors by orders of magnitude, rivaling the properties of current standards such as gold and aluminum (**Figure 9.1**).
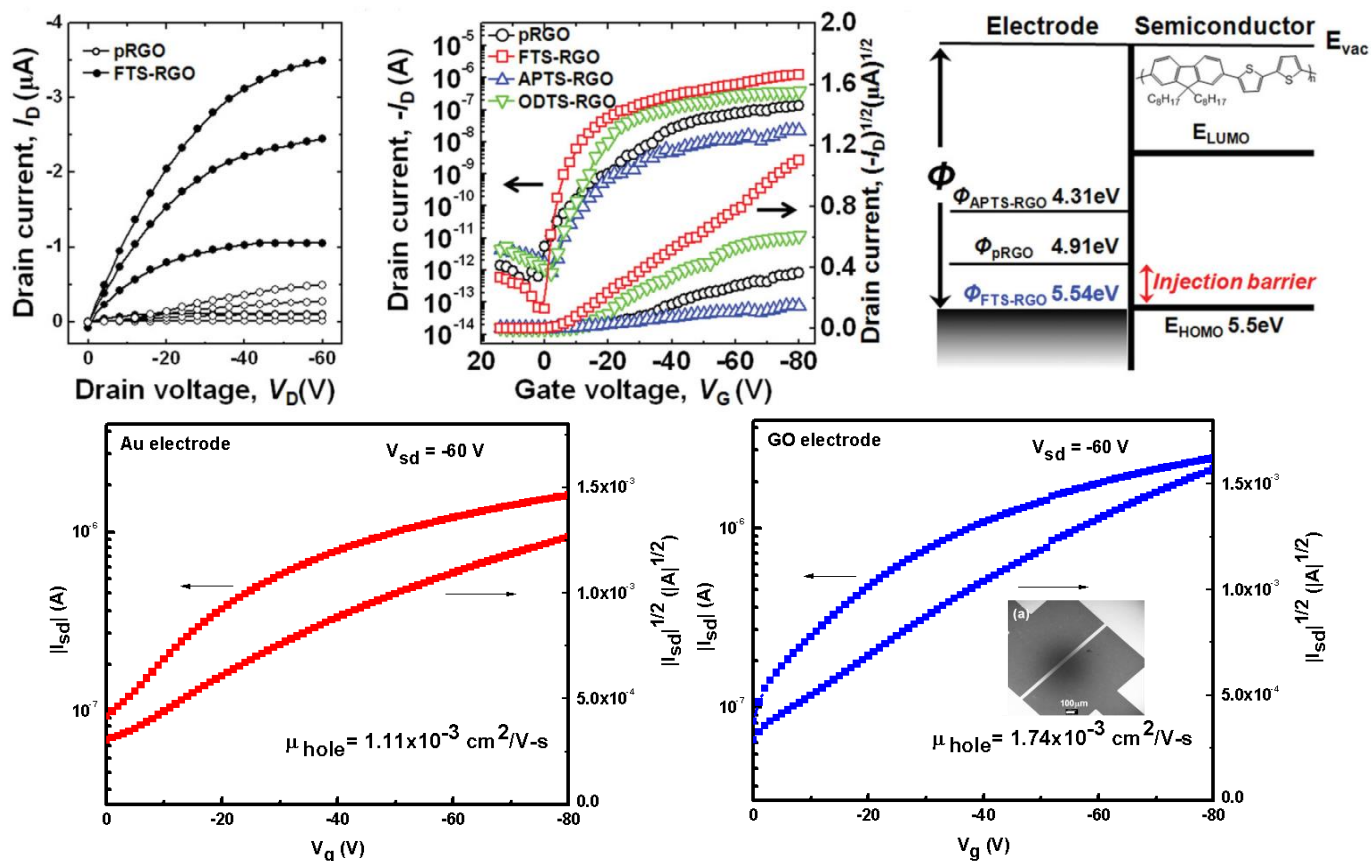
Figure 9.1 (Top) Left-Output characteristics of p-channel F8T2 (poly[(9,9-dioctylfl uorenyl-2,7-diyl)- *co* -bithiophene]) FETs with RGO S/D electrodes (*V* G steps: 0, –20, –40, –60 V). **Middle**- Transfer characteristics (*V* D = –80 V) of F8T2 FETs with RGO S/D electrodes. **Right**- Chemical structure of F8T2 and schematic band diagrams of F8T2 and SAM-functionalized RGOs.[3] **(Bottom) Left**-Transfer characteristics at a source-drain bias V_{SD}= -60V of P3HT OFET using evaporated 50nm gold S/D electrodes. **Right**- Transfer characteristics at a source-drain bias V_{SD}= -60V of P3HT OFET employing 35nm thick rGO S/D electrodes annealed at 1000˚C. **(Inset-Bottom right)** SEM overview of patterned GO electrode (after 1000˚C reduction in forming gas).
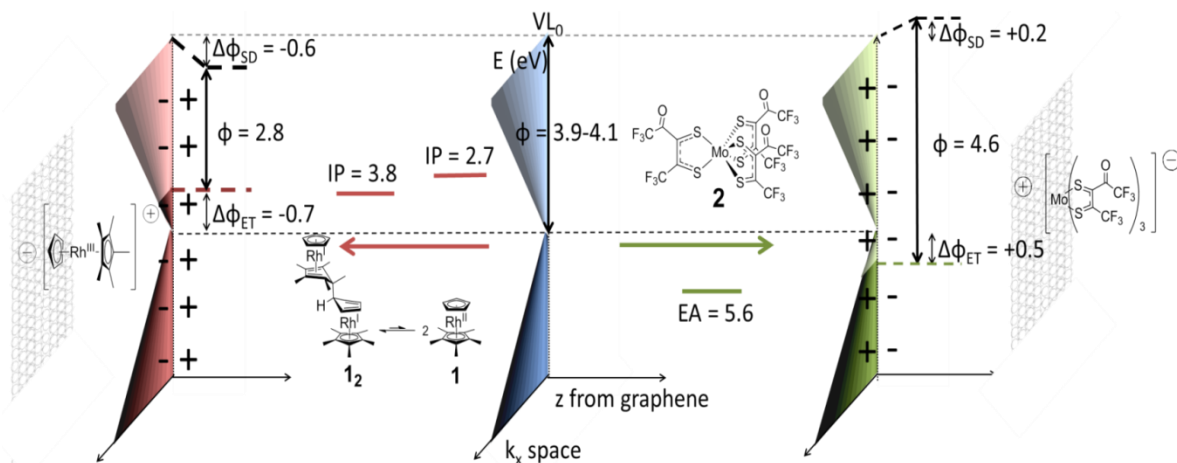
Figure 9.2 Schematic representation of n- and p-doping of graphene by redox-active metal-organic species, with associated energy levels. IP, EA and WF (φ) values were estimated from electrochemical and UPS data. The pristine graphene φ depended on the batch (4.1 eV for the sample before n-doping and 3.9 eV before p-doping). After treatment, the φ is affected by electron transfer (ET) between dopant and graphene, shifting the Fermi level (E_F) relative to the Dirac point (E_D), and the induced surface dipoles (SD) from the resulting charges, which change the local vacuum level (VL).[1]

All of these dopants can potentially be applied to modulate the electronic properties of graphene for use as transparent, conductive electrodes in a variety of electronic devices (LEDs, OFETs, organic photovoltaic, chemical sensors etc) where WF tuning and high conductivity are required. The next study could focus on developing a recipe for quick fabrication of multiple layer CVD graphene electrodes using such dopants, allowing for a better matching of the work-function of the graphene electrode with the HOMO (or LUMO) level of the organic semiconductors, and resulting in a better electron/hole injection and, therefore, higher mobility.[3,4]

Why stop at graphene? Currently other 2D material , such as MoS_2 (**Figure 9.3**), have demonstrated very interesting properties, and some dopants used in our studies

(SAM's) are already being explored in order to tune the carrier concentration.[5] Again, the

possibilities are endless, and more studies are critical in order to open new pathways and

broaden the application of PAH materials on electronic devices and other fields.[6]
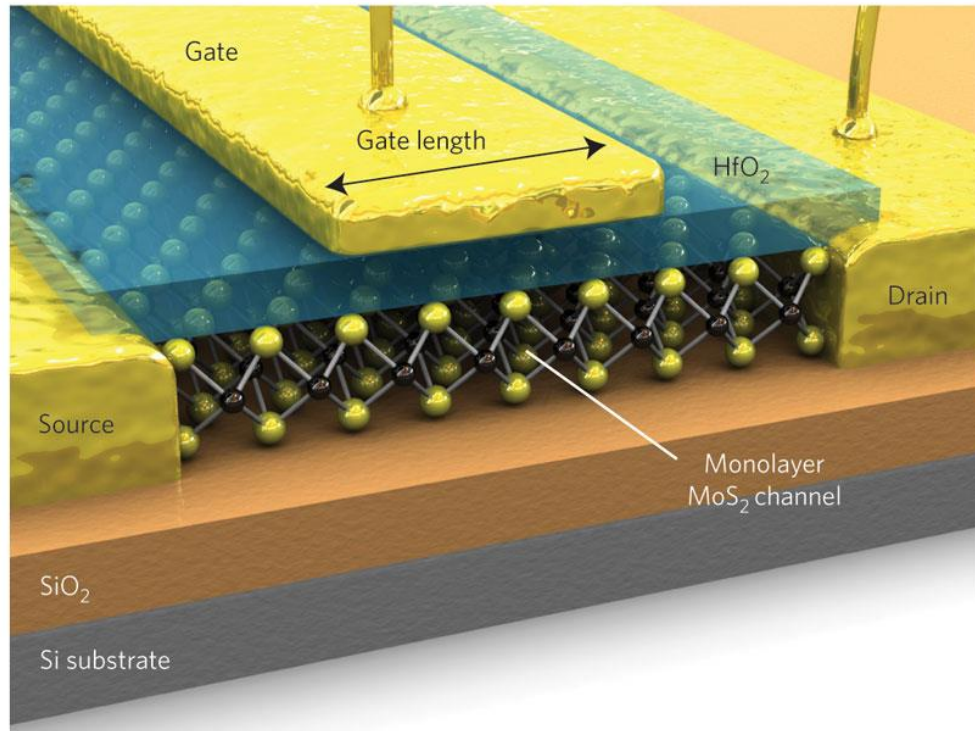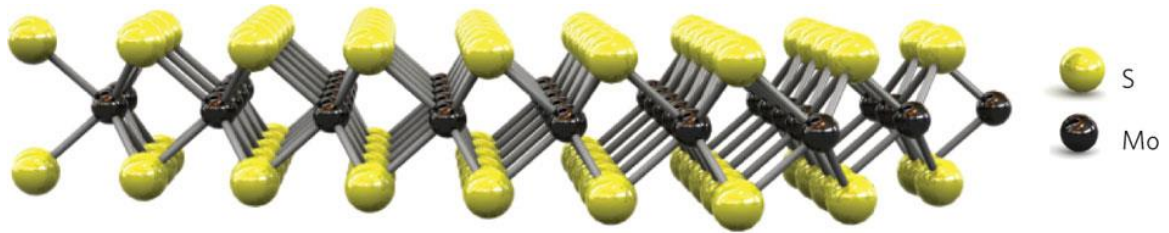
Figure 9.3 (Top) A single layer of MoS₂ is a few ångströms thick and consists of molybdenum atoms (black) sandwiched between two layers of sulphur atoms (yellow). (Bottom) Schematic (not to scale) of the MOSFET devices made by Kis and co-workers[7]: the channel is a layer of MoS₂ that is 1.5-µm long and 4-µm wide; the gate length is 500 nm. The source, drain and gate electrodes are made of gold, and hafnium dioxide (transparent layer) is used as the gate dielectric and also to boost the mobility of the channel. The devices are fabricated on silicon dioxide on silicon substrates.[8]

9.2.2   Graphene Growth

In addition to graphene doping, we also investigated approaches to lower temperature synthesis of few-layer graphene flakes, in order to improve or provide an understanding of current approaches. As a result, exfoliation of graphene sheets by an Electron Donor Surfactant was demonstrated, and surface Diels-Alder adducts on silica were explored as a controllable carbon precursor for pristine graphene.

For the exfoliation, a study started by Mason Risley should be continued in order to develop a way for self-assembly of these solution-exfoliated graphene flakes. This can be performed by modifying the surfactant or coming up with a method to transfer the flakes efficiently from solution, either via filtration/dip coating in pre-treated surfaces.

Regarding graphene growth via a copper catalytic surface, it is critical to understand the underlying mechanism of graphene formation. As we point out in Appendix 1, it is not clear in the literature what factors are critical for low-temperature graphene growth (UHV, hydrogen condition, surface treatment, oxygen concentration, precursors), and we were unable to reproduce results of some reports in the literature.[9] It is of course necessary to repeat the results found in the literature to insure the system is competent to grow graphene (and repeat the literature). Once a procedure has been established and a better understanding of the effects that each parameter has in the overall results, then new molecules, either commercially available or synthesized, can be used in order to grow graphene at low temperatures. Finally, if possible, growth conditions that do not require the pre-anneal step at 1000 ºC should be investigated, since by performing a pre-anneal step (at 1000 ºC), we are defeating the purpose of having a lower temperature based process.

Furthermore, new precursors (PAH) should be explored towards the growth of graphene nanoribbons. As we show is Appendix 2, encapsulation of polyaromatic inside nanotubes may provide a path towards low-temperature growth of "true-semiconducting" graphitic nanoribbons. Hence, a set experiments is necessary where the diameter and composition of the nanotubes are varied, as well as the use of different PAH starting materials (either commercially available or synthesized) in order to determine , which factors (nanotube size/composition, precursors) affect the resulting nanoribbon shape/size, possible opening the door to the synthesis of GNRs with dimensions suitable for mass device fabrication.[10-13]

9.3 References

1   Paniagua, S. A. *et al.* Production of heavily n- and p-doped CVD graphene with solution-processed redox-active metal-organic species. *Materials Horizonts* (2013).

2   Novoselov, K. S. *et al.* A roadmap for graphene. *Nature* **490**, 192-200, doi:10.1038/nature11458 nature11458 [pii] (2012).

3   Kang, B., Lim, S., Lee, W. H., Jo, S. B. & Cho, K. Work-Function-Tuned Reduced Graphene Oxide via Direct Surface Functionalization as Source/Drain Electrodes in Bottom-Contact Organic Transistors. *Adv Mater*, doi:10.1002/adma.201302358 (2013).

4   Zhou, Y. H. *et al.* A Universal Method to Produce Low-Work Function Electrodes for Organic Electronics. *Science* **336**, 327-332, doi:DOI 10.1126/science.1218829 (2012).

5   Li, Y., Xu, C. Y., Hu, P. & Zhen, L. Carrier Control of MoS Nanoflakes by Functional Self-Assembled Monolayers. *Acs Nano*, doi:10.1021/nn402682j (2013).

6   Mas-Balleste, R., Gomez-Navarro, C., Gomez-Herrero, J. & Zamora, F. 2D materials: to graphene and beyond. *Nanoscale* **3**, 20-30, doi:Doi 10.1039/C0nr00323a (2011).

7   Radisavljevic, B., Radenovic, A., Brivio, J., Giacometti, V. & Kis, A. Single-layer MoS2 transistors. *Nat Nanotechnol* **6**, 147-150, doi:Doi 10.1038/Nnano.2010.279 (2011).

8   Schwierz, F. NANOELECTRONICS Flat transistors get off the ground. *Nat Nanotechnol* **6**, 135-136, doi:DOI 10.1038/nnano.2011.26 (2011).

9   Li, Z. *et al.* Low-Temperature Growth of Graphene by Chemical Vapor Deposition Using Solid and Liquid Carbon Sources. *Acs Nano* **5**, 3385-3390, doi:10.1021/nn200854p (2011).

10 Yazyev, O. V. A Guide to the Design of Electronic Properties of Graphene Nanoribbons. *Accounts Chem Res* **46**, 2319-2328, doi:Doi 10.1021/Ar3001487 (2013).

11 James, D. K. & Tour, J. M. The Chemical Synthesis of Graphene Nanoribbons-A Tutorial Review. *Macromol Chem Phys* **213**, 1033-1050, doi:DOI 10.1002/macp.201200001 (2012).

12 Zhang, H. L., Zhang, C. Y. & Shi, D. D. A Review on Fabrication Methods of High-Quality Graphene Nanoribbons. *Adv Mater Res-Switz* **148-149**, 1737-1740, doi:DOI 10.4028/www.scientific.net/AMR.148-149.1737 (2011).

13   Jia, X. T., Campos-Delgado, J., Terrones, M., Meunier, V. & Dresselhaus, M. S. Graphene edges: a review of their fabrication and characterization. *Nanoscale* **3**, 86-95, doi:Doi 10.1039/C0nr00600a (2011).

APPENDIX 1:

SUPPORTING INFORMATION FOR EXPLORING SURFACE DIELS-ALDER ADDUCTS ON SILICA AS A CONTROLLABLE CARBON PRECURSOR FOR PRISTINE GRAPHENE

Abbreviations:
MPES = 3-(Triethoxysilyl)propyl maleimide
Maleimide-C12 = N-dodecylmaleimide
A-MPES= anthracene maleimide Diels-Alder adduct
B-MPES = 9,9'-Bianthryl/3-(triethoxysilyl)propyl maleimide Diels-Alder adduct
DA = Diels-Alder
rDA = retro Diels-Alder reaction

A1. Experiments

For the 3-(triethoxysilyl)propyl maleimide (MPES) layer deposition, the substrate was first cleaned and pre-treated by UV ozone for 15 min in order to produce a hydroxyl-terminated substrate, known to react efficiently with siloxane-coupling agents such as MPES. The substrate was immediately immersed in a 1%(v/v) solution of MPES in anhydrous toluene for three hours. The substrate was removed, sonicated for 15 min in pure toluene, and dried under flowing nitrogen. Deposition was confirmed by contact angle measurements using a VCA 2000 goniometry system,by x-ray photoelectron spectroscopy (XPS), and by XPS mapping acquired using a Thermo K-Alpha XPS (Thermoscientific) operating under ultra-high vacuum conditions with an Al Kα micro-focused monochromator.

The A-MPES and B-MPES coated substrates were coated with copper (300nm) using an electron beam evaporator. Graphene was synthesized in a low pressure Ar/H$_2$/CH$_4$ environment at 1000 °C. The sample was placed inside a quartz tube and pushed into the hot zone of a growth furnace operating at 1000°C. The growth was performed under

vacuum pressure ~ 1500 mTorr in an H_2/Ar (100/100 sccm) environment for 20 minutes. Then, the sample was rapidly cooled to room temperature under hydrogen and argon gas flow prior to sample removal.

Raman spectroscopy and microscopy measurements (Horiba HR800 µRaman system) were also used to characterize the resulting graphene. All spectra were excited with visible (532 nm) laser light and collected in a backscattering configuration with a laser power below 0.5 mW to reduce laser-induced heating. A 50X objective lens was used to focus the laser on the graphene samples during the Raman measurements. The stage was mounted onto an X-Y-Z micropositioning stage to control focusing and the measurement position. Raman spectra were acquired at multiple locations before and after heating and cooling to verify reproducibility.

XPS was collected using a Thermo K-Alpha XPS (Thermoscientific) operating under ultra-high vacuum conditions with an Al Kα micro-focused monochromator. XPS survey scan spectra were collected over the binding energy (B.E.) range from 0-800 eV with a step size of 1 eV and a spot size of 400 µm. XPS mapping was performed using a 30 µm spot size with a step size of 28 µm, and a Gaussian smoothing algorithm was applied to the raw data.
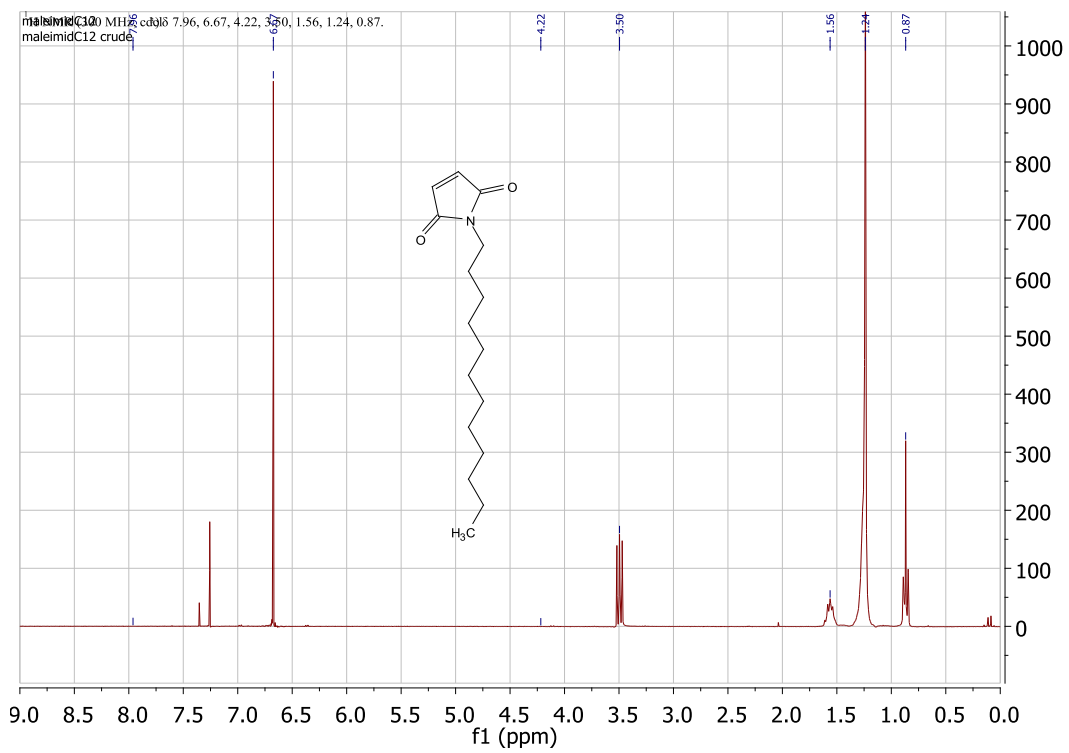
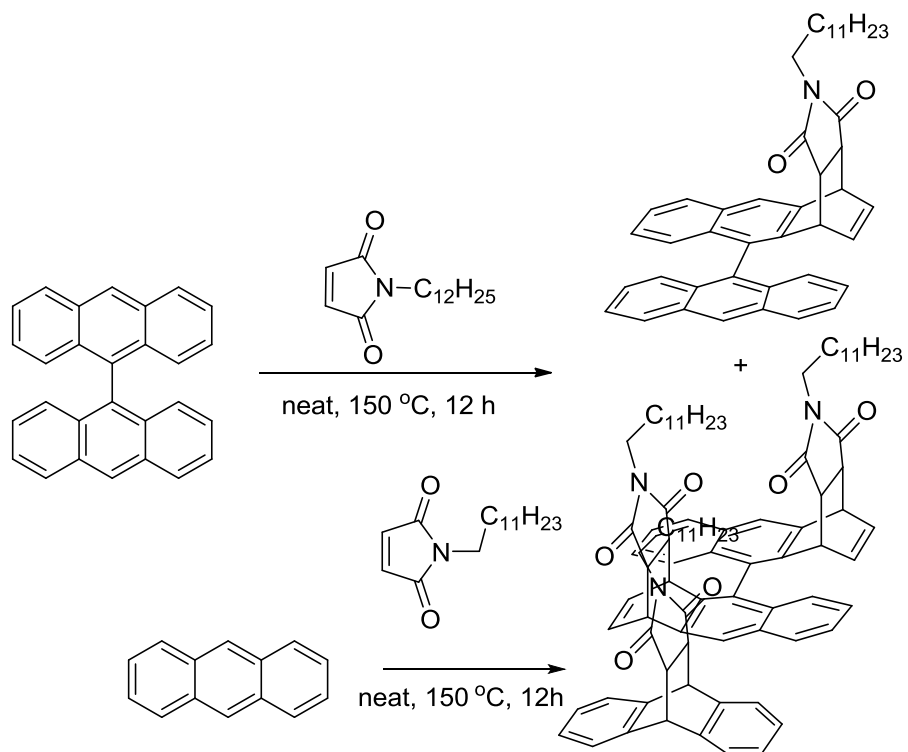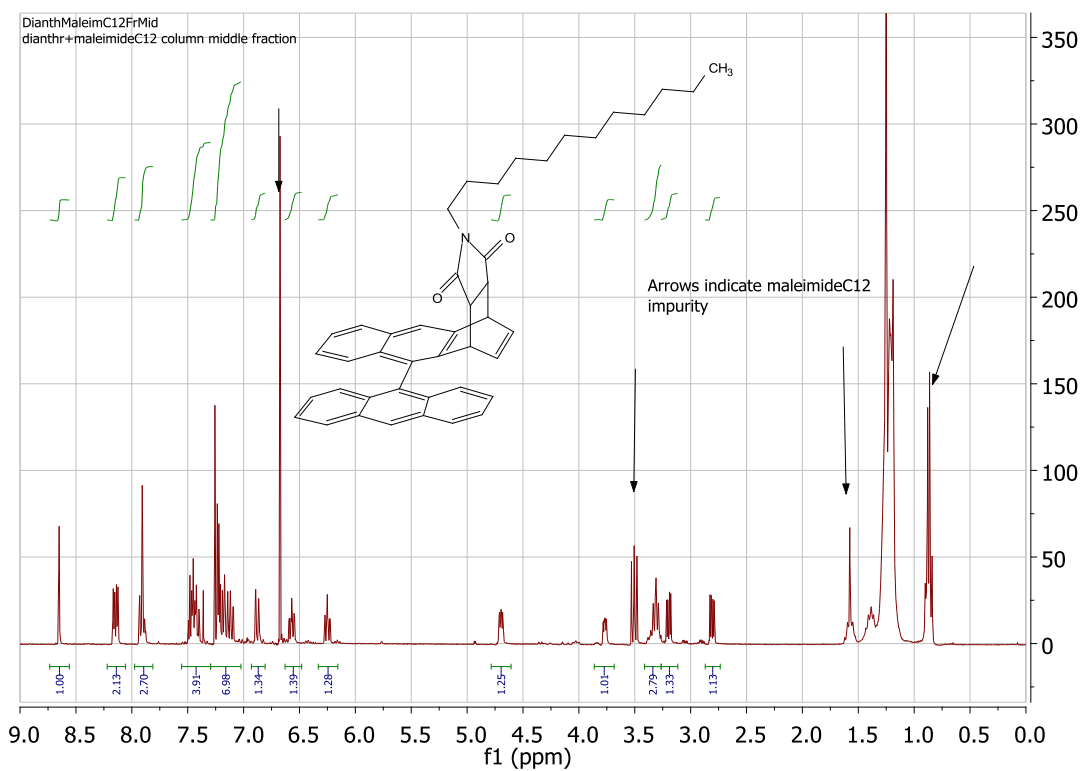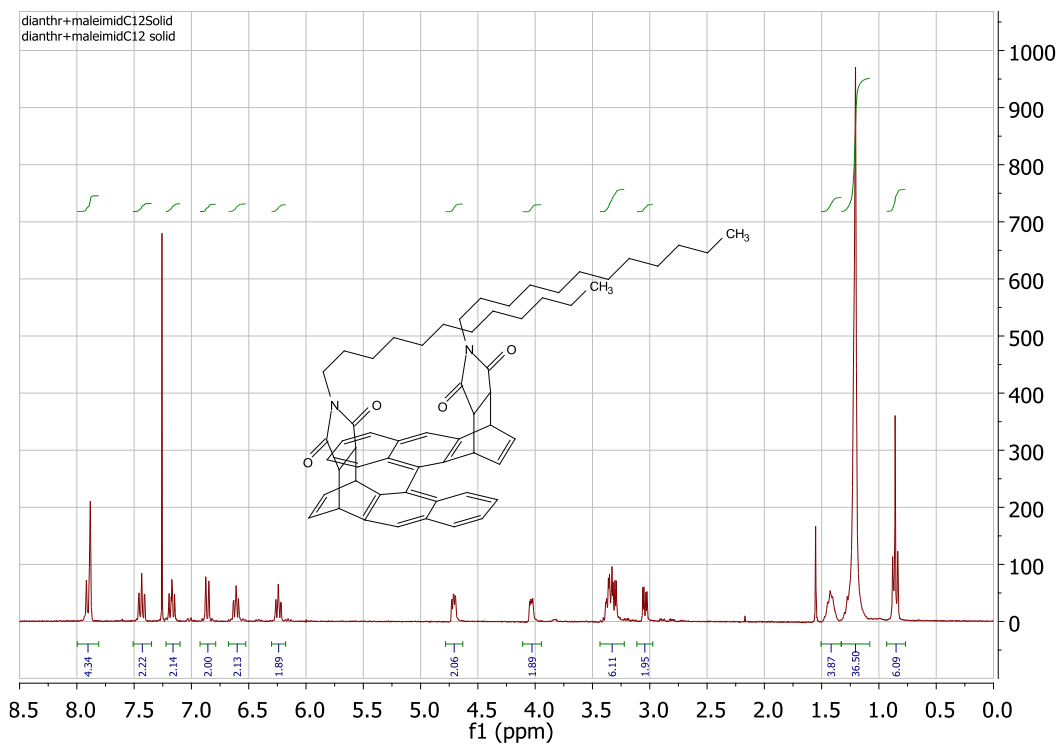**Figure A. 1– ¹H NMR spectrum of Maleimide-C12. Solvent: CDCl₃**
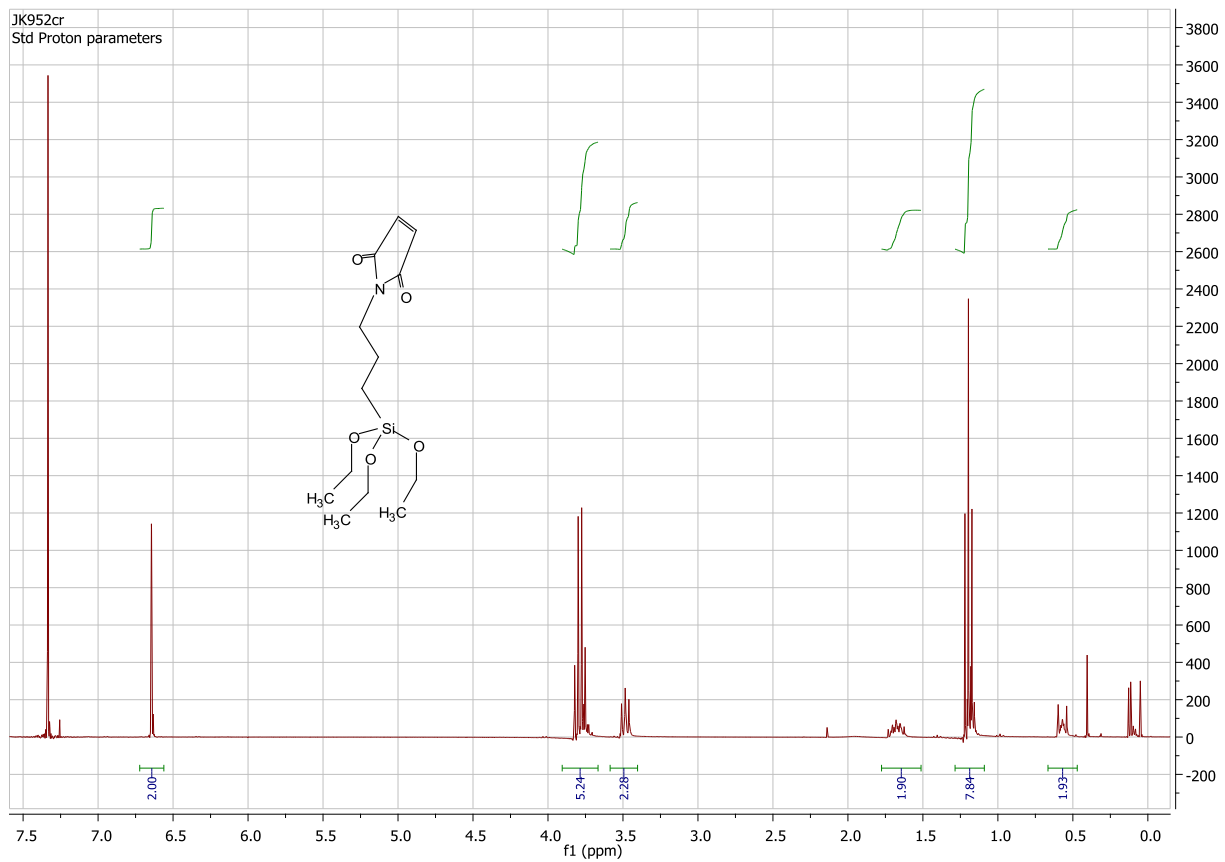
Figure A. 2 ^{1}H NMR spectrum of 3-(triethoxysilyl)propyl maleimide (MPES). Solvent: CDCl$_3$
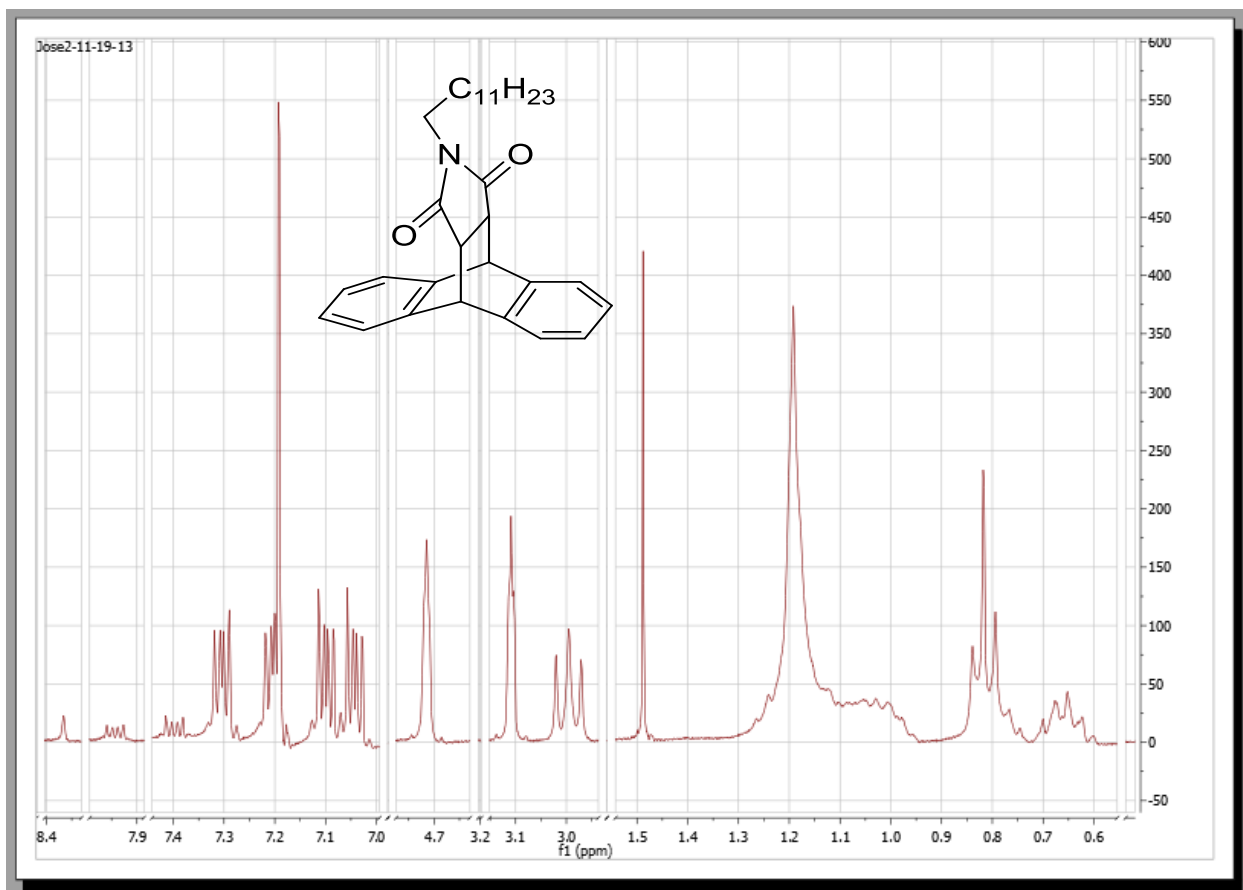
Scheme S1

Figure A. 3– ^{1}HNMR spectrum for monoadduct of 9,9'-Bianthryl and Maleimide-C12. Contains Maleimide-C12 as an impurity. Solvent: CDCl₃
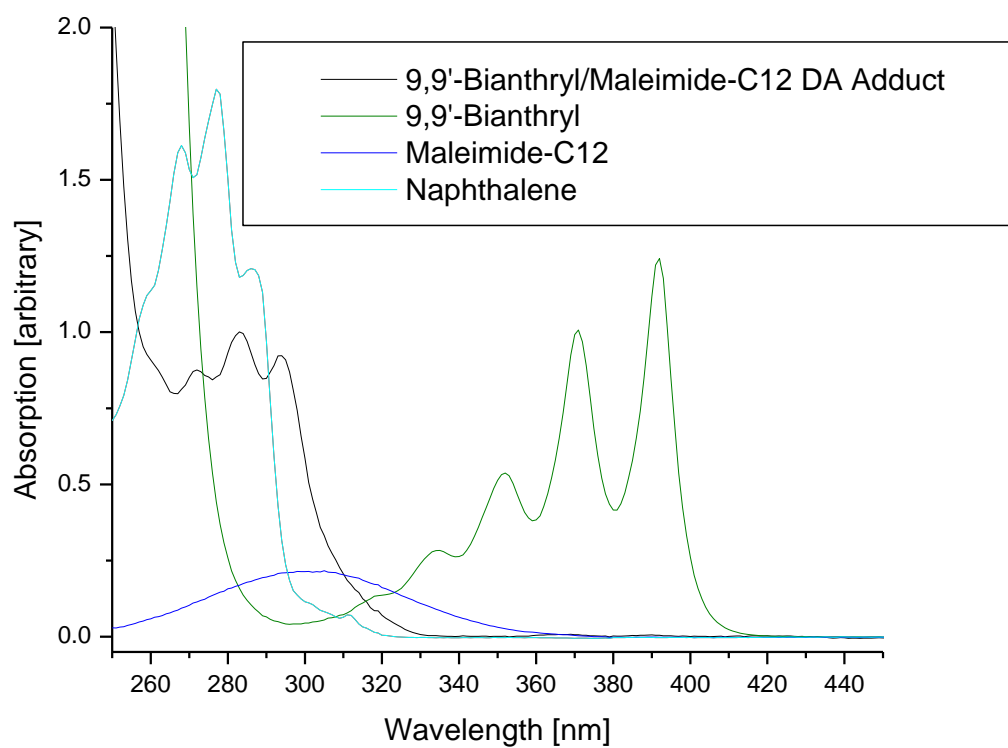
Figure A. 4– ^{1}H NMR spectrum of Diels-Alder bisadduct of 9,9'-Bianthryl with Maleimide-C12. Solvent: CDCl$_3$

Figure A. 5 – ^{1}H NMR spectrum of Diels-Alder adduct of anthracene with Maleimide-C12. Solvent: CDCl$_3$

Figure A. 6 –UV VIS spectra for Naphthalene, Maleimide-C12, 9,9'-Bianthryl and Diels-Alder bisadduct of 9,9'-Bianthryl with Maleimide-C12
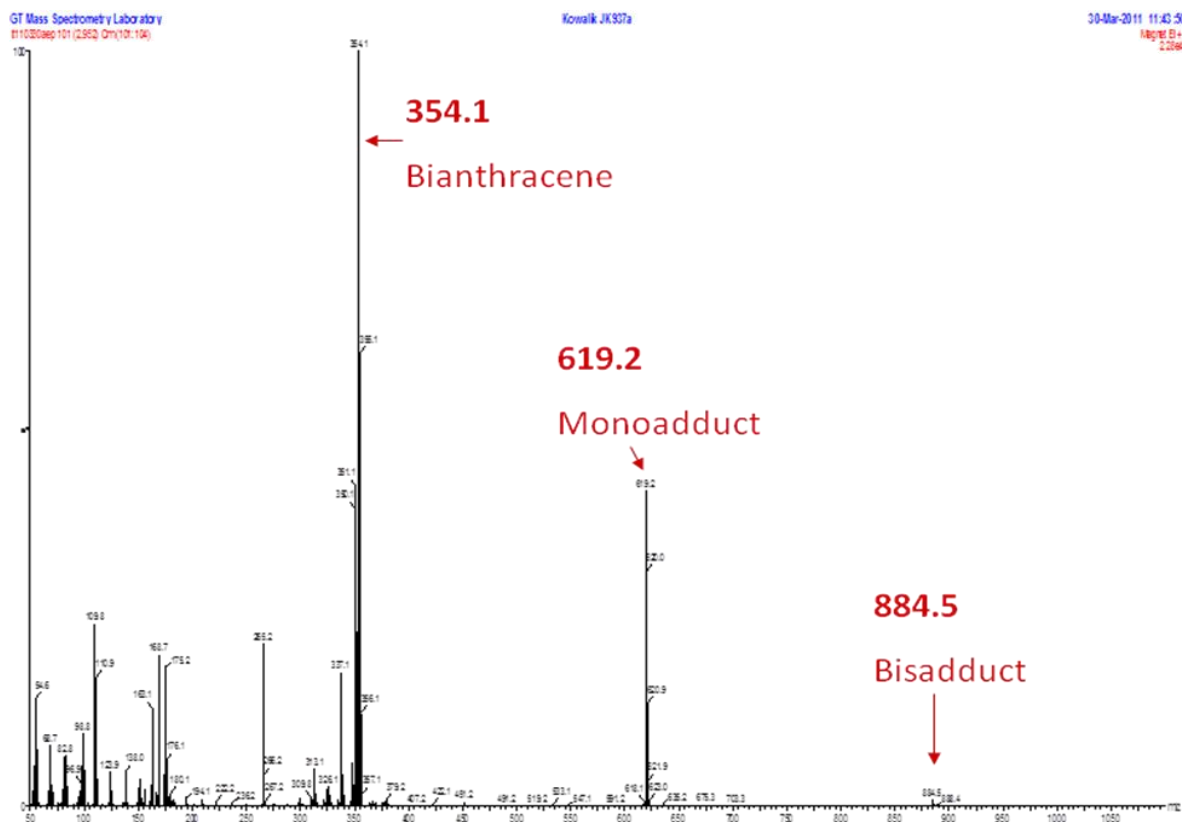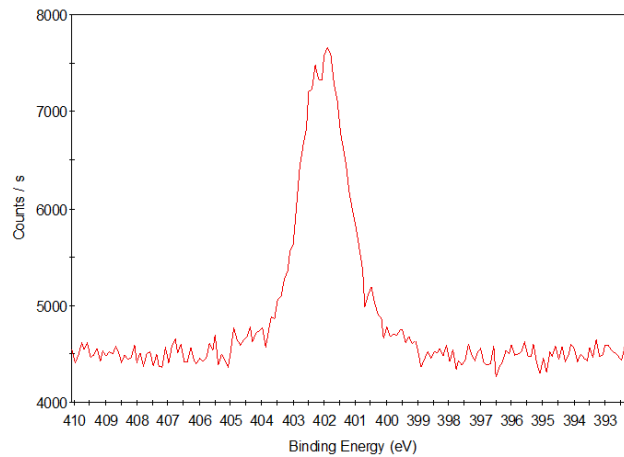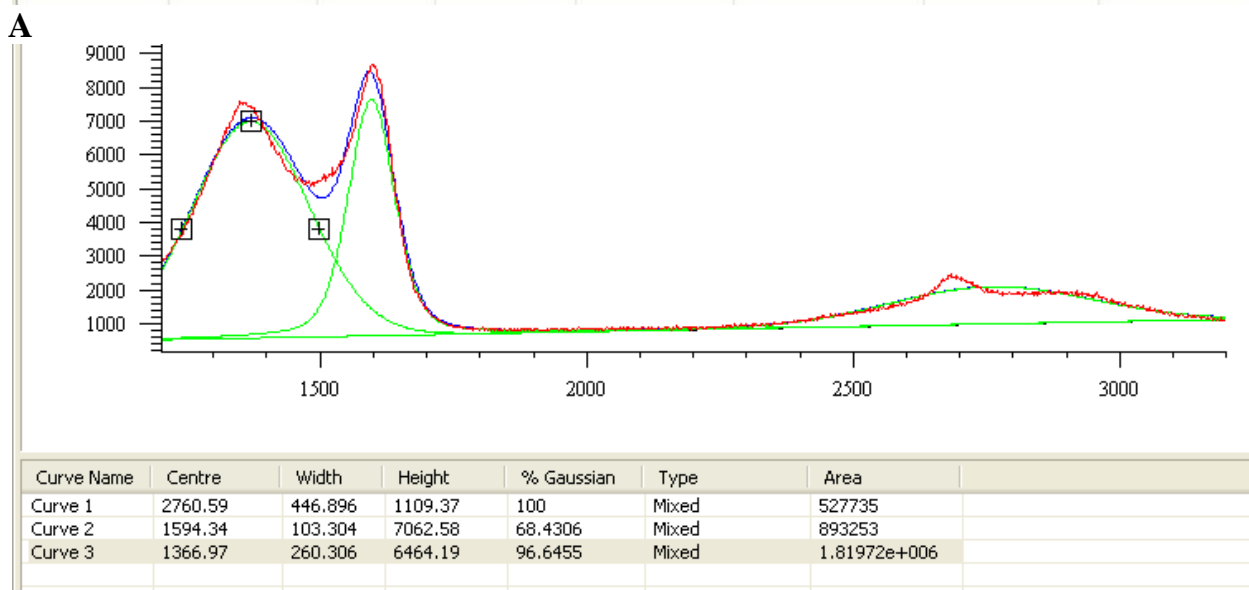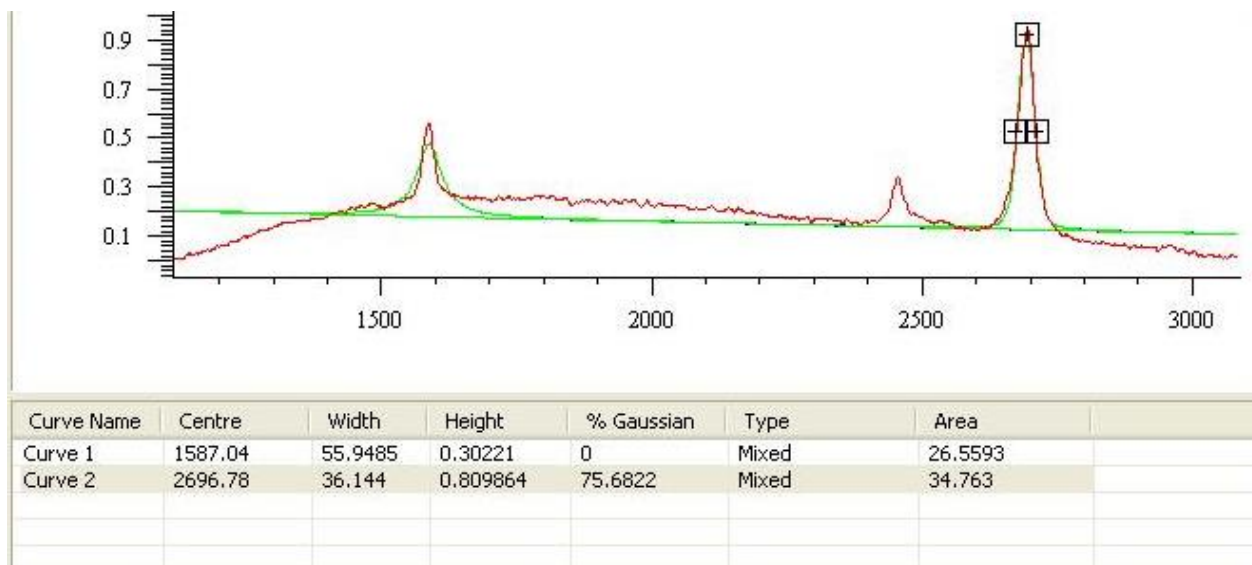
Figure A. 7– EIMS of Diels-Alder bisadduct of 9,9'-Bianthryl with Maleimide-C12

Table A1. XPS atomic percentage (Experimental) and expected percentages for MPES, A-MPES, B-MPES

	MPES		A-MPES		B-MPES	
	Expected	Experimental	Expected	Experimental	Expected	Experimental
C/N At. %	7:1	7.4 ± 1.0	21:1	17.9 ± 3.1	35:1	36.2 ± 7.1
O1s		51.9		38.8		16.4
Si2p		34.4		24.9		12.3
C1s		12.1		34.7		69.4
N1s		1.6		1.6		1.9

Figure A. 8. Typical High resolution XPS spectra for N1s for MPES, A-MPES and B-MPES immobilized on Si/SiO$_2$ surface,

Curve Name	Centre	Width	Height	% Gaussian	Type	Area
Curve 1	1587.04	55.9485	0.30221	0	Mixed	26.5593
Curve 2	2696.78	36.144	0.809864	75.6822	Mixed	34.763

A

Curve Name	Centre	Width	Height	% Gaussian	Type	Area
Curve 1	2760.59	446.896	1109.37	100	Mixed	527735
Curve 2	1594.34	103.304	7062.58	68.4306	Mixed	893253
Curve 3	1366.97	260.306	6464.19	96.6455	Mixed	1.81972e+006

B

Figure A. 9. Gauss-Lorentzian curve fits for (A) Graphene on Cu obtained from B-MPES anneal and (B) defective graphene on SiO$_2$.